Universitat
de les Illes Balears

DOCTORAL THESIS

2020

GRAVITATIONAL WAVES FROM GENERIC BINARY BLACK HOLES: FROM NUMERICAL SIMULATIONS TO OBSERVATIONAL RESULTS

by

Antoni Ramos Buades

Doctor by the Universitat de les Illes Balears

Universitat
de les Illes Balears

DOCTORAL THESIS

2020

Doctoral programme of physics

GRAVITATIONAL WAVES FROM GENERIC BINARY BLACK HOLES: FROM NUMERICAL SIMULATIONS TO OBSERVATIONAL RESULTS

by

Antoni Ramos Buades

Supervisor:

Sascha Husa

Doctor by the Universitat de les Illes Balears

List of publications derived from this thesis.

First author publications:

1) Antoni Ramos-Buades, Sascha Husa and Geraint Pratten Geraint. *Simple procedures to reduce eccentricity of binary black hole simulations.* Physical Review D **99**, 023003 (2019).

2) Antoni Ramos-Buades, Sascha Husa, Geraint Pratten, Héctor Estellés, Cecilio García-Quirós, Maite Mateu-Lucena, Marta Colleoni, Rafel Jaume. *First survey of spinning eccentric black hole mergers: Numerical relativity simulations, hybrid waveforms, and parameter estimation.* Physical Review D **101**, 083015 (2020).

3) Antoni Ramos-Buades, Patricia Schmidt, Geraint Pratten, Sascha Husa. *Validity of common modelling approximations for precessing binary black holes with higher-order modes.* Physical Review D **101**, 103014 (2020).

Other short author publications:

a) Geraint Pratten, Sascha Husa, Cecilio García-Quirós, Marta Colleoni, Antoni Ramos-Buades, Héctor Estellés, Rafel Jaume. *Setting the cornerstone for the IMRPhenomX family of models for gravitational waves from compact binaries: The dominant harmonic for non-precessing quasi-circular black holes.* arxiv:2001.1142 [gr-qc] (2020). Submitted to Physical Review D.

b) Cecilio García-Quirós, Marta Colleoni, Sascha Husa, Héctor Estellés, Geraint Pratten, Antoni Ramos-Buades, Maite Mateu-Lucena, Rafel Jaume. *IMRPhenomXHM: A multi-mode frequency-domain model for the gravitational wave signal from non-precessing black-hole binaries.* arXiv:2001.10914 [gr-qc] (2020). Submitted to Physical Review D.

c) Geraint Pratten, Cecilio García-Quirós, Marta Colleoni, Antoni Ramos-Buades, Héctor Estellés, Maite Mateu-Lucena, Rafel Jaume, Maria Haney, David Keitel, Jonathan E. Thompson, Sascha Husa. *Let's twist again: computationally efficient models for the dominant and sub-dominant harmonic modes of precessing binary black holes.* arXiv:2004.06503 [gr-qc] (2020). Submitted to Physical Review D.

d) Héctor Estellés, Antoni Ramos-Buades, Sascha Husa, Cecilio García-Quirós, Marta Colleoni, Leïla Haegel and Rafel Jaume. *IMRPhenomTP: A phenomenological time domain model for dominant quadrupole gravitational wave signal of coalescing binary black holes.* arxiv:2004.08302 [gr-qc] (2020). Submitted to Physical Review D.

During the last four years I have been a member of the LIGO Scientfic Collaboration, which in that time has published 40 scientific articles where I appear as a co-author.

Resum (en català)

Aquesta tesi és un recull del treball realitzat en els darrers quatre anys d'investigació enfocats a la producció de simulacions de relativitat numèrica de forats negres binaris en configuracions genèriques, així com a l'anàlisi de les ones gravitacionals extretes de dites simulacions, les seves conseqüències pel models de formes d'ones gravitacionals existents i les seves implicacions per a la cerca i l'estimació dels paràmetres d'aquests sistemes en la natura.

Per començar, he estudiat la prescripció de paràmetres inicials en les simulacions de relativitat numèrica. Un problema ben conegut a relativitat numèrica és la dificultat d'obtenir simulacions de forats negres en òrbites quasi-circulars, degut a imprecisions en la generació de les dades inicials que provoquen òrbites quasi-el·líptiques amb una excentricitat residual. El primer projecte d'aquesta tesi ha estat el desenvolupament d'un procediment iteratiu, senzill i computacionalment eficaç per a la reducció de l'excentricitat a simulacions de relativitat numèrica de forats negres binaris, veure Cap. 4. Amb aquest mètode s'han generat formes d'ona gravitacionals quasi-circulars amb una excentricitat negligible, $e \sim \mathcal{O}\left(10^{-4}\right)$, que han estat utilitzades pel nostre grup per generar models quasi-circulars de formes d'ona gravitacionals.

La flexibilitat del mètode anterior permet no tan sols reduir l'excentricitat de les simulacions numèriques, sinó també augmentar-la. Aquest fet ha permès la generació d'un banc de més de 60 simulacions de relativitat numèrica amb excentricitat moderada $e \leq 0.5$. Aquest ha estat el segon projecte d'investigació de la tesi, veure Cap. 5. Amb aquest grup de simulacions s'han generat formes d'ona híbrides pel mode dominant $(2,2)$ entre les ones obtingudes per la teoria post-Newtoniana i les de relativitat numèrica. A més, s'ha estimat les limitacions dels models quasi-circulars actuals per estimar paràmetres d'aquestes fonts. Els resultats obtinguts demostren que els models quasi-circulars de formes d'ona que inclouen modes subdominants redueixen el biaix en alguns paràmetres com la distància i el ràtio de massa, respecte a models sense modes subdominants.

Per altra banda, durant el doctorat també s'han estudiat les limitacions de dues aproximacions utilitzades habitualment per models d'ona quasi-circulars amb espins precessants, veure Cap. 6. Aquestes dues aproximacions s'han analitzat emprant únicament simulacions de relativitat numèrica incloent modes subdominants. Els resultats obtinguts confirmen el bon funcionament de les aproximacions pels modes dominants $(2, \pm 2)$, mentre que pel modes subdominants s'observa una degradació important degut a diferent causes depenent del mode estudiat, per exemple, els modes $(2, \pm 1)$ són molt sensibles a les asimetries entre modes que les aproximacions negligeixen, mentre que els modes $(4, \pm 3)$ i $(3, \pm 2)$ pateixen mescla de modes en la part del decaïment de l'ona que les aproximacions no tenen en compte.

Finalment, s'ha analitzat la sensibilitat de dos algorismes de cerca emprats per les col·laboracions LIGO i Virgo durant el segon període d'observació O2 per detectar

senyals completes d'ones gravitacionals procedents de binàries de forats negres eccèntriques, veure Cap. 7. En aquest treball preliminar s'ha quantificat l'impacte de l'excentricitat sobre dos algorismes de cerca: un codi de filtrat adaptat basat en el coneixement de la morfologia de la senyal, i un codi de cerca sense modelat. En aquest estudi s'estima per primera vegada la sensibilitat d'ambdós algorismes injectant senyals excèntriques calculades a partir de simulacions de relativitat numèrica incloent espins alineats amb el moment angular orbital del sistema. Els resultats obtinguts mostren una major degradació de la sensibilitat de l'algorisme de filtrat adaptat a mesura que l'excentricitat augmenta, mentre que la sensibilitat de l'algorisme sense modelat no es veu quasi afectada per l'increment de l'excentricitat, i per tant, es pot identificar aquest darrer com una eina robusta per a la detecció de senyals excèntriques.

Resumen (en castellano)

Esta tesis recoge el trabajo realizado en los últimos cuatro años de investigación enfocados en la producción de simulaciones de relatividad numérica de agujeros negros binarios en configuraciones genéricas, así como en el análisis de las ondas gravitacionales extraídas de dichas simulaciones, sus consecuencias para los modelos de formas de ondas existentes y sus implicaciones para la búsqueda y la estimación de los parámetros de dichos sistemas en la naturaleza.

Para empezar, he estudiado la prescripción de parámetros iniciales en las simulaciones de relatividad numérica. Un problema bien conocido en relatividad numérica es la dificultad de obtener simulaciones de agujeros negros en órbitas casi-circulares, debido a imprecisiones en la generación de los datos iniciales que provocan órbitas casi-elípticas con una excentricidad residual. El primer proyecto de esta tesis ha sido el desarrollo de un procedimiento iterativo, sencillo y computacionalmente eficaz para la reducción de la excentricidad en simulaciones de relatividad numérica de agujeros negros binarios, ver Cap. 4. Con este método se han generado formas de onda gravitacionales casi-circulares con una excentricidad negligible, $e \sim \mathcal{O}\left(10^{-4}\right)$, que han sido usadas por nuestro grupo para generar modelos de formas de onda casi-circulares.

La flexibilidad del método anterior permite no solo reducir la excentricidad de las simulaciones numéricas, sino también aumentarla. Este hecho ha permitido la generación de un banco de más de 60 simulaciones de relatividad numérica con excentricidad moderada $e \leq 0.5$. Este ha sido el segundo proyecto de investigación de la tesis, ver Cap. 5. Con este grupo de simulaciones he generado formas de onda híbridas para el modo dominante $(2, 2)$ entre las ondas obtenidas a partir de la teoría post-Newtoniana y las de relatividad numérica. Además, con colaboradores he estimado las limitaciones de los modelos casi-circulares actuales para estimar los parámetros de estas fuentes. Los resultados obtenidos demuestran que los modelos casi-circulares de formas de onda que incluyen modos subdominantes reducen el sesgo en algunos parámetros como la distancia y el ratio de masa, respecto a los modelos sin modos subdominantes.

Por otro lado, durante el doctorado también se han estudiado las limitaciones de dos aproximaciones utilizadas comúnmente para modelos de onda casi-circulares con espines precesantes, ver Cap. 6. Estas dos aproximaciones se han analizado usando únicamente simulaciones de relatividad numérica incluyendo modos subdominantes. Los resultados obtenidos confirman el buen funcionamiento de las aproximaciones para los modos dominantes $(2, \pm 2)$, mientras que para los modos subdominantes se observa una degradación importante debido a diferentes causas dependiendo del modo estudiado, por ejemplo, los modos $(2, \pm 1)$ son muy sensibles a las asimetrías entre modos que las aproximaciones negligen, mientras que los modos $(4, \pm 3)$ y $(3, \pm 2)$ padecen mezcla de modos en la parte del decaimiento de la onda que las aproximaciones no tienen en cuenta.

Finalmente, con colaboradores he analizado la sensibilidad de dos algoritmos de búsqueda, utilizados por las colaboraciones LIGO y Virgo durante el segundo período de observación O2, para detectar señales completas de ondas gravitacionales procedentes de binarias de agujeros negros excéntricos, ver Cap. 7. En este trabajo preliminar se ha cuantificado el impacto de la excentricidad sobre dos algoritmos de búsqueda: un código de filtrado adaptado y un código de búsqueda sin modelado. En este estudio se estima por primera vez la sensibilidad de ambos algoritmos inyectando señales excéntricas calculadas a partir de simulaciones de relatividad numérica. Los resultados muestran una mayor degradación de la sensibilidad del algoritmo de filtrado adaptado a medida que aumenta la excentricidad, mientras que el algoritmo sin modelado no se ve casi afectado por el aumento de la excentricidad, y por tanto, se puede identificar este último como una herramienta robusta para la detección robusta de señales excéntricas.

Summary (in English)

This thesis gathers all the work done in my last four years of research focused on the production of numerical relativity simulations of generic binary black holes, as well as the analysis of the gravitational waveforms from these simulations and their implications for searches and parameter estimation on those systems.

I have started studying the prescription of initial parameters in numerical relativity simulations. A well known problem in numerical relativity is the difficulty to obtain simulations of black holes orbiting in quasi-circular orbits due to inaccuracies of the initial data, which cause elliptical orbits with residual eccentricity. The first project of the thesis has been the development of a simple, iterative and computationally efficient procedure to reduce the eccentricity in binary black hole numerical relativity simulations, see Chap. 4. With this method we have produced quasi-circular waveforms with negligible eccentricity, $e \sim \mathcal{O}\left(10^{-4}\right)$, which have been used in our group to generate quasi-circular waveform models.

The flexibility of the previous method permits not only the reduction of the eccentricity, but also increasing it. Using this fact I have produced a data set of more than 60 numerical relativity simulations with moderate eccentricity $e \leq 0.5$. This has been the second project of the thesis, see Chap. 5. Taking this set of simulations, with collaborators I have generated hybrid waveforms for the dominant $(2, 2)$ mode between post-Newtonian and numerical relativity waveforms. Moreover, we have estimated the limitations of the current quasi-circular waveform models to estimate the parameters from those sources. We have found that the quasi-circular models which include higher order modes reduce the bias in some parameters like the mass ratio and luminosity distance, with respect to those models not including higher order modes.

Furthermore, during the Ph.D. I have also studied the limitations of two approximations commonly used by precessing quasi-circular waveform models, see Chap. 6. These two approximations have been analysed using exclusively numerical relativity simulations including higher order modes. The results confirm the good performance of the approximations for the $(2, \pm 2)$ modes, while one observes a clear degradation for higher order modes due to different reasons depending on the considered mode. For instance, the $(2, \pm 1)$ modes are found to be very sensitive to asymmetries which the approximations neglect, while the $(4, \pm 3)$ and $(3, \pm 2)$ modes, have mode-mixing in the ringdown part which is not properly taken into account by the simple approximations.

Finally, with collaborators I have analysed the sensitivity of two search pipelines, used by the LIGO and Virgo collaborations during the O2 Science Run, to the full gravitational wave signal of eccentric binary black holes, see Chap. 7. In this preliminary work we have quantified the impact of eccentricity on two search pipelines: a matched-filter and an unmodeled search algorithm. We have for the first time estimated the sensitivity of both algorithms injecting eccentric signals computed from

numerical relativity simulations. The results show a larger degradation of the sensitivity of the matched-filter algorithm with increasing eccentricity, while the sensitivity of the unmodeled search algorithm remains barely unaffected to the increase of eccentricity, thus, we consider the latter one a robust tool to detect such eccentric signals.

Acknowledgements

I would like to first thank my supervisor Prof. Sascha Husa not only for giving me the invaluable opportunity to make this thesis with him about gravitational waves at the apogee of the field with the first direct gravitational wave detection, but also for spending a lot of his time on discussions about the projects of this thesis and, especially, for his mentoring in the first years of this thesis which led to Chap. 4.

I would also like to thank Prof. Alicia Sintes, the leader of the Gravitational Wave Phyiscs group, for her financial support to attend conferences and travel to several collaborations meetings, and particularly, for letting me be part of her teaching staff and instructing me on teaching undergraduate students.

I would like to express my gratitude to Prof. Patricia Schmidt for allowing me to make a short stay at Radboud university. The time I spent working there with her on precession challenge myself. I would like to thank her support and the one from Dr. Geraint Pratten to make the presentation at Amsterdam university when I had a bad cold. The work done at Chap. 6 would have not been possible without their invaluable help and support. I also really appreciate the opportunity to meet new colleagues like Glenn, an extraordinary person and astrophysicist, who really ease my stay allowing me to play football in his team, and he is the best Belgium football player I know, and also old friends, like Martina and Jakub, thanks for inviting me to your Pumpkin party, I wish you the best for your life, you will always have a friend in Mallorca.

My last stay abroad was at Zurich university collaborating with Drs. Maria Haney and Shubhanshu Tiwari. I would like to first express my gratitude to Dr. Maria Haney for her financial support to make the visit and her lessons about eccentric post-Newtonian theory. I would like to thank Dr. Shubhanshu Tiwari for introducing me to a new topic of the gravitational wave field, like the searches of gravitational waves and for his invaluable time explaining me the basics of the unmodeled search algorithms for gravitational wave detections, which led to the work presented in Chap. 7. I would also like to thank Prof. Jetzer and the students, Michael, Dixeena and Adrien for their hospitality during my visit.

At this point I would like to express my gratitude to my office colleagues, who I have spent much of my time with and from each of them I have learnt different things, which have made me improve as a scientist and person. I would like to first mention Cecilio, we started our thesis the same year in the group and he has been a great support during my thesis, not only for his extraordinary intelligence and scientific capacity, but also as a reference, colleague and the most important, a friend. Rafel, the visualizer expert of the group and a better colleague, thanks for being a friend and the soul of the group. Héctor, one of the most generous persons I ever met, thanks for many valuable discussions on precession and for being such a good host in Valencia's meeting. Maite, an exceptional young researcher with an outstanding future, thanks

for helping me to learn the basics of parameter estimation. Pep, a brilliant researcher and a reference to follow, thanks for being a friend in so many conferences. Also to Marta, Rodrigo, Leïla and Alicia for your kindness and I wish you all the best in your future.

Dono també les gràcies a tots els meus companys de fútbol del Pla de Na Tesa que m'han permès ser el seu amic i capità durant aquests anys. Els entrenaments i els partits amb ells m'han permès desconnectar del món científic i disfrutar d'un esport que duc amb mí des de petit. Amb aquest esport he après a valorar el treball necessari per aconseguir les victòries i la importància d'aprendre de les derrotes per seguir millorant.

Els darrers però no per això menys importants, la meva família. Els meus pares Magdalena i Ramón, i el meu germà Damià gràcies per la vostra paciència infinita i el vostre suport incondicional. Al meus padrins Damià i Joana per ensenyar-me la taula de multiplicar i la importància de la constància en el treball. Tots vosaltres sou la força que m'impulsa a seguir millorant com a científic i ésser humà.

Contents

Preface

This thesis is composed of two different parts manifestly separating what corresponds to *Introductory concepts* from the *Original research results*. The first part introduces basic notions about gravitational waves from binary black hole coalescences, which is the main topic of the thesis, while the second part collects original scientific articles, which have been published or sent for publication to an international peer reviewed journal by the author of the thesis. The main reasons for using the previous structure are that the first part of the thesis has a pedagogical goal for the reader, but also for myself to thoroughly review derivations and fundamental concepts in the literature of gravitational wave physics. An additional purpose of the first part is to provide a broader introduction to basic concepts implicitly used to produce the original scientific results. Furthermore, with this format one clearly differentiates the original scientific results from results that can already be found in the literature, easing the reading and reviewing of the text.

The first three chapters in Part I provide an overview of basic concepts of the research field, which can be found in many textbooks and research articles from the literature. Specifically, Chap. 1 introduces the topic of gravitational radiation from compact binaries, Chap. 2 summarizes possible solutions to the two body problem within general relativity and Chap. 3 shortly describes data analysis techniques applied to gravitational waves emitted by compact binaries.

In Part II we present the main research lines of the thesis focused on gravitational waves from eccentric binary black holes and quasi-circular precessing binaries.

Regarding precessing binaries, we analyse two main approximations used to model the waveforms from quasicircular precessing binary black holes by phenomenological waveform models in Chap. 6. We discuss the validity of those approximations using numerical relativity simulations including higher order modes, with special attention to their performance and accuracy for the $(l, |m|) = \{(2,2), (2,1), (3,3), (3,2), (4,3), (4,4)\}$ modes.

Regarding eccentric binaries, we set the basis to model the waveform from such binaries in this thesis by developing new tools and methods and by adapting the current infrastructure of our group for quasicircular binaries to the eccentric ones. This work is expressed in the research projects of Chaps. 4, 5 and 7. In Chap. 4 we develop a new procedure to specify and measure the initial value of the eccentricity parameter in numerical relativity simulations. The method allows one to efficiently produce numerical relativity simulations controlling the amount of initial eccentricity at a given initial orbital separation of the binary.

Using this method we produce a numerical relativity data set of 60 simulations with moderate initial eccentricity $e \leq 0.5$ including dimensionless spin aligned with the orbital angular momentum of the system up to 0.75. We present this dataset in Chap. 5, where we study its properties, produce hybrid waveforms by gluing them

to post-Newtonian waveforms and show examples of their implications for parameter estimation with current waveform models used by the LIGO and Virgo collaborations.

Finally, in Chap. 7 we expand on the data analysis implications of the eccentric numerical relativity waveforms generated in Chap. 5 by estimating the sensitivity of two search pipelines used by the LIGO and Virgo collaborations during the O2 Science Run to them. We quantify the effect of eccentricity on two search pipelines: a matched-filter and an unmodeled search algorithm. The preliminary results show a large degradation of the sensitivity of the matched-filter algorithm with increasing eccentricity, while the sensitivity of the unmodeled search algorithm remains barely unaffected to the increase of eccentricity, hence, we identify the latter one as a solid tool to search for those signals.

We also take the opportunity to set notation and define some useful quantities. In most of the numerical relativity studies in this thesis we work with *geometrized units* in which $c = 1$ and $G = 1$, so that the mass and length are measured in units of time. We define the following quantities:

- Total mass: $M = m_1 + m_2$.

- Mass ratio: $q = \frac{m_1}{m_2}$, with $m_1 > m_2$.

- Symmetric mass ratio: $\eta = \frac{m_1 m_2}{m_1 + m_2} = \frac{q}{(1+q)^2}$, sometimes also referred to as ν in the literature.

- Chirp mass: $\mathcal{M} = \frac{(m_1 m_2)^{3/5}}{(m_1 + m_2)^{1/5}} = M \eta^{3/5}$.

- Post-Newtonian expansion parameter: $x = (\frac{GM\omega}{c^3})^{2/3}$.

Part I

Introductory concepts

Chapter 1

General introduction to gravitational waves

Guided by the equivalence principle, that all bodies fall the same way in a gravitational field, and Mach's principle, that all the matter in the universe affects the local motion of particles and vice versa, Einstein presented in 1916 [1] the theory of *general relativity* (GR), which reformulated gravitation as a geometric consequence of the distribution of masses located in spacetime. During the last century, GR has aced all the tests it has been subjected to. Starting with the 1919 solar eclipse [2], which made Einstein become famous, the description of the perihelion precession of Mercury [3], passing through the description of the rate of decay of the period of the Hulse-Taylor pulsar [4, 5, 6], and very recently, in 2015 with the first direct gravitational wave detection by the LIGO detectors [7].

Gravitational waves (GW) were one of the first predictions of GR [8]. They are ripples of spacetime caused by the motion of massive compact bodies. These warpages of the spacetime fabric travel through the Universe at the speed of light. As we will see, gravitational waves detectable by interferometric ground-based detectors like Advanced LIGO [9] and Advanced Virgo [10], are generated by the most catastrophic events of the universe like the merger of binary black holes (BBH) or binary neutron stars (BNS).

During the first observing run (O1) of the LIGO detectors in 2015, the first direct detection of GW from a BBH merger opened a new era of GW astronomy [7]. This detection was followed by several other GW detections coming from BBHs during O1 and the second observing run (O2) [11]. Apart from black holes in O2 there was also the first detection of GWs from a binary neutron star (BNS) merger [12], which supposed a breakthrough in GW astronomy, not only because it was the first detection of GWs from a BNS merger, but because it opened the path to multi-messenger astronomy by combining the information coming from the detection of gravitational waves with that from *electromagnetic* (EM) radiation [13, 14]. The combination of information from these two sources of radiation allowed a detailed description of this binary neutron star system, setting some constraints on its equation of state (EOS) [15] and the amount of elements ejected during the merger [16]. Furthermore, the precise location of the system thanks to the combination of both sources of radiation allowed an estimation of the the Hubble parameter [17], rate of expansion of the universe, which is independent from that measured by the *Planck* mission [18] and that calculated using type Ia supernovae (SNIa) calibrated with Cepheid distances [19]. The value for the Hubble parameter, H_0, calculated using GW information lies within the error bars of the values from the *Planck* mission and SNIa observations. Further multi-messenger detections of BNS systems will constrain more and more the values

of the Hubble parameter alleviating the current tension in its measurement between the values calculated from the cosmic microwave background and the supernovae type Ia.

During the preparation of this thesis the LIGO and Virgo detectors have been in the third observing run (O3). For O3 the detectors have upgraded their sensitivity to increase their detection volume, which increases the number of GW detections with respect to O1 and O2. Tens of GW candidates have already been detected [20] and public alerts are sent each time a GW candidate hits the detection threshold [21] to facilitate the detection of an EM counterpart. This is a clear signature of the start of the multi-messenger astronomy era, which will allow a more precise description of our universe and it will permit the measurement of cosmological parameters so decisive as H_0.

The detection of GWs also allows to test the validity of GR in the strong field regime. Using the GW events from compact binary coalescences (CBC) during O1/O2 the LIGO and Virgo scientific collaborations have already set some constraints on general relativity [22] with distinct types of tests aimed to constrain some physical parameters like the graviton mass or the speed of GWs. These tests rely not only on the current ability of the detectors to measure the passing gravitational wave radiation, but very strongly on the accuracy of the waveform models used to describe those GW signals. These waveform models are generated upon calibration to *numerical relativity* (NR) simulations. There are two main difficulties to generate such models, the first is the huge computational cost of the NR simulations describing CBCs mergers, and the second one is the construction of such models for the large parameter space of generic binary systems. Current uncertainties in GW detections are dominated by statistical errors set by the level of *signal-to-noise ratio* (SNR) the current detectors are able to achieve. However, the increase in the sensitivity of the ground-based detectors and the upcoming space mission, LISA, will augment our ability to detect GW from a large variety of astrophysical systems. This future scenario will require huge advances in the whole field of gravitational physics in the upcoming decade in order to be able to extract the maximum information from the upcoming detections so that we will construct a more accurate description of the universe providing answers to open questions in astrophysics, cosmology and fundamental physics.

1.1   Gravitational waves

Gravitational waves are perturbations of the spacetime metric propagating at the speed of light. Their nature is very different from the electromagnetic waves. This is why the detection of gravitational waves is usually claimed to open a new window to the Universe. In this chapter we will briefly review their basic properties and the fundamental equations governing their behaviour.

1.1.1   The Einstein equations: covariance and hyperbolicity

According to Einstein's general relativity the relation between the matter/energy content of the spacetime and its geometry is given by Einstein's equations

$$G_{ab} = \frac{8\pi G}{c^4} T_{ab}, \tag{1.1}$$

where G_{ab} denotes the Einstein tensor and T_{ab} indicates the stress-energy tensor of the matter field, c and G are the speed of light and Newton's gravitational constant, respectively. The left hand side of Eq. (1.1) represents the geometry of the spacetime. If we restrict to a four dimensional space, then the spacetime can be described by a four-dimensional Lorentzian manifold. The notion of distance is introduced in the manifold through the metric tensor g_{ab}, which defines the invariant spacetime interval between two nearby points of the manifold according to

$$ds^2 = g_{ab}dx^a dx^b, \tag{1.2}$$

where ds represents the line element between two nearby points and dx^a the infinitesimal displacement of the spacetime coordinates x^a. The metric tensor is at the core of the definition of the Einstein tensor of Eq. (1.1), which can be written in terms of the Ricci tensor, R_{ab}, as

$$G_{ab} = R_{ab} - \frac{1}{2}g_{ab}R, \tag{1.3}$$

where $R = R_{ab}g^{ab}$ is the Ricci scalar. The Ricci tensor is the trace part of the Riemann tensor, $R_{ab} = R_{acbd}g^{cd}$. The Riemann tensor can be written in a coordinate basis in terms of the Christoffel symbols, Γ^a_{bc}, as

$$R^a_{bcd} = \partial_c \Gamma^a_{bd} - \partial_b \Gamma^a_{cd} + \Gamma^e_{bd}\Gamma^a_{ce} + \Gamma^e_{bd}\Gamma^a_{ce}. \tag{1.4}$$

Recall that the connection coefficients, Christoffel symbols, can be written in a coordinate basis as

$$\Gamma^a_{bc} = \frac{1}{2}g^{ad}\left(\partial_b g_{dc} + \partial_c g_{db} - \partial_d g_{bc}\right). \tag{1.5}$$

Hence, Eq. (1.5) explicitly shows the relation of the left hand side of Eq. (1.1) with the geometry of the Lorentzian manifold on which the physical events occur.

General relativity is a covariant theory, i.e., the theory is invariant under any arbitrary change of coordinates. This huge symmetry group of arbitrary coordinates systems can be mathematically described through arbitrary diffeomorphisms,

$$x^a \to x'^a(x), \tag{1.6}$$

where $x'^a(x)$ has to be differentiable with respect to x^a, invertible and with a differentiable inverse. The covariance of the theory described by Eq. (1.6) implies the following transformation law of the metric tensor,

$$g'_{ab}(x') = \frac{\partial x^c}{\partial x'^a}\frac{\partial x^d}{\partial x'^b}g_{cd}(x). \tag{1.7}$$

Equation (1.7) is also known as the gauge freedom or gauge symmetry of general relativity in the literature. This shows that by an appropriate choice of coordinates one can reduce the number of components of $g'_{ab}(x')$, such that one has the metric tensor in the desired form to solve Einstein's equations.

Furthermore, a careful check of Eq. (1.1) shows that Einstein's equation are hyperbolic-type equations because the Riemann tensor in the left hand side contains second order terms in the metric derivatives together with non-linear terms in the metric and metric derivative. As a consequence, Einstein's equations are equivalent to a system of coupled differential equations in g_{ab}, which thanks to the Lorentzian signature of the metric, the purely time component has a different sign from the spatial ones implying

that the equations are of hyperbolic nature. Hence, many introductory texts first introduce the scalar wave equation

$$\Box\phi = \left(-\partial_t^2 + \Delta\right)\phi = 0, \tag{1.8}$$

where Δ is the Laplacian. Analysing the solution of Eq. (1.8), which is a much simpler hyperbolic equation, eases afterwards the understanding of the much more complicated system of partial differential equations which are the Einstein equations. As shown by Landau and Lifshitz [23] Einstein's equations can be recast, after imposing certain gauge conditions, in a form which shows their hyperbolic nature. Using the Landau-Lifshitz formulation Einstein's equations can be expressed as [23]

$$\partial_c\partial_d\left(\mathcal{G}^{ab}\mathcal{G}^{cd} - \mathcal{G}^{ac}\mathcal{G}^{bd}\right) = -16\pi(-g)\left(T^{ab} + t_{LL}^{ab}\right), \tag{1.9}$$

where $\mathcal{G}^{ab} = \sqrt{-g}g^{ab}$ and t_{LL}^{ab} is the Landau-Lifshitz pseudotensor composed of the second order terms of $\mathcal{G}^{ab}$ and its first derivative $\partial_c\mathcal{G}^{ab}$.
Choosing now the harmonic gauge defined by

$$\Box x^a = 0 \quad \rightarrow \partial_a\mathcal{G}^{ab} = 0, \tag{1.10}$$

where $\Box$ is the d'Alembertian operator in a curved space,

$$\Box = \frac{1}{\sqrt{-g}}\partial_a\left(\sqrt{-g}g^{ab}\partial_b\right). \tag{1.11}$$

With the gauge choice of Eq. (1.10), Eq. (1.9) can be written as

$$\sqrt{-g}\Box\mathcal{G}^{ab} = -16\pi(-g)\left(T^{ab} + t_L^{ab}L\right) + \left(\partial_c\mathcal{G}^{bd}\right)\partial_d\mathcal{G}^{ac}, \tag{1.12}$$

which displays a clear analogy with Eq. (1.8) and demonstrates that Einstein's equations can be viewed as a coupled system of 10 independent (6 equations are redundant due to the symmetry of the metric tensor) nonlinear second order partial differential hyperbolic equations for $\mathcal{G}^{ab}$. Hence, this result also implies that gravitational waves are perturbations of spacetime propagating at the speed of light, and solutions of the Einstein equations.

1.1.2   Generation of gravitational waves

In this section we briefly show using linear perturbation theory that gravitational waves are solutions of the Einstein equations and that those solutions in the four-dimensional case have only two physical degrees of freedom corresponding to two polarizations. We will not repeat the whole detailed calculation here, for details see [24, 25], but we will focus on the interpretation and discussion of the results.

Consider first a small linear perturbation of the spacetime metric, h_{ab}, around the flat-space background,

$$g_{ab} = \eta_{ab} + \epsilon h_{ab}, \quad \epsilon \ll 1, \tag{1.13}$$

where $\eta_{ab} = \text{diag}(-1, 1, 1, 1)$ is the Minkowski metric and ϵ is a small bookkeeping parameter. Note that by imposing Eq. (1.13) one chooses a specific frame, therefore, breaking the invariance of general relativity under coordinate transformations. However, there is still a residual gauge symmetry in the coordinate choice coming from the freedom to make an infinitesimal variation of order ϵ such that $x'^a = x^a + \epsilon\xi^a(x)$. This residual symmetry allows one to choose a gauge condition which, in this case, is again

the harmonic gauge, also known as Lorentz gauge in electromagnetism, condition,

$$\partial^a \bar{h}_{ab} = 0, \tag{1.14}$$

where $\bar{h}_{ab} = h_{ab} - \eta_{ab}h/2$ and $h = \eta^{ab}h_{ab}$. Replacing (1.13) in (1.1), employing the gauge condition (1.14) and assuming that T_{ab} is of order ϵ one obtains the following wave equation,

$$\Box_f \bar{h}_{ab} = -\frac{16\pi G}{c^4} T_{ab}, \tag{1.15}$$

where $\Box_f = \eta_{ab}\partial^a\partial^b$ is the flat space d'Alembertian operator. Equation (1.15) demonstrates that metric perturbations sourced by a matter field described by T_{ab} travel at the speed of light. Moreover, the combination of Eqs. (1.14) and (1.15) imply the conservation of the energy-momentum tensor

$$\partial^a T_{ab} = 0. \tag{1.16}$$

Setting for simplicity the matter term to zero, $T_{ab} = 0$, Eq. (1.15) reduces to

$$\Box_f \bar{h}_{ab} = 0, \tag{1.17}$$

which, thanks to the symmetry of the metric tensor g_{ab}, has 10 independent components and whose general solution are superposition of complex metric plane waves of the form

$$\bar{h}_{ab} = A_{ab}e^{ik_c x^c}, \tag{1.18}$$

where A_{ab} is the amplitude tensor and k_c is the wave co-vector. Inserting Eq. (1.18) into (1.17) one obtains that k^c is a null vector, i.e., $\eta^{ab}k_a k_b = k_a k^a = 0$, this confirms that $\bar{h}_{ab}$ propagates at the speed of light. Combining Eq. (1.18) with the Lorentz gauge given by (1.14) one obtains $A_{ab}k^b = 0$, which indicates that the amplitudes of the oscillations are *transverse* to the direction of propagation defined by the wave vector k^a. This transversality condition reduces the number of independent conditions from 10 to 6. As discussed above, the Lorentz gauge allows the freedom of a coordinate transformation $x^a \to x^a + \xi^a$ such that ξ^a satisfies $\Box\xi^a = 0$. This residual symmetry can be used to reduce the number of independent components from six to two. A gauge choice which allows such a simplification is the well-known *transverse-traceless* (TT) gauge condition. Using this gauge condition and assuming propagation of the gravitational waves towards the $+z-$direction one can write the metric perturbation h_{ab} in terms of two polarizations h_+ and $h_\times$,

$$h_{ab} = \begin{pmatrix} 0 & 0 & 0 & 0 \\ 0 & h_+ & h_\times & 0 \\ 0 & h_\times & -h_+ & 0 \\ 0 & 0 & 0 & 0 \end{pmatrix}, \tag{1.19}$$

where the matrix components are in order t, x, y, z. The main conclusion from Eq. (1.19) is that gravitational waves are the tranverse and tracefree part of the metric perturbation. From the explanation presented so far, it might appear that gravitational waves are a specific result due to some gauge choice and some linear expansion around flat spacetime. The question of whether gravitational radiation could be gauged away thanks to invariance of GR under arbitrary diffeomorphisms was a controversial topic within the first years of GR, which made even Einstein doubt about their own existence. The historical controversy came to an end in the sixties with the seminal works of Bondi, van der Burg and Metzner, and Sachs [26, 27, 28], where they defined GWs

in terms of the asymptotic behaviour of the gravitational field at null infinity confirming their reality and showing their transverse traceless nature for general spacetimes.

Restricting ourselves here for simplicity to the linearized theory, one can extract gravitational radiation in general coordinates using a projection operator $P_a^b = \delta_a^b - n^a n_b$, where n^a indicates a unit vector pointing in the direction of propagation of the waves. Then, the gravitational radiation can be extracted from the spacetime metric perturbation using the projection operator onto the spatial components of $h_{\mu\nu}$ as

$$h_{\mu\nu}^{GW} = \left[P_\mu^\alpha P_\nu^\beta - \frac{1}{2} P_{\mu\nu} P^{\alpha\beta} \right] h_{\alpha\beta}, \tag{1.20}$$

which ensures the transverse and traceless nature of h^{GW}.

We finalize this section outlining the effect of gravitational waves on freely falling particles, which is usually explained in the literature in terms of the relative gravitational acceleration of two nearby test bodies. The acceleration between two freely falling test bodies parametrized by $x^a(\tau)$ and $x^a(\tau) + \xi^a(\tau)$ is governed by the geodesic deviation equation which for a wave propagating in the $+z-$direction reduces to the following equations for the metric components,

$$\ddot{x} = \frac{1}{2} \left(\ddot{h}_+ x + \ddot{h}_\times y \right), \quad \ddot{y} = \frac{1}{2} \left(\ddot{h}_\times x - \ddot{h}_+ y \right). \tag{1.21}$$

The consequences of Eqs. (1.21) on the motion of a ring of test particles are displayed in Fig. 1.1, where the gravitational wave propagates in the direction perpendicular to the page surface. One observes the quadrupole deformation induced in a ring of test particles, which is initially at rest forming a circle and it is subsequently deformed to an ellipse. In general a gravitational wave propagating in the z-direction can be
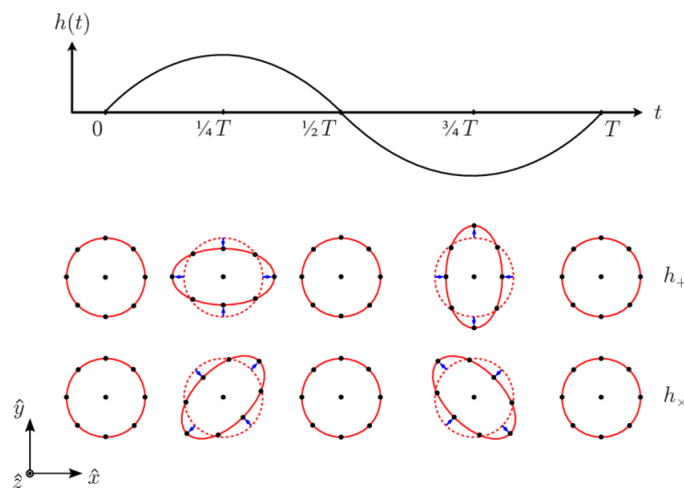
FIGURE 1.1: The upper plot represents a monochromatic gravitational wave with period T propagating in the $z-$direction. The lower plot shows the effect of the gravitational $+$ and $\times$ polarizations on a ring of freely falling test particles in the $x - y$ plane. Image taken from [29].

written as a linear combination of the two polarizations as,

$$\boldsymbol{h} = h_+ \boldsymbol{e}_+ + h_\times \boldsymbol{e}_\times, \tag{1.22}$$

where e_+ and $e_\times$ are the polarization tensors. Finally, note that the dephasing between the $+$ and $\times$ polarizations is $45°$ and that the effect of the gravitational wave on the rings is invariant under a rotation of $180°$ in the direction of propagation.

1.1.3 Gravitational wave energy

In Sec. 1.1.2 we obtained a solution for the metric perturbation for a vanishing energy-momentum tensor. We consider now the general case of a non-zero stress energy tensor. Then, the solution of Eq. (1.15) can be obtained using Green function methods,

$$\bar{h}_{ab}(t, x\mu) = 4 \int \frac{T_{ab}(t - |x^\mu - y^\mu|, y^\nu)}{|x^\mu - y^\mu|} d^3y, \tag{1.23}$$

where we have set $G = c = 1$ and adopted cartesian coordinates for the spatial coordinates, x^μ represents the position of the source with respect to the observer, y^μ describes the geometry of the source. Equation (1.23) can be further simplified noting that GW are defined in the wave zone, that is astrophysical objects are far from the detectors which implies that the distance from the gravitational wave source is much larger than the gravitational wavelength, λ. Therefore, we restrict to solutions of Eq. (1.23) for $r \sim |x^\mu| > \lambda$.

We also make the further assumption that the energy-momentum tensor is non-vanishing in a finite region close to the source with an extent R. The fact that the typical wavelength is much longer than R implies that $r \gg R$. Hence, supposing $|x^\mu| \gg |y^\mu|$, which means that distance from the observer to the source is much larger than the typical scale of the source, we can rewrite (1.23) as

$$\bar{h}_{ab}(t, x^\mu) = \frac{4}{r} \int T_{ab}(t - |x^\mu - y^\mu|, y^\nu) d^3y. \tag{1.24}$$

Noting that $|x^\mu - y^\mu| \approx r - \sum_\mu \frac{x^\mu y^\mu}{r}$ and $|y^\mu| \lesssim R$ one can Taylor expand the energy-momentum tensor around the retarded time $t_{\text{ret}} = t - r$ in the Minkowski spacetime as

$$T_{ab}(t - |x^\mu - y^\mu|, y^\nu) = T_{ab}(t_{\text{ret}}, y^\mu) + \frac{\sum_\mu x^\mu y^\mu}{r} \partial_t T_{ab}(t_{\text{ret}}, y^\mu) + \cdots. \tag{1.25}$$

The expansion of Eq. (1.25) is only valid in the far zone where the energy-momentum tensor of the source is zero. Furthermore, if we denote by τ the characteristic time scale of variation of T_{ab} then we can observe that the second term of (1.25) scales as $R/(c\tau)$ with respect to the first term, which is equivalent to an expansion in v/c where $v = R/\tau$ is the characteristic velocity of the gravitational wave source. Assuming that the characteristic speed of the gravitational wave source is small compared to the speed of light we can retain just the first term in (1.25) obtaining,

$$\bar{h}_{ab}(t, x^\mu) = \frac{4}{r} \int T_{ab}(t_{\text{ret}}, y^\mu) d^3y. \tag{1.26}$$

Using the stress-energy tensor of a perfect fluid and the conservation law $\partial_a T^{ab} = 0$ it can be shown [24, 25, 30] that one finally obtains

$$\bar{h}_{ab}(t, x^\mu) = \frac{2}{r} \frac{d^2}{dt^2} \int d^3x \rho x^a x^b = \frac{2}{r} \ddot{I}_{ab}(t_{\text{ret}}), \tag{1.27}$$

where I_{ab} indicates the quadrupole moment of the system. As shown in Sec. 1.1.2 the GW part has to be extracted using the projection operator which in this case leads to

$$\bar{h}_{ab}^{GW}(t,x^\mu) = \frac{2}{r}\frac{d^2\tilde{I}_{ab}^{TT}}{dt^2} = \left[P_a^c P_b^d - \frac{1}{2}P_{ab}P^{cd}\right]\frac{2}{r}\frac{d^2\tilde{I}_{cd}}{dt^2}, \qquad (1.28)$$

where $\tilde{I}_{ab}$ is the tracefree part of I_{ab} defined as

$$\tilde{I}_{ab} = I_{ab} - \delta_{ab}\sum_c I_{cc}. \qquad (1.29)$$

Equation (1.28) is known as the *quadrupole formula* of gravitational waves. A first consequence of Eq. (1.28) is that bodies with a non-vanishing quadrupole moment emit gravitational waves, while spherically symmetric and perfectly axisymmetric bodies do not as they have a constant quadrupole moment. Secondly, the quadrupole formula shows that the amplitude of the gravitational wave signal depends on the direction of the observer with respect to the source of gravitational wave radiation through the projection operator. Note also that the quadrupole formula in this section is derived within linearized theory, this is an expansion around flat spacetime. This implies that in principle the quadrupole formula cannot be used for self-gravitating objects like black holes or neutron stars. However, it can be shown using post-Newtonian theory [31], a weak-field and small velocity $v \ll c$ approximation, that the same expression as in Eq. (1.28) is obtained.

Once, we have obtained solutions for the gravitational wave signals we turn our attention to the energy carried by this form of radiation. We want to present some estimates of the typical observed energies in the detectors. Before presenting some equations we refer to [24, 25, 30] for details in their derivation. In GR, the definition of energy and momentum of GWs is a subtle problem due to the fact that they cannot be defined locally, but they have to be defined as global quantities in asymptotically flat spacetimes, spacetimes which at null infinity *resemble* Minkowski spacetime, and where the notion of energy and momentum acquires a physical meaning, like the Arnowitt-Deser-Misner (ADM) mass and momentum typically used in numerical relativity.

The gravitational wave energy flux can be expressed in terms of the quadrupole momenta as [24, 25, 30]

$$\frac{dE}{dt} = \frac{1}{5}\sum_{\mu,\nu}\left\langle\frac{d^3\tilde{I}_{\mu\nu}}{dt^3}\frac{d^3\tilde{I}_{\mu\nu}}{dt^3}\right\rangle, \qquad (1.30)$$

where $\langle\cdots\rangle$ denotes the average over a certain time duration, typically several periods of gravitational-wave cycles.

Now we have all the required tools to provide an estimate of the gravitational wave amplitude. In order to do that we recover the constants G and c and we define f_{GW} as the gravitational-wave frequency, D as the distance from the source to the observer, and T as the time duration of emission. Then, combining eqs. (1.20) and (1.30) we can estimate the gravitational wave luminosity as

$$\Delta E T^{-1} \sim c^3 G^{-1}(h_0 D)^2 f^2, \qquad (1.31)$$

where ΔE is the scale of the energy variation and h_0 the scale of the gravitational-wave amplitude. We can write the time duration of the signal in terms of the wave

cycles, N, as $T = N/f$ and $\Delta E = \epsilon_E M c^2$, where ϵ_E is the efficiency in converting binding energy into gravitational wave radiation, typically, $\epsilon_E \lesssim 1$. With all of this we obtain,

$$
h_0 \sim \frac{1}{D} \left[\epsilon_E \frac{GM}{cfN} \right]^{1/2},
$$
$$
h_0 \sim 10^{-17} \left(\frac{10\text{kpc}}{D} \right) \left(\frac{\epsilon_E}{0.01} \right)^{1/2} \left(\frac{M}{10 M_\odot} \right)^{1/2} \left(\frac{f}{1\text{kHz}} \right)^{-1/2} N^{-1/2}.
$$
(1.32)

For instance, suppose an astrophysical object with a total mass of $30 M_\odot$ collapses to a black hole at a distance $D \sim 50\text{kpc}$. The frequency of the system will be of the order of 1 kHz, the number of cycles of order 1 and just take the efficiency of 1%. Then, $h_0 \sim 10^{-18}$ which is a very small amplitude. As discussed in Sec. 1.1.2 the effect of gravitational waves is to change proper distances between two nearby freely falling particles. This modification of the distance can be translated to the relative change in length by

$$
h = 2 \frac{\Delta L}{L}.
$$
(1.33)

Then, taking a 4km detector the effect of a passing gravitational wave signal with amplitude $h_0 \sim 10^{-18}$ is a change in the length of the order 10^{-11} cm, which is smaller than the atomic radius. These rough numbers show the challenge of detecting gravitational waves and it also explains why it took nearly a century after their first prediction by GR to make the first direct detection of a passing gravitational wave signal through a ground-based interferometer.

1.2 Gravitational wave sources

According to linearized theory each body with a non-vanishing quadrupole moment radiates gravitational waves. However, as shown by the estimates of Sec. 1.1.3 they are very weak in nature. Hence, only very compact objects and catastrophic events like compact binary coalescences, supernova explosions or highly rotating neutron stars, etc., are able to produce detectable gravitational wave radiation. In this section we briefly summarize the properties of the known sources of gravitational waves.

The frequency range of astrophysical gravitational wave sources is limited to 10^4 Hz downward. This maximum frequency can be estimated assuming that a source of mass M cannot be much smaller than its Schwarzschild radius, $2GM/c^2$, and it cannot emit significantly at periods much smaller than the light-travel time $4\pi GM/c^3$ around its Schwarzschild radius. This restricts the emitted frequencies to [32]

$$
f \lesssim \frac{1}{4\pi GM/c^3} \approx 10^4 \text{Hz} \frac{M_\odot}{M}.
$$
(1.34)

In order to emit at its maximum frequency, i.e., reaching a size of the order its Schwarzschild radius, the object size should be larger than its Chandrasekhar limit[1], $M \gtrsim 1.44 M_\odot$. This sets the expected maximum frequency of the gravitational wave frequency band to $\sim 10^4$ Hz and it spans the whole range of frequencies downward. In the following subsections we will shortly describe some of the most promising sources of gravitational waves: Compact Binary Coalescences (CBC), Continuous Waves (CW), Bursts and the stochastic gravitational wave background. Some of these events have

---

[1]Or the limit observed for neutron stars which is similar.

already been detected by the LIGO and Virgo detectors, like the CBCs, and the rest are expected to be detected in the upcoming years.

Compact binary coalescences

Compact binary mergers include all systems of compact objects like binary black holes (BBH), binary neutron stars (BNS) or black hole neutron star (NSBH), which coalesce to form a Kerr black hole or a neutron star (this formation channel is only possible for BNS and NSBH systems). CBC, and specifically BBH coalescences, are the main topic of this thesis. Compact binaries are the only sources of gravitational waves which have been directly detected so far [11]. During O1 and O2 the LIGO and Virgo scientific collaborations confidently detected 11 GW events consistent with 10 stellar mass BBH mergers, with total mass ranges between $18.6^{+3.2}_{-0.7}M_\odot$ and $84.4^{+15.8}_{-11.1}M_\odot$ and range in distance between 320^{+120}_{-110} and 2840^{+1400}_{-1360} Mpc, and 1 BNS merger. These numbers confirm that BBHs are the most promising sources of gravitational waves in the near future.

Galactic white-dwarf binaries, another CBC type of source, will be detected with the advent of space-craft gravitational wave detectors like LISA. These sources constitute the more typical final stages of the stellar evolution and their detection will permit a better description of their population and possible formation channels [33]. Other expected sources for space-craft detectors are intermediate black-hole (IMBH) binary mergers and extreme mass ratio inspirals (EMRIs), providing the latter information about formation channels of the supermassive black holes in the galactic centers.

Continuous Waves

Continuous gravitational waves are expected to be produced by highly spinning compact objects, like a neutron star, with some asymmetries or imperfections which break the constancy of its quadrupole moment and allow the emission of gravitational waves. The system emits *continuously* at the same frequency and amplitude as it spins around its rotation axis.

The duration of gravitational-wave emission of these systems is much longer than for CBCs, although the amplitude of the signal is much weaker due to the small asymmetries causing the emission of gravitational radiation. Current search pipelines have set upper limits on the gravitational-wave strain amplitude for rapidly spinning neutron stars with an asymmetry in their rotation axis and prospects on their future detection [34]. Alternatively, a boson cloud scenario [35] has been recently suggested as another possible source of continuous waves. This exotic scenario requires a cloud of bosons around a highly spinning black-hole. This cloud of bosons could emit continuous gravitational wave radiation through the corresponding energy transitions of the bosons of the cloud.

Gravitational wave bursts

Gravitational wave bursts are produced by transient unmodeled gravitational wave sources, like core-collapse supernovae, high mass BBH mergers, highly eccentric BBH mergers, cosmic strings, etc. Other sources of burst signals are the gravitational wave emission associated with the short gamma-ray bursts (GRBs) of coalescing BNS and BH-NS binaries which could provide insight into the progenitors and the generation of these transient phenomena [36].

In this thesis one of the unmodeled search pipelines used by LIGO and Virgo to detect burst signals is used to analyse the sensitivity of this unmodeled search pipeline to eccentric binary black hole mergers. Hence, we explain in detail in Sec. 3.4.2 of Chapter 3 the algorithm used by a *burst* search pipeline, *coherent Wave Burst* (cWB), to detect these unmodeled signals.

Stochastic background

The stochastic gravitational-wave background is a superposition of sources which are too weak or too numerous to be detected individually. Current LIGO pipelines have not found evidence for a stochastic background in O1 and O2 [37] and they have set upper limits on the normalized energy density of gravitational waves in a frequency independent background. These uppers limits can be used to set some constraints in models of compact binaries and cosmic strings.

Space-craft detectors like LISA are expected to also detect a background caused by the superposition of the GW signals of the white-dwarf binary population in our galaxy. This makes the LISA detector strain to be signal dominated in contrast to ground-based detectors, which have a noise dominated strain. The removal of such a background is currently under investigation through mock data challenges [38].

Finally, a stochastic background can also have a cosmological origin [39]. The sources causing such a background are associated with phase transition models in the early universe which may produce an hypothetical fossil background.

1.3 Gravitational wave detectors

The firsts attempts to measure GW date from the 1960s when the pioneer Joseph Weber developed and constructed the first resonant-bar detectors. The underlying principle of these instruments is that they absorb a tiny fraction of the energy of the passing GW signal and transform it into mechanical oscillations. This conversion happens at a very specific frequency which is the resonant frequency of the object. Thus, resonant-mass detectors are narrow band detectors sensitive to very specific GW frequencies coincident with the resonant one of the material.

By the end of the sixties, a series of *failed* detections made resonant-mass detectors become unpopular among the scientific community. Furthermore, the low maximum accuracy in the measurement of $h \sim O\left(10^{-21}\right)$ set by the quantum limit poses a problem for detections of many astrophysical events using this type of detectors [40]. Hence, resonant bars were progressively abandoned in favour of large GW interferometric detectors. Nowadays, there are still some operating resonant-mass detectors like AURIGA [41], although they are also used to search for dark matter candidates [42].

Passing from resonant-mass detectors to interferometers constitutes a dramatic change of scale of the scientific effort required to operate it for confident detections. While the former can be operated with a scientific group of a dozen of scientists, the latter requires collaborations of hundreds of people and a financial cost several orders of magnitude higher. This is the reason why every large interferometer has associated with it some large scientific collaboration like LIGO, Virgo, GEO or Kagra. GW

interferometers are remarkably complex instruments with many degrees of freedom which have to be controlled to high accuracy. All this together explains why it took more than 50 years from its first theoretical descriptions in 1962 by M. Gertsenshtein and V.I. Pustovoit [43] to the first direct GW detection by LIGO in 2015 [7].

Focusing on the scientific part, we have to recall from Sec. 1.1.2 that the effect of a passing GW is the modification of the proper distance of the two directions orthogonal to the propagation direction of the wave. The relative length difference in each direction is $\Delta L/L = h/2$, which can also be associated with the relative length change induced by a passing GW signal. This formula also shows that the longer the distance L over which we are measuring length differences, the higher the accuracy at which one can determine the strain h. Moreover, the previous reasoning suggests that an L-shaped detector would be perfectly suited to perform the task of measuring such length differences and it led to the Michelson-Morley interferometer as the first alternative to resonant-mass detectors. The basic concept of a Michelson-Morley interferometer is shown in Fig. 1.2.
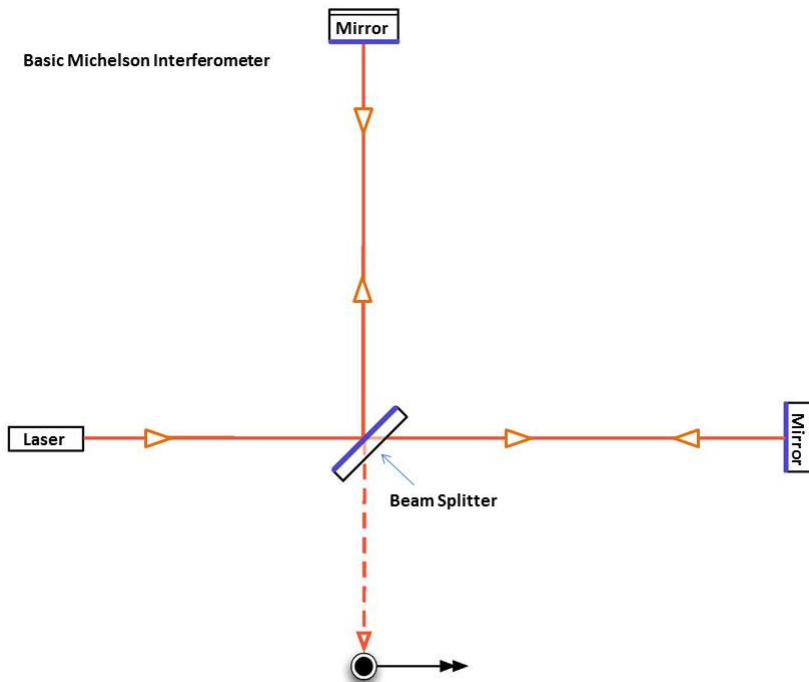
FIGURE 1.2: Basic design of a Michelson interferometer. The laser beam hits the beam splitter and half of the beam goes in one arm and the other half is sent to the other arm. They are reflected in the end mirror of each arm and recombined at the intersection where they interfere destructively. If a passing GW modifies slightly the length of one arm the interference will produce some light patterns in the detector output. [Image taken from https://www.ligo.caltech.edu/page/ligos-ifo]

The principle of the Michelson-Morley interferometer is at the core of the current ground-based detectors. However, some modifications in the design have to be applied

to increase the accuracy of the instrument. Here, we focus on the LIGO detectors and we list the main modifications to the Michelson interferometer to increase the accuracy. The arms of the instrument are increased from the original 11m of the Michelson interferometer to the 4km of LIGO. The increase in the arm length implies an increase of accuracy as explained before. However, 4km are not enough to reach the required accuracy, thus, in the arms *Fabry-Perot cavities* are inserted. These cavities are 4km long and they make the light of each arm bounce back and forth along the full path. The improvement coming from these reflections is two-fold, 1) it stores laser light for a longer time in the interferometer increasing the LIGO sensitivity and 2) it increases the light travel distance to 1600km, which supposes a significant increase of accuracy of the instrument.

So far, we have focused on increasing the length to augment the sensitivity, but a laser power increase also enhances the instrument sensitivity. Recycling the laser power allows to achieve a cleaner detector output as the interference pattern is better resolved by the photodetector. Nonetheless, only 200 W of laser power enter the interferometer while the detector performs at ~ 750 kW at full power. As it is impractical to build a 1600km interferometer it is impossible to have a laser with 750 kW as initial power. This is solved by the addition of *power recycling* mirrors which thanks to the alignment of the instruments allow a boost in the power of the laser beam. The consequent sharpening of the interference fringes at the photodetector allows better discrimination of passing GW signals. Finally, two more main modifications are implemented in LIGO detectors, 1) *signal recycling* mirrors, which enhance the output signal of the detector, and 2) LIGO's seismic isolation system, which is a specific system to damp out undesired seismic vibrations. With all these modifications, LIGO interferometers are known as *Dual Recycled Fabry-Perot Michelson* interferometers.

The interferometer detector output is contaminated by many noise sources whose amplitude is much higher than the searched GW signals. Thus, a confident detection of a GW signal requires the understanding and removal of the noise sources hitting our detector output. The main sources of noise acting on a LIGO interferometer are:

- **Displacement noise**. This name characterizes the noise sources which are not related to the passing GW. This category includes Newtonian and seismic noise caused by the inhomogeneous gravity gradient, thermal noise caused by pendulum thermal fluctuations or test-mass thermal fluctuations, and other noise sources like non-gaussian noise caused by residual gas.

- **Radiation pressure**. This noise is caused by the fluctuation in the number of photons hitting the mirror, which causes a stochastic force shaking the mirrors.

- **Shot noise**. This noise is caused by the quantum nature of light. The uncertainty principle causes quantum fluctuations of the laser light which produce undesired instrumental noise. However, some particular states of light, known as *squeezed* light, can reduce the contribution of this noise source.

Finally, we briefly mention current ground-based detectors and their properties:

a) *GEO-600*. It is a smaller interferometer with an arm length of 600m located near Hannover (Germany) [44]. It is operated by British and German scientists, mainly the Max Planck Institute of Hannover. Its sensitivity is more than one order of magnitude smaller than the one from the LIGO detectors. Currently, GEO600 is mainly used to push the available technologies to their limits and advance the interferometer technology.

b) *Kagra*. It is the first 2.5 generation interferometric gravitational wave detector located under the mountain of the Kamioka mine in Kamioka-cho (Japan) with 3km-long arms. It is operated by the international Kagra collaboration formed by more than 200 researchers from 90 institutions in 15 countries. Very recently, Kagra has joined the Advanced LIGO and Advanced Virgo detectors for the last part of the third observing run, although its current sensitivity is quite limited. It is expected to be decisive in the upcoming observing runs [45].

c) *LIGO*. The two 4km arm long Advanced LIGO [9] detectors are located at Hanford and Livingston (United States of America). They are operated by the LIGO scientific collaboration (LSC) consisting of more than 1000 scientists from over 100 institutions and 18 countries worldwide. It is currently on the third observing run and it has already sent public alerts for tens of GW candidates [20] which are currently under analysis.

d) *Virgo*. Advanced Virgo [10] is a 3 km-long arm detector situated in Cascina (Italy). It is operated by the Virgo collaboration composed of more than 500 members representing 99 institutions from 11 countries. Its sensitivity is approximately one order of magnitude smaller than the one of the LIGO detectors. However, it plays a crucial role determining the sky position of GW sources, as it occurred during O2 with the detection of GW170814 [46], the first three-detector observation of a BBH merger.

Apart from the current GW observatories, there are plans to construct third-generation ground-based GW detectors like LIGO India, the Einstein Telescope (Europe) and Cosmic Explorer (USA). Additionally, the prospects of space-based detectors like LISA ensure a fully operational gravitational wave detector network of ground-based and space-based detectors covering the high and low frequency bands $\left(10^{-4} - 2000\text{Hz}\right)$ with an unprecedented sensitivity by the early thirties, which will provide a much more complete picture of the universe and a deeper understanding of gravity and its nature.

References

[1] Albert Einstein. The Foundation of the General Theory of Relativity. *Annalen Phys.*, 49(7):769–822, 1916. [Annalen Phys.354,no.7,769(1916)].

[2] Peter Coles. Einstein, Eddington and the 1919 eclipse. *ASP Conf. Ser.*, 252:21, 2001. arXiv:astro-ph/0102462 [astro-ph].

[3] Ryan Park, William Folkner, Alexander Konopliv, James Williams, David Smith, and Maria Zuber. Precession of mercury's perihelion from ranging to the messenger spacecraft. *The Astronomical Journal*, 153:121, 02 2017.

[4] R. A. Hulse and J. H. Taylor. Discovery of a pulsar in a binary system. *Astrophys. J.*, 195:L51–L53, Jan 1975.

[5] J.M. Weisberg and J.H. Taylor. Observations of post-Newtonian timing effects in the Binary Pulsar PSR 1913+16. *Phys. Rev. Lett.*, 52:1348–1350, 1984.

[6] J. H. Taylor and J. M. Weisberg. Further Experimental Tests of Relativistic Gravity Using the Binary Pulsar PSR 1913+16. *Astrophys. J.*, 345:434, Oct 1989.

[7] B.P. Abbott et al. Observation of Gravitational Waves from a Binary Black Hole Merger. *Phys. Rev. Lett.*, 116(6):061102, 2016. arXiv:1602.03837 [gr-qc].

[8] Galina Weinstein. Einstein's discovery of gravitational waves 1916-1918. *arXiv e-prints*, page arXiv:1602.04040, Feb 2016. arXiv:1602.04040 [physics.hist-ph].

[9] J. Aasi et al. Advanced LIGO. *Class. Quant. Grav.*, 32:074001, 2015. arXiv:1411.4547 [gr-qc].

[10] F. Acernese et al. Advanced Virgo: a second-generation interferometric gravitational wave detector. *Class. Quant. Grav.*, 32(2):024001, 2015. arXiv:1408.3978 [gr-qc].

[11] B. P. Abbott et al. GWTC-1: A Gravitational-Wave Transient Catalog of Compact Binary Mergers Observed by LIGO and Virgo during the First and Second Observing Runs. *Phys. Rev.*, X9(3):031040, 2019. arXiv:1811.12907 [astro-ph.HE].

[12] B.P. Abbott et al. GW170817: Observation of Gravitational Waves from a Binary Neutron Star Inspiral. *Phys. Rev. Lett.*, 119(16):161101, 2017. arXiv:1710.05832 [gr-qc].

[13] B. P. Abbott et al. Gravitational Waves and Gamma-rays from a Binary Neutron Star Merger: GW170817 and GRB 170817A. *Astrophys. J.*, 848(2):L13, 2017. arXiv:1710.05834 [astro-ph.HE].

[14] B. P. Abbott et al. Multi-messenger Observations of a Binary Neutron Star Merger. *Astrophys. J.*, 848(2):L12, 2017. arXiv:1710.05833 [astro-ph.HE].

[15] B.P. Abbott et al. GW170817: Measurements of neutron star radii and equation of state. *Phys. Rev. Lett.*, 121(16):161101, 2018. arXiv:1805.11581 [gr-qc].

[16] B.P. Abbott et al. Properties of the binary neutron star merger GW170817. *Phys. Rev. X*, 9(1):011001, 2019. arXiv:1805.11579 [gr-qc].

[17] B. P. Abbott et al. A gravitational-wave standard siren measurement of the Hubble constant. *Nature*, 551(7678):85–88, 2017. arXiv:1710.05835 [astro-ph.CO].

[18] N. Aghanim et al. Planck 2018 results. VI. Cosmological parameters. 7 2018. arXiv:1807.06209 [astro-ph.CO].

[19] Adam G. Riess, Stefano Casertano, Wenlong Yuan, Lucas M. Macri, and Dan Scolnic. Large Magellanic Cloud Cepheid Standards Provide a 1% Foundation for the Determination of the Hubble Constant and Stronger Evidence for Physics beyond ΛCDM. *Astrophys. J.*, 876(1):85, 2019. arXiv:1903.07603 [astro-ph.CO].

[20] https://gracedb.ligo.org/superevents/public/O3/.

[21] https://emfollow.docs.ligo.org/userguide/. LIGO/Virgo Public Alerts User Guide, 2019.

[22] B.P. Abbott et al. Tests of General Relativity with the Binary Black Hole Signals from the LIGO-Virgo Catalog GWTC-1. *Phys. Rev. D*, 100(10):104036, 2019. arXiv:1903.04467 [gr-qc].

[23] L. D. Landau and E. M. Lifschitz. *The Classical Theory of Fields*, volume 2 of *Course of Theoretical Physics*. Pergamon Press, Oxford, 1975.

[24] Bernard F. Schutz. *A FIRST COURSE IN GENERAL RELATIVITY*. Cambridge Univ. Pr., Cambridge, UK, 1985.

[25] Charles W. Misner, K. S. Thorne, and J. A. Wheeler. *Gravitation*. W. H. Freeman, San Francisco, 1973.

[26] H. Bondi. Gravitational waves in general relativity. *Nature*, 186(4724):535–535, 1960.

[27] H. Bondi, M. G. J. van der Burg, and A. W. K. Metzner. Gravitational waves in general relativity. VII. Waves from axi-symmetric isolated systems. *Proceedings of the Royal Society. A. Mathematical, Physical and Engineering Sciences*, 269(1336), 8 1962.

[28] R. K. Sachs. Gravitational waves in general relativity. 6. The outgoing radiation condition. *Proc. Roy. Soc. Lond.*, A264:309–338, 1961.

[29] Alexandre Le Tiec and Jérôme Novak. *Theory of Gravitational Waves*, pages 1–41. 2017.

[30] Masaru Shibata. *Numerical Relativity*. World Scientific Publishing Co., Inc., River Edge, NJ, USA, 2015.

[31] Luc Blanchet. Gravitational Radiation from Post-Newtonian Sources and Inspiralling Compact Binaries. *Living Rev. Rel.*, 17:2, 2014. arXiv:1310.1528 [gr-qc].

[32] Kip S. Thorne. Gravitational waves. In *Particle and nuclear astrophysics and cosmology in the next millennium. Proceedings, Summer Study, Snowmass, USA, June 29-July 14, 1994*, pages 0160–184, 1995.

[33] B.P. Abbott et al. Binary Black Hole Population Properties Inferred from the First and Second Observing Runs of Advanced LIGO and Advanced Virgo. *Astrophys. J. Lett.*, 882(2):L24, 2019. arXiv:1811.12940 [astro-ph.HE].

[34] B.P. Abbott et al. All-sky search for continuous gravitational waves from isolated neutron stars using Advanced LIGO O2 data. *Phys. Rev. D*, 100(2):024004, 2019. arXiv:1903.01901 [astro-ph.HE].

[35] Keith Riles. Recent searches for continuous gravitational waves. *Mod. Phys. Lett.*, A32(39):1730035, 2017. arXiv:1712.05897 [gr-qc].

[36] B. P. Abbott et al. Search for gravitational-wave signals associated with gamma-ray bursts during the second observing run of Advanced LIGO and Advanced Virgo. *Astrophys. J.*, 886:75, 2019. arXiv:1907.01443 [astro-ph.HE].

[37] B.P. Abbott et al. Search for the isotropic stochastic background using data from Advanced LIGO's second observing run. *Phys. Rev. D*, 100(6):061101, 2019. arXiv:1903.02886 [gr-qc].

[38] Stanislav Babak et al. The Mock LISA Data Challenges: From Challenge 3 to Challenge 4. *Class. Quant. Grav.*, 27:084009, 2010. arXiv:0912.0548 [gr-qc].

[39] Chiara Caprini. Stochastic background of gravitational waves from cosmological sources. *J. Phys. Conf. Ser.*, 610(1):012004, 2015. arXiv:1501.01174 [gr-qc].

[40] Odylio Denys Aguiar. The Past, Present and Future of the Resonant-Mass Gravitational Wave Detectors. *Res. Astron. Astrophys.*, 11:1–42, 2011. arXiv:1009.1138 [astro-ph.IM].

[41] G. A. Prodi et al. The ultracryogenic gravitational wave detector AURIGA. In *International Conference on Gravitational Waves: Sources and Detectors Pisa, Italy, March 19-23, 1996*, pages 166–170, 1996.

[42] Antonio Branca et al. Search for an Ultralight Scalar Dark Matter Candidate with the AURIGA Detector. *Phys. Rev. Lett.*, 118(2):021302, 2017. arXiv:1607.07327 [hep-ex].

[43] M. E. Gertsenshtein and V. I. Pustovoit. On the Detection of Low Frequency Gravitational Waves. *Sov. Phys. JETP*, 16:433, 1962.

[44] Katherine L. Dooley. Status of GEO 600. *J. Phys. Conf. Ser.*, 610(1):012015, 2015. arXiv:1411.6588 [physics.ins-det].

[45] T. Akutsu et al. KAGRA: 2.5 Generation Interferometric Gravitational Wave Detector. *Nat. Astron.*, 3(1):35–40, 2019. arXiv:1811.08079 [gr-qc].

[46] B.P. Abbott et al. GW170814: A Three-Detector Observation of Gravitational Waves from a Binary Black Hole Coalescence. *Phys. Rev. Lett.*, 119(14):141101, 2017. arXiv:1709.09660 [gr-qc].

Chapter 2

Solutions to the two-body problem in general relativity

In this chapter we assemble some basic concepts of the two-body problem in Einstein's theory of general relativity which will help to better understand the original research work in the upcoming chapters. We focus on the merger of compact binary objects, particularly BBHs which are the main topic of this thesis. Regarding mergers of compact objects, one can clearly differentiate three stages in their evolution:

- **Inspiral:** In this regime the compact objects are far apart from each other, so the gravitational interaction between the two bodies is weak and their velocities are small compared to the speed of light. The binary is evolving quasi-adiabatically towards the merger. This phase is well described through post-Newtonian (PN) and Effective-One-Body (EOB) theories, which provide analytical expressions for the dynamics and the waveform during this phase[1]. We provide further details about PN theory in Sec. 2.2.

- **Merger:** As the compact objects approach each other, gravitational non-linear effects become larger and larger, until the assumptions of weak field and small velocities compared to the speed of light break down. At this point a numerical approach is required to accurately describe the complicated non-linear interactions. For this purpose one uses numerical relativity (NR), specifically in this thesis two finite difference NR codes have been used, the private BAM code and the open-source EinsteinToolkit (ET). However, the high computational cost of these simulations ($\sim 10^5$ CPU hours for a not very challenging simulation) reduces their application to a few orbits prior to merger, which motivates the construction of *hybrid* waveforms between PN/EOB-NR, and it also complicates populating the large parameter of space of a compact binary. We explain basic concepts of NR in Sec. 2.3.

- **Ringdown:** After merger, the final state will depend on the nature of the binary (BH-BH, NS-BH, NS-NS). If we restrict to BH-BH coalescences, the final state is a perturbed Kerr black-hole described by perturbation theory. After merger, the resulting black-hole tends to a stationary Kerr solution emitting the gravitational radiation through a spectrum of exponentially decaying modes, the quasinormal modes (QNMs), which are caused by disruptions and asymmetries in the black-hole horizon. The ringdown part of the waveform is a fundamental tool to look for deviations from general relativity in GW detections [1] and to constrain the final state of matter systems [2, 3].

---

[1]We note that EOB is also extended through the merger regime, although its accuracy degrades significantly with respect to the inspiral.

The above separation can be identified in Fig. 2.1, where the time domain plus polarization of a NR simulation is displayed. One distinguishes the three phases of the GW evolution. The construction of gravitational waveform models which reproduce the GW emission during these stages are called Inspiral-Merger-Ringdown (IMR) waveforms [4, 5]. IMR waveform models are semi-analytical approximations to the solution
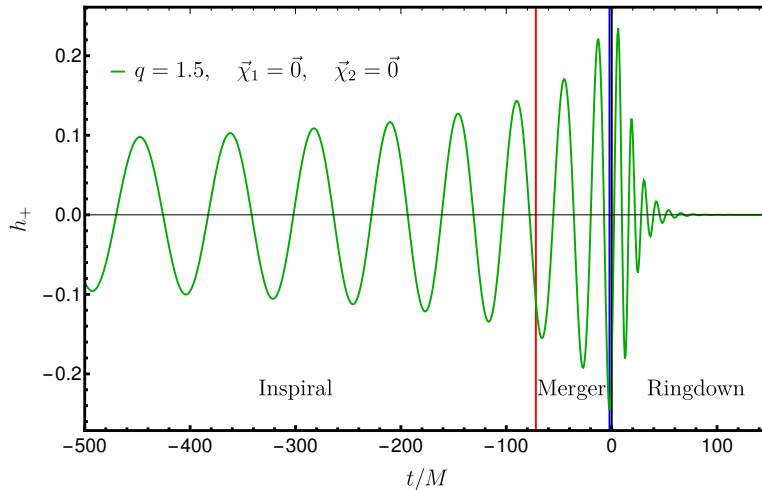
FIGURE 2.1: Representation of the time evolution of the plus polarization of the gravitational wave for a non-spinning BBH numerical relativity simulation with mass ratio $q = m_1/m_2 = 1.5$. From left to right, the three different stages of the BBH coalescence are displayed: the ending of the inspiral regime set by the time of the minimum energy circular orbit (MECO) [6] marked with a vertical red line, the merger regime until the peak of the waveform indicated with a blue vertical line, and the rindown regime characterized by the amplitude decay of the GW emission.

of the Einstein equations for the GW emission of BBH mergers. They are constructed upon calibration to hybrid PN/EOB-NR waveforms. Currently, the main limitations in constructing these models comes from the difficulty to construct waveform models for high-dimensional parameter spaces, this poses a challenge in the description of generic BBHs which include precession or eccentricity, and the huge computational cost of generic BBH NR simulations which impedes populating certain regions of the parameter space, like highly precessing, intermediate mass ratios ($q = m_1/m_2 > 10$) or very eccentric systems, with high quality simulations which can be used to extend and further improve the current IMR waveform models.

2.1   Parameters of a generic BBH coalescence

In this section we detail the physical parameters required to describe the GW signal of a BBH coalescence. The radiation of GW signals is typically described through three different reference frames: the source frame, the radiation frame and the detector frame. We refer the reader to [7, 8] for a detailed explanation. According to the No-Hair theorem a non-charged isolated black hole in equilibrium is described by only its mass and total angular momentum. Hence, in the case of a BBH coalescence, which describes the merger of two gravitationally bound black holes emitting GW radiation, one is left with 8 parameters $\Theta = \{m_1, m_2, \vec{S}_1, \vec{S}_2\}$, where m_i and $\vec{S}_i$ are the component masses and individual spin vectors, respectively. These are the 8 intrinsic parameters required to describe a quasi-circular binary, which quasi-adiabatically passes from a

quasi-circular orbit to another until merger. However, more generic BBH systems also require to take into account two additional parameters $\{e, \Omega\}$, eccentricity and the argument of the periapsis respectively. Thus, in the source frame the most generic BBH binary is described by 10 intrinsic parameters,

$$\zeta = \{q, M, \vec{S}_1, \vec{S}_2, e, \Omega\}, \tag{2.1}$$

where we have rewritten for later convenience the component masses m_1 and m_2 in terms of the mass ratio $q = m_1/m_2$ and the total mass of the system $M = m_1 + m_2$.

The description of the passing GW signal through an interferometric detector requires 7 additional parameters, called extrinsic parameters, which relate the detector frame coordinates with the sky location of the source,

$$\Delta = \{r, t_c, \iota, \varphi, \phi, \theta, \psi\}, \tag{2.2}$$

where r is the luminosity distance from the detector to the source, t_c the coalescence time, ι the inclination, φ the azimuthal angle, ϕ the right ascension, θ the declination and ψ the polarization angle. Then, the polarization tensors of eq. (1.22) can be projected onto the detector frame coordinates to obtain the strain induced in a detector from a passing gravitational wave [9] in terms of the extrinsic and intrinsic parameters as

$$\bar{h}(t, \zeta, \Delta) = F_+(\theta, \phi, \psi) h_+(t - t_c; \iota, \varphi, \zeta) + F_\times(\theta, \phi, \psi) h_\times(t - t_c; \iota, \varphi, \zeta), \tag{2.3}$$

where F_+ and $F_\times$ are the antenna pattern functions. For an L-shaped interferometer one obtains

$$
\begin{aligned}
F_+(\theta, \phi, \psi) &= \frac{1}{2}\left(1 + \cos^2\theta\right)\cos(2\phi)\cos(2\psi) - \cos\theta\sin(2\phi)\sin(2\psi), \\
F_\times(\theta, \phi, \psi) &= -\frac{1}{2}\left(1 + \cos^2\theta\right)\cos(2\phi)\sin(2\psi) - \cos\theta\sin(2\phi)\cos(2\psi).
\end{aligned}
\tag{2.4}
$$

As a spin-2 field the complex waveform defined in terms of the two polarisations can be written in the basis of the spin-weighted $(s = -2)$ spherical harmonics as

$$h(t) = h_+ - ih_\times = \sum_{l=2}^{\infty}\sum_{m=-l}^{l} Y_{lm}^{-2}(\iota, \varphi) h_{lm}(t - t_c; \zeta), \tag{2.5}$$

From eqs. (2.3) and (2.5) one can observe that there is a separation between intrinsic and extrinsic parameters, which allows factoring out the contribution from the extrinsic ones in the GW strain induced in a detector. This property allows to produce models of the signal for the intrinsic parameters of a binary system and, afterwards, add trivially the dependency on the extrinsic parameters. Furthermore, from the 10 intrinsic parameters of a binary system, in vacuum GR the total mass of the system is just a scale factor which is typically set to 1, $M = m_1 + m_2 = 1$, and it is not taken into account when modelling BBH mergers. Hence, the most generic BBH system has 9 intrinsic parameters $\eta, \vec{S}_1, \vec{S}_2, e, \Omega$, where we have written by convenience the symmetric mass ratio $\eta = m_1 m_2/(m_1 + m_2)^2$, $\eta \in [0, 0.25]$ instead of the mass ratio.

2.2   Post-Newtonian theory

Post-Newtonian theory is an approximation to the full Einstein equations in the weak gravitational field regime and slow motion of the bodies with respect to the speed of light. In this chapter we provide a brief overview of the basic concepts of the theory focusing on the theoretical notions which are necessary to understand the calculations done in the original research chapters. For detailed derivations and more involved explanations we refer the reader to [10, 11, 12]. Specifically, we focus on the Hamiltonian formulation used to develop the method in Chapter 4 and the current status of eccentric PN theory, employed in the work of Chapter 5 .

As discussed in Sec. 1.1.2, the linearized theory cannot be applied to self-gravitating objects as the background metric is not correctly described by the Minkowski one. In order to apply PN theory to describe a self-gravitating object emitting gravitational radiation it turns out useful to take into account the different scales involved in the problem and separate the domain according to those. This fact motivates the definitions of the *near zone* and the *far zone*, also called the *wave zone*. Introducing the characteristic time scale of the source, t_c, which is the typical time for any noticeable change in the source and the characteristic wavelength of the radiation $\lambda_c = ct_c$, one can define

$$
\begin{aligned}
\text{near zone:} &\quad r \ll \lambda_c, \\
\text{far zone:} &\quad r \gg \lambda_c,
\end{aligned}
\tag{2.6}
$$

where $r = |\boldsymbol{x}|$ is the position vector. Taking into account the retarded time $\tau = t - r/c$, one observes that in the near zone differences between τ and t are small, indicating that retardation effects are unimportant, while in the wave zone differences between τ and t are large, implying that retardation effects become relevant, as a consequence spatial derivatives are comparable to time derivatives.

Moreover, if the source is confined to a bounded region in space one can define the characteristic length scale of the source R_c, and the characteristic velocity of the source $v_c = R_c/t_c$, which represents the speed at which modifications in the source propagate to the region defined by R_c. This new scale definitions permit the introduction of the *slow motion condition* which can be formulated in terms of the characteristic velocity or the characteristic wavelength as

$$
\begin{aligned}
\text{slow motion condition:} &\quad v_c/c \ll 1, \\
\text{slow motion condition:} &\quad R_c/\lambda_c \ll 1.
\end{aligned}
\tag{2.7}
$$

The first condition implies that all the velocities within the source distribution must be much smaller than the speed of light, while the second one implies that the region occupied by the source is small compared to the characteristic wavelength of the emitted gravitational radiation. Consequently, the second condition implies that the source of GW is profoundly placed in the near zone defined by $r \ll \lambda_c$.

Under these assumptions one can develop a formalism to compute the dynamics and the gravitational radiation emitted by such a confined matter distribution. An accurate description of such a formalism is far beyond the scope of this introductory chapter. We remark two additional important points regarding PN theory, 1) it is an asymptotic series whose convergence has not been proven. The convergence of the PN series expansion is not ensured because there is not a unique dimensionless

small expansion parameter for the Einstein equations 2) there are currently two main approaches developed to perform such an expansion, the Direct Integration of the Relaxed Einstein equations (DIRE) developed by Will and Wiseman [13, 14, 15] and the multipolar expansion of the source potential developed by Blanchet, Damour and Iyer [10]. Furthermore, there are two other approaches to compute the dynamics of a compact binary based on an effective field theory formalism (EFT) [16] and a Hamiltonian formulation [12].

Finally, we note that the PN expansion suffers from two main problems, 1) a technical complication due to the appearance of divergences at high PN orders, this is solved by applying regularization techniques and proper boundary conditions, 2) mathematically, the PN expansion is an example of a singular perturbation theory, i.e., a expansion of a function $G(v/c, r)$ of the form

$$G(v/c, r) = \sum_n c_n(r) \left(\frac{v}{c}\right)^n,$$ (2.8)

around $v/c = 0$, with the coefficients $c_n(r)$ depending on a second parameter r, which diverges as $r \to \infty$. Hence, the PN expansion is not uniform in r and it is only valid in the near region of the source. This also implies that no-incoming radiation boundary conditions at infinity, which are suited to a radiation problem, can be imposed for this problem. The solution to the issue of the boundary conditions at infinity is circumvented with a technique called *matched asymptotic expansion* which allows to match the PN series with a post-Minkowskian (PM) expansion, a series expansion in terms of G. This technique permits the application of the correct boundary conditions for the radiation problem and a solution valid for the whole spatial domain.

2.2.1 Hamiltonian formulation of GR

The main motivation behind a Hamiltonian formalism is, apart from being a powerful mathematical tool to explore the applications of a mathematical theory, that Hamiltonians are generators of the time evolution of all quantities in a physical theory. In the case of isolated systems the total Hamiltonian is conserved in time. A typical feature of Hamiltonian formalisms is the splitting between time and spatial coordinates in the so called, (3+1)-decomposition of spacetime, which we revisit in 2.2.2.

The Hamiltonian formalism of GR was originally developed by Arnowitt, Deser and Misner (ADM) [17, 18, 19] in the sixties. In this formalism the Hamiltonian, called nowadays *ADM Hamiltonian*, is written as volume integral of the divergence of a vector over a three dimensional space-like hypersurface. In the two thousands, the ADM formalism in GR has been used by Jaranowski, Schäfer, Steinhoff and collaborators [12] to push forward post-Newtonian theory and extend it to account for matter deformation [20, 21] and classical spin effects [22, 23]. We note also that other Hamiltonian formalisms of GR developed by Dirac [24, 25] and Schwinger [26, 27] exist, although the most commonly used one for applications describing gravitating objects is the ADM formalism. We remark also that the Hamiltonian framework has motivated also other approaches like the effective one body (EOB) formalism [28, 29, 30].

One of the most relevant applications of the ADM formalism is the analytical treatment of the problem of motion of gravitating compact bodies. Within the ADM formalism one can compute Hamiltonians to describe the motion of post-Newtonian

sources. The current knowledge of ADM Hamiltonians at different PN orders is as follows:

- For non-spinning point particles the Hamiltonian is known up to 4PN order [31, 32, 33].

- Spin-orbit Hamiltonians have been computed up to 3.5PN order [31, 34, 35].

- Spin-spin Hamiltonians are known up to 4PN order [36, 37, 38].

2.2.2 3+1 decomposition of spacetime

We derive the ADM equations by separating the spacetime into spatial and time coordinates, which it is also commonly done to study formulations of the Einstein equations in numerical relativity. Assuming a globally hyperbolic spacetime, a spacetime which preserves causality, we can foliate it into non-intersecting spacelike hypersurfaces (Cauchy surfaces), $\sum_t$, parametrized by a global time function $\boldsymbol{t}$. We define a future-directed timelike four vector $\boldsymbol{n}$ normal to the hypersurfaces $\sum_t$, satisfying $n^a \propto \nabla_a t$ and $n^a n_a = -1$. Then, the spacetime metric g_{ab} induces a spatial metric γ_{ab} on the spatial hypersurfaces given by

$$\gamma_{ab} = g_{ab} + n_a n_b. \tag{2.9}$$

It is straightforward to show that $n^a \gamma_{ab} = 0$, which means that γ_{ab} is a projection tensor which maps spacetime tensors onto spatial hypersurfaces. If we now take a timelike vector t^a of the spacetime tangent to the time axis, i.e. $t^a = (\partial/\partial t)^a$ and $t^a \nabla_a t = 1$, then, as shown in Fig. 2.2, t^a is not always normal to spatial hypersurfaces and it can be decomposed into timelike and spacelike components as

$$\alpha = -t^a n_a, \quad \beta^a = t^b \gamma_b^a, \tag{2.10}$$

where α is the *lapse* function, which measures the proper time elapsed between neighbouring time slices along the normal unit vector, and β^a is the *shift* vector, which describes the change of coordinates from one slice to another with respect to the normal vector. Both α and β^a are related to the degrees of freedom in the choice of coordinates. The components of n^a and the spatial metric can be written in terms of the lapse and the shift as

$$n^a = \left(\alpha^{-1}, -\beta^i \alpha^{-1}\right), \quad n_a = (-\alpha, 0, 0, 0), \tag{2.11}$$

with $\beta_i = \gamma_{ij} \beta^j$ and $\beta^a = (0, \beta^i)$. Using the above relations one obtains the following expression for the four dimensional spacetime metric,

$$g_{ab} = \begin{pmatrix} -\alpha^2 + \beta_m \beta^m & \beta_i \\ \beta_j & \gamma_{ij} \end{pmatrix}, \tag{2.12}$$

or equivalently, the line element can be written as

$$ds^2 = -\alpha^2 dt^2 + \gamma_{ij}(dx^i + \beta^i dt)(dx^j + \beta^j dt), \tag{2.13}$$

which is sometimes referred as the $3 + 1$ form of the metric. Eq. (2.13) may be interpreted as the invariant interval, a generalization of the Euclidean concept of distance for a 4-dimensional spacetime, between the two points $x^i(t)$ and $x^i(t + dt)$ of Fig. 2.2.
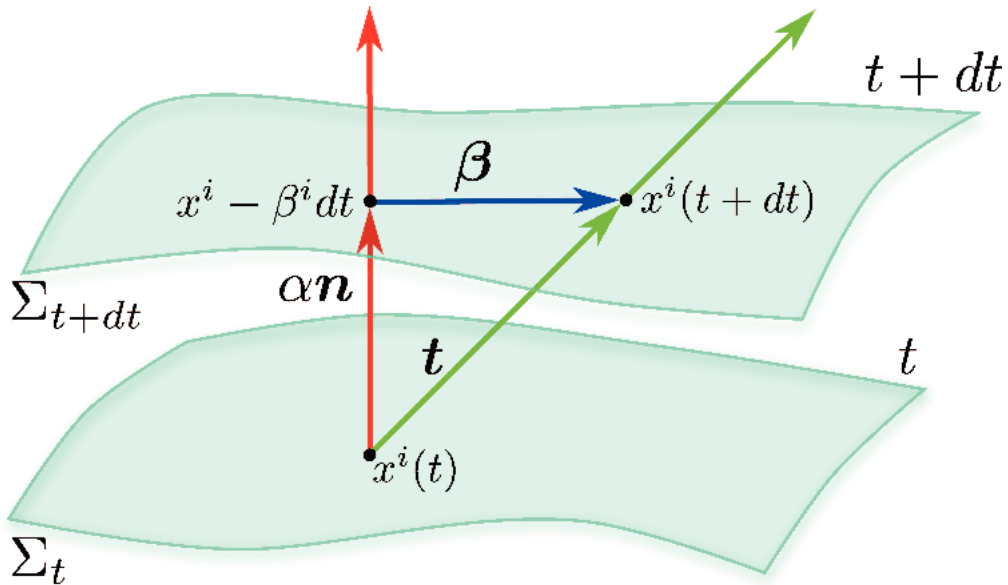
FIGURE 2.2: Representation of the 3+1 decomposition of the space-
time in spatial slices of constant time coordinate $\sum_t$ and $\sum_{t+dt}$. The
four vector $\boldsymbol{t}$ represents the direction of evolution of the coordinate
time t, this can be decomposed into a timelike component $\alpha\boldsymbol{n}$ and
spacelike component $\boldsymbol{\beta}$. $\boldsymbol{n}$ is a timelike unit vector normal to the
hypersurface and α is called the *lapse* representing the proper time
elapsed from one hypersurface to the next one, while $\boldsymbol{\beta}$ is the *shift*
vector which describes the change of the spatial coordinates between
both hypersurfaces. Graphic taken from [39].

The extrinsic curvature or second fundamental form describes the rate of change
between two nearby normal vectors, n^a and $n^a + \delta n^a$ in the spacelike hypersurface,
thus, it is calculated projecting the derivative of the normal vector onto the spacelike
hypersurfaces $\sum_t$,

$$K_{ab} = -\gamma_a^c \nabla_c n_b = -\frac{1}{2}\mathcal{L}_n \gamma_{ab}, \tag{2.14}$$

where $\mathcal{L}_n$ indicates the Lie derivative with respect to n^a.

With the notation and the definitions introduced in this section one can obtain the
standard 3+1 equations, which we list below. This formalism uses different projection
operators to decompose the Einstein equations into constraint and evolution equations.
We refer the reader to [40, 41, 42, 43] for details in the derivation of these expressions.
In the case of Einstein equations one has four constraint equations. The *Hamiltonian
constraint*,

$$\mathcal{H} \equiv R + K^2 - K_{ij}K^{ij} - 16\pi\rho = 0, \tag{2.15}$$

where $K = \gamma^{ab}K_{ab}$ is the trace of the extrinsic curvature K_{ab} and $\rho = n_a n_b T^{ab}$ is the
total energy density measured by a normal observer n^a.

The remaining three constraint equations are the so-called *momentum constraint*
equations,

$$\mathcal{M}_i \equiv D_j(K_i^j - K\delta_j^i) - 8\pi S_i = 0, \tag{2.16}$$

where D_j is the 3-dimensional covariant derivative compatible with the spatial metric,
i.e. $D_a\gamma_{bc} = 0$, and $S_a = -\gamma_a^b n^c T_{bc}$ is the momentum density measured by a normal
observer. These constraint equations involve only the spatial metric, extrinsic curva-
ture and their spatial derivatives and not time derivatives, hence, these are a set of

equations which have to be satisfied on each hypersurface.

  The evolution equations for the spatial metric,

$$\partial_t \gamma_{ij} = -2\alpha K^{ij} + D_i\beta_j + D_j\beta_i, \tag{2.17}$$

and the extrinsic curvature,

$$
\begin{aligned}
\partial_t K_{ij} = {}& - D_i D_j\alpha + \alpha(R_{ij} - 2K_{ik}K_j^k + KK_{ij}) - 8\pi\alpha(S_{ij} - \frac{1}{2}\gamma_{ij}(S - \rho)) \\
& + \beta^k D_k K_{ij} + K_{ik}D_j\beta^k + K_{kj}D_i\beta^k,
\end{aligned}
\tag{2.18}
$$

where R_{ab} is the Ricci tensor, $S_{ab} = \gamma_a^c\gamma_b^d T_{cd}$ is the spatial stress energy tensor and $S = S_a^a$ its trace. Equations (2.17) and (2.18) are a coupled system of differential equations for the evolution of (γ_{ab}, K_{ab}), which together with the constraint equations (2.15) and (2.16) are equivalent to the Einstein equations (1.1). In the $3 + 1$ decomposition the Einstein equations have been recast in the form of a constrained initial value problem, from a system of coupled equations of second order in time in their original form to first order time in the new formulation. Note also that as in the case of electrodynamics, the evolution equations for the spatial metric and the extrinsic curvature preserve the constraint equations, thus, if the constraints are satisfied at a given time t they will also be satisfied at all later times.

The above geometrical description of the $(3 + 1)$-splitting of spacetime is the one commonly explained in introductory textbooks of numerical relativity [42, 43]. The above description is totally equivalent to the classical field approach typically used to analytically compute Hamiltonians at different PN orders. Starting from (2.13) and considering only asymptotically flat spacetimes it can be shown that the Hamiltonian generating the Einstein field equations is [44, 45]

$$H\left[\gamma_{ij}, \pi^{ij}, \alpha, \beta^i; q^A, \pi_A\right] = \int d^3x(\alpha\mathcal{H} + \beta^i\mathcal{M}_i) + \frac{c^4}{16\pi G}\oint_{i^0} dS_i\partial_j(\gamma_{ij} - \delta_{ij}\gamma_{kk}), \tag{2.19}$$

where π^{ij} is related to the ADM canonical momentum by $c^3\pi^{ij}/(16\pi G)$ with

$$\pi_{ij} = -\gamma^{1/2}(K_{ij} - K\gamma_{ij}). \tag{2.20}$$

Furthermore, (q^A, π_A) represent the canonical matter variables appearing in the matter part of the Hamiltonian density, $\mathcal{H}$, and momentum density, $\mathcal{M}_i$, defined as

$$\mathcal{H} = \frac{c^4}{16\pi G}\left[-\gamma^{1/2}R + \frac{1}{\gamma^{1/2}}\left(\gamma_{ik}\gamma_{jl}\pi^{ij}\pi^{kl} - \frac{1}{2}\pi^2\right)\right] + \mathcal{H}_{\boldsymbol{m}}, \tag{2.21a}$$

$$\mathcal{M}_i = \frac{c^3}{8\pi G}\gamma_{ij}\nabla_k\pi^{jk} + \mathcal{M}_{\boldsymbol{m},i}, \tag{2.21b}$$

where $\mathcal{H}_{\boldsymbol{m}} \equiv \rho$ and $\mathcal{M}_{\boldsymbol{m},i} \equiv S_i$ introduced in Eqs. (2.15) and (2.16), respectively. Then, varying Eq. (2.19) with respect to the lapse and shift one reproduces the constraint equations (2.15) and (2.16),

$$\mathcal{H} = 0, \quad \mathcal{M}_i = 0. \tag{2.22}$$

Adopting the following coordinate conditions, also called ADMTT coordinates or ADMTT gauge,

$$\pi^{ii} = 0, \quad \partial_j \gamma_{ij} - \partial_i \gamma_{jj} = 0 \text{ or } \gamma_{ij} = \psi \delta_{ij} + h_{ij}^{TT}, \tag{2.23}$$

where ψ is a field function and h_{ij}^{TT} denotes the transverse and traceless part. Taking these gauge conditions, four coordinate conditions, and the four constraint equations one obtains the Hamiltonian of Eq. (2.19) in a reduced form

$$\begin{aligned} H_{\text{red}}\left[h_{ij}^{TT}, \pi_{TT}^{ij}; q^A, \pi_A\right] &= \frac{c^4}{16\pi G} \oint_{i^0} dS_i \partial_j(\gamma_{ij} - \delta_{ij}\gamma_{kk}) \\ &= \frac{c^4}{16\pi G} \int d^3x \partial_i \partial_j(\gamma_{ij} - \delta_{ij}\gamma_{kk}). \end{aligned} \tag{2.24}$$

The reduced Hamiltonian of Eq. (2.24) generates the field equations for the two unfixed degrees of freedom (10 metric coefficients - 4 constraint equations - 4 gauge conditions) corresponding to two metric degrees of freedom which correspond to the gravitational radiation.

2.2.3 Post-Newtonian description of quasicircular binaries

In the case of BBHs the Hamiltonian for point particles has been analytically calculated to different PN orders depending on the inclusion of spin effects as indicated in Sec. 2.2.1. The total PN Hamiltonian can be used then to compute the Hamilton equations of a spinning point particle in the center of mass frame described by the canonical coordinates (x^i, p_i, S^i),

$$\dot{p}_i = -\frac{\partial H}{\partial x^i}, \qquad \dot{x}^i = \frac{\partial H}{\partial p_i} \qquad \dot{S}^i = g^{im}\epsilon_{mjk}\frac{\partial H}{\partial S_j}S_k. \tag{2.25}$$

One ingredient of the description of a BBH is the calculation of the equations of motion in the near region. The other ingredient is the waveform computed at null infinity. As explained in Sec. 2.2 there are two main approaches to tackle the calculation of the waveform, the Blanchet-Damour approach, consisting in a multipolar expansion of the gravitational field, and the direct integration of the relaxed Einstein equations. We directly present the results of the calculation of the PN waveforms and refer the reader to [10, 46, 13, 14, 15] for details of the calculations.

We focus on quasicircular BBHs characterized by a quasi-adiabatic evolution where the black holes approach each other with increasing velocity, which implies that the PN approximation is less and less valid. Several criteria exists to determine the end of the inspiral regime, i.e., the breakdown of the PN expansion. One is the usage of the Innermost Stable Circular Orbit (ISCO) [47], another is the Minimum Energy Circular Orbit (MECO) [6]. We remark that although the ISCO and MECO separations mark the end of the inspiral, the accuracy of the PN approximation tends to degrade much earlier due to the lack of knowledge of higher PN order terms which make the PN waveforms faithfully reproduce numerical relativity waveforms [48, 49].

One of the applications of the PN approach is the calculation of the evolution of the orbital phase $\phi(t)$ of a compact binary (we focus here on BBHs) as an expansion

in a small parameter, x, where

$$x = v^2 = (M\omega)^{2/3}, \quad \omega = \frac{d\phi}{dt}, \tag{2.26}$$

and v is the characteristic speed of the binary, ω the orbital frequency and M is the total mass of the system. In the adiabatic approximation one can work with orbit averaged quantities. From the energy conservation condition one obtains,

$$\left\langle \frac{dE_{orb}}{dt} \right\rangle = -\langle \mathcal{F} \rangle, \tag{2.27}$$

where E_{orb} is the orbital energy and $\mathcal{F}$ is the gravitational wave energy flux. Combining Eqs. (2.26) and (2.27) one obtains the following system of equations for the orbital phase

$$\frac{dv}{dt} = -\frac{\mathcal{F}}{dE_{orb}/dv}, \tag{2.28a}$$

$$\frac{d\phi}{dt} = \frac{v^3}{M}. \tag{2.28b}$$

Equivalently, Eqs. (2.28a) and (2.28b) can be expressed as

$$t(v) = t_{\text{ref}} + M \int_v^{v_{\text{ref}}} dv \frac{E'(v)}{\mathcal{F}(v)}, \tag{2.29a}$$

$$\phi(v) = \phi_{\text{ref}} + \int_v^{v_{\text{ref}}} dv v^3 \frac{E'(v)}{\mathcal{F}(v)}, \tag{2.29b}$$

where $E'(v) \equiv dE_{orb}/dv$. Using the 3PN conserved energy [10], E^{3PN}, and the 3.5PN energy flux, $\mathcal{F}_{3.5}(v)$, as an expansion of the small parameter v [50]

$$
\begin{aligned}
E^{3PN}(v) = \quad - \quad & \frac{1}{2}\eta v^2 \left[1 - \left(\frac{3}{4} + \frac{1}{12}\eta \right) v^2 - \left(\frac{27}{8} - \frac{19}{8}\eta + \frac{1}{24}\eta^2 \right) v^4 \right. \\
- \quad & \left. \left\{ \frac{675}{64} - \left(\frac{34445}{576} - \frac{205}{96}\pi^2 \right) \eta + \frac{155}{96}\eta^2 + \frac{35}{5184}\eta^3 \right\} v^6 \right],
\end{aligned}
\tag{2.30}
$$

$$
\begin{aligned}
\mathcal{F}^{3.5PN}(v) = \quad + \quad & \frac{32}{5}\eta^2 v^{10} \left[1 - \left(\frac{1247}{336} + \frac{35}{12}\eta \right) v^2 + 4\pi v^3 - \left(\frac{44711}{9072} - \frac{9271}{504}\eta - \frac{65}{18}\eta^2 \right) v^4 \right. \\
- \quad & \left(\frac{8191}{672} + \frac{583}{24}\eta \right) \pi v^5 + \left\{ \frac{6643739519}{69854400} + \frac{16}{3}\pi^2 - \frac{1712}{105}\gamma \right. \\
+ \quad & \left(\frac{41}{48}\pi^2 - \frac{134543}{7776} \right) \eta - \frac{94403}{3024}\eta^2 - \frac{775}{324}\eta^3 - \frac{856}{105}\log\left(16v^2\right) \right\} v^6 \\
- \quad & \left. \left(\frac{16285}{504} - \frac{214745}{1728}\eta - \frac{193385}{3024}\eta^2 \right) \pi v^7 \right],
\end{aligned}
\tag{2.31}
$$

different PN approximants have been developed depending on the treatment of the ratio $\mathcal{F}(v)/E'(v)$ [50, 51, 52], although all of them equivalent to the same PN order.

The previous equations for the orbital energy and the energy flux are restricted to non-spinning systems. However, generic BBHs can have arbitrarily oriented spins. The description of spinning systems is typically separated into systems with the spin

vectors (anti)parallel to the orbital angular momentum of the system, called *non-precessing*, and systems with spins misaligned with the orbital angular momentum, called *precessing*. For the latter relativistic interactions between the orbital and spin angular momenta induce precessing motion of the spin vectors and the orbital plane [53, 54]. Precession introduces complex phase and amplitude modulations to the GW waveforms complicating substantially their description and modelling. We discuss further precession in Chapter 6, where we present results on the analysis of several approximations used to describe quasi-circular precessing waveforms.

TaylorT1

The TaylorT1 approximant is obtained by taking directly the PN expansions for $\mathcal{F}(v)$ and $E'(v)$ as in Eqs. (2.28a) and (2.28b). Thus, the expressions are left as a ratio of polynomials and the differential equations are solved numerically.

$$\frac{dv^{(\mathrm{T1})}}{dt} = -\frac{\mathcal{F}}{dE_{orb}/dv^{(\mathrm{T1})}}, \tag{2.32a}$$

$$\frac{d\phi^{(\mathrm{T1})}}{dt} = \frac{\left(v^{(\mathrm{T1})}\right)^3}{M}. \tag{2.32b}$$

The initial conditions are typically chosen such that at $v(t = 0) = v_0$ and the initial phase set initially to 0 or $\pi/2$, when taking into account only the $(2, \pm 2)$ modes in order to have two orthogonal templates [50].

TaylorT2

The TaylorT2 approximant is calculated taking Eqs. (2.29a) and (2.29b), expanding the ratio $E'(v)/\mathcal{F}(v)$ to a consistent PN order and integrating term by term. As a result one obtains a pair of equations of the form [55]

$$\phi_n^{(\mathrm{T2})}(v) = \phi_{\mathrm{ref}}^{(\mathrm{T2})} + \sum_{k=0}^{n} \hat{\phi}_k^v v^k, \tag{2.33a}$$

$$t_n^{(\mathrm{T2})}(v) = t_{\mathrm{ref}}^{(\mathrm{T2})} + \sum_{k=0}^{n} \hat{t}_k^v v^k, \tag{2.33b}$$

where n indicates the post-Newtonian order. We note that TaylorT2 is a computationally expensive approximant as it requires solving a couple of trascendental equations. The initial conditions for t_{ref} are usually chosen such that at $t = 0$, $v = v_0$.

TaylorT3

This approximant is based upon TaylorT2, which provides analytical expressions for $\phi^{(\mathrm{T2})}(v)$ and $t^{(\mathrm{T2})}(v)$ as polynomials of v [55]. The TaylorT3 approximant consists then in inverting the series $\phi(v)$ and $t(v)$ to obtain $v(t)$ and $\phi(t)$,

$$\phi_n^{(\mathrm{T3})}(t) = \phi_{\mathrm{ref}}^{(\mathrm{T3})} + \sum_{k=0}^{n} \hat{\phi}_k^t \theta^k, \tag{2.34a}$$

$$\omega_n^{(\mathrm{T3})}(t) = \sum_{k=0}^{n} \hat{\omega}_k^t \theta^k, \tag{2.34b}$$

where $\theta = [\eta(t_{\rm ref} - t)/(5M)]^{-1/8}$ and n indicates the post-Newtonian order. For this case we have computed the 3.5PN expressions for $\omega^{\rm (T3)}$ and $\phi^{\rm (T3)}$ including non-precessing spin effects,

$$
\phi_{3.5\rm PN}^{\rm (T3)}(t) = -\frac{1}{\eta\theta^5}\left[1 + \theta^2\frac{5(924\eta + 743)}{8064} + \frac{\theta^3}{128}\left(\left(-113\left(\sqrt{1 - 4\eta} - 1\right) - 76\eta\right)\chi_1\right.\right.
$$

$$
+ \left(113\left(\sqrt{1 - 4\eta} + 1\right) - 76\eta\right)\chi_2 - 96\pi\right) + \frac{5\theta^4}{14450688}\left(2617776\eta^2\right.
$$

$$
+ 56\eta\left(61236\chi_1^2 - 119448\chi_2\chi_1 + 61236\chi_2^2 + 56975\right)
$$

$$
+ 1714608\left(\sqrt{1 - 4\eta} - 1\right)\chi_1^2 - 1714608\sqrt{1 - 4\eta}\chi_2^2 - 1714608\chi_2^2
$$

$$
\left. + 1855099\right) + \frac{\theta^5}{1548288}\left(\chi_1\left(1008\eta^2(549 - 340\log(8))\right.\right.
$$

$$
+ 60\left(146597\left(\sqrt{1 - 4\eta} - 1\right) + 112\eta\left(153\eta + 63\sqrt{1 - 4\eta} + 1213\right)\right)\log(\theta)
$$

$$
+ 4\eta\left(113589\sqrt{1 - 4\eta} - 560\left(63\sqrt{1 - 4\eta} + 1213\right)\log(8) + 643322\right)
$$

$$
\left. - \left(\sqrt{1 - 4\eta} - 1\right)(2931940\log(8) - 3183817)\right) + \chi_2\left(1008\eta^2(549 - 340\log(8))\right.
$$

$$
- 60\left(146597\left(\sqrt{1 - 4\eta} + 1\right) - 112\eta\left(153\eta - 63\sqrt{1 - 4\eta} + 1213\right)\right)\log(\theta)
$$

$$
+ 4\eta\left(-113589\sqrt{1 - 4\eta} + 560\left(63\sqrt{1 - 4\eta} - 1213\right)\log(8)\right.
$$

$$
\left.\left. + 643322\right) + \left(\sqrt{1 - 4\eta} + 1\right)(2931940\log(8) - 3183817)\right)
$$

$$
+ 24\pi(15(7729 - 1092\eta)\log(\theta) + 84\eta(67 + 65\log(8))
$$

$$
+ 47561 - 38645\log(8)))\right) + \theta^6\left(-\frac{1179625\eta^3}{1769472}\right.
$$

$$
+ \frac{\chi_1^2}{27525120}\left(-18767224\eta^2 + 2\left(6352738\sqrt{1 - 4\eta} - 23281001\right)\eta\right.
$$

$$
\left. - 16928263\left(\sqrt{1 - 4\eta} - 1\right)\right) - \frac{\chi_2^2}{27525120}\left(18767224\eta^2\right.
$$

$$
\left. + 2\left(6352738\sqrt{1 - 4\eta} + 23281001\right)\eta - 16928263\left(\sqrt{1 - 4\eta} + 1\right)\right)
$$

$$
+ \frac{154565\eta^2}{1835008} + \frac{\pi\chi_2}{2560}\left(6127\left(\sqrt{1 - 4\eta} + 1\right)\right.
$$

$$
\left. - 4204\eta\right) + \frac{\chi_1}{6881280}\left(\eta(13665988\eta + 9433625)\chi_2\right.
$$

$$
\left. - 2688\pi\left(6127\left(\sqrt{1 - 4\eta} - 1\right) + 4204\eta\right)\right) + \frac{2255\pi^2\eta}{2048}
$$

$$
- \frac{126510089885\eta}{4161798144} - \frac{107\log(\theta)}{56} - \frac{53\pi^2}{40} - \frac{107\gamma}{56}
$$

$$
\left. + \frac{831032450749357}{57682522275840} - \log(4) + \frac{5\log(2)}{56}\right) + \frac{7938\theta^7}{520224768}\left(\left(8876\eta^2\right.\right.
$$

$$
+ \left(71931\sqrt{1 - 4\eta} - 206917\right)\eta - 67493\left(\sqrt{1 - 4\eta} - 1\right)\chi_1^3
$$

$$
- 7938\left(-8876\eta^2 + \left(71931\sqrt{1 - 4\eta} + 206917\right)\eta\right.
$$

$$
\left. - 67493\left(\sqrt{1 - 4\eta} + 1\right)\right)\chi_2^3 + 3\pi\left(-47634384\eta^2\right.
$$

$$
\left. + 164245200\eta + 188516689\right) + \chi_1\left(169753248\eta^3\right.
$$

$$
+ 84\left(870576\sqrt{1 - 4\eta} + 840149\right)\eta^2 - 7938(5372\eta
$$

$$-192709\left(\sqrt{1-4\eta}+1\right)\right)\eta\chi_2^2-1796909184\pi\eta\chi_2-7\left(429508815\sqrt{1-4\eta}\right.$$

$$-1496368361)\,\eta+6579635551\left(\sqrt{1-4\eta}-1\right)\right)+\left(169753248\eta^3\right.$$

$$-84\left(870576\sqrt{1-4\eta}-840149\right)\eta^2-1496368361\right)\eta$$

$$+6579635551\left(\sqrt{1-4\eta}-1\right)\right)+7\left(429508815\sqrt{1-4\eta}+1496368361\right)\eta$$

$$-6579635551\left(\sqrt{1-4\eta}+1\right)\right)\chi_2+7938\chi_1^2\left(\left(-192709\left(\sqrt{1-4\eta}-1\right)\right.\right.$$

$$-5372\eta)\,\eta\chi_2+58608\pi\left(2\eta+\sqrt{1-4\eta}-1\right)\right)$$

$$-465230304\pi\left(-2\eta+\sqrt{1-4\eta}+1\right)\chi_2^2\Big)\Big],\tag{2.35a}$$

$$\omega^{(\mathrm{T3})}_{3.5\mathrm{PN}}(t)=\frac{\theta^3}{8}\left[1+\theta^2\frac{924\eta+743}{2688}+\frac{\theta^3}{320}\left(-96\pi-76\eta\left(\chi_1+\chi_2\right)\right.\right.$$

$$-113\left(\sqrt{1-4\eta}-1\right)\chi_1+113\left(\sqrt{1-4\eta}+1\right)\chi_2\Big)$$

$$+\frac{\theta^4}{14450688}\left(2617776\eta^2-6689088\eta\chi_1\chi_2\right.$$

$$+1714608\left(2\eta+\sqrt{1-4\eta}-1\right)\chi_1^2-1714608\left(-2\eta\right.$$

$$+\sqrt{1-4\eta}+1\right)\chi_2^2+3190600\eta+1855099\Big)$$

$$+\frac{\theta^5}{129024}\left(-17136\eta^2\left(\chi_1+\chi_2\right)+56\eta\left(-2\left(63\sqrt{1-4\eta}+1213\right)\chi_1\right.\right.$$

$$+2\left(63\sqrt{1-4\eta}-1213\right)\chi_2+117\pi\right)-146597\left(\left(\sqrt{1-4\eta}\right.\right.$$

$$-1)\chi_1-\left(\sqrt{1-4\eta}+1\right)\chi_2\right)-46374\pi\Big)$$

$$+\theta^6\left(\frac{235925\eta^3}{1769472}-\frac{1}{137625600}\left(-18767224\eta^2\right.\right.$$

$$+2\left(6352738\sqrt{1-4\eta}-23281001\right)\eta-16928263\left(\sqrt{1-4\eta}\right.$$

$$-1)\right)\chi_1^2+\frac{1}{137625600}\left(\left(18767224\eta^2\right.\right.$$

$$+2\left(6352738\sqrt{1-4\eta}+23281001\right)\eta-16928263\left(\sqrt{1-4\eta}+1\right)\right)\chi_2^2\Big)$$

$$-\frac{30913\eta^2}{1835008}-\frac{\pi\chi_2}{12800}\left(6127\left(\sqrt{1-4\eta}+1\right)\right.$$

$$-4204\eta)+\frac{\chi_1}{34406400}\left(2688\pi\left(6127\left(\sqrt{1-4\eta}-1\right)\right.\right.$$

$$+4204\eta)-\eta(13665988\eta+9433625)\chi_2\right)-\frac{451\pi^2\eta}{2048}$$

$$+\frac{25302017977\eta}{4161798144}+\frac{107\log(\theta)}{280}+\frac{53\pi^2}{200}$$

$$+\frac{107\gamma}{280}-\frac{720817631400877}{288412611379200}+\frac{107\log(2)}{280}\Big)$$

$$+\frac{\theta^7}{1300561920}\left(-7938\left(8876\eta^2+\left(71931\sqrt{1-4\eta}-206917\right)\eta\right.\right.$$

$$-67493\left(\sqrt{1-4\eta}-1\right)\right)\chi_1^3+7938\left(-8876\eta^2\right.$$

$$+\left(71931\sqrt{1-4\eta}+206917\right)\eta-67493\left(\sqrt{1-4\eta}+1\right)\right)\chi_2^3$$

$$
\begin{aligned}
&+ 3\pi \left(47634384\eta^2 - 164245200\eta - 188516689 \right) - \chi_1 \left(169753248\eta^3 \right. \\
&+ 84 \left(870576\sqrt{1-4\eta} + 840149 \right) \eta^2 - 7938 \left(5372\eta \right. \\
&- 192709 \left(\sqrt{1-4\eta} + 1 \right) \left. \right) \eta\chi_2^2 - 1796909184\pi\eta\chi_2 \\
&- 7 \left(429508815\sqrt{1-4\eta} - 1496368361 \right) \eta + 6579635551 \left(\sqrt{1-4\eta} - 1 \right) \left. \right) \\
&+ \left(-169753248\eta^3 + 84 \left(870576\sqrt{1-4\eta} - 840149 \right) \eta^2 \right. \\
&- 7 \left(429508815\sqrt{1-4\eta} + 1496368361 \right) \eta + 6579635551 \left(\sqrt{1-4\eta} \right. \\
&+ \left. 1 \right) \left. \right) \chi_2 - 7938\chi_1^2 \left(\left(-192709 \left(\sqrt{1-4\eta} - 1 \right) \right. \right. \\
&- 5372\eta \left. \right) \eta\chi_2 + 58608\pi \left(2\eta + \sqrt{1-4\eta} - 1 \right) \left. \right) \\
&+ 465230304\pi \left(-2\eta + \sqrt{1-4\eta} + 1 \right) \chi_2^2 \left. \right) \left. \right],
\end{aligned}
\tag{2.35b}
$$

where $\chi_i = \vec{S}_i \cdot \hat{L}/m_i^2$, $i = 1,2$; $\vec{S}_i$ indicates the spin vector and $\hat{L} = \vec{L}/|\vec{L}|$ is a unit vector in the direction of the orbital angular momentum of the system. For this approximant as $t \to t_{\mathrm{ref}}$, then ω diverges. Additionally, given an initial orbital frequency ω_0 at $t = 0$, one has to solve numerically Eq. (2.35b) to find t_{ref}.

TaylorT4

The TaylorT4 approximant [55] is an extension of TaylorT1 resulting from expanding the ratio $\mathcal{F}(v)/E'(v)$ to a consistent PN order. The equations to solve for a non-spinning binary at 3.5PN order are

$$
\begin{aligned}
\frac{dv}{dt} = \frac{32}{5}\frac{\eta}{M}v^9 &\left[1 - \left(\frac{743}{336} + \frac{11}{4}\eta \right) v^2 + 4\pi v^3 + \left(\frac{34103}{18144} + \frac{13661}{2016}\eta + \frac{59}{18}\eta^2 \right) v^4 \right. \\
&- \left(\frac{4159}{672} + \frac{189}{8}\eta \right) \pi v^5 + \left(\frac{16447322263}{139708800} + \frac{16}{3}\pi^2 - \frac{1712}{105}\gamma \right. \\
&+ \left(\frac{451}{48}\pi^2 - \frac{56198689}{217728} \right) \eta + \frac{541}{896}\eta^2 - \frac{5605}{2592}\eta^3 - \frac{856}{105}\log(16v^2) \left. \right) v^6 \\
&- \left(\frac{4415}{4032} - \frac{358675}{6048}\eta - \frac{91495}{1512}\eta^2 \right) \pi v^7 \left. \right],
\end{aligned}
\tag{2.36a}
$$

$$
\frac{d\phi^{(T4)}}{dt} = \frac{v^3}{M},
\tag{2.36b}
$$

where $\gamma = 0.57721$ is the Euler constant. This PN template agrees better with numerical simulations of the inspiral than TaylorT1 [55]. We note also that while TaylorT1 can have a pole in the right hand side of the equation for dv/dt, that is not possible when taking (2.36a). The setup of initial conditions for this approximant is the same as with TaylorT1.

TaylorF2

This approximant is the analogue of the TaylorT2 approximant in Fourier domain. It is calculated using the *stationary phase approximation* (SPA), which assumes that the amplitude is a slowly-varying function with respect to the orbital phase. Using

the SPA the frequency domain waveform can be expressed as [55]

$$\tilde{h}^{SPA}(f) = \frac{a(t_f)}{\sqrt{\ddot{\phi}(t_f}}e^{i[\psi_f(t_f)-\pi/4]}, \qquad \psi_f(t) \equiv 2\pi ft - 2\phi(t), \qquad (2.37)$$

where t_f is defined such that $d\psi_f(t)/dt = 0$ and $a(t_f)$ is an amplitude coefficient. Within the adiabatic approximation t_f and $\psi_f(t)$ can be computed from the following equations

$$\frac{d\psi}{df} - 2\pi t = 0, \quad \frac{dt}{df} + \frac{\pi M^2}{3v^2}\frac{E'(f)}{\mathcal{F}(f)} = 0, \qquad (2.38)$$

which characterize the TaylorF1 approximant. Truncating the energy and flux functions in Eq. (2.38) to consistent PN order and integrating each term, one obtains the phase and amplitude of the Fourier domain waveform [55, 49]. For this approximant the constants t_c and ϕ_c are chosen freely.

2.2.4 Post-Newtonian description of eccentric binaries

In this section we briefly present the PN description of eccentric BBHs. A binary evolving in an elliptical orbit requires two additional parameters, apart from the eight parameters determining the quasicircular case, to unequivocally determine its orbit, *eccentricity*, e, and the relative position of its components in the orbit, *periapsis argument*, Ω. Apart from the orbital, radiation reaction and spin-precession[2] timescales of the gravitational two-body problem, eccentricity introduces a new timescale due to periastron precession. Neglecting spin-precession, the hierarchy of timescales in the binary problem is

$$T_{\mathrm{orb}} \ll T_{\mathrm{prec}} \ll T_{RR}. \qquad (2.39)$$

This new timescale induces oscillations in the dynamical quantities and the waveform due to the asymmetric gravitational interaction along the elliptical orbit. In Fig. 2.3 we exhibit the separation and the orbital frequency of a mass ratio 2 non-spinning PN configuration for initial eccentricities 10^{-4} and 0.2. The PN evolution code and the initial eccentricities are specified using the method of [56]. The PN evolution is stopped at separation $4M$ as can be observed in the top panel of Fig. 2.3.

As displayed in Fig. 2.3, the description of eccentric binary black holes (eBBHs) complicates substantially with respect to the quasicircular (QC) case, due to the introduction of oscillations caused by eccentricity. Next, we highlight the current state-of-art of commonly used analytical descriptions for eBBHs.

Quasi-Keplerian parametrization

The quasi-Keplerian (QK) parametrization [57, 58] is typically used to describe non-spinning eccentric binaries. This parametrization describes the conservative dynamics and it also incorporates effects of radiation reaction [59, 60] describing the three timescales of Eq. (2.39). Furthermore, the secular evolution of the orbital elements has been calculated to 3PN order [61, 62, 63]. These theoretical results have been used to develop a pletora of waveform models [64, 65, 66, 67, 68] in the last years.

At 3PN order, the conservative dynamics is specified by the following equations,

$$r = a_r \left(1 - e_r \cos u\right), \qquad (2.40a)$$

---

[2]Only when spins are misaligned with the orbital angular momentum of the system.
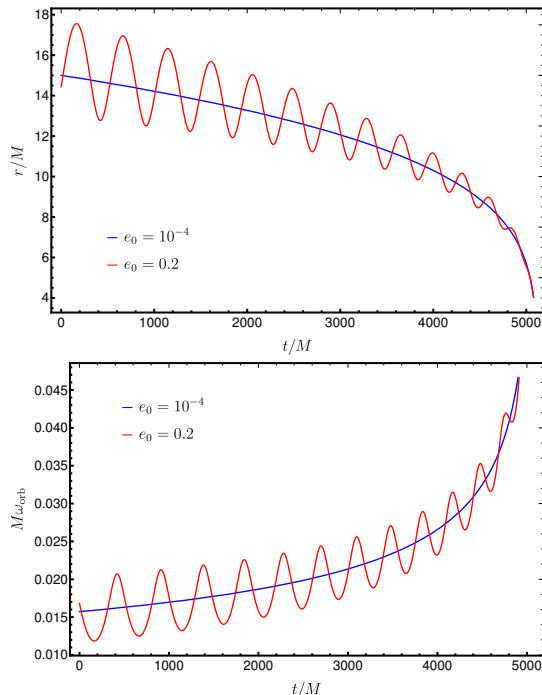
FIGURE 2.3: Top panel: Time domain evolution of the orbital separation of a mass ratio 2 non-spinning binary. The blue (red) line corresponds to a configuration with initial eccentricity $e_0 = 10^{-4}$ ($e_0 = 0.2$). Bottom panel: Time domain evolution of the orbital frequency of a mass ratio 2 non-spinning binary. The blue (red) line corresponds to a configuration with initial eccentricity $e_0 = 10^{-4}$ ($e_0 = 0.2$).

$$\phi - \phi_0 = (1+k)v + (f_{4\phi} + f_{6\phi})\sin(2v) + (g_{4\phi} + g_{6\phi})\sin(3v)$$
$$+ i_{6\phi}\sin(4v) + h_{6\phi}\sin(5v)\,, \tag{2.40b}$$

$$v = 2\arctan\left[\left(\frac{1+e_\phi}{1-e_\phi}\right)^{1/2}\tan\frac{u}{2}\right]\,. \tag{2.40c}$$

We note that in Eqs. (2.40a), (2.40b) and (2.40c) two different eccentricity parameters appear, the radial and angular eccentricities, e_r and e_ϕ, respectively, such that the expressions for r and ϕ take a similar form as in the Keplerian case. The parameter k is the periastron advance per orbital period, a_r is the semi-major axis, $f_{4\phi}$, $f_{6\phi}$, $g_{4\phi}$, $g_{6\phi}$, $i_{6\phi}$, and $h_{6\phi}$ are functions of the orbital energy and angular momentum [58].

The variable u is the eccentric anomaly related to the mean anomaly l through the 3PN Kepler equation

$$l = u - e_t \sin u + (g_{4t} + g_{6t})(v - u)$$
$$+ (f_{4t} + f_{6t})\sin v + i_{6t}\sin(2v) + h_{6t}\sin(3v)\,, \tag{2.41}$$

where e_t is the time eccentricity, another eccentricity parameter, and g_{4t}, g_{6t}, f_{4t}, f_{6t}, i_{6t}, and h_{6t} are functions of the energy and angular momentum of the system [58]. We remark that the three eccentricity parameters are not independent, and there exist explicit relations among all of them [58] at consistent PN order, hence, in practice one chooses to express the equations in terms of the time eccentricity parameter $e \equiv e_t$ and the PN parameter $x = (GM\omega/c^3)^{2/3}$.

In order to solve the Kepler equation (2.41) several methods exist [69, 70, 71]. The analytical procedure of [71] yields

$$u = l + \sum_{s=1}^{\infty} A_s \sin(sl) \,, \tag{2.42a}$$

$$A_s = \frac{2}{s} J_s(se_t) + \sum_{j=1}^{\infty} \alpha_j \left\{ J_{s+j}(se_t) - J_{s-j}(se_t) \right\} \,, \tag{2.42b}$$

where J_s are Bessel functions of the first kind of order s and α_j are PN functions of the energy and angular momentum [71].

The prescription presented so far, concerns only the conservative dynamics. Radiation reaction effects are typically introduced through the conservation of the gravitational wave energy and angular flux, and provide two differential equations for the secular evolutions of x and e [72]

$$M\dot{x} = x^5 \left(\dot{x}_{0\mathrm{PN}} + \dot{x}_{1\mathrm{PN}}x + \dot{x}_{1.5\mathrm{PN}}x^{3/2} + \dot{x}_{2\mathrm{PN}}x^2 + \dot{x}_{2.5\mathrm{PN}}x^{5/2} + \dot{x}_{3\mathrm{PN}}x^6 \right) \,, \tag{2.43a}$$

$$M\dot{e} = x^4 \left(\dot{e}_{0\mathrm{PN}} + \dot{e}_{1\mathrm{PN}}x + \dot{e}_{1.5\mathrm{PN}}x^{3/2} + \dot{e}_{2\mathrm{PN}}x^2 + \dot{e}_{2.5\mathrm{PN}}x^{5/2} + \dot{e}_{3\mathrm{PN}}x^6 \right) \,, \tag{2.43b}$$

where the different coefficients in (2.43a) and (2.43b) can be found in [72, 73].

Regarding the waveform, very recently [74, 75] have completed the 3PN description of an eccentric inspiral including the hereditary, post-adiabatic and memory contributions to the waveform for moderate eccentricities.

In order to obtain eccentric waveforms using the QK parametrization one has to solve Eqs. (2.43a) and (2.43b) providing initial conditions for x and e, replace those solutions into the conservative equations of motion by solving the Kepler equation and, then, compute the waveform. The main advantage of this approach is the simplicity to provide eccentric waveforms, while the main drawbacks are that its extension to eccentric spinning binaries is challenging and makes the method much more computationally inefficient, although there has been recently promising work on extending to this parametrization to the spinning case [68]. Finally, we note that we have neglected the introduction of memory and post-adiabatic contributions to ease the discussion. The reader may see [74, 75] for further details.

Effective-One-Body formalism

Eccentric EOB models [76, 77, 78, 79] are IMR waveform models currently describing moderately eccentric systems up to eccentricity $e \sim 0.3$. These eccentric models rely on a quasicircular description of the merger-ringdown part provided by quasicircular EOB models [80, 81, 82] fitted to quasicircular NR simulations and different approaches to model the eccentric inspiral.

We remark here that the EOB framework is a Hamiltonian formalism, which does not parametrize the orbits as the quasi-Keplerian parametrization, and relies on three independent pieces:

1) A Hamiltonian describing the conservative part of the dynamics.

2) The radiation reaction forces describing the loss of energy and angular momentum of the system through gravitational radiation.

3) Analytical expressions to compute the waveform from the dynamics.

Eccentric EOB models require the modification of steps 2 and 3 to incorporate the radial component of the radiation reaction force, which is set to 0 in the quasicircular case, and the prescription to compute the non-quasicircular terms of the waveform in order to properly describe eccentric binaries [79].

Finally, we note that in the EOB framework do not appear several definitions of eccentricity as in the QK case, although eccentricity remains as a gauge dependent quantity, and the eccentricity is read from the orbital or wave quantities using some fitting procedure [56, 83]. Furthermore, the extension of the EOB models to incorporate spin effects seems to be more straightforward than in the QK case due to flexibility and modularity of the framework [79].

2.3   Numerical Relativity

We briefly introduce in this section some basic concepts of numerical relativity intended to ease the understanding of the numerical simulations performed during this thesis. Starting from the 3+1-decomposition explained in Sec. 2.2.2 we present the moving punctures method [84, 85], with brief descriptions of the initial data, the evolution part based on the Baumgarte-Shibata-Shapiro-Nakamura-Oohara-Kojima (BSSNOK) formulation [86, 87] of the ADM equations and the possible gauge choices.

The moving punctures method is the basis of most finite difference NR codes, in particular of the ones used to produce simulations of BBH mergers during this thesis, the ET [88, 89] and BAM [90]. For further details on other methods and formulations we refer the reader to [40, 41, 43, 42] for introductory explanations.

2.3.1   Moving punctures method

The puncture method [91, 92, 93] was initially developed as a procedure for the construction of black hole initial data. The puncture method descomposes the metric as a sum or product of one term which contains the singularity, but it can be computed analytically, and a correction term which is regular, but it has to be calculated numerically.

Soon after the method was extended to perform 'fixed' puncture evolutions [94, 95] in which the gauge was chosen such that the punctures were not allowed to move across the grid. However, these methods did not succeed in producing long-term stable evolutions. Then, in 2005 [84, 85] introduced modifications to the puncture method allowing the evolution of a singular conformal factor, were the location of the puncture is also allowed to move across the grid. Subsequent work [96] clarified geometrical aspects and regularity of the moving puncture formalism. Therefore, these approaches became very successful in producing long-term stable evolutions and they have become standard methods for the evolution of BBH mergers with finite difference codes.

Initial Data

The binary black-hole initial data are typically modelled adopting the Brill-Lindquist wormhole topology [97] with 3 asymptotically flat ends, each Einstein-Rosen bridge connects to its own asymptotically flat region, and the presence of two throats. Each asymptotically flat end is then compactified and identified with points r_i on $\mathcal{R}^3$. The points r_i, known as punctures, are coordinates singularities due to the compactification.

The construction of initial data for any NR code consists in the specification of the spatial metric and extrinsic curvature (γ_{ij}, K_{ij}) on an initial spatial hypersurface Σ_t defined by a timelike unit normal vector n^i as in Fig. 2.2. Following the York-Lichnerowicz conformal decomposition [98, 99, 100] one introduces a conformal transformation of the metric,

$$\gamma_{ij} = \psi^4 \bar{\gamma}_{ij}, \tag{2.44a}$$

$$K_{ij} = \psi^{-2} \bar{A}_{ij} + \frac{1}{3} \gamma_{ij} K, \tag{2.44b}$$

where ψ is a positive defined function called the conformal factor, and we have additionally decomposed the extrinsic curvature into its trace K and its trace-free part $\bar{A}_{ij} = \psi^2 K_{ij}$. Choosing a conformally flat spatial metric $\gamma_{ij} = \delta_{ij}$ and a maximal slicing condition, $K = 0$, the extrinsic curvature can be solved analytically as [101, 102]

$$K_{ij} = \psi^{-2} \left\{ \frac{3}{2r^2} \left[n_i P_j + n_j P_i + n_k P^k (n_i n_j - \delta_{ij}) \right] - \frac{3}{r^3} \left(\epsilon_{ilk} n_j + \epsilon_{jlk} n_i \right) n^l S^k \right\}, \tag{2.45}$$

where ϵ_{ijk} is the Levi-Civita symbol and P^i and S^i can be identified with the ADM linear momentum and spin associated with the punctures. Eq. (2.45) is known as Bowen-York solutions [101, 102].

Once calculated K_{ij} one has to calculate the solution for the conformal factor ψ. This is done applying the conformal transformation (2.44a) to the Hamiltonian constraint (2.15), which can then be written as

$$8\bar{D}^2\psi - \bar{R}\psi + \psi^5 \left(K_{ij} K^{ij} - K^2 \right) = 0, \tag{2.46}$$

where $\bar{R}$ and $\bar{D}^2$ are the Ricci tensor and the Laplace operator of the spatial metric γ_{ij}. Assuming a *moment of time symmetry* in the initial slide, i.e., all time derivatives of γ_{ij} are zero and the 4-dimensional line interval has to be invariant under the transformation $t \rightarrow -t$. The latter condition implies that $\beta^i = 0$, which according to Eq. (2.17) imposes $K_{ij} = K = 0$. With this simplifications the equation for the conformal factor is $\bar{D}^2\psi = 0$, which admits solutions given by the superposition of punctures [97]

$$\psi = 1 + \sum_{i=1}^{N} \frac{m_i}{2|\vec{r} - \vec{r}_i|} = 1 + \psi_{BL}, \tag{2.47}$$

where m_i parametrize the mass of each black hole, $|\vec{r} - \vec{r}_i|$ is the coordinate distance between punctures and for BBHs, $N = 2$, Eq. (2.47) is known as Brill-Linquist initial data. In the general case, the Brill-Lindquist solution also takes into account source terms which modify the above prescription to [92]

$$\psi = u + \psi_{BL}. \tag{2.48}$$

Assuming $\bar{\gamma}_{ij} = \delta_{ij}$ and $K = 0$, the Hamiltonian constraint then takes the form of an elliptic equation for u,

$$\bar{D}^2 u + \frac{1}{8\psi_{BL}^7} \bar{A}_{ij} \bar{A}^{ij} = 0. \tag{2.49}$$

This is the so-called puncture method. We remark that the Brill-Linquist initial data evolves towards a Kerr solution. However, a Kerr spacetime cannot be represented by Bowen-York initial data [103]. This situation leads to an initial spacetime with a residual gravitational energy content, which is radiated away at the initial stages

of the evolution, and it constitutes the so-called *junk radiation*. This outburst of unphysical gravitational radiation is a consequence of the choice of conformally flat initial data and restricts the initial values of mass and spins to $0.812 \gtrsim M \leq 1$ and $\chi \lesssim 0.93$ [104, 103, 105].

The definition of the initial data is completed specifying initial values for the gauge quantities, the lapse function α and the shift vector β^i. Here, the typical criteria is the use of conditions such that they simplify the solution of initial data and the subsequent evolution. For instance, in the case of the BAM code,

$$\alpha = \psi^{-2}, \quad \beta^i = 0, \tag{2.50}$$

where the *pre-collapsed* lapse suggested in [84, 106] is used because it reduces initial gauge dynamics.

Evolution system: BSSNOK formulation

The ADM equations in the form presented in Sec. 2.2.2 are only weakly hyperbolic when used to set up a free evolution problem, thus, they do not have a well-posed initial value problem. As a consequence, other formulations are necessary to evolve the initial data. One commonly used in finite difference codes is the BSSNOK system [86, 87]. Here we briefly review the BSSNOK formulation. We start with the conformal decomposition of the metric,

$$\tilde{\gamma}_{ij} = \psi^{-4}\gamma_{ij}, \tag{2.51}$$

which is the same as Eq. (2.44a), but using the tilde for the conformally transformed variables to differentiate them from the ones used for the construction of the initial data. The conformal metric is chosen to have unit determinant, $\tilde{\gamma} = 1$, during the whole evolution, which translates into the following relation between the conformal factor and the spatial metric,

$$\psi = \gamma^{1/2}. \tag{2.52}$$

The extrinsic curvature is decomposed as in Eq. (2.44b) into its trace and tracefree parts,

$$A_{ij} = K_{ij} - \frac{1}{3}\gamma^{ij}K, \qquad \tilde{A}_{ij} = \psi^{-4}A_{ij}. \tag{2.53}$$

At this point it is important to remark that the pure conformal formulation is still not suitable for numerical relativity, (see Section 2.3.2 of [43]). The key element to achieve strong hyperbolicity for the BSSNOK formulation is the introduction of a conformal connection function defined by

$$\tilde{\Gamma}^i = \tilde{\gamma}^{jk}\tilde{\Gamma}^i_{jk} = -\partial_j\tilde{\gamma}^{ij}, \tag{2.54}$$

with $\tilde{\Gamma}^i_{jk}$ being the Christoffel symbols of the conformal metric. This new variable with its own evolution equation, Eq. (2.54), can be interpreted as a new algebraic constraint, and it additionally removes mixed second derivatives in the evolution equations which are inappropriate for numerical evolutions. In terms of these new variables the ADM Eqs. (2.17) and (2.18) can be expressed as,

$$\partial_0\tilde{\gamma}_{ij} = -2\alpha\tilde{A}_{ij}, \tag{2.55a}$$

$$\partial_0\phi = \frac{1}{6}\alpha K, \tag{2.55b}$$

$$\partial_0\tilde{A}_{ij} = e^{-4\phi}(\alpha R_{ij} - D_i D_j\alpha)^{\mathrm{TF}} + \alpha(K\tilde{A}_{ij} - 2\tilde{A}_i^m\tilde{A}_{mj}), \tag{2.55c}$$

$$\partial_t K = -D^i D_i \alpha + \alpha \left(\tilde{A}^{mn} \tilde{A}_{mn} + \frac{1}{3} K^2 \right), \tag{2.55d}$$

$$\partial_t \tilde{\Gamma}^i = \tilde{\gamma}^{jk} \partial_j \partial_k \beta^i + \frac{1}{3} \gamma^{ij} \partial_j \partial_k \beta^k + \beta^j \partial_j \tilde{\Gamma}^i \partial_j \beta^j - 2 \left(\alpha \partial_j \tilde{A}^{ij} + \tilde{A}^{ij} \partial_j \alpha \right), \tag{2.55e}$$

$$\tag{2.55f}$$

where $\partial_0 = \partial_t - \mathcal{L}_{\vec{\beta}}$ with $\mathcal{L}_{\vec{\beta}}$ being the Lie derivative with respect to the shift vector, D_i is the covariant derivative associated to the spatial metric γ_{ij}, TF denotes the trace free part of the expression. In the above formulation we have chosen the ϕ method [90] for the conformal factor, i.e., $\phi = \ln\psi = 1/12 \log \gamma$. The number of independent variables in the ADM equations, Eqs. (2.15) to (2.18) is 12, while in Eqs. (2.55a) to (2.55e) is 17: ϕ, K, $\tilde{\gamma}^{ij}$, $\tilde{A}_{ij}$ and $\tilde{\Gamma}_i$. With the conditions $Tr(\tilde{A}_{ij}) = 0$ and $\tilde{\gamma} = 1$ this gets reduced to 15.

Applying the same conformal transformations to the constraint equations, Eqs. (2.15) and (2.16), and replacing the momentum constraint in the evolution equations one obtains the following two equations,

$$\partial_j \tilde{A}^{ij} = \tilde{\Gamma}^i_{jk} \tilde{A}^{jk} - 6\tilde{A}^{ij} \partial_j \phi + \frac{2}{3} \tilde{\gamma}^{ij} \partial_j K, \tag{2.56a}$$

$$\partial_t \tilde{\Gamma}^i = \beta^m \partial_m \tilde{\Gamma}^i - \tilde{\Gamma}^m \partial_m \beta^i + \frac{2}{3} \tilde{\Gamma}^i \partial_m \beta^m + 2\alpha \tilde{\Gamma}^i_{mn} \tilde{A}^{mn} + \frac{1}{3} \tilde{\gamma}^{im} \partial_m \partial_n \beta^n$$
$$+ \tilde{\gamma}^{mn} \partial_m \partial_n \beta^i - \frac{4}{3} \alpha \tilde{\gamma}^{im} \partial_m K + 2\tilde{A}^{im} \left(6\alpha \partial_m \phi - \partial_m \alpha \right). \tag{2.56b}$$

Equations (2.56a) and (2.56b) complete the system of equations and make it well posed. However, the system of Eqs. (2.55a) to (2.56b) is still missing a crucial part provided by the specifications of the slicing conditions for α and β^i which are discussed in the following section.

Gauge choices

One crucial part of the moving punctures method is the choice of the gauge conditions. Current simulations with BAM and ET [56, 83, 107] in our group use the *covariant* form of the '1 + log' slicing [108] for the lapse function

$$(\partial_t - \beta^i \partial_i)\alpha = -2\alpha K. \tag{2.57}$$

We note that the shift advection term in Eq. (2.57) avoids the appearance of zero speed modes in the BSSNOK system [109, 110], which is the case when this term is dropped from Eq. (2.57) and it was the typical choice in the fixed puncture approach.

We use the *Gamma-freezing* condition [111] for the evolution of the shift vector

$$\partial_0 \frac{3}{4} B^i, \quad \partial_0 B^i = \partial_0 \tilde{\Gamma}^i - \eta B^i, \tag{2.58}$$

where $\partial_0 = \partial_t - \beta^i \partial_i$, B^i is an auxiliary vector field which reduces perturbations in the constraints at the positions of the punctures [41], and η is a parameter typically on the order of $1/(2M)$, with M being the total mass of the system. Variants of the *Gamma-freezing* condition [85, 112, 109] modify some or all the ∂_0 derivatives with ∂_t, providing also successful numerical evolutions [112, 110].

We conclude this chapter emphasizing that the ADM evolution equations in the form presented in Sec. 2.2.2 are ill posed when set up as a free evolution problem because they are not strongly hyperbolic. Thus, new formulations are required to

numerically evolve the spacetimes. We have focused on the BSSNOK formulation, although other successful variants exist like a constrained formulation [113, 114] or the Z4-formulations [115, 116, 117, 118]. We finally remark that the dynamical gauge conditions, Eqs. (2.57) and (2.58), although mathematically motivated, could have not been found without a lot of effort in numerical experiments, which are essential for numerical relativity advances.

References

[1] B.P. Abbott et al. Tests of General Relativity with the Binary Black Hole Signals from the LIGO-Virgo Catalog GWTC-1. *Phys. Rev. D*, 100(10):104036, 2019. arXiv:1903.04467 [gr-qc].

[2] B. P. Abbott et al. Search for Post-merger Gravitational Waves from the Remnant of the Binary Neutron Star Merger GW170817. *Astrophys. J.*, 851(1):L16, 2017. arXiv:1710.09320 [astro-ph.HE].

[3] B. P. Abbott et al. Search for gravitational waves from a long-lived remnant of the binary neutron star merger GW170817. *Astrophys. J.*, 875(2):160, 2019. arXiv:1810.02581 [gr-qc].

[4] Sascha Husa, Sebastian Khan, Mark Hannam, Michael Pürrer, Frank Ohme, Xisco Jiménez Forteza, and Alejandro Bohé. Frequency-domain gravitational waves from nonprecessing black-hole binaries. I. New numerical waveforms and anatomy of the signal. *Phys. Rev.*, D93(4):044006, 2016. arXiv:1508.07250 [gr-qc].

[5] Andrea Taracchini, Alessandra Buonanno, Gaurav Khanna, and Scott A. Hughes. Small mass plunging into a Kerr black hole: Anatomy of the inspiral-merger-ringdown waveforms. *Phys. Rev.*, D90(8):084025, 2014. arXiv:1404.1819 [gr-qc].

[6] Miriam Cabero, Alex B. Nielsen, Andrew P. Lundgren, and Collin D. Capano. Minimum energy and the end of the inspiral in the post-Newtonian approximation. *Phys. Rev. D*, 95(6):064016, 2017. arXiv:1602.03134 [gr-qc].

[7] Miquel Trias Cornellana. *Gravitational wave observation of compact binaries: Detection, parameter estimation and template accuracy*. PhD thesis, University of the Balearic Islands, Carretera de Valldemossa km. 7.5, 07122 Palma de Mallorca, Spain, 11 2010.

[8] Bernard F. Schutz. *A FIRST COURSE IN GENERAL RELATIVITY*. Cambridge Univ. Pr., Cambridge, UK, 1985.

[9] Lee Samuel Finn and David F. Chernoff. Observing binary inspiral in gravitational radiation: One interferometer. *Phys. Rev. D*, 47:2198–2219, 1993. arXiv:gr-qc/9301003.

[10] Luc Blanchet. Gravitational Radiation from Post-Newtonian Sources and Inspiralling Compact Binaries. *Living Rev. Rel.*, 17:2, 2014. arXiv:1310.1528 [gr-qc].

[11] Eric Poisson and Clifford M. Will. *Gravity: Newtonian, Post-Newtonian, Relativistic*. Cambridge University Press, 2014.

[12] Gerhard Schäfer and Piotr Jaranowski. Hamiltonian formulation of general relativity and post-Newtonian dynamics of compact binaries. *Living Rev. Rel.*, 21(1):7, 2018. arXiv:1805.07240 [gr-qc].

[13] Clifford M. Will and Alan G. Wiseman. Gravitational radiation from compact binary systems: Gravitational wave forms and energy loss to second postNewtonian order. *Phys. Rev. D*, 54:4813–4848, 1996. arXiv:gr-qc/9608012.

[14] Michael E. Pati and Clifford M. Will. PostNewtonian gravitational radiation and equations of motion via direct integration of the relaxed Einstein equations. 1. Foundations. *Phys. Rev. D*, 62:124015, 2000. arXiv:gr-qc/0007087.

[15] Michael E. Pati and Clifford M. Will. PostNewtonian gravitational radiation and equations of motion via direct integration of the relaxed Einstein equations. 2. Two-body equations of motion to second postNewtonian order, and radiation reaction to 3.5 postNewtonia order. *Phys. Rev. D*, 65:104008, 2002. arXiv:gr-qc/0201001.

[16] Michele Levi. Effective Field Theories of Post-Newtonian Gravity: A comprehensive review. 2018. arXiv:1807.01699 [hep-th].

[17] R. Arnowitt, S. Deser, and C. W. Misner. Dynamical structure and definition of energy in general relativity. *Phys. Rev.*, 116:1322–1330, Dec 1959.

[18] Stanley Deser, R. Arnowitt, and C. W. Misner. Consistency of Canonical Reduction of General Relativity. *J. Math. Phys.*, 1:434, 1960.

[19] R. Arnowitt, S. Deser, and C. W. Misner. Canonical variables for general relativity. *Phys. Rev.*, 117:1595–1602, Mar 1960.

[20] Piotr Jaranowski and Gerhard Schäfer. Radiative 3.5 post-Newtonian ADM Hamiltonian for many-body point-mass systems. *Phys. Rev. D*, 55:4712–4722, Apr 1997.

[21] Piotr Jaranowski and Gerhard Schaefer. Third postNewtonian higher order ADM Hamilton dynamics for two-body point mass systems. *Phys. Rev. D*, 57:7274–7291, 1998. arXiv:gr-qc/9712075, [Erratum: Phys.Rev.D 63, 029902 (2001)].

[22] Jan Steinhoff and Gerhard Schaefer. Canonical formulation of self-gravitating spinning-object systems. *EPL*, 87(5):50004, 2009. arXiv:0907.1967 [gr-qc].

[23] Jan Steinhoff. Canonical formulation of spin in general relativity. *Annalen Phys.*, 523:296–353, 2011. arXiv:1106.4203 [gr-qc].

[24] Paul A. M. Dirac. The Theory of gravitation in Hamiltonian form. *Proc. Roy. Soc. Lond.*, A246:333–343, 1958.

[25] P. A. M. Dirac. Fixation of Coordinates in the Hamiltonian Theory of Gravitation. *Phys. Rev.*, 114:924–930, May 1959.

[26] Julian Schwinger. Quantized gravitational field. *Phys. Rev.*, 130:1253–1258, May 1963.

[27] Julian Schwinger. Quantized gravitational field. ii. *Phys. Rev.*, 132:1317–1321, Nov 1963.

[28] A. Buonanno and T. Damour. Effective one-body approach to general relativistic two-body dynamics. *Phys. Rev.*, D59:084006, 1999. arXiv:gr-qc/9811091 [gr-qc].

[29] Thibault Damour. Coalescence of two spinning black holes: an effective one-body approach. *Phys. Rev.*, D64:124013, 2001. arXiv:gr-qc/0103018 [gr-qc].

[30] Thibault Damour, Bala R. Iyer, and Alessandro Nagar. Improved resummation of post-Newtonian multipolar waveforms from circularized compact binaries. *Phys. Rev. D*, 79:064004, 2009. arXiv:0811.2069 [gr-qc].

[31] Alessandra Buonanno, Yanbei Chen, and Thibault Damour. Transition from inspiral to plunge in precessing binaries of spinning black holes. *Phys. Rev. D*, 74:104005, 2006. arXiv:gr-qc/0508067.

[32] Thibault Damour, Piotr Jaranowski, and Gerhard Schäfer. Nonlocal-in-time action for the fourth post-Newtonian conservative dynamics of two-body systems. *Phys. Rev. D*, 89(6):064058, 2014. arXiv:1401.4548 [gr-qc].

[33] Piotr Jaranowski and Gerhard Schäfer. Derivation of local-in-time fourth post-Newtonian ADM Hamiltonian for spinless compact binaries. *Phys. Rev. D*, 92(12):124043, 2015. arXiv:1508.01016 [gr-qc].

[34] Thibault Damour, Piotr Jaranowski, and Gerhard Schaefer. Hamiltonian of two spinning compact bodies with next-to-leading order gravitational spin-orbit coupling. *Phys. Rev.*, D77:064032, 2008. arXiv:0711.1048 [gr-qc].

[35] Johannes Hartung and Jan Steinhoff. Next-to-next-to-leading order post-Newtonian spin-orbit Hamiltonian for self-gravitating binaries. *Annalen Phys.*, 523:783–790, 2011. arXiv:1104.3079 [gr-qc].

[36] Johannes Hartung, Jan Steinhoff, and Gerhard Schafer. Next-to-next-to-leading order post-Newtonian linear-in-spin binary Hamiltonians. *Annalen Phys.*, 525:359–394, 2013. arXiv:1302.6723 [gr-qc].

[37] Michele Levi and Jan Steinhoff. Leading order finite size effects with spins for inspiralling compact binaries. *JHEP*, 06:059, 2015. arXiv:1410.2601 [gr-qc].

[38] Michele Levi and Jan Steinhoff. Complete conservative dynamics for inspiralling compact binaries with spins at fourth post-Newtonian order. 2016. arXiv:1607.04252 [gr-qc].

[39] Nigel T. Bishop and Luciano Rezzolla. Extraction of Gravitational Waves in Numerical Relativity. *Living Rev. Rel.*, 19:2, 2016. arXiv:1606.02532 [gr-qc].

[40] Carles Bona, Carlos Palenzuela-Luque, and Carles Bona-Casas. *Elements of numerical relativity*. Springer, Berlin, Germany, 2009.

[41] Miguel Alcubierre. *Introduction to 3+1 numerical relativity*. International series of monographs on physics. Oxford Univ. Press, Oxford, 2008.

[42] Thomas W. Baumgarte and Stuart L. Shapiro. *Numerical Relativity: Solving Einstein's Equations on the Computer*. Cambridge University Press, 2010.

[43] Masaru Shibata. *Numerical Relativity*. World Scientific Publishing Co., Inc., River Edge, NJ, USA, 2015.

[44] Bryce S. DeWitt. Quantum Theory of Gravity. I. The Canonical Theory. *Phys. Rev.*, 160:1113–1148, Aug 1967.

[45] Tullio Regge and Claudio Teitelboim. Role of surface integrals in the Hamiltonian formulation of general relativity. *Annals of Physics*, 88(1):286 – 318, 1974.

[46] K.G. Arun, Alessandra Buonanno, Guillaume Faye, and Evan Ochsner. Higher-order spin effects in the amplitude and phase of gravitational waveforms emitted by inspiraling compact binaries: Ready-to-use gravitational waveforms. *Phys. Rev. D*, 79:104023, 2009. arXiv:0810.5336 [gr-qc], [Erratum: Phys.Rev.D 84, 049901 (2011)].

[47] Marc Favata. Conservative corrections to the innermost stable circular orbit (ISCO) of a Kerr black hole: A New gauge-invariant post-Newtonian ISCO condition, and the ISCO shift due to test-particle spin and the gravitational self-force. *Phys. Rev. D*, 83:024028, 2011. arXiv:1010.2553 [gr-qc].

[48] Geraint Pratten, Sascha Husa, Cecilio Garcia-Quiros, Marta Colleoni, Antoni Ramos-Buades, Hector Estelles, and Rafel Jaume. Setting the cornerstone for the IMRPhenomX family of models for gravitational waves from compact binaries: The dominant harmonic for non-precessing quasi-circular black holes. 2020. arXiv:2001.11412 [gr-qc].

[49] Cecilio García-Quirós, Marta Colleoni, Sascha Husa, Héctor Estellés, Geraint Pratten, Antoni Ramos-Buades, Maite Mateu-Lucena, and Rafel Jaume. IMRPhenomXHM: A multi-mode frequency-domain model for the gravitational wave signal from non-precessing black-hole binaries. 2020. arXiv:2001.10914 [gr-qc].

[50] Alessandra Buonanno, Bala Iyer, Evan Ochsner, Yi Pan, and B.S. Sathyaprakash. Comparison of post-Newtonian templates for compact binary inspiral signals in gravitational-wave detectors. *Phys. Rev. D*, 80:084043, 2009. arXiv:0907.0700 [gr-qc].

[51] Thibault Damour, Bala R. Iyer, and B.S. Sathyaprakash. A Comparison of search templates for gravitational waves from binary inspiral. *Phys. Rev. D*, 63:044023, 2001. arXiv:gr-qc/0010009, [Erratum: Phys.Rev.D 72, 029902 (2005)].

[52] Thibault Damour, Bala R. Iyer, and B.S. Sathyaprakash. A Comparison of search templates for gravitational waves from binary inspiral - 3.5PN update. *Phys. Rev. D*, 66:027502, 2002. arXiv:gr-qc/0207021.

[53] Theocharis A. Apostolatos, Curt Cutler, Gerald J. Sussman, and Kip S. Thorne. Spin-induced orbital precession and its modulation of the gravitational waveforms from merging binaries. *Phys. Rev. D*, 49:6274–6297, Jun 1994.

[54] Lawrence E. Kidder. Coalescing binary systems of compact objects to post-Newtonian 5/2 order. 5. Spin effects. *Phys. Rev. D*, 52:821–847, 1995. arXiv:gr-qc/9506022.

[55] Alessandra Buonanno, Yan-bei Chen, and Michele Vallisneri. Detecting gravitational waves from precessing binaries of spinning compact objects: Adiabatic limit. *Phys. Rev. D*, 67:104025, 2003. arXiv:gr-qc/0211087, [Erratum: Phys.Rev.D 74, 029904 (2006)].

[56] Antoni Ramos-Buades, Sascha Husa, and Geraint Pratten. Simple procedures to reduce eccentricity of binary black hole simulations. *Phys. Rev. D*, 99(2):023003, 2019. arXiv:1810.00036 [gr-qc].

[57] Thibault Damour and Nathalie Deruelle. General relativistic celestial mechanics of binary systems. I. The post-Newtonian motion. *Annales de l'I.H.P. Physique théorique*, 43(1):107–132, 1985.

[58] Raoul-Martin Memmesheimer, Achamveedu Gopakumar, and Gerhard Schaefer. Third post-Newtonian accurate generalized quasi-Keplerian parametrization for compact binaries in eccentric orbits. *Phys. Rev.*, D70:104011, 2004. arXiv:gr-qc/0407049 [gr-qc].

[59] Thibault Damour, Achamveedu Gopakumar, and Bala R. Iyer. Phasing of gravitational waves from inspiralling eccentric binaries. *Phys. Rev. D*, 70:064028, 2004. arXiv:gr-qc/0404128.

[60] Christian Konigsdorffer and Achamveedu Gopakumar. Phasing of gravitational waves from inspiralling eccentric binaries at the third-and-a-half post-Newtonian order. *Phys. Rev. D*, 73:124012, 2006. arXiv:gr-qc/0603056.

[61] K.G. Arun, Luc Blanchet, Bala R. Iyer, and Moh'd S.S. Qusailah. Tail effects in the 3PN gravitational wave energy flux of compact binaries in quasi-elliptical orbits. *Phys. Rev. D*, 77:064034, 2008. arXiv:0711.0250 [gr-qc].

[62] K.G. Arun, Luc Blanchet, Bala R. Iyer, and Moh'd S.S. Qusailah. Inspiralling compact binaries in quasi-elliptical orbits: The Complete 3PN energy flux. *Phys. Rev. D*, 77:064035, 2008. arXiv:0711.0302 [gr-qc].

[63] K.G. Arun, Luc Blanchet, Bala R. Iyer, and Siddhartha Sinha. Third post-Newtonian angular momentum flux and the secular evolution of orbital elements for inspiralling compact binaries in quasi-elliptical orbits. *Phys. Rev. D*, 80:124018, 2009. arXiv:0908.3854 [gr-qc].

[64] Nicolas Yunes, K.G. Arun, Emanuele Berti, and Clifford M. Will. Post-Circular Expansion of Eccentric Binary Inspirals: Fourier-Domain Waveforms in the Stationary Phase Approximation. *Phys. Rev. D*, 80(8):084001, 2009. arXiv:0906.0313 [gr-qc], [Erratum: Phys.Rev.D 89, 109901 (2014)].

[65] E.A. Huerta et al. Eccentric, nonspinning, inspiral, Gaussian-process merger approximant for the detection and characterization of eccentric binary black hole mergers. *Phys. Rev. D*, 97(2):024031, 2018. arXiv:1711.06276 [gr-qc].

[66] Sashwat Tanay, Maria Haney, and Achamveedu Gopakumar. Frequency and time domain inspiral templates for comparable mass compact binaries in eccentric orbits. *Phys. Rev. D*, 93(6):064031, 2016. arXiv:1602.03081 [gr-qc].

[67] Ian Hinder, Lawrence E. Kidder, and Harald P. Pfeiffer. Eccentric binary black hole inspiral-merger-ringdown gravitational waveform model from numerical relativity and post-Newtonian theory. *Phys. Rev. D*, 98(4):044015, 2018. arXiv:1709.02007 [gr-qc].

[68] Antoine Klein, Yannick Boetzel, Achamveedu Gopakumar, Philippe Jetzer, and Lorenzo de Vittori. Fourier domain gravitational waveforms for precessing eccentric binaries. *Phys. Rev. D*, 98(10):104043, 2018. arXiv:1801.08542 [gr-qc].

[69] A. W. Odell and R. H. Gooding. Procedures for solving Kepler's equation. *Celestial mechanics*, 38(4):307–334, Apr 1986.

[70] M. Zechmeister. Cordic-like method for solving kepler's equation. *Astronomy & Astrophysics*, 619:A128, Nov 2018.

[71] Yannick Boetzel, Abhimanyu Susobhanan, Achamveedu Gopakumar, Antoine Klein, and Philippe Jetzer. Solving post-Newtonian accurate Kepler Equation. *Phys. Rev. D*, 96(4):044011, 2017. arXiv:1707.02088 [gr-qc].

[72] Ian Hinder, Frank Herrmann, Pablo Laguna, and Deirdre Shoemaker. Comparisons of eccentric binary black hole simulations with post-Newtonian models. *Phys. Rev. D*, 82:024033, 2010. arXiv:0806.1037 [gr-qc].

[73] E. A. Huerta, Prayush Kumar, Sean T. McWilliams, Richard O'Shaughnessy, and Nicolás Yunes. Accurate and efficient waveforms for compact binaries on eccentric orbits. *Phys. Rev. D*, 90(8):084016, 2014. arXiv:1408.3406 [gr-qc].

[74] Yannick Boetzel, Chandra Kant Mishra, Guillaume Faye, Achamveedu Gopakumar, and Bala R. Iyer. Gravitational-wave amplitudes for compact binaries in eccentric orbits at the third post-Newtonian order: Tail contributions and postadiabatic corrections. *Phys. Rev. D*, 100(4):044018, 2019. arXiv:1904.11814 [gr-qc].

[75] Michael Ebersold, Yannick Boetzel, Guillaume Faye, Chandra Kant Mishra, Bala R. Iyer, and Philippe Jetzer. Gravitational-wave amplitudes for compact binaries in eccentric orbits at the third post-Newtonian order: Memory contributions. *Phys. Rev. D*, 100(8):084043, 2019. arXiv:1906.06263 [gr-qc].

[76] Tanja Hinderer and Stanislav Babak. Foundations of an effective-one-body model for coalescing binaries on eccentric orbits. *Phys. Rev. D*, 96(10):104048, 2017. arXiv:1707.08426 [gr-qc].

[77] Xiaolin Liu, Zhoujian Cao, and Lijing Shao. Validating the Effective-One-Body Numerical-Relativity Waveform Models for Spin-aligned Binary Black Holes along Eccentric Orbits. 2019. arXiv:1910.00784 [gr-qc].

[78] Chen Zhang, Wen-Biao Han, and Shu-Cheng Yang. Analytical effective-one-body formalism for extreme-mass-ratio inspirals: eccentric orbits. 2020. arXiv:2001.06763 [gr-qc].

[79] Danilo Chiaramello and Alessandro Nagar. A faithful analytical effective one body waveform model for spin-aligned, moderately eccentric, coalescing black hole binaries. 2020. arXiv:2001.11736 [gr-qc].

[80] Andrea Taracchini, Yi Pan, Alessandra Buonanno, Enrico Barausse, Michael Boyle, Tony Chu, Geoffrey Lovelace, Harald P. Pfeiffer, and Mark A. Scheel. Prototype effective-one-body model for nonprecessing spinning inspiral-merger-ringdown waveforms. *Phys. Rev. D*, 86:024011, Jul 2012.

[81] Alessandro Nagar et al. Time-domain effective-one-body gravitational waveforms for coalescing compact binaries with nonprecessing spins, tides and self-spin effects. *Phys. Rev. D*, 98(10):104052, 2018. arXiv:1806.01772 [gr-qc].

[82] Alessandro Nagar, Gunnar Riemenschneider, Geraint Pratten, Piero Rettegno, and Francesco Messina. A multipolar effective one body waveform model for spin-aligned black hole binaries. 2020. arXiv:2001.09082 [gr-qc].

[83] Antoni Ramos-Buades, Sascha Husa, Geraint Pratten, Héctor Estellés, Cecilio García-Quirós, Maite Mateu-Lucena, Marta Colleoni, and Rafel Jaume. First survey of spinning eccentric black hole mergers: Numerical relativity simulations, hybrid waveforms, and parameter estimation. *Phys. Rev. D*, 101(8):083015, 2020. arXiv:1909.11011 [gr-qc].

[84] Manuela Campanelli, C.O. Lousto, P. Marronetti, and Y. Zlochower. Accurate evolutions of orbiting black-hole binaries without excision. *Phys. Rev. Lett.*, 96:111101, 2006. arXiv:gr-qc/0511048.

[85] John G. Baker, Joan Centrella, Dae-Il Choi, Michael Koppitz, and James van Meter. Gravitational wave extraction from an inspiraling configuration of merging black holes. *Phys. Rev. Lett.*, 96:111102, 2006. arXiv:gr-qc/0511103 [gr-qc].

[86] Masaru Shibata and Takashi Nakamura. Evolution of three-dimensional gravitational waves: Harmonic slicing case. *Phys. Rev. D*, 52:5428–5444, Nov 1995.

[87] Thomas W. Baumgarte and Stuart L. Shapiro. On the numerical integration of Einstein's field equations. *Phys. Rev. D*, 59:024007, 1999. arXiv:gr-qc/9810065.

[88] Maria Babiuc-Hamilton et al. The Einstein Toolkit, October 2019. To find out more, visit http://einsteintoolkit.org.

[89] Frank Loffler et al. The Einstein Toolkit: A Community Computational Infrastructure for Relativistic Astrophysics. *Class. Quant. Grav.*, 29:115001, 2012. arXiv:1111.3344 [gr-qc].

[90] Bernd Bruegmann, Jose A. Gonzalez, Mark Hannam, Sascha Husa, Ulrich Sperhake, and Wolfgang Tichy. Calibration of Moving Puncture Simulations. *Phys. Rev.*, D77:024027, 2008. arXiv:gr-qc/0610128 [gr-qc].

[91] R. Beig and N.O. Murchadha. Trapped surfaces in vacuum space-times. *Class. Quant. Grav.*, 11:419–430, 1994. arXiv:gr-qc/9304034.

[92] Steven Brandt and Bernd Bruegmann. A Simple construction of initial data for multiple black holes. *Phys. Rev. Lett.*, 78:3606–3609, 1997. arXiv:gr-qc/9703066.

[93] S. R. Brandt and Bernd Bruegmann. BH punctures as initial data for general relativity. In *Recent developments in theoretical and experimental general relativity, gravitation, and relativistic field theories. Proceedings, 8th Marcel Grossmann meeting, MG8, Jerusalem, Israel, June 22-27, 1997. Pts. A, B*, pages 738–740, 1997.

[94] Bernd Bruegmann. Binary black hole mergers in 3-d numerical relativity. *Int. J. Mod. Phys.*, D8:85, 1999. arXiv:gr-qc/9708035 [gr-qc].

[95] Miguel Alcubierre, Werner Benger, Bernd Bruegmann, Gerd Lanfermann, Lars Nerger, Edward Seidel, and Ryoji Takahashi. The 3-D grazing collision of two black holes. *Phys. Rev. Lett.*, 87:271103, 2001. arXiv:gr-qc/0012079.

[96] Mark Hannam, Sascha Husa, Denis Pollney, Bernd Bruegmann, and Niall O'Murchadha. Geometry and regularity of moving punctures. *Phys. Rev. Lett.*, 99:241102, 2007. arXiv:gr-qc/0606099.

[97] Dieter R. Brill and Richard W. Lindquist. Interaction energy in geometrostatics. *Phys. Rev.*, 131:471–476, Jul 1963.

[98]   A. Lichnerowicz. *L'intégration des équations de la gravitation relativiste et le problème des n corps. Journal de Mathématiques Pures et Appliquées*, **23**:37–63, 1944.

[99]   James W. York. Gravitational Degrees of Freedom and the Initial-Value Problem. *Phys. Rev. Lett.*, 26:1656–1658, Jun 1971.

[100] James W. York. Role of Conformal Three-Geometry in the Dynamics of Gravitation. *Phys. Rev. Lett.*, 28:1082–1085, Apr 1972.

[101] Jeffrey M. Bowen. General form for the longitudinal momentum of a spherically symmetric source. *General Relativity and Gravitation*, 11(3):227–231, Oct 1979.

[102] Jeffrey M. Bowen and James W. York. Time-asymmetric initial data for black holes and black-hole collisions. *Phys. Rev. D*, 21:2047–2056, Apr 1980.

[103] Sergio Dain, Carlos O. Lousto, and Ryoji Takahashi. New conformally flat initial data for spinning black holes. *Phys. Rev. D*, 65:104038, 2002. arXiv:gr-qc/0201062.

[104] Gregory B. Cook and James W. York. Apparent horizons for boosted or spinning black holes. *Phys. Rev. D*, 41:1077–1085, Feb 1990.

[105] Mark A. Scheel, Matthew Giesler, Daniel A. Hemberger, Geoffrey Lovelace, Kevin Kuper, Michael Boyle, B. Szilágyi, and Lawrence E. Kidder. Improved methods for simulating nearly extremal binary black holes. *Class. Quant. Grav.*, 32(10):105009, 2015. arXiv:1412.1803 [gr-qc].

[106] Miguel Alcubierre, Bernd Bruegmann, Peter Diener, Michael Koppitz, Denis Pollney, Edward Seidel, and Ryoji Takahashi. Gauge conditions for long term numerical black hole evolutions without excision. *Phys. Rev. D*, 67:084023, 2003. arXiv:gr-qc/0206072.

[107] Antoni Ramos-Buades, Patricia Schmidt, Geraint Pratten, and Sascha Husa. Validity of common modeling approximations for precessing binary black holes with higher-order modes. *Phys. Rev. D*, 101(10):103014, 2020. arXiv:2001.10936 [gr-qc].

[108] C. Bona, J. Masso, E. Seidel, and J. Stela. First order hyperbolic formalism for numerical relativity. *Phys. Rev. D*, 56:3405–3415, 1997. arXiv:gr-qc/9709016.

[109] James R. van Meter, John G. Baker, Michael Koppitz, and Dae-Il Choi. How to move a black hole without excision: Gauge conditions for the numerical evolution of a moving puncture. *Phys. Rev. D*, 73:124011, 2006. arXiv:gr-qc/0605030.

[110] Carsten Gundlach and Jose M. Martin-Garcia. Well-posedness of formulations of the Einstein equations with dynamical lapse and shift conditions. *Phys. Rev. D*, 74:024016, 2006. arXiv:gr-qc/0604035.

[111] Miguel Alcubierre, Bernd Bruegmann, Peter Diener, Michael Koppitz, Denis Pollney, Edward Seidel, and Ryoji Takahashi. Gauge conditions for long term numerical black hole evolutions without excision. *Phys. Rev.*, D67:084023, 2003. arXiv:gr-qc/0206072 [gr-qc].

[112] John G. Baker, Joan Centrella, Dae-Il Choi, Michael Koppitz, and James van Meter. Binary black hole merger dynamics and waveforms. *Phys. Rev. D*, 73:104002, 2006. arXiv:gr-qc/0602026.

[113] Isabel Cordero-Carrion, Pablo Cerda-Duran, and Jose Maria Ibanez. Dynamical spacetimes and gravitational radiation in a Fully Constrained Formulation. *J. Phys. Conf. Ser.*, 228:012055, 2010. arXiv:1003.0868 [gr-qc].

[114] Silvano Bonazzola, Eric Gourgoulhon, Philippe Grandclement, and Jerome Novak. A Constrained scheme for Einstein equations based on Dirac gauge and spherical coordinates. *Phys. Rev. D*, 70:104007, 2004. arXiv:gr-qc/0307082.

[115] C. Bona, T. Ledvinka, C. Palenzuela, and M. Zacek. General covariant evolution formalism for numerical relativity. *Phys. Rev. D*, 67:104005, 2003. arXiv:gr-qc/0302083.

[116] Carsten Gundlach, Jose M. Martin-Garcia, Gioel Calabrese, and Ian Hinder. Constraint damping in the Z4 formulation and harmonic gauge. *Class. Quant. Grav.*, 22:3767–3774, 2005. arXiv:gr-qc/0504114.

[117] Sebastiano Bernuzzi and David Hilditch. Constraint violation in free evolution schemes: Comparing BSSNOK with a conformal decomposition of Z4. *Phys. Rev. D*, 81:084003, 2010. arXiv:0912.2920 [gr-qc].

[118] Daniela Alic, Carles Bona-Casas, Carles Bona, Luciano Rezzolla, and Carlos Palenzuela. Conformal and covariant formulation of the Z4 system with constraint-violation damping. *Phys. Rev. D*, 85:064040, 2012. arXiv:1106.2254 [gr-qc].

Chapter 3

Analysis of gravitational wave data from compact binaries

The extraction and analysis of the gravitational wave signals hidden in the noise dominated strain of ground-based detectors, like Advanced LIGO [1] and Advanced Virgo [2] is a challenging task, which requires the application of optimized statistical methods in order to obtain the maximum amount of information possible. We provide in this chapter a brief introduction to detection techniques and parameter estimation of gravitational wave signals from compact binary coalescences. We refer the reader to [3, 4, 5] for more detailed explanations and derivations of the expressions presented in this chapter.

3.1 Description of detector noise as a random process

A random or stochastic process is a sequence of random variables $x(t)$, $t \in T$, where T is a subset of real numbers, $T \subset \mathcal{R}$, defined on the same probability space. Instrumental noise is an example of a random process representing detector's time series $x(t)$. Introducing the probability density function p_x for the value of x at some time t, the expectation value of x is calculated as an ensemble average

$$\langle x \rangle = \int x p_x(x) dx. \tag{3.1}$$

In the case of a stationary random process, for which its statistical properties do not vary with time, the expectation value is equivalent to a long time average,

$$\langle x \rangle = \lim_{T \to \infty} \frac{1}{T} \int_{-T/2}^{T/2} x(t) dt. \tag{3.2}$$

For a stationary process the *autocorrelation function* only depends on some time shift τ,

$$R_x(\tau) = \langle x(t)x(t+\tau) \rangle. \tag{3.3}$$

In the case of the gravitational wave detector noise one deals with a Gaussian random process, which is a special class of stationary random process characterized by Gaussian random variables and its power spectral density (PSD). The general definition of a (double-sided) power spectral density is in terms of the Fourier transform of the autocorrelation function

$$S_x(f) = 2 \int_{-\infty}^{+\infty} R_x(\tau) e^{-2\pi i f \tau} d\tau. \tag{3.4}$$

Assuming uncorrelated stationary noise with zero mean $\langle x \rangle = 0$, the power spectral density can also be expressed as

$$S_x(f) = \lim_{T \to \infty} \frac{2}{T} \left| \int_{-T/2}^{T/2} x(t) e^{-2\pi i f t} dt \right|^2, \tag{3.5}$$

where we have assumed a windowed signal of duration T. From Eq. (3.5) one can derive a useful expression for the power spectral density as

$$\langle \tilde{x}^*(f') \tilde{x}(f) \rangle = \frac{1}{2} S_x(f) \delta(f - f'), \tag{3.6}$$

where $\delta(f - f')$ is the Dirac delta function. Assuming that the noise timeseries, $x(t)$, is formed of N samples separated by Δt, then, $x_j = x(j \Delta t)$ for $j = 1, \ldots, N$. In the case of independent Gaussian random variables with zero mean and standard deviation σ, the joint probability distribution of getting $\{x_j\}$ is

$$p_x(\{x_j\}) = \left(\frac{1}{\sqrt{2\pi\sigma^2}} \right)^N \exp \left\{ -\frac{1}{2\sigma^2} \sum_{j=1}^{N} x_j^2 \right\}. \tag{3.7}$$

If the samples x_j are independent, then the noise is denominated *white noise*. In the case of white noise, noticing that $R_{jk} = \langle x_j x_k \rangle = \sigma^2 \delta_{jk}$, the PSD can be written as

$$S_x(f) = 2 \int_{-\infty}^{+\infty} R_x(\tau) e^{-2\pi i f \tau} d\tau = \lim_{\Delta t \to 0} 2\sigma^2 \Delta t. \tag{3.8}$$

Hence, in the case of white noise the PSD is constant and independent of the frequency. In the continuum limit the probability density of $x(t)$ is [4]

$$p_x[x(t)] \propto \exp \left\{ -\frac{1}{2} 4 \int_0^{\infty} \frac{|\tilde{x}(f)|^2}{S_x} \right\} df. \tag{3.9}$$

So far, we have restricted to white noise, but it turns out that Eq. (3.9) is also valid for *coloured noise*, for which the PSD is a frequency dependent function. In particular, it can be shown that the probability density p_x for a stationary Gaussian process $x(t)$ (with white or coloured noise) is [4]

$$p_x[x(t)] \propto e^{(x|x)}, \tag{3.10}$$

where $(x|x)$ denotes the noise-weighted inner product (*Wiener scalar product*) defined as

$$(a|b) = 2\mathrm{Re} \int_{-\infty}^{+\infty} \frac{\tilde{a}(f) \tilde{b}^*(f)}{S(f)} df = 4\mathrm{Re} \int_0^{+\infty} \frac{\tilde{a}(f) \tilde{b}^*(f)}{S(|f|)} df, \tag{3.11}$$

where $a(t)$ and $b(t)$ are two timeseries with $\tilde{a}(f)$, and $\tilde{b}(f)$, their respective Fourier transforms. In the last equality of Eq. (3.11) we have assumed that $a(t)$ and $b(t)$ are real functions. $S(f)$ is the one-sided power spectral density, which satisfies $S(-f) = S(f)$. Its associated norm is

$$|a|^2 = (a|a) = 4\mathrm{Re} \int_0^{+\infty} \frac{\tilde{a}(f) \tilde{a}^*(f)}{S(f)} df. \tag{3.12}$$

We remark that the Wiener inner product is real and symmetric. The inner product in Eq. (3.11) is usually normalized for the noise, $\langle |n(t)|^2 \rangle = 1$, which through Eq. (3.6) implies the property $\langle (a|n)(n|b) \rangle = \langle (a|b) \rangle$.

Assuming additive noise, the output of a gravitational-wave detector $s(t)$ can be written as a sum of the the GW signal $h(t, \boldsymbol{\Theta})$, described by the set of parameters $\boldsymbol{\Theta}$, and the noise $n(t)$,

$$s(t) = h(t, \boldsymbol{\Theta}) + n(t). \tag{3.13}$$

3.2 Matched filtering and optimal detection statistic

Given the statistical properties of the noise presented in Sec. 3.1, one wants to construct a quantity whose value expresses the probability that the data contains the GW signal. This quantity is called the *optimal detection statistic*. In this Section we present a brief introduction to optimal detection statistics as well as to *matched filtering*, the optimal procedure to search for a known GW signal buried in detector noise.

Regarding the strain detector output, Eq. (3.13), one wants to discriminate between two hypothesis, that the data does not contain a GW signal or it does,

- Null Hypothesis H_0 : $\qquad\qquad s(t) = n(t).$

- Alternative Hypothesis H_1 : $\qquad s(t) = n(t) + h(t).$

This hypothesis testing problem can be faced in two ways, using a frequentist or a Bayesian approach. In the case of a Bayesian approach [5, 4], one calculates the odds ratio $O(H_1|s) = P(H_1|s)/P(H_0|s)$, which is the ratio between the probability that the alternative hypothesis is true given $s(t)$ and the probability that the null hypothesis is true given $s(t)$.

Before going into the details of the gravitational wave detection problem we recall the basics of Bayesian inference. At the core of the Bayesian framework it is Bayes' theorem,

$$P(B|A) = \frac{P(B)P(A|B)}{P(A)}, \tag{3.14}$$

where $P(A)$ is the probability of an event A being true, also known as evidence, $P(B)$ is the probability of an event B being true and it is also known as the prior probability of B being true, and $P(A|B)$ is the conditional probability, i.e., the probability of A being true given B is true. The conditional probability, also called *likelihood*, is defined in terms of the joint probability $P(A, B)$ for both A and B being true as

$$P(A|B) = \frac{P(A, B)}{P(B)}. \tag{3.15}$$

Taking into account that the probability of A being false, $P(\bar{A})$, can be written as $P(\bar{A}) = 1 - P(A)$, then the likelihood ratio can be expressed as

$$\Lambda(B|A) = \frac{P(A|B)}{P(A|\overline{B})}. \tag{3.16}$$

Eq. (3.16) can also be rewritten in terms of the odds ratio of B being true if A is true as

$$O(B|A) = O(B)\Lambda(B|A), \tag{3.17}$$

where $O(B) = P(B)/P(\bar{B})$ is the prior odds ratio of B being true.

Going back to the problem of gravitational wave detection, we recall that given the data $s(t)$, we want to compute the odds ratio for H_1, i.e., $O(H_1|s)$. Looking at Eq. (3.17), and replacing probabilities by probability densities, we observe that the quantity we want to calculate is proportional to the likelihood ratio

$$\Lambda(H_1|s) = \frac{p(s|H_1)}{p(s|H_0)}, \tag{3.18}$$

and the prior odds ratio which does not depend on the data. As the odds and likelihood ratios are related to each other by a factor independent from the data, then, one can decide for simplicity to focus on the likelihood ratio. Assuming Gaussian noise, we can compute the probability densities under the null hypothesis, $H_0: \quad n(t) = s(t)$, and the alternative hypothesis $H_1: \quad n(t) = s(t) - h(t)$ as

$$p(s|H_0) = p_n(s(t)) \propto e^{-(s|s)/2}, \qquad p(s|H_1) = p_n(s(t) - h(t)) \propto e^{-(s-h|s-h)/2}. \tag{3.19}$$

Then, the likelihood ratio is

$$\Lambda(H_1|s) = e^{(s|h)} e^{-(h|h)/2}. \tag{3.20}$$

The only dependence of Eq. (3.20) on the data is through the inner product $(s|h)$. Therefore, this implies that any bound on the value of the odds ratio is translated, via an overall factor, into a bound on the value of $(s|h)$, which is denominated the *matched filter*. It can also be shown that $(s|h)$ is the optimal detection statistic [4]. We note that the efficiency of the matched filter strongly depends on knowing the form of the signal in the data. We now introduce the matched-filtered signal-to-noise ratio (SNR) as a normalized matched filter [6, 7, 5, 4],

$$\rho(\mathbf{\Theta}) = \frac{(h|s)}{\text{r.m.s}[(h|n)]} = \frac{(h|s)}{\langle (h|n)(h|n) \rangle} = \frac{(h|s)}{\sqrt{(h|h)}} = (\hat{h}|s), \tag{3.21}$$

where $\hat{h} = h/\sqrt{(h|h)}$ is the normalized signal template, $(\hat{h}|\hat{h}) = 1$, and $\mathbf{\Theta}$ denotes the parameters of the signal. It can be shown that the maximizing the likelihood is equivalent to maximizing the SNR [6, 7], hence, the SNR is also an optimal detection statistic. Furthermore, given a template model h_m for the signal h contained in the data $s(t)$, the ensemble average, see Eq. (3.1), of the SNR is

$$\langle \rho \rangle = \langle (\hat{h}_m|h) \rangle + \langle (\hat{h}_m|n) \rangle = (\hat{h}|h). \tag{3.22}$$

To obtain the last equality we have assumed that the noise and the signal are uncorrelated, i.e., $\langle (\hat{h}_m|n) \rangle = 0$. Then, in the case the template is identical to the signal, $h_m = h$, one obtains

$$\langle \rho \rangle_{\text{opt}} = \sqrt{h|h}, \tag{3.23}$$

which is the optimal SNR.

Finally, we remark that in this section we have focused on a Bayesian approach as current parameter estimation techniques are based on it, although we note that the detection hypothesis testing problem can also be faced with a frequentist approach obtaining, through the Neyman-Pearson lemma, that the likelihood ratio is also the optimal detection statistics. As we will see in the upcoming sections, the detection problem is substantially more complicated in a real detector as the assumption of stationary Gaussian noise does not hold anymore and the optimal detection statistic for such simplified noise cannot be used to claim real detections. As a consequence,

more advanced techniques have to be developed to detect real GW signals.

3.3 Gravitational wave parameter estimation

The calculation of the optimal detection statistic provides, under the hypothesis of stationary Gaussian noise, the probability of a signal present in the data $p(H_1|d)$, where H_1 is the alternative hypothesis, i.e., the hypothesis that data contains a signal, and d are the data. When the signal is parametrized by a set of parameters $\boldsymbol{\Theta} = \{\theta_1, \theta_2, \ldots, \theta_N\}$ one can construct the probability density $p(H_{\boldsymbol{\Theta}}|d)$ as a function of $\boldsymbol{\Theta}$ and estimate the values of the set of parameters. This task is called parameter estimation and it is performed through a Bayesian analysis on the observed data to estimate (or set constraints on) the unknown parameters of the source using waveform models.

The aim of parameter estimation is the description of the state of knowledge of the values of a set of parameters $\boldsymbol{\Theta}$ under a certain hypothesis H and probability density $p(\boldsymbol{\Theta}|H)$. Then, one uses Bayes theorem, Eq. (3.14), to update the prior probability distribution $p(\boldsymbol{\Theta}|d, H)$ with the new data of the experiment by computing the posterior probability distribution $p(\boldsymbol{\Theta}|d, H)$,

$$p(\boldsymbol{\Theta}|d, H) = \frac{p(\boldsymbol{\Theta}|H)p(d, |\boldsymbol{\Theta}, H)}{p(d|H)}, \qquad (3.24)$$

where $p(d|\boldsymbol{\Theta}, H) \equiv \mathcal{L}(d|\boldsymbol{\Theta})$ is the likelihood function and $p(d|H)$ is the evidence or the fully marginalized likelihood. As explained in Sec. 2.1 of Chapter 2, gravitational waveform models are described by a large number of parameters[1] which makes $p(\boldsymbol{\Theta}|d, H)$ a multi-dimensional probability density with a large parameter space and with complicated relations among its parameters. The probability density for a specific parameter is found marginalizing over the remaining parameters,

$$p(\theta_1|d, H) = \int d\theta_2 \cdots d\theta_N p(\boldsymbol{\Theta}|d, H), \qquad (3.25)$$

while the evidence, $Z = p(d|H)$, is calculated as

$$Z = p(d|H) = \int d\theta_1 \cdots d\theta_N p(d|\boldsymbol{\Theta}, H)p(\boldsymbol{\Theta}|H). \qquad (3.26)$$

The evidence does not depend on any parameters and, thus, in parameter estimation is treated as a normalization constant for a particular model. However, evidence becomes a key tool in model selection problems, like the determination of which gravitational waveform model better describes the detected signal. The comparison between two competing models, A and B, is calculated using the ratio of posterior distributions,

$$O_{AB} = \frac{p(H_A|d)}{p(H_B|d)} = \frac{p(H_A)}{p(H_B)} \times B_{AB}, \qquad (3.27)$$

where $B_{AB} = Z_A/Z_B$ is the Bayes factor between the two competing models describing how much is model A more strongly supported by the data than model B. For gravitational wave purposes the large dimensionality of the parameter space and the amount of data to analyse make it impossible to perform the calculations described above with a fixed sampling of the parameter space. Thus, stochastic methods based

---

[1]The set of unkown parameters contains also typically parameters not related to the source, but describing the calibration or the noise of the detector [8, 9].

on Markov chain Monte Carlo (MCMC) and Nested Sampling have been developed [8, 9, 10, 11] to sample over the parameter space and solve problems of Bayesian inference like model selection and parameter estimation.

Gravitational wave data model

As explained in Chapter 1, the data of a gravitational wave detector, $d = h + n$, can be described by a signal and noise components, h and n, respectively. Here, we focus on the description of the observed data with the inclusion of the detector noise which permits us to construct a model of the data which can be used to perform parameter estimation analyses.

The data of the detector is a time series d_i sampled uniformly at times t_i. The data are originally sampled at $f_s = 16834$ Hz, and down sampled to a lower rate to reduce the volume of data [8]. The lower rate is usually chosen such that it contains the maximum frequency $f_{\max}$ of the lowest mass signal used by the prior distribution, i.e., $f_s \geq 2f_{\max}$. For instance, in the case of a not very massive BBH signal one typically uses 2048 Hz.

The simplest model for the data in absence of a signal is that of Gaussian stationary noise described by a power spectral density, $S_n(f)$, and zero mean. The analyzed segment d spans an interval $[t_c - T + 2, t_c + 2]$, where the coalescence time t_c is computed by the search pipelines which have detected the event, T is a time which ends after 2s after the trigger, the 2s are added to safely account for inaccuracies in the determination of t_c. The PSD is calculated using data adjacent to the analyzed segment not containing the signal, i.e., ending before $t_c - T$. Then, assuming stationary Gaussian noise with zero mean and a variance calculated from the PSD, the likelihood function for the noise model can be expressed a product of Gaussian distributions in each frequency bin [8]

$$p(d|H_0, S_n(f)) = \exp \sum_i \left[-\frac{2|\tilde{d}_i|^2}{TS_n(f_i)} - \frac{1}{2}\log\left(\frac{\pi}{2}TS_n(f_i)\right) \right], \qquad (3.28)$$

where H_0 is the null hypothesis and the $\tilde{d}$ denotes the discrete Fourier transform of d,

$$\tilde{d}_i = \frac{T}{N}\sum_{k=1}^{N} d_k \exp(-2\pi ijk/N). \qquad (3.29)$$

For completeness, we display in Fig. 3.1 the *amplitude spectral density*, defined as the square-root of the PSD, $S_n(f)^{1/2}$, in terms of equivalent gravitational wave strain of the LIGO Hanford and LIGO Livingston detectors for times near the first GW detection GW150914 [12].

In the presence of a signal h the mean of the likelihood is modified such that the likelihood becomes

$$p(d|H_S, S_n(f), \boldsymbol{\Theta}) = \exp \sum_i \left[-\frac{2|\tilde{h}_i(\boldsymbol{\Theta}) - \tilde{d}_i|^2}{TS_n(f_i)} - \frac{1}{2}\log\left(\frac{\pi}{2}TS_n(f_i)\right) \right]. \qquad (3.30)$$

A network of detectors is typically analyzed assuming uncorrelated noise among them, which allows to express the coherent likelihood for the data as a product of likelihoods
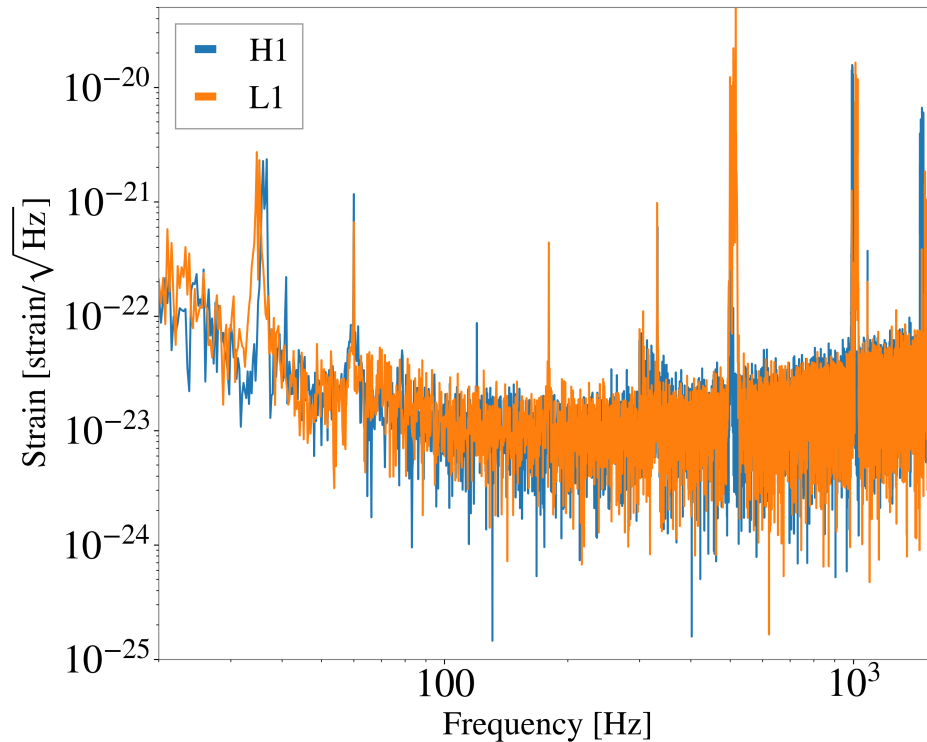
FIGURE 3.1: Amplitude spectral noise density expressed in terms of equivalent gravitational wave strain of the LIGO Hanford (H1) and LIGO Livingston (L1) detectors close to the time of signal detection of GW150914 [12].

in each detector [13]

$$p(d_{H,L,\dots}|H_S, S_{n,\{H,L,\dots\}}(f), \mathbf{\Theta}) = \prod_{i \in \{H,L,\dots\}} p(d_i|H_S, S_{n,i}(f)). \tag{3.31}$$

Markov Chain Monte Carlo

Markov chain Monte Carlo (MCMC) sampling [14, 15] methods estimate a posterior distribution by stochastically walking through the parameter space drawing samples proportional to the target posterior distribution. The probability of a point ('walker') to move to another point of the parameter space is determined by the proposal density function or transition probability distribution $Q(\mathbf{\Theta}'|\mathbf{\Theta})$. The generation of a new sample $\mathbf{\Theta}'$ depends on the present sample $\mathbf{\Theta}$ and its acceptance is based on the probability,

$$r_s = \min(1, \alpha), \qquad \alpha = \frac{Q(\mathbf{\Theta}|\mathbf{\Theta}')p(\mathbf{\Theta}'|d, H)}{Q(\mathbf{\Theta}'|\mathbf{\Theta})p(\mathbf{\Theta}|d, H)}. \tag{3.32}$$

In case of acceptance $\mathbf{\Theta}'$ is added to the Markov chain, otherwise the operation is repeated until an accepted sample is found.

The behaviour of the chains at early times is strongly dependent on the initial conditions. Thus, some iterations are required before the dependence is lost, this is the *burn-in* period. Burn-in samples have to be discarded when estimating the posterior distribution due to their dependence on the prior probabilities [8]. Moreover, the position of a walker in a chain is normally autocorrelated, thus, the position of the walkers do not faithfully represent the sampling from a posterior distribution. This

causes and underestimation of the width of the posterior distribution. To avoid this, a *thinning* procedure is applied to the chains [8, 9] by selecting samples separated by a certain autocorrelation time,

$$\tau = 1 + 2 \sum_i \hat{c}(i), \tag{3.33}$$

where i are the iterations of the chain and $\hat{c}(i)$ is the Pearson correlation coefficient [16].

The efficiency of the MCMC algorithm is mainly dependent on the choice of the transition probability distribution, since this governs the acceptance rates and the autocorrelation times. Using a standard Gaussian distribution as a proposal distribution becomes inefficient for GW parameter estimation and a range of jump proposals have been developed to sample more efficiently the parameter space of a compact binary coalescence as discussed in [8].

Furthermore, posterior distributions of GW parameters normally contain multiple local maxima, or modes, separated by regions of low probability. In order to ensure proper mixing of the samples from different modes, a technique called *parallel tempering* [17, 18] is commonly used. This method introduces an inverse *temperature* to the likelihood function, resulting in a posterior distribution

$$p_T(\Theta|\mathrm{d}) \propto \mathrm{p}(\Theta|\mathrm{H})\mathcal{L}(\Theta)^{1/\mathrm{T}}. \tag{3.34}$$

Temperatures larger than 1 smooth the likelihood surface, broadening the peaks, with a distribution tending to the priors as the temperature increases. The algorithm constructs a set of tempered chains with temperatures $T = 1, \ldots, T_{\max}$. Distributions at high temperatures are more likely to explore a larger parameter space by moving between modes. At high temperatures high probability regions are passed to low temperature chains by proposing exchanges in the locations of adjacent chains, $T_i < T_j$ at an acceptance rate $r_s = \min(1, \omega_{ij})$, with

$$\omega_{ij} = \left(\frac{\mathcal{L}(\Theta_j)}{\mathcal{L}(\Theta_i)}\right)^{\frac{1}{T_i} - \frac{1}{T_j}}. \tag{3.35}$$

This procedure increases significantly the sampling efficiency of the $T = 1$ chain, at the cost of calculating samples with $T > 1$ which are eventually discarded for the calculation of the final posterior distribution [8] as they are not drawn from the target posterior distribution. Moreover, each run can be run independently in parallel increasing the computational efficiency of the algorithm.

Nested Sampling

Nested sampling is a Monte Carlo technique to calculate the evidence [19] which produces samples of the posterior distribution as a by-product. The multidimensional integral of Eq. (3.26) is replaced by a one-dimensional integral over the prior volume X, defined as

$$X(\lambda) = \int_{p(d|\Theta,H)>\lambda} d\Theta p(\Theta|H), \tag{3.36}$$

where the integral is calculated within a likelihood contour defined by $p(d|\boldsymbol{\Theta}, H) = \lambda$. Using the definition of Eq. (3.36), Eq. (3.26) can be expressed as

$$Z = \int_0^1 \mathcal{L}(X)dX, \tag{3.37}$$

where $\mathcal{L}(X)$ is the likelihood distribution as a function of the prior volume obtained by using the inverse form of Eq. (3.36). The larger the prior volume enclosed the lower the likelihood, thus, $\mathcal{L}(X)$ is a monotonically decreasing function of X. We show in Fig. 3.2 two cartoon pictures representing a 2D posterior distribution and the corresponding $\mathcal{L}(X)$ function which associates directly each prior volume X_i with the likelihoods $\mathcal{L}_i$.
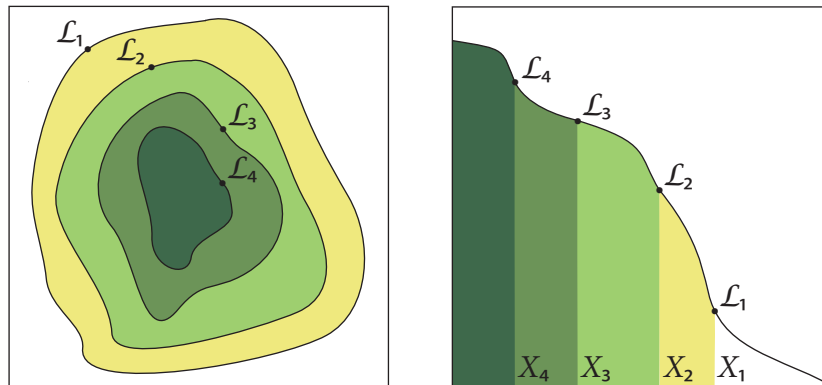
FIGURE 3.2: Pictures representing in the left plot a two-dimensional posterior distribution and, in the right panel the transformed $\mathcal{L}(X)$ function where the prior volumes X_i are directly related to the likelihoods $\mathcal{L}_i$. Pictures taken from [20].

Given a sequence of monotonically decreasing prior volumes X_i, such that, $0 < X_M < \cdots < X_0 = 1$, one can evaluate the likelihoods $\mathcal{L}_i = \mathcal{L}(X_i)$ and approximate the evidence distribution, for instance, through the trapezoidal as

$$Z = \sum_{i=1}^{M} \frac{1}{2}(X_{i-1} - X_{i+1})\mathcal{L}_i. \tag{3.38}$$

The algorithm to apply this sampling procedure can be summarized as follows:

1) Choose initial *live* points sampling the prior distribution.

2) Remove the value with the lowest likelihood (*dead* point) and replace it by a new sample with higher likelihood. The proposal distributions in Nested Sampling are based on MCMC chains and are very similar to the ones for MCMC sampling [8].

3) The removal and replacement of points is repeated until a stopping condition is met. The stopping condition is normally set in GW analysis [8, 11] such that the change in evidence calculation is less than a factor of 0.1 assuming that the remaining prior distribution was at maximum likelihood, i.e., $\mathcal{L}_{\max}X_i/Z_i > e^{0.1}$.

The posterior samples can be produced by resampling the chain of dead and live points as

$$p(\Theta|d, H) = \frac{(X_{i-1} - X_{i+1})}{2} \times \frac{\mathcal{L}_i}{Z}. \tag{3.39}$$

Finally, we remark that the computation of the prior volumes and the generation of new samples vary between implementations, we refer the interested reader to [21, 8, 11] for details on these calculations within the nested sampling method. From the parameter estimation methods presented in this section, the nested sampling algorithms will be used in Chapter 5 to obtain original results on the estimation of the parameters of injected numerical relativity eccentric GW signals into detector noise.

3.4   Detection of gravitational waves

The basic concepts presented so far on the optimal detection statistic restricted to the case of stationary Gaussian noise, which is not the case of a real gravitational wave detector where transient noise artefacts, known as *glitches*, can faithfully resemble a GW signal [22, 23]. A search algorithm optimal for Gaussian stationary noise can perform poorly on real data, missing events or identifying glitches as GW signals. Thus, these algorithms need to be equipped with additional tools to measure the robustness of a signal in order to reject noise artefacts and retain GW signals, like the calculation of the false alarm probability and the detection efficiency of our detection statistic. The detection problem is equivalent to a hypothesis testing problem, where we have to decide between the null hypothesis, H_0 (only noise in the data) and the alternative hypothesis H_1 (signal contained in the data). Given a detection statistic of the data $\Lambda(d)$ and a certain threshold value Λ', one may have the following situations:

- $\Lambda(d) < \Lambda'$: we accept H_0 and there is no signal.

- $\Lambda(d) < \Lambda'$: we should accept H_0, but there is a GW signal in the data. In this case, one can compute the *false alarm dismissal*, which is the probability of the threshold not being crossed even when H_1 is true,

$$\text{FAD}(\Lambda' < \Lambda|H_1) = \int_{-\infty}^{\Lambda'} p(\Lambda(d)|H_1)d\Lambda. \tag{3.40}$$

- $\Lambda(d) \geq \Lambda'$: we accept H_1 and there is a signal.

- $\Lambda(d) \geq \Lambda'$: we should accept H_1, but there is no signal in the data. In order to prevent this situation one calculates the probability of passing over the threshold notwithstanding H_0 being true, this is the definition of the *false alarm probability*,

$$\text{FAP}(\Lambda' > \Lambda|H_0) = \int_{\Lambda'}^{\infty} p(\Lambda(d)|H_0)d\Lambda. \tag{3.41}$$

In practice, apart from these two quantities which evaluate the detection probability of a search algorithm, there are a pletora of techniques developed to prevent misidentification of noise transient as GW signals like the application of *vetoes*, *coincidences*, *time-slides*, ... The use of one or another highly depends on the targeted source of GW signal and we refer the reader to [4, 3, 22, 23] for an introduction with further details on those concepts.

In the following two subsections we briefly describe two methods used in this thesis to search for stellar mass eccentric binary black holes. These two methods are 1) a modeled search algorithm, specifically the PyCBC [24, 25] pipeline, based on match filtering with a known template, and 2) an unmodeled search algorithm, particularly coherent Wave Burst (cWB) [26, 27], based on a coherent excess power in a network of detectors.

3.4.1 Matched filter search algorithm

In the LIGO analyses of GW events during O2 two independent modeled search algorithms have been used [28], PyCBC[24, 25] and GstLAL [29, 30, 31]. Both pipelines use a bank of template waveforms to grid up the parameter space such that the maximum likelihood ratio can be approximately identified with the best match of the data with the template bank [32, 33, 34, 35, 36, 37]. We focus here on the PyCBC pipeline. For PyCBC, template banks are generated such that the loss in matched filter SNR due to the discrete placement of templates is not larger than 3%.

In Sec. 3.2 we introduced the basic concepts of matched filtering. In the following we show the implementation of the matched filter in the PyCBC pipeline. Although recent progress has been achieved on testing the implementation of additional physical effects on the search pipeline, like spin precession or eccentricity [38, 39], current searches are restricted to template banks produced with quasi-circular aligned-spin $(2, \pm2)$ modes waveforms. The simplification of using only the $(2, \pm2)$ modes implies that effects the sky location and binary orientation are an overall factor in the amplitude and phase of the waveform, which are computationally efficiently maximized by projecting the template $h(t)$ into two orthogonal space $h_{\sin}$ and $h_{\cos}$ [24]. In terms of this decomposition the SNR can be expressed as

$$\rho^2(t) = \frac{(d|h_{\cos})^2}{(h_{\cos}|h_{\cos})} + \frac{(d|h_{\sin})^2}{(h_{\sin}|h_{\sin})}, \tag{3.42}$$

where $(\cdot|\cdot)$ is the noise-weighted inner product defined in Eq. (3.11).

Triggers are generated by the pipeline according to excesses of matched-filter SNR over a predetermined threshold. However, some of those triggers can be caused by non-stationary and non-gaussian detector noise, thus, an additional signal consistency test between the data and the template, known as *chi-squared* test, is applied. The chi-squared test assesses if the time frequency distribution of the data is consistent with the expected power in the template [24]. This test is evaluated by dividing the template in p frequency bins with equal contributions to the power of the matched filter SNR. Then, the matched-filter SNR, ρ_i, is calculated for each frequency bin. For a real signal ρ_i contains a $1/p$ fraction of the total SNR. This motivates the definition of the χ^2 statistic,

$$\chi^2 = p \sum_{i=1}^{p} \left[\left(\frac{\rho_{\cos}^2}{p} - \rho_{\cos,i}^2 \right)^2 + \left(\frac{\rho_{\sin}^2}{p} - \rho_{\sin,i}^2 \right)^2 \right], \tag{3.43}$$

where $\rho_{\cos}^2, \rho_{\sin}^2$ are the SNRs of the two orthogonal phases. This statistic compares the expected with the measured power in each frequency bin. Given a value of the matched filter SNR, large values of χ^2 indicate high probability of a noise transient nature of the trigger. In order to have a magnitude of the expected order of the χ^2 statistic in the case of a signal, it is defined the reduced chi-squared statistic as

$$\chi_r^2 = \chi^2/(2p - 2), \tag{3.44}$$

which for signals should be close to 1. The matched filter SNR can also be redefined to down weight the triggers caused by noise fluctuations [24]

$$\hat{\rho} = \begin{cases} \rho/[1 + (\chi_r^2)^3/2]^{1/6}, & \text{if } \chi_r^2 > 1, \\ \rho, & \text{if } \chi_r^2 \leq 1, \end{cases} \tag{3.45}$$

which is known as the re-weighted SNR. The reweighted SNR is computed for each trigger and those triggers with $\hat{\rho}$ smaller than a predetermined threshold are discarded. The search requires that the observed signals are consistent within the detector network by first vetoing instrumental noise glitches, and afterwards performing a *coincidence* test on the remaining triggers [25]. For instance, signals observed by the LIGO Hanford and LIGO Livingston detectors have to be seen within a time difference of 15 ms (∼10 ms travel time between detector +5 ms for timing errors).

Triggers passing the coincidence test are named as *coincident events*, which, in the case of a two-detector network are ranked according to the quadrature sum of the reweighted SNR of each detector,

$$\hat{\rho}_c = \sqrt{\hat{\rho}_1^2 + \hat{\rho}_2^2}. \tag{3.46}$$

Finally, the pipeline computes the false-alarm rate (FAR) of the search as a function of the detection statistic $\hat{\rho}_c$ to assign statistical significances to candidate events. The false alarm rate of the pipeline is calculated using a *time shift* procedure for a two detector network [25]. We note that very recently the PyCBC pipeline has been extended to three or more detectors [40].

The sensitivity of a search pipeline can be estimated using the *sensitive volume* of the pipeline, defined as

$$V(\mathcal{F}) = \int \epsilon(\mathcal{F}; \mathrm{x}, \Theta)\phi(\mathrm{x}, \Theta)\mathrm{dxd}\Theta, \tag{3.47}$$

where x is a spatial coordinate, $\phi(\mathrm{x}, \Theta)$ is the distribution of signals in the Universe and ϵ is the efficiency of the pipeline at detecting events with parameters Θ in a volume specified by x with a false alarm rate $\mathcal{F}$. For PyCBC the sensitivity volume is calculated injecting a large number N_I of simulated signals into the data and measuring the ability of the pipeline to find them. Assuming that the astrophysical distribution for the simulated and real signals is the same, the sensitive volume can be calculated as

$$V(\mathcal{F}) \approx \frac{1}{N_I} \sum_{i=1}^{N_I} \mathcal{H}(\mathcal{F}|\mathcal{F}_i) \equiv \langle \mathcal{H}(\mathcal{F}) \rangle, \tag{3.48}$$

where $\mathcal{F}_i$ is the FAR associated with each simulated signals and $\mathcal{H}(\mathcal{F}|\mathcal{F}_i)$ is a step function defined as

$$\mathcal{H}(\mathcal{F}|\mathcal{F}_i) = \begin{cases} 1, & \text{if } \mathcal{F} \leq \mathcal{F}_i, \\ 0, & \text{otherwise.} \end{cases} \tag{3.49}$$

For each simulated signal the FAR is calculated using the most significant event within a 1 second window of the time of arrival of the simulated signal. When no event is found within that window, the detection statistic is set to 0.

3.4.2   Unmodeled search algorithm

Bursts of gravitational wave radiation are short-lived signals with a duration shorter than the observational timescale. These transient signals can have a known morphology, as the case of a binary coalescence, can be poorly modeled as in the case of core-collapse supernovae, or can be emitted from a totally unknown source. In any case, all of them are characterized by their short duration compared to the observation time. In this section we focus on the description of an unmodeled search pipeline, coherent Wave Burst (cWB) and its application [26, 27] for detecting eccentric BBH

mergers. cWB is a search algorithm for detection and reconstruction of unknown burst signals based on the excess of coherent energy in a detector network.

The first operation of cWB is the application of a time frequency (TF) transform [41, 42, 43] to the detector data $x_k[i]$, where k and i represent the detector index (assuming a network of K detectors) and the data sampling index ($\equiv$ TF pixel), respectively. Specifically, a Wilson-Daubechies-Meyer (WDM) transform is applied to the detector time series. For each data sample the detector noise is estimated by the WDM PSD $S_k[i]$. Then, the one defines the noise-scaled (whitened) data as

$$w_k[i] = x_k[i]/\sqrt{S_k[i]}. \tag{3.50}$$

The TF series of whitened data from all the detectors are combined to obtain TF energy maps maximized over all possible sky locations,

$$E[i] = \sum_k w_k^2[i]. \tag{3.51}$$

These energy maps identify regions of the TF space, also called clusters C with $i \in C$, with excess energy power over the detector noise threshold. These TF clusters, identified by a clustering algorithm [44], characterize the burst event from which one extracts the sky location, waveform and polarizations. This is called the inverse problem.

In the case of GW burst searches, one has to determine the amplitudes of the GW polarizations $(h_+, h_\times)$ and the sky location (θ, ϕ) from a coincident output, $\boldsymbol{x}[i]$ of a network of detectors. The data vector $\boldsymbol{x}[i]$ can be expressed in terms of the passing GW signal $\boldsymbol{h}[i] = \{h_+[i], h_\times[i]\}$ at a certain sky location (ϕ, θ) as

$$\boldsymbol{x} = \mathcal{F}\boldsymbol{h}[i] + \boldsymbol{n}[i], \tag{3.52}$$

where $\mathcal{F}$ is the network antenna pattern matrix

$$\mathcal{F} = \begin{pmatrix} F_{1,+} & F_{1,\times} \\ \cdots & \cdots \\ F_{K,+} & F_{K,\times} \end{pmatrix}. \tag{3.53}$$

We note that the polarization angle is not included in the above expressions as the network response is invariant under rotations of the polarization angle, thus, its contribution is included in the definition of the signal $\boldsymbol{h}$.

The inverse problem can be addressed by calculating the likelihood ratio [6]

$$\Lambda(\boldsymbol{x}, \boldsymbol{\Theta}) = \frac{p(\boldsymbol{x}|\boldsymbol{h}(\boldsymbol{\Theta}))}{p(\boldsymbol{x}|H_0)}, \tag{3.54}$$

where $p(\boldsymbol{x}|\boldsymbol{h}(\boldsymbol{\Theta}))$ is the joint probability of a GW signal $\boldsymbol{h}$ contained in the data $\boldsymbol{x}$, while $p(\boldsymbol{x}|H_0)$ is the probability of the null hypothesis being true. Then, the likelihood ratio is completely determined by the noise and signal models.

In the case of unmodeled searches the signal can be described by $\boldsymbol{\Theta} = (h_+, h_\times, \phi, \theta)$ which are calculated by numerically or analytically varying Λ as shown below. Assuming an unconstrained source model and quasistationary Gaussian noise, the noise-scaled data can be expressed as [44]

$$\boldsymbol{w}[i] = \frac{x_1[i, \tau_1(\phi, \theta)]}{\sqrt{S_1[i]}}, \ldots, \frac{x_K[i, \tau_K(\phi, \theta)]}{\sqrt{S_K[i]}}, \tag{3.55}$$

where $S_1, \cdots, S_K$ are the PSDs, $x_k[i, \tau_k(\phi, \theta)]$ the detector amplitudes defined by the time-flight delays τ_k and the sky position (ϕ, θ). The noise-scaled network response is defined as

$$\boldsymbol{\xi}[i] = \boldsymbol{F}[i]\boldsymbol{h}[i], \quad \text{with} \quad \boldsymbol{F}[i] = \begin{pmatrix} \frac{F_{1,+}(\phi,\theta)}{\sqrt{S_1[i]}} & \frac{F_{1,\times}(\phi,\theta)}{\sqrt{S_1[i]}} \\ \cdots & \cdots \\ \frac{F_{K,+}(\phi,\theta)}{\sqrt{S_K[i]}} & \frac{F_{K,\times}(\phi,\theta)}{\sqrt{S_K[i]}}, \end{pmatrix}. \tag{3.56}$$

where $\boldsymbol{F}[i]$ is the noise-scaled antenna pattern matrix. We introduce the likelihood functional $\mathcal{L}$ as twice the logarithm of the likelihood ratio Λ,

$$\mathcal{L}[h] = 2(\boldsymbol{w}|\boldsymbol{\xi}) - (\boldsymbol{\xi}|\boldsymbol{\xi}), \tag{3.57}$$

where inner products are calculated on each cluster. The solution for $\boldsymbol{h}$ is found by the variation of $\mathcal{L}[h]$. In order to that, a transformation of $\boldsymbol{F}$ into the *dominant polarization frame* (DPF) [45] is applied to obtain the network matrix $\boldsymbol{f}$. The network matrix can be expressed in terms of the antenna pattern vectors $\boldsymbol{f} = (\boldsymbol{f}_+, \boldsymbol{f}_\times)$, which through the relations

$$(\boldsymbol{f}_+, \boldsymbol{f}_\times) = 0 \quad \text{and} \quad |\boldsymbol{f}_\times| \leq |\boldsymbol{f}_+|, \tag{3.58}$$

define a plane where the GW response $\boldsymbol{\xi}$ can be located. The variation of the likelihood provides the following system of linear equation for h_+ and $h_\times$ in the DPF,

$$\begin{pmatrix} \boldsymbol{w}[i] \cdot \boldsymbol{e}_+[i] \\ \boldsymbol{w}[i] \cdot \boldsymbol{e}_\times[i] \end{pmatrix} = \begin{pmatrix} |\boldsymbol{f}_+[i]| & 0 \\ 0 & |\boldsymbol{f}_\times[i]| \end{pmatrix} \begin{pmatrix} h_+[i] \\ h_\times[i] \end{pmatrix}, \tag{3.59}$$

where $(\boldsymbol{e}_+, \boldsymbol{e}_\times)$ are unit vectors in the directions of $(\boldsymbol{f}_+, \boldsymbol{f}_\times)$. Eq. (3.59) determines the network sensitivity to the GW polarizations. The maximum likelihood ratio statistic [4] is obtained in this case replacing the solution of Eq. (3.59) into Eq. (3.57),

$$\mathcal{L}_{\max} = \sum_{i \in C} \boldsymbol{w}[i]P[i]\boldsymbol{w}^T[i], \quad \text{with} \quad P_{nm}[i] = e_{n+}[i]e_{m+}[i] + e_{n\times}[i]e_{m\times}[i], \tag{3.60}$$

where P is the projection matrix into the $(f_+, f_\times)$ axes. The axis orthogonal to $(f_+, f_\times)$ defines the residual detector noise and it is known as the *null stream*.

In order to construct event selection quantities in burst searches, the maximum likelihood statistic is decomposed into coherent E_c and incoherent E_i contributions,

$$E_c = \sum_{i \in C} \sum_{n \neq m} w_n[i]P_{nm}[i]w_n[i], \tag{3.61}$$

$$E_i = \sum_{i \in C} \sum_{n} w_n[i]P_{nn}[i]w_n[i]. \tag{3.62}$$

Then, using also the null stream energy E_n, the *network correlation coefficient* is defined as [26]

$$c_c = E_c = \sum_{i \in C} \sum_{n} w_n[i]P_{nn}[i]w_n[i]. \tag{3.63}$$

The network correlation coefficient provides a very useful tool to perform event consistency tests, as it allows to discriminate between noise artefacts ($c_c \ll 1$) and real GW events ($c_c \approx 1$). The network correlation coefficient together with the coherent energy E_c, statistic providing correlations between detector pairs, are employed to

define the *burst detection statistic* [44]

$$\eta_c = \sqrt{\frac{c_c E_c K}{K-1}}.$$ (3.64)

The burst detection statistic estimates the network coherent energy ($\equiv$ SNR) for correlated GW signals measured by a network of K GW detectors.

At this point we remark that the sensitivity of the search can also be estimated using the general definition given by Eq. (3.47). We refer the interested reader to [26, 27, 44, 45] for more details on methods used by the cWB pipeline as well as the procedure to reconstruct the waveform of the detected GW signal.

References

[1] J. Aasi et al. Advanced LIGO. *Class. Quant. Grav.*, 32:074001, 2015. arXiv:1411.4547 [gr-qc].

[2] F. Acernese et al. Advanced Virgo: a second-generation interferometric gravitational wave detector. *Class. Quant. Grav.*, 32(2):024001, 2015. arXiv:1408.3978 [gr-qc].

[3] Piotr Jaranowski and Andrzej Krolak. Analysis of Gravitational-Wave Data. *Analysis of Gravitational-Wave Data, by Piotr Jaranowski , Andrzej Krolak, Cambridge, UK: Cambridge University Press, 2009*, 08 2009.

[4] Jolien D. E. Creighton and Warren G. Anderson. *Gravitational-wave physics and astronomy: An introduction to theory, experiment and data analysis*. 2011.

[5] Michele Maggiore. Gravitational waves. Volume 1: Theory and experiments. *Gen. Rel. Grav.*, 41:1667–1669, 2009.

[6] Eanna E. Flanagan and Scott A. Hughes. Measuring gravitational waves from binary black hole coalescences: 1. Signal-to-noise for inspiral, merger, and ringdown. *Phys. Rev. D*, 57:4535–4565, 1998. arXiv:gr-qc/9701039.

[7] Fernando Echeverria. Gravitational-wave measurements of the mass and angular momentum of a black hole. *Phys. Rev. D*, 40:3194–3203, Nov 1989.

[8] J. Veitch et al. Parameter estimation for compact binaries with ground-based gravitational-wave observations using the LALInference software library. *Phys. Rev. D*, 91(4):042003, 2015. arXiv:1409.7215 [gr-qc].

[9] Eric Thrane and Colm Talbot. An introduction to Bayesian inference in gravitational-wave astronomy: Parameter estimation, model selection, and hierarchical models. *Publications of the Astronomical Society of Australia*, 36:e010, March 2019. arXiv:1809.02293 [astro-ph.IM].

[10] C.M. Biwer, Collin D. Capano, Soumi De, Miriam Cabero, Duncan A. Brown, Alexander H. Nitz, and V. Raymond. PyCBC Inference: A Python-based parameter estimation toolkit for compact binary coalescence signals. *Publ. Astron. Soc. Pac.*, 131(996):024503, 2019. arXiv:1807.10312 [astro-ph.IM].

[11] Gregory Ashton et al. BILBY: A user-friendly Bayesian inference library for gravitational-wave astronomy. *Astrophys. J. Suppl.*, 241(2):27, 2019. arXiv:1811.02042 [astro-ph.IM].

[12] B.P. Abbott et al. Observation of Gravitational Waves from a Binary Black Hole Merger. *Phys. Rev. Lett.*, 116(6):061102, 2016. arXiv:1602.03837 [gr-qc].

[13] Lee Samuel Finn and David F. Chernoff. Observing binary inspiral in gravitational radiation: One interferometer. *Phys. Rev. D*, 47:2198–2219, 1993. arXiv:gr-qc/9301003.

[14] Nicholas Metropolis, Arianna W. Rosenbluth, Marshall N. Rosenbluth, Augusta H. Teller, and Edward Teller. Equation of state calculations by fast computing machines. *The Journal of Chemical Physics*, 21(6):1087–1092, 1953.

[15] W. K. Hastings. Monte Carlo sampling methods using Markov chains and their applications. *Biometrika*, 57(1):97–109, 1970. *Preprint:*http://biomet.oxfordjournals.org/cgi/reprint/57/1/97.pdf.

[16] Andrew Gelman, Gareth O. Roberts, and Walter R. Gilks. Efficient Metropolis jumping rules. 1995.

[17] W.R. Gilks, S. Richardson, and D. Spiegelhalter. *Markov Chain Monte Carlo in Practice*. Chapman & Hall/CRC Interdisciplinary Statistics. Taylor & Francis, 1995.

[18] David J. Earl and Michael W. Deem. Parallel tempering: Theory, applications, and new perspectives. *Phys. Chem. Chem. Phys.*, 7:3910–3916, 2005.

[19] John Skilling. Nested sampling for general Bayesian computation. *Bayesian Anal.*, 1(4):833–859, 12 2006.

[20] F. Feroz, M. P. Hobson, E. Cameron, and A. N. Pettitt. Importance Nested Sampling and the MultiNest Algorithm. 2013. arXiv:1306.2144 [astro-ph.IM].

[21] D. S. Sivia and J. Skilling. *Data Analysis - A Bayesian Tutorial*. Oxford Science Publications. Oxford University Press, 2nd edition, 2006.

[22] L. Nuttall et al. Improving the Data Quality of Advanced LIGO Based on Early Engineering Run Results. *Class. Quant. Grav.*, 32(24):245005, 2015. arXiv:1508.07316 [gr-qc].

[23] B. P. Abbott et al. Characterization of transient noise in Advanced LIGO relevant to gravitational wave signal GW150914. *Class. Quant. Grav.*, 33(13):134001, 2016. arXiv:1602.03844 [gr-qc].

[24] Bruce Allen, Warren G. Anderson, Patrick R. Brady, Duncan A. Brown, and Jolien D.E. Creighton. FINDCHIRP: An Algorithm for detection of gravitational waves from inspiraling compact binaries. *Phys. Rev. D*, 85:122006, 2012. arXiv:gr-qc/0509116.

[25] Samantha A. Usman et al. The PyCBC search for gravitational waves from compact binary coalescence. *Class. Quant. Grav.*, 33(21):215004, 2016. arXiv:1508.02357 [gr-qc].

[26] S. Klimenko, I. Yakushin, A. Mercer, and Guenakh Mitselmakher. Coherent method for detection of gravitational wave bursts. *Class. Quant. Grav.*, 25:114029, 2008. arXiv:0802.3232 [gr-qc].

[27] Shubhanshu Tiwari. *Gravitational waves from eccentric binary black hole mergers: Searches and astrophysical interpretations*. PhD thesis, GSSI, Aquila, 2018.

[28] B. P. Abbott et al. GWTC-1: A Gravitational-Wave Transient Catalog of Compact Binary Mergers Observed by LIGO and Virgo during the First and Second Observing Runs. *Phys. Rev.*, X9(3):031040, 2019. arXiv:1811.12907 [astro-ph.HE].

[29] Cody Messick et al. Analysis framework for the prompt discovery of compact binary mergers in gravitational-wave data. *Phys. Rev. D*, 95(4):042001, February 2017. arXiv:1604.04324 [astro-ph.IM].

[30] Kipp Cannon et al. Toward Early-Warning Detection of Gravitational Waves from Compact Binary Coalescence. *Astrophys. J.*, 748:136, 2012. arXiv:1107.2665 [astro-ph.IM].

[31] Stephen Privitera, Satyanarayan R.P. Mohapatra, Parameswaran Ajith, Kipp Cannon, Nickolas Fotopoulos, Melissa A. Frei, Chad Hanna, Alan J. Weinstein, and John T. Whelan. Improving the sensitivity of a search for coalescing binary black holes with nonprecessing spins in gravitational wave data. *Phys. Rev. D*, 89(2):024003, 2014. arXiv:1310.5633 [gr-qc].

[32] B. S. Sathyaprakash and S. V. Dhurandhar. Choice of filters for the detection of gravitational waves from coalescing binaries. *Phys. Rev. D*, 44:3819–3834, Dec 1991.

[33] S. V. Dhurandhar and B. S. Sathyaprakash. Choice of filters for the detection of gravitational waves from coalescing binaries. II. Detection in colored noise. *Phys. Rev. D*, 49:1707–1722, Feb 1994.

[34] Benjamin J. Owen. Search templates for gravitational waves from inspiraling binaries: Choice of template spacing. *Phys. Rev. D*, 53:6749–6761, 1996. arXiv:gr-qc/9511032.

[35] Benjamin J. Owen and B.S. Sathyaprakash. Matched filtering of gravitational waves from inspiraling compact binaries: Computational cost and template placement. *Phys. Rev. D*, 60:022002, 1999. arXiv:gr-qc/9808076.

[36] S. Babak, R. Balasubramanian, D. Churches, T. Cokelaer, and B. S. Sathyaprakash. A Template bank to search for gravitational waves from inspiralling compact binaries. I. Physical models. *Class. Quant. Grav.*, 23:5477–5504, 2006. arXiv:gr-qc/0604037 [gr-qc].

[37] Ian W. Harry, Bruce Allen, and B.S. Sathyaprakash. A Stochastic template placement algorithm for gravitational wave data analysis. *Phys. Rev. D*, 80:104014, 2009. arXiv:0908.2090 [gr-qc].

[38] Ian Harry, Stephen Privitera, Alejandro Bohé, and Alessandra Buonanno. Searching for Gravitational Waves from Compact Binaries with Precessing Spins. *Phys. Rev. D*, 94(2):024012, 2016. arXiv:1603.02444 [gr-qc].

[39] Alexander H. Nitz, Amber Lenon, and Duncan A. Brown. Search for Eccentric Binary Neutron Star Mergers in the first and second observing runs of Advanced LIGO. 2019. arXiv:1912.05464 [astro-ph.HE].

[40] Gareth S. Davies, Thomas Dent, Márton Tápai, Ian Harry, and Alexander H. Nitz. Extending the PyCBC offline search to a global detector network. 2020. arXiv:2002.08291 [astro-ph.HE].

[41] Ingrid. Daubechies. *Ten Lectures on Wavelets*. Society for Industrial and Applied Mathematics, 1992.

[42] Y. Meyer and D.H. Salinger. *Wavelets and Operators: Volume 1*. Cambridge Studies in Advanced Mathematics. Cambridge University Press, 1992.

[43] V Necula, S Klimenko, and G Mitselmakher. Transient analysis with fast Wilson-Daubechies time-frequency transform. *Journal of Physics: Conference Series*, 363:012032, jun 2012.

[44] S. Klimenko et al. Method for detection and reconstruction of gravitational wave transients with networks of advanced detectors. *Phys. Rev. D*, 93(4):042004, 2016. arXiv:1511.05999 [gr-qc].

[45] S. Klimenko, S. Mohanty, Malik Rakhmanov, and Guenakh Mitselmakher. Constraint likelihood analysis for a network of gravitational wave detectors. *Phys. Rev. D*, 72:122002, 2005. arXiv:gr-qc/0508068.

Part II

Original research results

Chapter 4

Eccentricity reduction in numerical relativity simulations

The following publish article is included in this chapter:

- Antoni Ramos-Buades, Sascha Husa and Geraint Pratten Geraint. *Simple procedures to reduce eccentricity of binary black hole simulations.* Physical Review D **99**, 023003 (2019). [27 pages]

December 11, 2018

Simple procedures to reduce eccentricity of binary black hole simulations

Antoni Ramos-Buades,[1] Sascha Husa,[1] and Geraint Pratten[1]

[1]*Departament de Física, Universitat de les Illes Balears, IAC3 – IEEC, Crta. Valldemossa km 7.5, E-07122 Palma, Spain*

We present simple procedures to construct quasi-circular initial data for numerical evolutions of binary black hole spacetimes. Our method consists of using Post-Newtonian theory in three ways: first to provide an initial guess for the initial momenta at 3.5PN order that implies low residual eccentricity, second to measure the resulting eccentricity, and third to calculate corrections to the momenta or initial separation which further reduce the eccentricity. Regarding the initial guess, we compare numerical evolutions in post-Newtonian theory to the post-circular and post-post-circular analytical approximations to quasi-circular data. We discuss a robust fitting procedure to measure eccentricity from numerical simulations using the orbital frequency Ω, and derive from the quasi-Keplerian parametrization at 1PN oder the correction factors for the tangential and radial momentum components required to achieve reduce the measured eccentricity to zero. We first test our procedure integrating PN equations of motion at 3.5PN where low eccentric initial data is easily obtained, and then apply our method to sets of binary black hole numerical relativity simulations with different mass ratios ($q = m_2/m_1 = 1, 2, ..., 8$), spin configurations and separations. Our set of simulations contains non-spinning, spin-aligned and precessing simulations. We observe that the iterative procedure produces low eccentric simulations with eccentricities of the order $O\left(10^{-4}\right)$ with only one iteration. The simplicity of the procedure allows to obtain low eccentric NR simulations easily and saving computational resources. Moreover, the analytical PN formulas derived in this paper will be useful to generate eccentric hybrid waveforms.

PACS numbers: 04.25.Dg, 04.25.Nx, 04.30.Db, 04.30.Tv

I.   INTRODUCTION

The first detection of a gravitational wave signal [1] in 2015 by the LIGO detectors [2], as well as the subsequent detections [3–7], have been found consistent with models of the waveform emitted from the merger of compact objects under the assumption of quasi-circularity of the binary's orbit prior to the merger. These models have been used to infer the parameters of the sources from the measured data, see e.g. the detailed discussion of parameter estimation results for the first detection [8]. Indeed, efforts to model the gravitational wave signals from compact binary coalescence have to a large degree neglected eccentricity, as motivated by the efficient circularisation of binaries as a consequence of the emission of gravitational waves [9, 10].

Only a decade before the first detection of gravitational waves, breakthroughs in numerical relativity (NR) [11–13] have made it possible to compute the evolution of binary black holes until the merger in general relativity (GR), and to extract the gravitational waves emitted from such systems. Numerical simulations of compact binaries are now performed routinely [14–17], and models synthesized from numerical parameter studies and perturbative results are routinely used to analyse the data from the LIGO and Virgo detectors [18–22].

Initial data for numerical relativity simulations of black hole binaries are typically constructed in a five-step procedure, which can be roughly summarised as follows:

1) One chooses the separation and the spin components.

2) One chooses the momenta or velocities of the black holes such as to result in a low eccentricity. This step is usually guided by post-Newtonian (PN) approximations [23].

3) The constraint equations of general relativity are solved numerically for the chosen parameters, often using the approximation of conformal flatness.

4) The data are evolved numerically until the eccentricity can be estimated reliably from the corresponding oscillations in the separation, or orbital and gravitational wave frequency, as well as in other quantities. Residual eccentricy can lead to parameter biases when using the resulting waveforms for parameter estimation in gravitational wave analysis, and complicate the construction of quasi-circular waveform models from the numerical data. In GR there is however no unique definition of eccentricity, and a specific quantity usually referred to as "eccentricity estimator" needs to be chosen, which reduces to the Newtonian concept of eccentricity in the Newtonian limit. Determining eccentricity from the orbital frequency Ω, one would, for example, typically choose the eccentricity estimator

$$e_\Omega = \frac{\Omega(t) - \Omega(e = 0)}{2\Omega(e = 0)}, \qquad (1.1)$$

which measures the time dependent oscillations in the orbital frequency relative to the case with vanishing eccentricity. The factor of two normalizes the quantity e_Ω to be consistent eccentricity in radial oscillations (without the corresponding factor of two).

5) A correction to the initial parameters is applied, and steps 2-5 (or 1-5) are applied until the eccentricity is deemed low enough for applications, taking into account the computational cost of short evolutions required to measure the eccentricity and the human effort to carry out or automatize the procedure.

In this paper we first discuss steps two, four, and five, and then a version of changing the momenta in step two where we also correct for the initial coordinate separation, thus changing step one. In order to guess initial conditions, determine the eccentricity of a numerical simulation, and to guess improved initial momenta, PN approximations at different orders in the PN expansion parameter v/c are used. A key problem in relating post-Newtonian quantities to numerically constructed spacetimes are the different coordinate systems that are employed. For our numerical evolutions, we use the moving puncture approach [12, 17, 24, 25] with conformally flat Bowen-York initial data [26]. The coordinates used to construct the initial data for the numerical relativity simulations are close to the ADMTT coordinates [27] typically employed in the Hamiltonian approach to the post-Newtonian expansion. However, the standard puncture data we employ are consistent with the PN description in the ADMTT gauge only up to order $(v/c)^3$, see [28–30]. In [31] it is argued that as a consequence, only low order PN expressions should be used in constructing low-eccentricity initial data. However, since high-order PN expressions are routinely used in modelling the gravitational wave signal from compact binaries, and therefore readily available, in this work we take the point of view that it is simplest to just use the highest PN order available to guess the initial momenta in step two. In addition, we show that while a low PN order expression of the radial initial momentum is enough to build low eccentric initial data, the tangential momentum benefits from the knowledge of high PN orders, and the higher the PN order the closer to the low eccentric value.

The simplest post-Newtonian description of quasi-circular (QC) initial parameters is to set the radial momentum to zero, which is inconsistent with an actual inspiral (at least in the absence of precession). A straightforward way to improve the post-Newtonian description is to numerically solve the PN/Effective-One-Body (EOB) [32] dynamics from a larger separation down to the desired starting separation for a numerical relativity simulation, and to use the momenta read from this numerical calculation as input parameters to numerically solve the constraints [33]. This procedure benefits from the fact that radiation reaction circularizes the orbit during the long inspiral, and for a sufficiently long inspiral, the eccentricity present in the PN data can be neglected. This will not lead to negligible eccentricity of the NR evolution due to the finite order used for the PN expansion, and the difference in the PN and NR coordinate systems as discussed above. A second method [34] specifies the values of the initial momenta at a given separation using analytical expressions at 3PN derived from a Hamiltonian formalism, which approximately take into account the radial momentum. In this work we follow the second approach, since it simplifies the construction of precessing initial data with chosen directions of the spins at a given separation. When numerically integrating the PN equations from a larger distance, constructing low eccentricity momenta with fixed spin directions would require an iteration of numerical integrations of the PN equations, which complicates setting up a grid of NR simulations to cover (portions of) the precessing parameter space.

In Section II we discuss and compare these different approaches in more detail, and provide analytical formulas for the momenta in terms of initial separation, mass ratio and spins, including spin precession, updating the expressions presented in [34] to 3.5PN order. We also implement the post-post-circular (PPC) approximation [35, 36] commonly used in the Effective One Body (EOB) theory and provide a recipe to compute it. This approximation consists in correcting analytically for the tangential momenta by iterating over the post-circular (PC) approximation.

In Section III we develop the post-Newtonian methods to deal with steps four and five: we first discuss our procedure to determine the eccentricity of numerical data using the eccentricity estimator defined in equation (1.1). Then, from the 1PN Quasi-Keplerian parametrization [37] we compute explicit expressions for the correction factors for the tangential and radial momentum to achieve approximately vanishing eccentricity. Due to the deviations between the post-Newtonian equations and the full Einstein equations in the chosen gauge, as well as the noise that is present in numerical relativity simulations, this procedure may have to be iterated, although in many cases we find that a single step is sufficient for our purposes. Finally, we compute a similar formula that instead corrects the radial momentum and separation, thus directly compensating for the difference between the PN and NR coordinate systems.

We test our procedures in section IV, first applying them to post-Newtonian data, and check that the PPC approximation is indeed an excellent approximation to carry out full numerical solutions of the post-Newtonian inspiral. One practical application of such low-eccentricity post-Newtonian data is the construction of hybrid waveforms, where residual eccentricity in the post-Newtonian part leads to undesired oscillations [38]. Finally, we apply our procedures to several precessing and non-precessing numerical relativity simulations.

To date the most accurate procedures used to construct low eccentricity inspirals in numerical relativity are two iterative methods [39, 40]. The method consists in running first a simulation with quasi-circular (QC) parameters, modify the tangential and radial velocities of the simulation and rerun the simulation with the updated values. The iterative method in [39] is highly successful and can reduce eccentricities to below 10^{-5} in two iterations. Nevertheless, as discussed in [40] its application to moving puncture simulations shows some difficulties. The iterative method presented in [40] is designed for moving puncture simulation, but it is computationally expensive, and we have found it significantly more cumbersome than the method presented here .

We summarise and discuss our results in Sec. V.

Throughout this text we are working in geometric units $G = c = 1$. To simplify expressions we will also set the total mass of the system $M = 1$, and we define the mass ratio $q = m_2/m_1$ with the choice $m_2 > m_1$, so that $q > 1$. We also introduce the symmetric mass ratio $\eta = q/(1 + q)^2$, and we will denote the black hole's dimensionless spin vectors by $\vec{\chi}_i = \vec{S}_i/m_i^2$, for $i = 1, 2$.

II.   POST-NEWTONIAN INITIAL DATA

We prepare initial data for our simulations within PN theory in the Arnowitt-Deser-Misner transverse-traceless (ADMTT) gauge. We describe the particles in the center of mass (CM) frame, so that the motion of the two point particles can be described by the motion of one effective particle. We choose our z-axis in the direction of the initial orbital angular momentum, and initially locate the particles on the x-axis with $y = z = 0$, then $p_\phi = L_z$ with the standard definition of spherical polar coordinates. We define the tangential momentum as

$$p_t = \frac{p_\phi}{r}. \tag{2.1}$$

Using the standard relation between Cartesian and polar coordinates one can write (p_x, p_y) in terms of (p_ϕ, p_t) as

$$p_x = \frac{xp_r - yp_t}{\sqrt{x^2 + y^2}} = p_r\cos\phi - p_t\sin\phi, \tag{2.2}$$

$$p_y = \frac{xp_t + yp_r}{\sqrt{x^2 + y^2}} = p_r\sin\phi + p_t\cos\phi. \tag{2.3}$$

To compute the initial parameters we use the ADMTT Hamiltonian in the CM frame which is currently completely known up to 3.5PN order,

$$H = H_{NS} + H_{SO} + H_{SS} + H_{SSS}, \tag{2.4}$$

where H_{NS} is the non-spinning part of the Hamiltonian,

$$H_{NS} = H_{Newt} + H_{1PN} + H_{2PN} + H_{3PN}. \tag{2.5}$$

The Hamiltonians in equation (2.5) can be found in [41]. The spin-orbit Hamiltonian is

$$H_{SO} = H_{SO,1.5PN} + H_{SO,2.5PN} + H_{SO,3.5PN}. \tag{2.6}$$

The expression for $H_{SO,1.5PN}$, $H_{SO,2.5PN}$ and $H_{SO,3.5PN}$ can be found in [41], [42] and [43], respectively. The spin-spin interaction Hamiltonian is

$$H_{SS} = H_{S^2,2PN} + H_{S_1S_2,2PN} + H_{S^2,3PN} + H_{S_1S_2,3PN}, \tag{2.7}$$

where explicit formulas for $H_{S^2,2PN}$ and $H_{S_1S_2,2PN}$ can be found in [41] while for $H_{S^2,3PN}$, $H_{S_1S_2,3PN}$ in [44] and [45], respectively. Finally, H_{SSS} is given in [46].

A.   Post-circular approximation

Using the Hamiltonian of (2.4) one can compute the circular conditions for the orbit of the binary in absence of radiation reaction:

$$p_r = 0, \qquad \left(\frac{\partial H}{\partial r}\right)_{p_r=0} = 0. \tag{2.8}$$

Equation (2.8) gives a set of conditions to solve in PN order by order for $p_\phi(r)$. Once we have computed p_ϕ, or equivalently $p_t(r)$, we can then compute

$$\Omega = \left(\frac{\partial H}{\partial p_\phi}\right)_{p_r=0} \tag{2.9}$$

and obtain an expression for the orbital frequency as a function of r. For completeness, we can also obtain an expression for the ADM mass defined by

$$M_{ADM} = M + H, \tag{2.10}$$

where M is the total mass and H is the 3.5PN Hamiltonian in ADMTT gauge.

Taking into account equations (2.4), (2.8 - 2.10) we obtain explicit expressions for the orbital frequency, tangential momentum and ADM mass as a function of the orbital separation r. These expressions can be found in Appendix A and are given by equations (A1), (A2) and (A3). The expression for the initial tangential momentum in terms of the orbital separation, equation (A2), is obtained from the conservative part of the dynamics. It remains to specify a value for the radial component of the momentum vector, p_r. The inclusion of radiation reaction through the gravitational wave flux of energy allows us to derive an expression to compute p_r, following the procedure described in [41]. First, we consider the definition of the ADM mass given in (2.10) for circular orbits:

$$M_{ADM} = M + H_{circ}, \tag{2.11}$$

where H_{circ} is the energy corresponding to circular orbits, i.e., the Hamiltonian corresponding to equation (2.4) evaluated at the values of $p_r = 0$ and p_t derived in Appendix A. Taking a time derivative of (2.11) we get

$$\frac{dM_{ADM}}{dt} = \frac{dM}{dt} + \frac{dH_{circ}}{dt}. \tag{2.12}$$

The loss of ADM mass corresponds to a flux of gravitational wave energy leaving the binary, which has to be equal to the energy of the orbital motion plus the change in mass of the black holes. Consequently,

$$-\frac{dE_{GW}}{dt} = \frac{dM}{dt} + \frac{dH_{circ}}{dt}, \tag{2.13}$$

the derivative of the orbital energy can be rewritten as

$$\frac{dH_{circ}}{dt} = \left(\frac{dr}{dt}\right)\left(\frac{dH_{circ}}{dr}\right). \tag{2.14}$$

The expression for dM/dt was derived in [47] for the spin-aligned or anti-aligned with respect to the orbital angular momentum. We use that expression taking into account the contribution related to the change in mass of the two black holes because the leading order term of dM/dt is comparable in magnitude to a relative 2.5PN spin effect in the flux. The expression for the gravitational wave flux [23, 48] in terms of the basic dynamical variables in ADM coordinates for quasi-circular orbits can be found in Appendix A.

Then, we can use the Hamilton's equations to compute the time derivative of the orbital separation as

$$\frac{dr}{dt} = \frac{\partial H}{\partial p_r}. \tag{2.15}$$

If we expand the right hand side of equation (2.15) for p_r around 0, we can solve it for p_r and obtain a first order approximation to the radial momentum.

$$
p_r = \left[-\frac{dr}{dt} + \frac{1}{r^{7/2}} \left(-\frac{(6q+13)q^2\chi_{1x}\chi_{2y}}{4(q+1)^4} - \frac{(6q+1)q^2\chi_{2x}\chi_{2y}}{4(q+1)^4} + \chi_{1y}\left(-\frac{q(q+6)\chi_{1x}}{4(q+1)^4} - \frac{q(13q+6)\chi_{2x}}{4(q+1)^4} \right) \right) + \frac{1}{r^4}\left(\chi_{1z}\left(\frac{3q(5q+2)\chi_{1x}\chi_{2y}}{2(q+1)^4} \right. \right. \right.
$$
$$
\left. \left. \left. - \frac{3q^2(2q+5)\chi_{2x}\chi_{2y}}{2(q+1)^4} \right) + \chi_{1y}\chi_{2z}\left(\frac{3q^2(2q+5)\chi_{2x}}{2(q+1)^4} - \frac{3q(5q+2)\chi_{1x}}{2(q+1)^4} \right) \right) \right] \times \left[-\frac{(q+1)^2}{q} - \frac{1\left(-7q^2 - 15q - 7\right)}{2qr} \right.
$$
$$
- \frac{47q^4 + 229q^3 + 363q^2 + 229q + 47}{8q(q+1)^2 r^2} - \frac{1}{r^{5/2}}\left(\frac{\left(4q^2 + 11q + 12\right)\chi_{1z}}{4q(q+1)} + \frac{\left(12q^2 + 11q + 4\right)\chi_{2z}}{4(q+1)} \right)
$$
$$
- \frac{1}{r^{7/2}}\left(\frac{\left(-53q^5 - 357q^4 - 1097q^3 - 1486q^2 - 842q - 144\right)\chi_{1z}}{16q(q+1)^4} + \frac{\left(-144q^5 - 842q^4 - 1486q^3 - 1097q^2 - 357q - 53\right)\chi_{2z}}{16q(q+1)^4} \right)
$$
$$
- \frac{1}{r^3}\left(\frac{\left(q^2 + 9q + 9\right)\chi_{1x}^2}{2q(q+1)^2} + \frac{\left(3q^2 + 5q + 3\right)\chi_{2x}\chi_{1x}}{(q+1)^2} + \frac{\left(3q^2 + 8q + 3\right)\chi_{1y}\chi_{2y}}{2(q+1)^2} - \frac{9q^2\chi_{2y}^2}{4(q+1)} + \frac{\left(3q^2 + 8q + 3\right)\chi_{1z}\chi_{2z}}{2(q+1)^2} - \frac{9q^2\chi_{2z}^2}{4(q+1)} \right.
$$
$$
\left. + \frac{\left(9q^3 + 9q^2 + q\right)\chi_{2x}^2}{2(q+1)^2} + \frac{-363q^6 - 2608q^5 - 7324q^4 - 10161q^3 - 7324q^2 - 2608q - 363}{48q(q+1)^4} - \frac{9\chi_{1y}^2}{4q(q+1)} - \frac{9\chi_{1z}^2}{4q(q+1)} - \frac{\pi^2}{16} \right]^{-1}.
$$
$$\tag{2.16}$$

The expression for dr/dt can be computed combining equations (2.13) and (2.14):

$$\frac{dr}{dt} = \left[\frac{dE_{GW}}{dt} \right]\left[\frac{dH_{circ}}{dr} \right]^{-1}. \tag{2.17}$$

The procedure to obtain a post-circular expression for the radial momentum can be summarized in the following algorithm:

1) Compute the circular expression for $p_t(r)$.

2) Use the expression for $p_t(r)$ and $p_r = 0$ to compute dH_{circ}/dr.

3) Combine dH_{circ}/dr with the gravitational wave flux for the quasi-circular orbits, dE_{GW}/dt, to obtain dr/dt.

4) Use Hamilton's equations to compute $dr/dt = \partial H/\partial p_r$. Taylor expand at first order in p_r around $p_r = 0$ of the right hand side and isolate p_r as a function of dr/dt.

5) From step 4 compute an expression of p_r using the value of dr/dt calculated in step 3.

B. Post-post-circular approximation

The post-post circular approximation, first presented in [36], keeps the value of the tangential momentum p_t from the PC approximation, but applies a further correction to the radial momentum p_r, and has been extensively used to construct initial data for EOB dynamics. We start with the post-circular values for p_t and p_r derived in the previous Section II A and define a bookkeeping parameter ϵ to arrange the orders of approximation, writing the tangential and radial momenta as

$$p_t = p_t^0 + \epsilon^2 p_t^2 + O\left(\epsilon^4\right), \tag{2.18}$$

$$p_r = \epsilon p_r^1 + O\left(\epsilon^3\right). \tag{2.19}$$

Here p_t^0 is the circular approximation, p_r^1 is the post-circular approximation and p_t^2 is the post-post-circular value that we want to compute. The parameter ϵ is also related to the order of the radiation reaction terms of the ϕ coordinate in the PN equations of motion.

Hamilton's equation for the radial momentum reads

$$\frac{dp_r}{dt} = -\frac{\partial H}{\partial r}. \tag{2.20}$$

The left hand side of equation (2.20) can be approximated using the chain rule and the post-circular solution to

$$\frac{dp_r}{dt} = \frac{dp_r}{dr}\frac{dr}{dt} \approx \frac{dp_r^1}{dr}\frac{dr}{dt} = \frac{dp_r^1}{dr}\frac{\partial H}{\partial p_r}. \tag{2.21}$$

Then, combining equations (2.20) and (2.21) we obtain

$$-\left[\frac{\partial H}{\partial r} \right]_{p_r = p_r^1} \approx \left(\frac{dp_r^1}{dr} \right)\left[\frac{\partial H}{\partial p_r} \right]_{p_r = p_r^1}. \tag{2.22}$$

Given the values of the radial momentum p_r, the separation r, the masses of the particles m_1 and m_2 and the dimensionless spin vectors $\vec{\chi}$; one can solve equation (2.22) for p_t using a numerical root finding method.

III. ECCENTRICITY REDUCTION ITERATION

In order to reduce the eccentricity further beyond the post-circular or post-post-circular initial data, we will now develop two methods that iteratively reduce the eccentricity. The first method corrects the initial momenta by factors (λ_t, λ_r) such that $(p_t, p_r) \rightarrow (\lambda_t p_t, \lambda_r p_r)$, the second method corrects the initial separation by δr such that $r \rightarrow r + \delta r$, and the radial momentum p_r as for the first method. We will provide analytical expressions to compute the λ_t, λ_r and δr in terms of the measured eccentricity and an initial phase of the oscillations that characterize eccentricity, thus both methods are very straightforward to apply.

A. Quasi-Keplerian 1PN equations of motion

At 1PN order, bound orbits in the center of mass frame [37] are described by:

$$
\begin{aligned}
n_t(t - t_0) &= u - e_t \sin u, \\
(\phi - \phi_0) &= (1 + k)A_{e_\phi}(u), \\
A_{e_\phi}(u) &= 2 \arctan\left[\left(\frac{1 + e_\phi}{1 - e_\phi}\right)^{1/2} \tan\left(\frac{u}{2}\right)\right], \\
r &= a_r(1 - e_r \cos u).
\end{aligned} \quad (3.1)
$$

Where e_t, e_r and e_ϕ are the temporal, radial and angular eccentricities, n_t is called the mean anomaly, u is the true anomaly and k is the fractional periastron advance per orbit.

The frequency of the radial oscillations is directly related to the mean anomaly by

$$
n_t = \Omega_r = 2\pi/P_r, \quad (3.2)
$$

where P_r is the time between two consecutive periastron passages. The average orbital frequency can be related to the radial oscillations by the expression

$$
\Omega_\phi = (1 + k)\Omega_r. \quad (3.3)
$$

The orbital quantities can be written in terms of the reduced energy, $E_n = E/\mu$, and angular momentum, $h = J/\mu$, where E and $J = |\mathbf{J}|$ are the respective dimensionful quantities and $\mu = m_1 m_2/M$ is the reduced mass. Moreover, defining $\gamma = c^{-2}$ at 1PN order the orbital elements can be written as

$$
e_t^2 = 1 + 2E_n\left(\gamma E_n\left(\frac{17}{2} - \frac{7\eta}{2}\right) + 1\right)\left(h^2 + \gamma(2 - 2\eta)\right), \quad (3.4)
$$

$$
e_\phi^2 = 1 + 2E_n\left(\gamma E_n\left(\frac{\eta}{2} - \frac{15}{2}\right) + 1\right)\left(h^2 - 6\gamma\right), \quad (3.5)
$$

$$
e_r^2 = 1 + 2E_n\left(\gamma E_n\left(\frac{5\eta}{2} - \frac{15}{2}\right) + 1\right)\left(h^2 + \gamma(\eta - 6)\right), \quad (3.6)
$$

$$
a_r = -\frac{\left(1 - \frac{1}{2}\gamma E_n(\eta - 7)\right)}{2E_n}. \quad (3.7)
$$

$$
n_t = 2\sqrt{2}(-E_n)^{3/2}\left(1 - \gamma\frac{E_n}{4}(\eta - 15)\right). \quad (3.8)
$$

The eccentricities e_t, e_r and e_ϕ can be related to each other in terms of the fractional periastron advance,

$$
e_\phi = e_t\left[1 - \frac{1}{3}\left(1 - e_t^2\right)(\eta - 4)k\right], \quad (3.9)
$$

$$
e_r = e_t\left[1 + \frac{1}{6}\left(1 - e_t^2\right)(8 - 3\eta)k\right], \quad (3.10)
$$

where the fractional periastron advance k is defined as

$$
k = \frac{h}{\sqrt{h^2 - 6\gamma}} - 1. \quad (3.11)
$$

Combining equations (3.8) and (3.11) we can get a relation between the mean anomaly and the fractional periastron advance,

$$
k = 3\gamma\frac{n_t^{2/3}}{1 - e_t^2}. \quad (3.12)
$$

Note that this 1PN parametrization does not take into account the spins of the particles, which only enter at higher PN order.

B. Eccentricity measurement

The eccentricities e_t, e_r, e_ϕ introduced in (3.1) determine the amplitude of oscillations in the orbital quantities relative to the non-eccentric values. At Newtonian order the three eccentricities agree, but they differ in general, starting at 1PN. For general solutions, such as those obtained from numerical relativity, it is useful to define eccentricity estimators as time dependent functions which measure the relative deviation from the non-eccentric case, normalized to agree with the eccentricities e_t, e_r, e_ϕ at Newtonian order. For this work, for simplicity, we will only use the eccentricity estimator for the orbital frequency,

$$
e_\Omega = \frac{\Omega(t) - \Omega(e = 0)}{2\Omega(e = 0)}. \quad (3.13)
$$

Here $\Omega(t) = d\phi/dt$ can be obtained from the coordinate motion of the orbiting objects, and $\Omega(e = 0)$ refers to the orbital frequency setting the eccentricities to zero. For examples of using eccentricity estimators for other quantities, related to the orbital dynamics or gravitational wave signal, see [49], and for

a discussion of eccentricity estimators, in particular the differences between using the strain or Newman-Penrose scalar Ψ_4, see [40].

In this work, we choose an orbital quantity as our eccentricity estimator for simplicity and to save computational resources for numerical relativity simulations: Using wave quantities like the strain or ψ_4 require longer numerical evolutions to allow the waves to travel to the extraction sphere. Also, obtaining a clean wave signal for the first few orbits, where eccentricity reduction is typically applied, may require significant computational effort to carry out the simulations, or effort to post-process and de-noise the signal [40]. However, the methods developed in this paper can be easily reused together with other eccentricity estimators. Among quantities related to the orbital dynamics, the orbital frequency is convenient due to its weak gauge dependence, e.g. compared to the separation.

In the context of numerical data, obtained from a numerical relativity simulation or numerical evolution of the PN EOM, $\Omega(e = 0)$ could be represented by data from a simulation corresponding to negligible eccentricity (which is straightforward to achieve for PN solutions by starting at a very large separation), or be determined by a fit to the numerical data, $\Omega^0_{\text{fit}}(t)$, which does not contain oscillating terms corresponding to eccentricity (which is common practice in numerical relativity).

A simple way to fit the secular orbital frequency evolution as a function of time, averaging out oscillations due to eccentricity, coordinate gauge, or numerical artefacts, over a small number of cycles is to use a low-order polynomial of coordinate time, however such fits typically look pathological outside of the fitting interval, and are prone to pick up the oscillations due to eccentricity, gauge effects or spin evolution, when using too many terms in the attempt of creating an accurate fit. A natural ansatz which avoids these problems uses the orbital frequency evolution of a non-eccentric binary in the form of the TaylorT3 quasi-circular PN approximant [50, 51]. For the same reasons a similar fitting strategy has been used in [52]. There however, only two PN-like terms are used, with all coefficents determined by the fit. Here instead we use all known PN terms up to third PN order, and our ansatz A_0 for the quasicircular frequency evolution is

$$A_0 = \frac{a\,\theta^3}{8}\left(1 + b_1\theta^2 + b_2\theta^3 + b_3\theta^4 + b_4\theta^5 + b_5\theta^6\right), \quad (3.14)$$

where the known coefficients b_i as determined by PN theory are listed in Appendix B, θ is defined as

$$\theta = \left[\frac{\eta}{5}\,|t_{\text{max}}t_0 - t|\right]^{-1/8}, \quad (3.15)$$

and we fit two parameters, a and t_0. To accelerate the convergence of the fit, t_{max} is chosen of the order of the merger time of the numerical simulation, thus t_0 is of order unity. The parameter a would be unity in PN theory, and fitting it leads to an unphysical low frequency behaviour, which would be inappropriate for waveform modelling purposes. For our application however, we are only interested in the time scale corresponding to a numerical simulation, no inconsistency arises, and we

find that our choice of fitting parameters leads to robust and accurate fits.

Once we have obtained a non-eccentric fit to our numerical data, we can measure eccentricity by fitting the data using an extended ansatz A_e, which adds a sinusoidal function to the non-eccentric ansatz A_0,

$$A_e = A_0 + e(1 + |k_1|\,t)\cos\left[(1 + t\,|k_2|)\Omega_1\Omega_0 t + t_1\right]. \quad (3.16)$$

Here Ω_0 is the quasi-circular value given by equation (A1), and the coefficients to fit are a, t_0, e, Ω_1, k_1, k_2 and t_1. The coefficients k_1 and k_2 have been added to capture the decreasing eccentricity during the inspiral. In this work the fits have been performed using the function `NonlinearModelFit` from `Mathematica` with a global minimization method to avoid problems related to fitting the behaviour corresponding to local minima of the data. We have found the differential evolution method of the `NonlinearModelFit` function to result in particularly robust fits.

Furthermore, we have tested this procedure to measure the eccentricity of genuinely eccentric NR simulations, and we found accurate measurements up to eccentricities $e_t = 0.1$. For higher eccentricities the measurements are inaccurate due to the fact that the single harmonic function of the ansatz of equation (3.16) is not able to reproduce the high peak amplitudes in the orbital frequency. As a solution one should replace the single harmonic function in equation (3.16) by a sum of different harmonics in order to correctly capture the amplitude of those peaks. However, for the purposes of the present paper we found an ansatz with a single harmonic function sufficiently accurate, and we leave extensions of this measurement procedure to the high eccentricity limit for future work.

C. Tangential momentum correction from Quasi-Keplerian parametrization

In order to reduce the eccentricity resulting from the choice of initial momenta, we need to know how much the momentum changes from its quasi-circular value as a function of eccentricity. We can split the momentum into a tangential and radial part, and will first compute the dependence of the tangential momentum component on the orbital eccentricity e_Ω at 1PN order.

We start by using eq. (3.1) to compute e_Ω as a function of the eccentricities e_t and e_ϕ defined in eqs. (3.4) and (3.5),

$$e_\Omega = f\left(e_t, e_\phi\right). \quad (3.17)$$

From the equations of motion (3.1) it is straightforward to write at 1PN the radial coordinate, r, and the orbital frequency, $\Omega = \dot\phi$ up to linear order in eccentricity as:

$$r = a_r(1 - e_r\cos\left[\Omega_r t\right]), \quad (3.18)$$

$$\Omega \equiv \dot\phi = \Omega_\phi\left(1 + (e_\phi + e_t)\cos\left[\Omega_r t\right]\right). \quad (3.19)$$

Combining equations (3.19) and (3.13), we get the following expression for the orbital frequency estimator

$$e_\Omega = \frac{e_\phi + e_t}{2}. \quad (3.20)$$

We now proceed as follows:

a) In equation (3.20) write the eccentricities e_ϕ, e_t in terms of the energy and the angular momentum using the quasi-Keplerian solution of the compact binaries in eccentric orbits.

b) Write the eccentricities, energy and angular momentum in terms of the p_r and p_t using the Hamiltonian and the angular momentum expressions in ADM coordinates.

c) Multiply the momenta by the factors λ_t and λ_r.

d) Substitute the values of p_t and p_r by the circular ones.

e) Taylor expand equation (3.20) in powers of $(\lambda_t - 1)$ and $(\lambda_r - 1)$ up to linear order in $(\lambda_t - 1)$ and $(\lambda_r - 1)$.

f) Solve for λ_t, setting $\lambda_r = 1$.

Using the fact that the energy and the total angular momentum can be written in terms of the momenta p_t and p_r, and inserting that expressions into the definitions of equations (3.5) and (3.4) we get at 1PN order:

$$
e_t = \sqrt{\frac{\eta^4 + r p_t^2 \left[r\left(p_r^2 + p_t^2\right) - 2\eta^2\right]}{\eta^4}} + \gamma \left[\frac{\eta^4 + r p_t^2 \left(r\left(p_r^2 + p_t^2\right) - 2\eta^2\right)}{\eta^4}\right]^{-1/2} \times \left[-\frac{(\eta-4)r^2 p_t^6}{2\eta^6}\right.
$$
$$
-\frac{(\eta-4)r^2 p_r^4 p_t^2}{2\eta^6} + p_r^2 \left(\frac{1-\eta}{\eta^2} - \frac{(\eta-4)r^2 p_t^4}{\eta^6} + \frac{5(\eta-4)r p_t^2}{2\eta^4}\right) + \frac{(3\eta-10)r p_t^4}{\eta^4} + \frac{(20-9\eta)p_t^2}{2\eta^2}
$$
$$
\left.+\frac{2(\eta-1)}{r}\right],
\tag{3.21}
$$

$$
e_\phi = \sqrt{\frac{\eta^4 + r p_t^2 \left[r\left(p_r^2 + p_t^2\right) - 2\eta^2\right]}{\eta^4}} + \gamma \left[\frac{\eta^4 + r p_t^2 \left[r\left(p_r^2 + p_t^2\right) - 2\eta^2\right]}{\eta^4}\right]^{-1/2} \times \left[\frac{(\eta-4)r^2 p_t^6}{2\eta^6}+\right.
$$
$$
\frac{(\eta-4)r^2 p_r^4 p_t^2}{2\eta^6} + p_r^2 \left(-\frac{3}{\eta^2} + \frac{(\eta-4)r^2 p_t^4}{\eta^6} - \frac{3(\eta-4)r p_t^2}{2\eta^4}\right) - \frac{(\eta-6)r p_t^4}{\eta^4} + \frac{(\eta-20)p_t^2}{2\eta^2} + \frac{6}{r}\right].
\tag{3.22}
$$

Then, we make the substitutions

$$
p_t \to \lambda_t p_t, \qquad p_r \to \lambda_r p_r.
\tag{3.23}
$$

If we replace equations (3.21) and (3.22) into (3.20) and Taylor expand around $\lambda_t^0 = 1$ and use the circular value solutions of p_t and $p_r = 0$ we obtain at 1PN order:

$$
e_\Omega = 2(\lambda_t - 1) + \gamma(\lambda_t - 1)\left(\frac{2\eta}{r} + \frac{4}{r}\right).
\tag{3.24}
$$

We can invert equation (3.24) to obtain an expression for λ_t in terms of the eccentricity estimator

$$
\lambda_t = 1 + \frac{e_\Omega}{2} - \gamma\frac{e_\Omega}{2r}(\eta + 2).
\tag{3.25}
$$

Equation (3.25) directly relates the eccentricity of the simulation to the correction factor of p_t, at 1PN order, and linear in eccentricity, we can thus read off the momentum correction factor λ_t directly from the value of the measured eccentricity.

Although this equation has been derived in the low eccentricity limit, it can be used to generate approximate eccentric initial data for NR simulations. Given a configuration described by the masses of the particles, the spins, the initial linear momenta and the orbital separation, one can choose an initial eccentricity of the simulation and then obtain how

much one has to change the tangential momentum to generate that eccentric simulation.

The computation of λ_t in (3.25) solves the one parameter problem of correcting p_t to reduce the eccentricity. However, the reduction of the eccentricity is a two dimensional problem in the absence of precession. In the precessing case, eccentricity reduction is in principle a three-dimensional problem, however it appears that no correction to the small out-of-the orbital plane momentum is necessary at the current level of accuracy, so we restrict ourselves to a two-dimensional method. We have previously used a different two-dimensional method that uses PN information see [40], our new method is however significantly simpler to apply. There is a threshold of how much the eccentricity can be reduced correcting only p_t, which we find typically around 10^{-3} for the cases we consider. Hence, one needs not only to correct p_t, but also p_r if one wants to efficiently reduce the eccentricity, and we develop a two-parameter method in the next section.

D. Correcting both tangential and radial momenta from 1PN residuals

We will describe the relative oscillations in the orbital frequency by the ansatz

$$\mathcal{R}_\Omega = A + B\cos\left(\Omega_r t + \Psi\right), \qquad (3.26)$$

where Ω_r is the frequency of the radial oscillations, and A, B and Ψ are coefficients to be determined.

We will now derive explicit formulas in terms of the amplitude B and the phase Ψ of the ansatz (3.26) to rescale both the tangential momentum by λ_t, and the radial momentum by a factor λ_r, in order to reduce the eccentricity resulting from the choice of initial data. In order to do that we compute the residual of the orbital frequency, i.e., the difference between the configuration perturbing p_r and p_t and the unperturbed configuration with zero eccentricity. To our knowledge, the effects of perturbing such a residual were first studied in [40].

We will assume that the total residual is a linear combination of the residual, $\mathcal{R}_\Omega^{\lambda_t p_t^0}$, computed perturbing only p_t^0, the residual, $\mathcal{R}_\Omega^{\lambda_r p_r^0}$, calculated just perturbing p_r^0, and the residual, $\mathcal{R}_\Omega^{\lambda_t p_t^0, \lambda_r p_r^0}$, computed perturbing both momenta. In the rest of the section we are going to compute these three residuals and obtain from them analytical expressions for the correction factors (λ_t, λ_r).

We start writing the residual corresponding to a perturbation λ_t of the initial tangential momentum p_t^0,

$$\mathcal{R}_\Omega^{\lambda_t p_t^0} = \Omega^{\lambda_t p_t^0} - \Omega^{p_t^0}. \qquad (3.27)$$

In equation (3.27), $\Omega \equiv \Omega(t)$ refers to equation (3.19), the analytical 1PN solution at linear order in eccentricity. The magnitude of the eccentricities we are working with, usually well below 10^{-2}, justifies to take just the linear order in eccentricity in the equations of motion.

Note that Ω_ϕ in equation (3.19) also depends on p_t. Therefore, we begin computing the effect of perturbing p_t in Ω_ϕ. Combining equations (3.12), (3.2) and (3.3) we obtain the following expression

$$\Omega_\phi = \left(1 + 3\gamma\frac{n_t^{2/3}}{1 - e_t^2}\right)n_t. \qquad (3.28)$$

We can now use equations (3.4) and (3.8) to write Ω_ϕ in terms of the energy and the angular momentum, which at the same time can be written in terms of the radial and tangential momenta. Then, we perturb the tangential momentum a factor λ_t and we Taylor expand up to linear order in λ_t around $\lambda_t^0 = 1$. As a result we obtain

$$\Omega_\phi^{\lambda_t} = \gamma\left(\frac{(-5\eta - 9)\lambda_t}{2r_0^{5/2}} + \frac{6\eta + 6}{2r_0^{5/2}}\right) - \frac{3\lambda_t}{r_0^{3/2}} + \frac{4}{r_0^{3/2}}. \qquad (3.29)$$

Defining $\Omega_0 = r_0^{-3/2}$ as the Newtonian-like orbital frequency we can rewrite (3.29) as

$$\Omega_\phi^{\lambda_t} = \gamma\Omega_0\left(\frac{3(\eta + 1)}{r_0} - \frac{(5\eta + 9)\lambda_t}{2r_0}\right) + \Omega_0\left(4 - 3\lambda_t\right). \qquad (3.30)$$

For the expression of the unperturbed Ω_ϕ we will use the analytical circular solution, equation (A1), which coincides with the unperturbed expression of the orbital frequency Ω, assuming p_t^0 and p_r^0 are given by the circular values,

$$\Omega_\phi^0 = \Omega^{p_t^0} = \Omega_0\left[1 + \frac{\gamma(\eta - 3)}{2r_0}\right]. \qquad (3.31)$$

The perturbed configuration is calculated replacing (3.30) in (3.19) to obtain

$$\begin{aligned}
\Omega^{\lambda_t p_t^0} = {}& \Omega_0\left[1 + (\lambda_t - 1)\left(4\cos(\Omega_r t) - 3\right)\right] + \gamma\Omega_0\left[\frac{(\eta - 3)}{2r_0}\right.\\
& + (\lambda_t - 1)\left(\frac{(6\eta + 2)\cos(\Omega_r t)}{r_0} - \frac{5\eta + 9}{2r_0}\right)\right]\\
& + O\left((\lambda_t - 1)^2\right).
\end{aligned}$$

$$(3.32)$$

Replacing equations (3.31) and (3.32) in equation (3.27), we finally obtain

$$\begin{aligned}
\mathcal{R}_\Omega^{\lambda_t p_t^0} = {}& \Omega_0\left(\lambda_t - 1\right)\left(4\cos(\Omega_r t) - 3\right)\\
& + \frac{\gamma\Omega_0\left(\lambda_t - 1\right)\left(4(3\eta + 1)\cos(\Omega_r t) - 5\eta - 9\right)}{2r_0}\\
& + O\left((\lambda_t - 1)^2\right).
\end{aligned} \qquad (3.33)$$

We can follow the same procedure to obtain the residual corresponding to just perturbing p_r^0. We will expand now in powers of $(\lambda_r - 1)$ and we will maintain p_r^0 in the expressions for a better comparison with the formulas of [40]. In practical computations, p_r^0 will be replaced by its post-circular value. Note that in the following derivation of the residual, Ω_ϕ does not depend on p_r. Another important fact is that equations (3.1) assume that the motion starts at the periastron, $\phi_0 = 0$, this condition combined with the negative value of p_r^0 that the post-circular approximation yields, causes a shift of the periastron by $\pi/2$. Consequently, the radial perturbations will be dominated by a sine mode [40].

As in equation (3.27) we can write the residual as

$$\mathcal{R}_\Omega^{\lambda_r p_r^0} = \Omega_0^{\lambda_r p_r^0} - \Omega_0^{p_t^0, p_r^0}. \qquad (3.34)$$

In equation (3.34), $\Omega_0^{p_r^0}$ is given by the unperturbed configuration assuming a non-zero value of p_r^0.

The calculations to obtain $\Omega_0^{p_t^0, p_r^0}$ are the following:

1) Write e_t and e_ϕ in equation (3.19) in terms of E_n and h.

2) Write E_n and h in terms of p_t^0 and p_r^0.

3) Substitute the value of p_t^0 by equation (A2).

The result of applying steps $1) - 3)$ is

$$\Omega_0^{p_t^0, p_r^0} = \Omega_0\left(1 - \frac{2r_0^{1/2}\left|p_r^0\right|}{\eta}\sin(\Omega_r t)\right) + \gamma\frac{2\Omega_0\left|p_r^0\right|}{\eta r_0^{1/2}}\sin(\Omega_r t). \qquad (3.35)$$

The recipe to obtain the perturbed configuration is quite similar with some additional steps:

a) Write e_t and e_ϕ in equation (3.19) in terms of E_n and h.

b) Write E_n and h in terms of p_t^0 and $\lambda_r p_r^0$.

c) Substitute the value of p_t^0 by equation (A2).

d) Taylor expand up to linear order in $(\lambda_r - 1)$.

As a result of performing steps a) – d) we obtain

$$\Omega_0^{\lambda_r p_r^0} = \Omega_0 + \gamma \frac{2\Omega_0 \lambda_r \sin(\Omega_r t)\left|p_r^0\right|}{\eta r_0^{1/2}} - \frac{2r_0^{1/2}\Omega_0 \lambda_r \sin(\Omega_r t)\left|p_r^0\right|}{\eta}$$
$$+ O\left((\lambda_r - 1)^2\right). \tag{3.36}$$

Combining equations (3.35) and (3.36) we now get

$$\mathcal{R}_\Omega^{\lambda_r p_r^0} = \frac{2\Omega_0 \left|p_r^0\right|}{\eta}\left(r_0^{1/2} - \gamma r_0^{-1/2}\right)(\lambda_r - 1)\sin(\Omega_r t) \tag{3.37}$$
$$+ O\left((\lambda_r - 1)^2\right).$$

The next step of the calculation is computing the residual produced by the simultaneous perturbation of p_t^0 and p_r^0. The procedure to follow is quite similar to the algorithms presented so far. The residual we want to calculate is

$$\mathcal{R}_\Omega^{\lambda_t p_t^0, \lambda_r p_r^0} = \Omega_0^{\lambda_t p_t^0, \lambda_r p_r^0} - \Omega_0^{p_t^0, p_r^0}, \tag{3.38}$$

where $\Omega_0^{p_t^0, p_r^0}$ is given by equation (3.35). The procedure we follow to compute the residual is summarized as:

A) Write e_t and e_ϕ in equation (3.19) in terms of E_n and h.

B) Write E_n and h in terms of $\lambda_t p_t^0$ and $\lambda_r p_r^0$.

C) Substitute the value of p_t^0 by equation (A2) and maintain the value of p_r^0.

D) Taylor expand up to linear order in $(\lambda_t - 1)$ and $(\lambda_r - 1)$.

After following steps A) – D) we obtain

$$\Omega_0^{\lambda_t p_t^0, \lambda_r p_r^0} = \Omega_0 + \frac{2\sqrt{r_0}\Omega_0 \lambda_r \lambda_t \left|p_r^0\right|}{\eta}\sin(\Omega_r t) + \gamma \frac{2\Omega_0 \lambda_r \left|p_r^0\right|}{\eta r_0^{1/2}}\left[(\eta\right.$$
$$\left.+1)\lambda_t - (\eta + 2)\right]\sin(\Omega_r t) + O\left((\lambda_r - 1)^2\right)$$
$$+ O\left((\lambda_t - 1)^2\right) + O\left((\lambda_t \lambda_r)^2\right). \tag{3.39}$$

Inserting equations (3.35) and (3.39) into (3.38) gives

$$\mathcal{R}_\Omega^{\lambda_t p_t^0, \lambda_r p_r^0} = \frac{2r_0^{1/2}\Omega_0}{\eta}\sin(\Omega_r t)\left|p_r^0\right|(\lambda_r \lambda_t - 1)$$
$$+ \gamma \frac{2\Omega_0}{\eta r_0^{1/2}}\sin(\Omega_r t)\left|p_r^0\right|\left[\lambda_r\left(\eta\left(\lambda_t - 1\right) + \lambda_t - 2\right) + 1\right]. \tag{3.40}$$

Finally, the total residual at 1PN can be understood as the sum of (3.33), (3.37) and (3.40), this is

$$\mathcal{R}_\Omega^{1PN} = \mathcal{R}_\Omega^{\lambda_t p_t^0} + \mathcal{R}_\Omega^{\lambda_r p_r^0} + \mathcal{R}_\Omega^{\lambda_t p_t^0, \lambda_r p_r^0}$$
$$= -3\Omega_0\left(\lambda_t - 1\right) - \frac{\gamma(5\eta + 9)\Omega_0\left(\lambda_t - 1\right)}{2r_0} + \sin(\Omega_r t)2\Omega_0$$
$$\times \left|p_r^0\right|\left[\frac{\sqrt{r_0}(\lambda_r - 1)}{\eta} + \gamma\left(\frac{(\lambda_r(\eta(\lambda_t - 1) + \lambda_t - 2) + 1}{\eta\sqrt{r_0}}\right.\right.$$
$$\left.-\frac{(\lambda_r - 1)}{\eta\sqrt{r_0}}\right) + \sqrt{r_0}\frac{(\lambda_r \lambda_t - 1)}{\eta}\right] + \cos(\Omega_r t)\left[4\Omega_0\left(\lambda_t - 1\right)\right.$$
$$\left.+\gamma\left(\frac{6\eta\Omega_0\left(\lambda_t - 1\right)}{r_0} + \frac{2\Omega_0\left(\lambda_t - 1\right)}{r_0}\right)\right]. \tag{3.41}$$

Once we have derived the expression (3.41) for the residual, we want to compare it to (3.26) in order to obtain expressions of λ_t and λ_r in terms of the amplitude and the phase of the residual. We do not take into account the offset terms because the 1PN order is not accurate enough to described the full PN dynamics and even less the dynamics of the full Einstein equations dynamics of a NR simulation.

The total residual, equation (3.41), is a sum of sine and cosine terms that we want to express as a single cosine plus a phase as in equation (3.26). The result of such a transformation gives two expressions for the amplitude B and the phase C in terms of λ_t and λ_r:

$$B = \left[a_1^2 + a_2^2\right]^{1/2}, \tag{3.42}$$

$$\Psi = \arctan\left(a_1/a_2\right), \tag{3.43}$$

where a_1 and a_2 are given by,

$$a_1 = 4\Omega_0\left(\lambda_t - 1\right) + \frac{2\gamma(3\eta + 1)\Omega_0\left(\lambda_t - 1\right)}{r_0}, \tag{3.44}$$

$$a_2 = \frac{2\sqrt{r_0}\Omega_0\left(\lambda_r - 1\right)\left|p_r^0\right|}{\eta} + \gamma\frac{2\Omega_0\left|p_r^0\right|}{r_0^{1/2}\eta}\left[\lambda_r\left(\eta\left(\lambda_t - 1\right) + \lambda_t\right.\right.$$
$$\left.\left.-2\right) + 1 - (\lambda_r - 1)\right] + \frac{2\Omega_0\left|p_r^0\right|(\lambda_r \lambda_t - 1)}{\eta r_0^{-1/2}}. \tag{3.45}$$

The solution of the equations (3.44) and (3.45) consistently at 1PN order for λ_r and λ_t provides the formulas

$$\lambda_t = 1 + \left[\frac{B}{4\Omega_0} - \gamma\frac{B(3\eta + 1)}{8r_0\Omega_0}\right]\cos\Psi, \tag{3.46}$$

$$\lambda_r = 1 + \frac{B\eta}{2r_0^{1/2}\Omega_0\left|p_r^0\right|}\left[1 + \gamma\frac{1}{r_0}\right]\sin\Psi. \tag{3.47}$$

Equations (3.46) and (3.47) can be used to compute the corrections of the momenta from a measured eccentricity oscillation amplitude B and phase shift Ψ. The accuracy of the procedure is limited by carrying out the computations at 1PN order, but more importantly by the noise in numerical relativity data, due to both numerical and gauge artefacts.

E.   Separation correction from 1PN Residual

We will now develop an alternative method of eccentricity reduction, where we replace the correction of the tangential momentum with a correction of the coordinate separation where the NR momentum is identified with the PN momentum. This is motivated by the fact that the PN and NR coordinates for the initial data only agree to 2PN order [28–30], and we will again calculate the required correction to the initial orbital separation of the binary at 1PN order.

We compute the residual coming from the variation δr of the initial separation given by

$$\mathcal{R}_\Omega^{\delta r + r_0} = \Omega_0^{r_0 + \delta r} - \Omega_0^{r_0}. \qquad (3.48)$$

In equation (3.48), $\Omega_0^{r_0}$ is the unperturbed configuration, which is computed assuming that p_t^0 and p_r^0 take the circular values. We obtain

$$\Omega_0^{r_0} = \Omega_0 \left[1 + \gamma \frac{(\eta - 3)}{2r_0} \right], \qquad (3.49)$$

where $\Omega_0 = r_0^{-3/2}$ is the Newtonian-like orbital frequency. To compute the perturbed term, we need to calculate first the effect of perturbing the initial separation in Ω_ϕ. The calculation is similar to the one performed in section III D. We make the replacement

$$r_0 \to r_0 + \delta r, \qquad (3.50)$$

and expand in Taylor Series around $\delta r = 0$ up to linear order in δr. As a result we obtain

$$\Omega_\phi^{r_0 + \delta r} = \Omega_0 \left[1 - \frac{3\delta r}{2r_0} - \gamma \frac{(\eta - 3)(5\delta r - 2r_0)}{4r_0^2} \right]. \qquad (3.51)$$

Then, for the perturbed configuration we obtain

$$\Omega_0^{\delta r + r_0} = \Omega_0 \left[1 + \frac{\delta r}{r_0} \left(2\cos(\Omega_r t) - \frac{3}{2} \right) + \gamma \left(\frac{\eta - 3}{2r_0} \right. \right.$$
$$\left. \left. + \frac{\delta r}{4r_0^2} \left[12(\eta + 3)\cos(\Omega_r t) - 5(\eta - 3) \right] \right) \right]. \qquad (3.52)$$

Inserting equations (3.49) and (3.52) into (3.48) we get

$$\mathcal{R}_\Omega^{\delta r + r_0} = \frac{\delta r \Omega_0}{r_0} \left[-\frac{3}{2} + 2\cos(t\Omega_r) + \frac{\gamma}{r_0} \left(-\frac{5(\eta - 3)}{4} \right. \right.$$
$$\left. \left. + 3(\eta + 3)\cos(t\Omega_r) \right) \right]. \qquad (3.53)$$

As in the previous section III D, equation (3.53) can be written as a generic cosine function with an offset, an amplitude and a phase of the form

$$\mathcal{R} = M + N\cos(\Omega_r t + \chi). \qquad (3.54)$$

Again, the amplitude N and the phase χ can be expressed by the equations

$$N = \left[b_1^2 + b_2^2 \right]^{1/2}, \qquad \chi = \arctan(b_1/b_2), \qquad (3.55)$$

where b_1 and b_2 are given by,

$$b_1 = \frac{Nr_0}{2\Omega_0} - \frac{3N\gamma\left(3q^2 + 7q + 3\right)}{4(q + 1)^2\Omega_0}, \qquad b_2 = 0. \qquad (3.56)$$

Consistent with the fact that for the separation we have performed a one-parameter analysis toward reducing the eccentricity, we have obtained the result that the phase does not provide information and the whole information is encoded in the amplitude of the residual. Solving equations (3.55) and (3.56) consistently at 1PN order gives

$$\delta r = \frac{Nr_0}{2\Omega_0} - \gamma \frac{3N\left(3q^2 + 7q + 3\right)}{4(q + 1)^2\Omega_0} \qquad (3.57)$$

Equation (3.57) provides an expression to compute a correction to the initial separation of the binary. Note that the application of the separation correction and the tangential momentum correction are degenerate because both describe the conservative dynamics of the binary. We could now perform a full two-parameter analysis combining radial separation and radial momentum, in analogy to Sec. III D, but instead we note that we can also extend Eq. (3.57) to a 2-dimensional iterative scheme by combining the correction for the separation with the correction for the radial momentum derived previously, Eq. (3.47), and we will use this 2-dimensional prescription for successful eccentricity reduction in an example case in Section IV B.

IV.   ECCENTRICITY REDUCTION FOR NUMERICAL DATA

In this section we apply the analytical formulae we have previously derived (3.46), (3.47) and (3.57), relating amplitude and phase of time dependent eccentricity estimators to corrections of the momenta or radial separation, to numerical data obtained from NR simulations, or, as a test case, to numerical post-Newtonian data. We compute the orbital frequency Ω from the position vector $\vec{r}$ in the center of mass frame, with $r = |\vec{r}|$, and its time derivative $\vec{v}$ as

$$\Omega = |\vec{\Omega}| = \frac{|\vec{r} \times \vec{v}|}{r^2}, \qquad (4.1)$$

In the PN simulations $\vec{r}$ and $\vec{v}$ are computed from the motion of the point-particles, whereas in the NR simulations they are computed from the coordinate positions of the punctures. Our NR setup is described in Appendix C. For the NR simulations we use two codes, `BAM` [17, 53] and the `EinsteinToolkit` [54], which implement a discretized version of the BSSN [55, 56] formulation of the Einstein equations. Both codes use the moving puncture approach [12, 17, 24, 25] with the "1 + log" slicing and the Γ-driver shift condition [57]. The initial conditions for the evolving coordinate conditions (i.e. for the lapse and shift), in particular the choice of vanishing shift, lead to gauge transients, which manifest themselves as decaying oscillations in the orbital frequency and separation. As

discussed in detail in [40] for one binary black hole config-
uration, these gauge transients complicate reading off the ec-
centricity, but can be suppressed by choosing a sufficiently
small value of the Γ-driver "damping" parameter η (not to be
confused with the symmetric mass ratio used in Secs. II and
III), such as $\eta = 0.25$. The parameter η does in fact have
the dimension of inverse mass, and one might expect that for
larger mass ratios, a smaller value of $\eta = 0.25$ is required to
avoid large gauge transients. However, for larger mass ratios
gauge transients turn out to be damped out faster in general,
possibly related to the faster time scale of the smaller black
hole, and in our study we find that the choice $\eta = 0.25$ indeed
works well for all the simulations we have performed.

We will first apply eccentricity reduction to PN data as a
test case, and then apply our methods to different numerical
relativity data sets, with and without precession. As expected,
we will find that in PN the PPC prescription for initial data
leads to smaller eccentricities than the PC prescription, with
the lowest eccentricities obtained with a PN integration start-
ing at a sufficiently large separation [33]. For NR simulations
we will, however, find that PC initial data typically lead to
lower eccentricity than the PPC approximation. We also find
that for the cases we have studied, a single iteration of our
eccentricity reduction procedure is sufficient to obtain an ec-
centricity below 10^{-3}.

A.   PN example

The dynamics of PN particles can be described using
Hamilton's equations of motion,

$$\frac{d\mathbf{X}}{dt} = \frac{\partial H}{\partial \mathbf{P}}, \qquad \frac{d\mathbf{P}}{dt} = -\frac{\partial H}{\partial \mathbf{X}} + \mathbf{F}. \qquad (4.2)$$

with $\mathbf{X}$ and $\mathbf{P}$ the position and the momentum vectors, respec-
tively, in the CM frame, H the Hamiltonian given by equation
(2.4) and $\mathbf{F}$ is the radiation reaction force given by equation
(3.27) in [41]. The equation of motion for the i-th spin is

$$\frac{d\mathbf{S}_i}{dt} = \frac{\partial H}{\partial \mathbf{S}_i} \times \mathbf{S}_i. \qquad (4.3)$$

The solution of such a system of equations describes the mo-
tion of a binary point-particle system in the inspiral regime.
In this section we discuss our method to reduce eccentricity in
PN, where the low computational cost of numerical solutions
and the avoidance of the initial gauge transients present in NR
greatly simplify the analysis.

To illustrate the procedure with an example black hole con-
figuration, we choose mass ratio 4, which is significantly dif-
ferent from unity, and large spins with dimensionless Kerr
paramaters $\vec{\chi}_1 = (0., 0., 0.8)$ and $\vec{\chi}_2 = (0., 0., -0.8)$ at an ini-
tial separation $D_i = 12M$, where M is the total mass of the
binary system. We integrate the PN equations of motion until
a minimal separation $D_f = 6M$. We run two PN simulations,
with initial momenta computed with the post-circular (PC),
and alternatively the post-post-circular (PPC) approximation.

For both simulations we measure the eccentricity using a fit
to the ansatz (3.16), and apply two iterations employing the

correction factors for the tangential and radial momenta given
by equations (3.46) and (3.47). The corresponding eccentric-
ity time evolution of the eccentricity estimators for each iter-
ation are plotted in Figure 1, which shows that the post-post-
circular approximation indeed produces a simulation with a
smaller eccentricity than the post-circular approximation, as
one would expect. Moreover, in Figure 1 we have added the
result of initialising the momenta at $D_i = 12M$ from another
PN evolution starting at a larger initial separation $D_0 = 30M$
with PC initial momenta, which we have integrated to a sep-
aration of $D_i = 12M$. In this case the eccentricity is much
smaller, $e_\Omega = (5 \pm 2) \cdot 10^{-5}$, due to some initial eccentricity be-
ing radiated away during inspiral before reaching $D_i = 12M$,
and to the high accuracy of PC momenta at $D = 30M$.
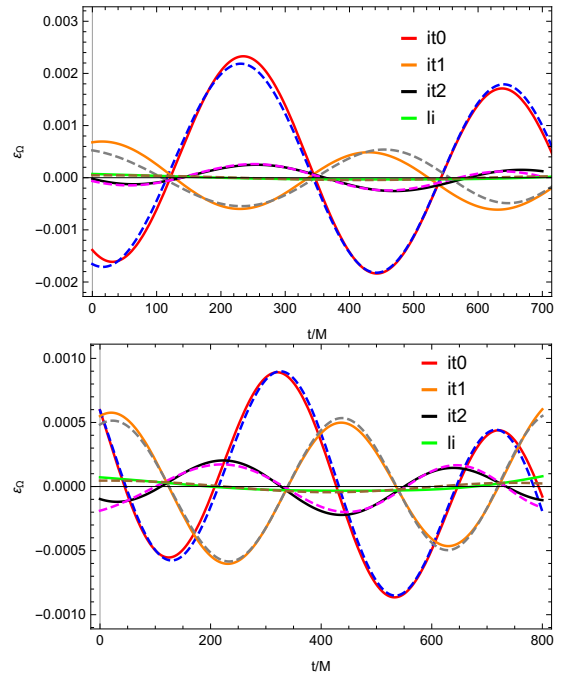
Figure 1: Eccentricity reduction iterations for the configuration $q = 4$, $\chi_{1z} = 0.8$, $\chi_{2z} = -0.8$. The upper panel shows the time evolu-
tion of e_Ω specifying PC momenta at iteration 0 (red curve) and the
lower panel shows the same quantity specifying PPC momenta at it-
eration 0. Afterwards, two more iterations are performed (orange and
black curves). The continuous curves correspond to the data, and the
dashed ones to the fits for each iteration (blue, gray, magenta, brown).
Additionally the result of integrating from a longer separation (li) is
shown in each panel.

The eccentricity measurement yields a time dependent re-
sult corresponding to the choice of the ansatz (3.16). For ex-
ample, for iteration 0 in the post-circular approximation, one
obtains the following expressions for the eccentricity and the
amplitude,

$$\varepsilon_\Omega = 0.00197344 - 1.97129 \cdot 10^{-7}t, \qquad (4.4)$$

$$A = 0.00008561 - 8.55168 \cdot 10^{-9}t. \qquad (4.5)$$

However, as in this case the time dependent terms are typically very small and can be neglected, and we simply use the eccentricity values at $t = 0$.

The values of the eccentricity and the different correction factors are shown in Table I. In addition, Table I contains the values of eccentricity and the corresponding correction factors when one corrects not only the momenta, but also the radial momenta and the distance of the binary. Consistent with Fig. 1 we see that PPC initial data produce lower eccentricity than PC for the first iteration. The final eccentricities after 2 iterations are however very similar, although the ratio of efficiency gets worse in each iteration due to the fact that a highly accurate measurement of the amplitude and the phase of the residual is required. One observes that the method can easily obtain eccentricities of the order $2 \cdot 10^{-4}$ for a case with a relatively high mass ratio and high spins, and that one can equally well choose to correct the tangential and radial momenta or the orbital separation and the radial momentum.

Post-Circular correcting for (λ_t, λ_r)				
Iteration	$(\varepsilon_\Omega \pm \delta\varepsilon_\Omega) \cdot 10^{-3}$	$10 \cdot p_t$	$p_r \cdot 10^3$	λ_t	λ_r
0	1.973 ± 0.006	0.56477	0.238712	1.00085	1.19247
1	0.561 ± 0.015	0.56529	0.284657	0.99974	0.94794
2	0.221 ± 0.007	0.56516	0.271206		
Post-Post-Circular correcting for (λ_t, λ_r)				
Iteration	$(\varepsilon_\Omega \pm \delta\varepsilon_\Omega) \cdot 10^{-3}$	$10 \cdot p_t$	$p_r \cdot 10^3$	λ_t	λ_r
0	0.833 ± 0.005	0.56517	0.238712	1.00013	1.19737
1	0.567 ± 0.003	0.56525	0.285827	0.99974	0.96201
2	0.197 ± 0.005	0.56510	0.274971		
Post-Circular correcting for $(\delta r, \lambda_r)$				
Iteration	$(\varepsilon_\Omega \pm \delta\varepsilon_\Omega) \cdot 10^{-3}$	D	$p_r \cdot 10^3$	δr	λ_r
0	1.973 ± 0.006	12.0	0.238712	0.01432	1.19247
1	0.718 ± 0.004	12.0143	0.284657	0.00445	0.999083
2	0.230 ± 0.003	12.0099	0.284396		

Table I: Eccentricity estimator and its corresponding statistical error for the configuration $q = 4$, $\chi_{1z} = 0.8$, $\chi_{2z} = -0.8$.

We have also tested our eccentricity reduction method in the PN description of precessing binaries, with similar results: even for high spins we can obtain eccentricities of the order of 10^{-4} in one or two iterations. In the precessing case the method of integrating from a longer separation still yields lower eccentricities, but it does not provide control of the initial spin components of the binary at separation D_i due to the fact that the spins also evolve in time during the integration. Controlling the spins at D_i would require to set up another iteration procedure to define the spins at the larger "auxiliary separation" ($D = 30M$ in our example) in terms of the desired spins at D_i. Specifying the initial data using the PC or PPC prescription can significantly simplify setting up parameter studies where control of the spin configurations is desired at D_i. As we will see below, this argument is even stronger in NR, where due to the deviations between PN and full GR there is no significant advantage in integrating from a large

initial separation as compared with PC or PPC data.

B. Numerical relativity examples

Applying our eccentricity reduction procedure to numerical relativity simulations adds several complications compared with the post-Newtonian example: Apart form the increase in computational cost by 6-7 orders of magnitude, the main technical problem are gauge transients resulting from the procedure of initialising the coordinate conditions of the moving puncture evolutions (in particular the initially vanishing velocity of the punctures). We address this problem by using a small value of the shift parameter η, of $\eta = 0.25$, for the evolutions we report on below, and by cutting away the first $\sim 200M$ of time evolution. Black-hole binary puncture initial data also exhibit a burst of junk radiation due to unphysical gravitational wave content in the initial data. Here we do not take into account the resulting small change to initial masses, spins, and momenta, although this may be beneficial when attempting to construct initial data with even lower eccentricities. For the cases we have studied so far, our choice of $\eta = 0.25$, together with the robust setup of our fitting method to determine eccentricity presented in Sec. IV, provides sufficiently accurate estimates not only of the eccentricity, but also of the phase shift defined in Eq. (3.26), which is required to determine the change in radial momentum or separation to implement a 2-parameter eccentricity reduction algorithm.

We first discuss our procedure for the example of a precessing binary with mass ratio $q = 2$ and dimensionless spin vectors $\vec{\chi}_1 = (0, 0, 0)$, $\vec{\chi}_2 = (0.3535, 0.3535, 0.5)$, and initial orbital separation $D = 10.8M$. First, we run a simulation with PC initial data with BAM at low resolution with $N = 64$ points to measure the eccentricity, fitting the oscillations of Ω computed using eq. (4.1). Then, we adjust the values of the tangential and radial momenta according to eqs. (3.46) and (3.47) to reduce eccentricity, and we run two low resolution simulations with the corrected momenta, one with BAM another with ET with the same numerical resolution and gauge conditions. The results for the time evolution of the eccentricity estimator for the three simulations are shown in Figure 2.

After one iteration the eccentricity has been notably reduced with both codes. The values of eccentricity for iteration 1 in both codes is quite similar. However, the ET residual is cleaner than for the BAM evolution, which contains more high frequency noise which we attribute to different settings for numerical dissipation in this simulation, and which complicates the measurement of the phase and the amplitude of the residual and leads to different results in iteration 1. The sign of the correction to the tangential momentum is read from the value of the residual at the initial time of the evolution, according to the expression for the residual computed in Section III: For positive residual, as is the case in iteration 0, the momentum has to be decreased; while for negative residual the momenta should be increased. The values of the eccentricity as well as the correction factors used are shown in Table II. After a single iteration the eccentricity is well below 10^{-3},
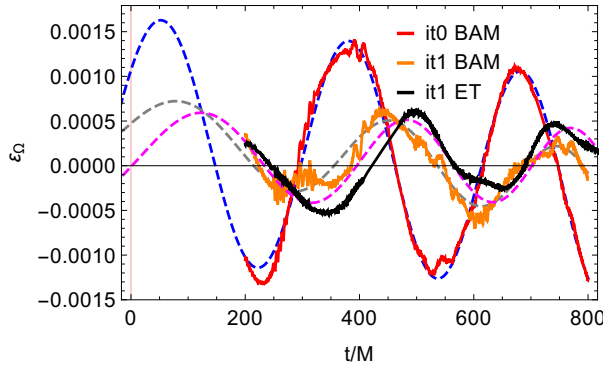
Figure 2: Time evolution of the eccentricity estimator for the configuration $q = 2$, $\vec{\chi}_1 = (0,0,0)$, $\vec{\chi}_2 = (0.3535, 0.3535, 0.5)$ and $D = 10.8M$. The thick curves corresponds to the data and the dashed ones to the fits. For the three simulations we have discarded the initial $t = 200M$ of evolution time.

which we have considered sufficient to neglect eccentricity in our waveform modelling applications, and we have not carried out further iterations. For completeness we also show in Figure 3 the time evolution of the orbital separation and the orbital frequency of that configuration. One can observe from the plots that the oscillations remaining after one iteration of the eccentricity reduction procedure cannot be appreciated on that scale of the plot any more.

Iteration	Code	$(\varepsilon_\Omega \pm \delta\varepsilon_\Omega) \cdot 10^{-3}$	λ_t	λ_r
0	BAM	1.37 ± 0.02	0.9996	0.8456
1	BAM	0.48 ± 0.02		
1	ET	0.51 ± 0.03		

Table II: Eccentricity estimator and its corresponding statistical error for the configuration $q = 2$, $\vec{\chi}_1 = (0,0,0)$, $\vec{\chi}_2 = (0.3535, 0.3535, 0.5)$ and $D = 10.8M$.

In a second example we apply the correction of the separation and radial momentum to a NR simulation, combining the corrections in the radial momentum and the initial orbital separation,

$$p_r^1 = \lambda_r p_r^0, \qquad r_0^1 = r_0^0 + \delta r. \qquad (4.6)$$

We choose the spin-aligned configuration ID13 of Table V, i.e., $q = 1$, $\chi_{1z} = -0.5$, $\chi_{2z} = 0.5$ with $D = 11M$. The results of applying the eccentricity reduction procedure are shown in Table III. The eccentricity residual is plotted in Figure 4.

Looking at Figure 4 one checks that the eccentricity estimator is dominated by high frequency noise. That is the reason why the quality of the fit is so bad and its statistical error so large. One can also check comparing the value of the eccentricity after one iteration for ID13 from Table V where one corrects the momenta and the value from Table III that both results are consistent and similar providing eccentricity of the same magnitude.
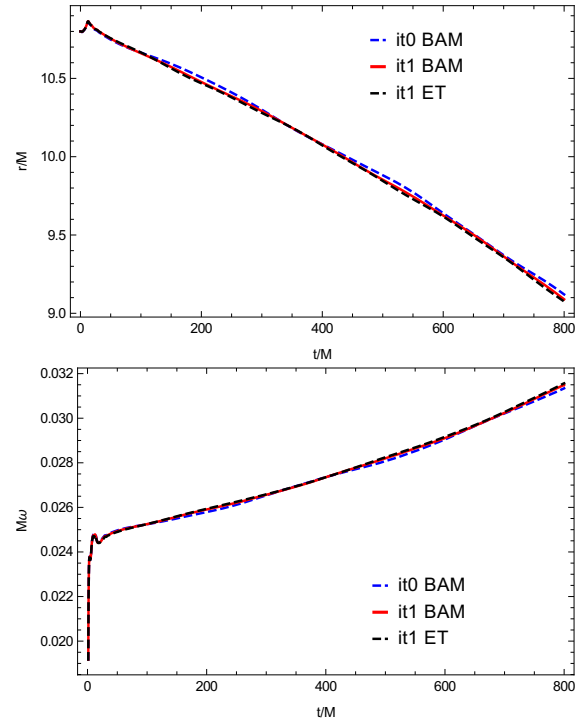
Figure 3: Time evolution of the orbital quantities for the configuration $q = 2$, $\vec{\chi}_1 = (0,0,0)$, $\vec{\chi}_2 = (0.3535, 0.3535, 0.5)$ and initial separation $D = 10.8M$. In the upper panel we plot the time evolution of the orbital separation of the binary. In the lower panel the orbital frequency of the binary is plotted for the different iterations. The blue dashed curve corresponds to iteration 0 run with the BAM code and PC initial data. The red curve corresponds to iteration 1 run the BAM code and the black dashed one to the simulation performed with the ET code.

Iteration	Code	N	δr	λ_r	$(\varepsilon_\Omega \pm \delta\varepsilon_\Omega) \cdot 10^{-3}$
0	BAM	64			1.24 ± 0.03
1	BAM	64	-0.0023	0.8581	0.2 ± 0.2

Table III: Eccentricity estimator and its corresponding statistical error for the configuration ID2 of Table V.

C.　Post-Circular and Post-post-circular in NR

In order to compare PC and PPC initial data, we have run 12 pairs of simulations, ranging from equal mass non-spinning to mass ratio $q = 8$ and precessing simulations, using both PC and PPC initial data for each case. The results are shown in Table IV. All the simulations in Table IV have been computed using the BAM code, at low resolution with $N = 64$ points in the innermost box, and setting the gauge parameter $\eta = 0.25$ as before.

Figure 5 shows a graphical representation of Table IV. Overall, the PC initial data seem to work better in NR than PPC, except for the configuration 9, where PPC initial data
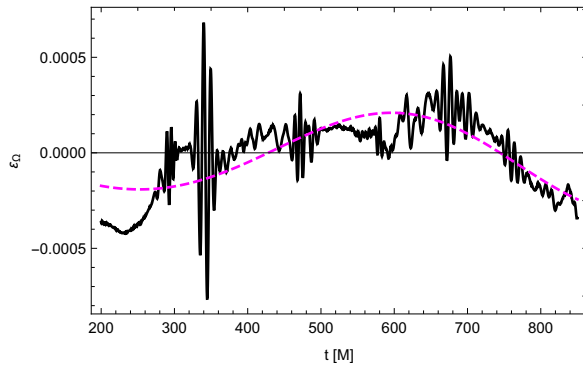
Figure 4: Time evolution of the eccentricity estimator for the configuration $q = 1$, $\chi_{1z} = -0.5$, $\chi_{2z} = 0.5$. The black curve corresponds to the data and the dashed pink line to the fit to the data.
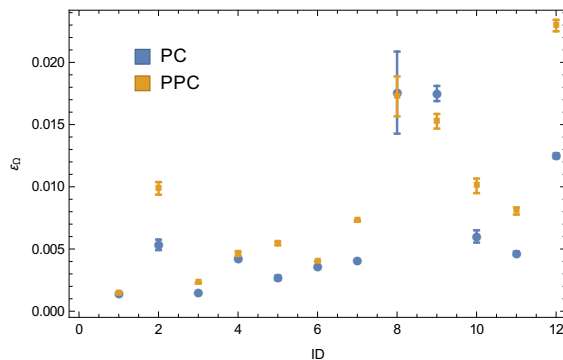

Figure 5: Measured eccentricity, with statistical error bars computed from the nonlinear fits, for the 12 configurations reported Table IV, comparing PC initial data (rounded blue points) and PPC data (yellow squares).

ID	Approx.	q	$\vec{\chi}_1$	$\vec{\chi}_2$	D/M	$(\varepsilon_\Omega \pm \delta\varepsilon_\Omega) \cdot 10^3$
1	PC	1	$(0,0,0)$	$(0,0,0)$	11	1.42 ± 0.02
1	PPC	1	$(0,0,0)$	$(0,0,0)$	11	1.43 ± 0.04
2	PC	1	$(0,0,-0.5)$	$(0,0,-0.5)$	11	5.3 ± 0.4
2	PPC	1	$(0,0,-0.5)$	$(0,0,-0.5)$	11	9.8 ± 0.5
3	PC	1	$(0,0,0.5)$	$(0,0,-0.5)$	11	1.5 ± 0.05
3	PPC	1	$(0,0,0.5)$	$(0,0,-0.5)$	11	2.27 ± 0.04
4	PC	2	$(0,0,-0.75)$	$(0,0,-0.75)$	12.6	4.22 ± 0.07
4	PPC	2	$(0,0,-0.75)$	$(0,0,-0.75)$	12.6	4.61 ± 0.16
5	PC	2	$(0,0,0)$	$\vec{\alpha}$	10.8	2.68 ± 0.17
5	PPC	2	$(0,0,0)$	$\vec{\alpha}$	10.8	5.43 ± 0.13
6	PC	2	$(0,0,0)$	$\vec{\beta}$	10.8	3.61 ± 0.017
6	PPC	2	$(0,0,0)$	$\vec{\beta}$	10.8	4.003 ± 0.018
7	PC	4	$(0,0,-0.8)$	$(0,0,0.8)$	11	4.05 ± 0.07
7	PPC	4	$(0,0,-0.8)$	$(0,0,0.8)$	11	7.25 ± 0.06
8	PC	4	$(0,0,-0.8)$	$(0,0,-0.8)$	11	17.9 ± 1.5
8	PPC	4	$(0,0,-0.8)$	$(0,0,-0.8)$	11	17.5 ± 1.5
9	PC	4	$(0,0,0.8)$	$(0,0,-0.8)$	11	17.4 ± 0.6
9	PPC	4	$(0,0,0.8)$	$(0,0,-0.8)$	11	15.3 ± 0.5
10	PC	4	$(0,0,0.8)$	$(0,0,0.8)$	11	5.5 ± 0.5
10	PPC	4	$(0,0,0.8)$	$(0,0,0.8)$	11	9.9 ± 0.6
11	PC	8	$(0,0,0.5)$	$(0,0,-0.5)$	11	4.64 ± 0.14
11	PPC	8	$(0,0,0.5)$	$(0,0,-0.5)$	11	8.0 ± 0.2
12	PC	8	$(0,0,-0.5)$	$(0,0,-0.5)$	11	12.49 ± 0.18
12	PPC	8	$(0,0,-0.5)$	$(0,0,-0.5)$	11	22.9 ± 0.4

Table IV: Simulations performed to compare PC and PPC initial data. In the first column an identifier is assigned to each configuration which is run with the PC and PPC approximations. In the following columns the mass ratio, the dimensionless spin vectors of each black hole are specified, with the vectors $\vec{\alpha} = (0.3535, -0.3535, -0.5)$ and $\vec{\beta} = (0.3535, -0.3535, 0.5)$. It is also shown the initial orbital separation and the value of the eccentricity estimator and its corresponding statistical error.

lead to a lower eccentricity than PC data. This apparently counter-intuitive result is not particularly surprising: the numerical relativity evolutions differ from PN not only because of missing higher order PN terms, but also because the ADMTT [27] gauge underlying our post-Newtonian results differs from the gauge used in our numerical relativity code beyond 2*PN* order [28]. While in post-Newtonian theory the PPC approximation is indeed superior, the deviation of PC data could either lead to momenta that are closer to NR, or indeed show larger eccentricities than PPC.

D. Eccentricity reduction for post-circular initial data for a range of numerical relativity simulations

In Table V we present results from single step eccentricity reduction for a variety of configurations, using both the BAM and ET codes, and starting with PC initial momenta, which as we have seen in the previous section IV C typically yield smaller eccentricities than PPC momenta for numerical rela-

tivity gauge and initial separations we use. All the simulations using PC initial data, labelled as iteration 0 of the eccentricity reduction procedure, are carried out with gauge parameter $\eta = 0.25$ and low numerical resolution of 64^3 grid points for the innermost grid (containing the black holes). While we have used the same setup for some of the iteration 1 simulations, for others we use our typical setup for productions runs: a higher resolution of 80^3 or 96^3 points, and a gauge parameter of $\eta = 1$, which increases initial gauge transients, but tends to reduce high frequency noise. For all the cases shown, a single eccentricity reduction step reduces the eccentricity to below 10^{-3}.

However, we show that the η parameter can also be set to 1 in the first iteration and one can also get an important reduction of the eccentricity, as happens with the case ID19. The residuals of such a configuration are shown in Figure 6. For that configuration one can also observe the poor quality of the fit in iteration 1, which is consistent with the high value of the
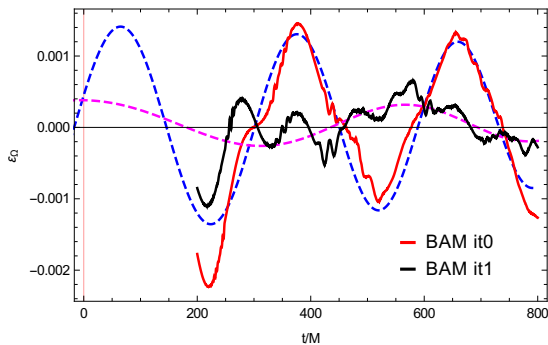
Figure 6: Time evolution of the eccentricity estimator for the configuration $q = 3$ non-spinning. The red curve corresponds to iteration 0 and the black one to iteration 1. The dashed lines are fits to the data. Both simulations were run with $\eta = 1$.

error of the eccentricity in Table V.

The lower the value of the eccentricity, the more difficult becomes the eccentricity measurement because some features due to the lack of resolution of the code can appear, like high frequency noise coming from the finite difference scheme. Furthermore, it becomes difficult to disentangle gauge oscillations from eccentricity oscillations. As one can observe in Figure 7 where the eccentricity estimators of the configurations ID1, ID7, ID18 and ID23 from Table V are plotted.

Finally, the results of Table V allow one to discuss which PN order in the PN expressions for the initial momenta (p_t, p_r) is closer to the corrected momenta which provide low eccentric initial data. The results are displayed in Figure 8. We have computed the difference in absolute value between the corrected tangential or radial momentum (p_t^{ref}, p_r^{ref}) and the PC and PPC values at a given PN order (p_t^i, p_r^i), with $i = 0, 1, 1.5, 2, 2.5, 3, 3.5$.

On the one hand, the upper and intermediate plots of Figure 8 show that in order to have low-eccentricity initial data one requires the knowledge of high PN orders for the tangential momentum. In addition, when comparing the top and intermediate panels of Figure 8 one can check that the PPC approximation has larger values than the PC, and also one observes that for the PC the difference between 3PN and 3.5PN is very small.

On the other hand, the lower panel of Figure 8 reveals that the use of higher PN orders for the radial momentum does not help significantly to reduce the eccentricity. In fact, the lower PN orders seem to provide lower differences. This is in agreement with some of the statements of [31] with respect to the use of low PN order expressions in eccentricity reduction procedures and explains the success of their method. However, note that small changes in the tangential momentum translate into large changes in the eccentricity, while the eccentricity is less sensitive to changes in the radial momentum [58], this is due to the fact that $\partial e_t/\partial \lambda_t \gg \partial e_r/\partial \lambda_r$. In addition, the small difference between the different PN orders implies that the use of different PN orders for the radial momentum provides very

similar results. Therefore, while the differences between the values of p_r at different PN do not have a large effect on the eccentricity, the smaller differences for p_t between the PN orders are large enough to directly affect the eccentricity.

V.   SUMMARY AND CONCLUSIONS

In this paper we have developed a suite of methods which use post-Newtonian approximations to produce low eccentricity initial data for binary black hole evolutions in numerical relativity. The methods rely on working with sufficiently large numerical separations to allow for several orbits before merger, so that an accurate fit can be performed to determine the eccentricity of the numerical data, and to avoid a breakdown of the post-Newtonian approximations which we use. These requirements are consistent with the usual requirements for waveform modelling, where e.g. waveforms need to be long enough to be able to glue NR data to PN data and construct a PN-NR hybrid waveform. Length requirements for numerical relativity waveforms have been discussed e.g. in [59–61].

We have first compared three alternatives to set initial momenta from PN calculations: numerical integration from a large distance, and the PPC and PC approximations. We have found that, as expected, integration from a large distance indeed leads to PN evolutions with negligible eccentricity, and that PPC initial data yield smaller eccentricity than PC initial data for PN evolutions. When using the same prescriptions for the initial momenta in NR evolutions however, PC initial data typically lead to smaller eccentricities. The fact that PC initial data result in particularly low eccentricities of puncture initial data for NR simulations has previously been noted in [34], and we extend their explicit formulas for the momenta in the post-circular approximation to 3.5PN order.

We have also discussed the post-post-circular approximation, which provides an analytical correction to the tangential momentum, maintaining the radial momentum from the PC approximation. We have explicitly shown the success of the PPC approximation in PN, and the ability to generate low eccentric PN initial data without any further iteration. However, we have also checked performing 24 simulations corresponding to 12 configurations that PPC momenta do not provide lower eccentric initial data than PC in NR. This is mainly due to the fact that PPC corrections does not provide the appropriate correction in NR, because the difference due to the fact that PN and NR have different coordinate systems up to 2.5PN overshoots the correction.

The key idea of our eccentricity reduction procedure is to derive explicit formulas to the correction of either the tangential and radial momentum, or alternatively the separation and radial momentum, in terms of the measured eccentricity and the initial phase of the oscillations related to eccentricity. We have found that fitting the orbital frequency evolution to the TaylorT3 approximant provides a robust method to determine the eccentricity and initial phase with sufficient accuracy to be able to reduce the eccentricity below 10^{-3} in a single iteration. Reducing the eccentricity below 10^{-4} for our moving puncture

ID	Iteration	Code	N	η	q	$\vec{\chi}_1$	$\vec{\chi}_2$	D/M	$10 \cdot p_t$	$10^3 \cdot p_r$	λ_t	λ_r	$(\varepsilon_\Omega \pm \delta\varepsilon_\Omega) \cdot 10^3$
1	0	BAM	64	0.25	1	$(0,0,0)$	$(0,0,0)$	12	0.850941	0.53833	0.9997	0.8695	1.42 ± 0.02
	1	BAM	96	0.25	1	$(0,0,0)$	$(0,0,0)$	12	0.850686	0.468113			0.22 ± 0.02
13	0	BAM	64	0.25	1	$(0,0,-0.5)$	$(0,0,0.5)$	11	0.901836	0.722706	0.9998	0.8581	1.24 ± 0.03
	1	BAM	64	0.25	1	$(0,0,-0.5)$	$(0,0,0.5)$	11	0.901688	0.620187			0.27 ± 0.02
14	0	BAM	64	0.25	1	$(0,0,0.5)$	$(0,0,0.5)$	11	0.874251	0.601797	0.999237	0.9346	1.64 ± 0.03
	1	BAM	64	0.25	1	$(0,0,0.5)$	$(0,0,0.5)$	11	0.873583	0.562465			0.39 ± 0.03
15	0	ET	64	0.24	1.5	$(0,0,-0.6)$	$(0,0,0.6)$	10.8	0.868557	0.699185	0.999737	0.9168	1.12 ± 0.05
	1	ET	80	0.24	1.5	$(0,0,-0.6)$	$(0,0,0.6)$	10.8	0.856941	0.641051			0.84 ± 0.165
16	0	ET	64	0.2314	1.75	$(0,0,0.6)$	$(0,0,-0.6)$	10.8	0.856941	0.685199	0.999643	0.8525	1.52 ± 0.08
	1	ET	80	0.2314	1.75	$(0,0,0.6)$	$(0,0,-0.6)$	10.8	0.856636	0.584173			0.43 ± 0.07
17	0	ET	64	0.2314	1.75	$(0,0,-0.6)$	$(0,0,0.6)$	10.8	0.834827	0.649957	0.999903	0.8941	1.12 ± 0.14
	1	ET	80	0.2314	1.75	$(0,0,-0.6)$	$(0,0,0.6)$	10.8	0.834746	0.581178			0.66 ± 0.13
18	0	BAM	64	0.2222	2	$(0,0,0.75)$	$(0,0,0.75)$	11.1117	0.760924	0.450647	0.999937	0.6566	2.38 ± 0.07
	1	BAM	96	0.2222	2	$(0,0,0.75)$	$(0,0,0.75)$	11.1117	0.760876	0.295898			0.47 ± 0.05
19	0	BAM	80	0.1875	3	$(0,0,0)$	$(0,0,0)$	10	0.72377	0.575703	0.999914	0.8629	1.41 ± 0.07
	1	BAM	64	0.1875	3	$(0,0,0)$	$(0,0,0)$	10	0.723708	0.496774			0.29 ± 0.24
7	0	BAM	64	0.16	4	$(0,0,-0.8)$	$(0,0,0.8)$	11	0.559207	0.336564	0.998501	0.7341	4.05 ± 0.07
	1	BAM	64	0.16	4	$(0,0,-0.8)$	$(0,0,0.8)$	11	0.558369	0.24708			0.45 ± 0.4
20	0	BAM	64	0.0987	8	$(0,0,0.5)$	$(0,0,0.5)$	11	0.102969	0.345755	1.00066	1.3512	2.2 ± 0.4
	1	BAM	64	0.0987	8	$(0,0,0.5)$	$(0,0,0.5)$	11	0.139132	0.345985			0.45 ± 0.4
21	0	BAM	64	0.2222	2	$(0,0,0)$	$(0.4949,0.4949,0)$	10.8	0.811783	0.649957	0.999788	0.9802	6.4 ± 1.7
	1	ET	80	0.2222	2	$(0,0,0)$	$(0.4949,0.4949,0)$	10.8	0.811611	0.581178			0.40 ± 0.05
22	0	BAM	64	0.2222	2	$(0,0,0)$	$(0.1767,0.1767,0)$	10.8	0.812379	0.610965	0.999534	0.9009	1.46 ± 0.02
	1	ET	80	0.2222	2	$(0,0,0)$	$(0.1767,0.1767,0)$	10.8	0.812001	0.550427			0.54 ± 0.05
23	0	ET	64	0.2222	2	$(0,0,0)$	$(-0.1767,0.1767,0.5)$	10.8	0.793749	0.53149	0.99994	0.881549	1.88 ± 0.01
	1	ET	80	0.2222	2	$(0,0,0)$	$(-0.1767,0.1767,0.5)$	10.8	0.793701	0.468535			0.28 ± 0.05
24	0	ET	64	0.2222	2	$(0,0,0)$	$(-0.3535,0.3535,0.5)$	10.8	0.7935	0.531374	0.999772	0.843376	2.13 ± 0.03
	1	ET	80	0.2222	2	$(0,0,0)$	$(-0.3535,0.3535,0.5)$	10.8	0.79332	0.448148			0.48 ± 0.05
25	0	ET	64	0.2222	2	$(0,0,0)$	$(-0.3535,0.3535,0.)$	10.8	0.812118	0.611108	0.999848	0.895657	1.78 ± 0.07
	1	ET	80	0.2222	2	$(0,0,0)$	$(-0.3535,0.3535,0.)$	10.8	0.811994	0.547343			0.69 ± 0.07

Table V: Summary of the eccentricity reduced simulations. In the first column we label each configuration, the second one specifies the iteration. The code used and the number of points N used in the innermost level of the codes are displayed, as well as the value of the parameter η appearing in the $\Gamma-$driver shift condition. Then, the mass ratio $q = m_2/m_1$, and the dimensionless spin vectors, $\vec{\chi}_1, \vec{\chi}_2$, the orbital separation D/M, the tangential momenta p_t multiplied by 10 and the radial momentum p_r multiplied by a factor 10^3 are shown. The correction factors λ_t and λ_r computed from iteration zero are described. The values of the eccentricity estimators ε_Ω and their corresponding statistical error $\delta\varepsilon_\Omega$ from the fit are also given.

evolutions will require to reduce the numerical noise with improved choices for numerical dissipation, on which we will report elsewhere, and will also require a discussion of spin oscillations in the context of spin precession. Such a study has been performed in [52], where eccentricities below 10^{-4} have been achieved for precessing simulations in four iterations, while we can reach eccentricities of the order $O(10^{-4})$ in one iteration. We also note that in [52] the test cases start at separation $d = 16M$, which would improve the performance of the PC approximation and of the PN expressions on which we base our eccentricity reduction method, however here we want to show that the method works well for simulations of intermediate length, of typically between 5 and 10 orbits, which can be performed with moderate computational cost and are

still very beneficial for waveform modelling purposes.

When only moderately low eccentricities are desired, or as the first step in an iterative procedure, it is possible to only correct the tangential momentum, using Eq. (3.25). In this case it is important to accurately determine the eccentricity, but not the phase Ψ in Eq. (3.46). The two-dimensional schemes, where also the radial momentum is changed, rely on an accurate extrapolation of the residual (3.26) to the initial time $t = 0$ of the simulation. This is made possible by fitting the frequency evolution to the TaylorT3 approximant. This ansatz avoids artefacts outside of the numerical fitting region, which are characteristic for polynomial fits.

In this paper we use the orbital frequency, which is coordinate dependent, to measure eccentricity. In order to suppress
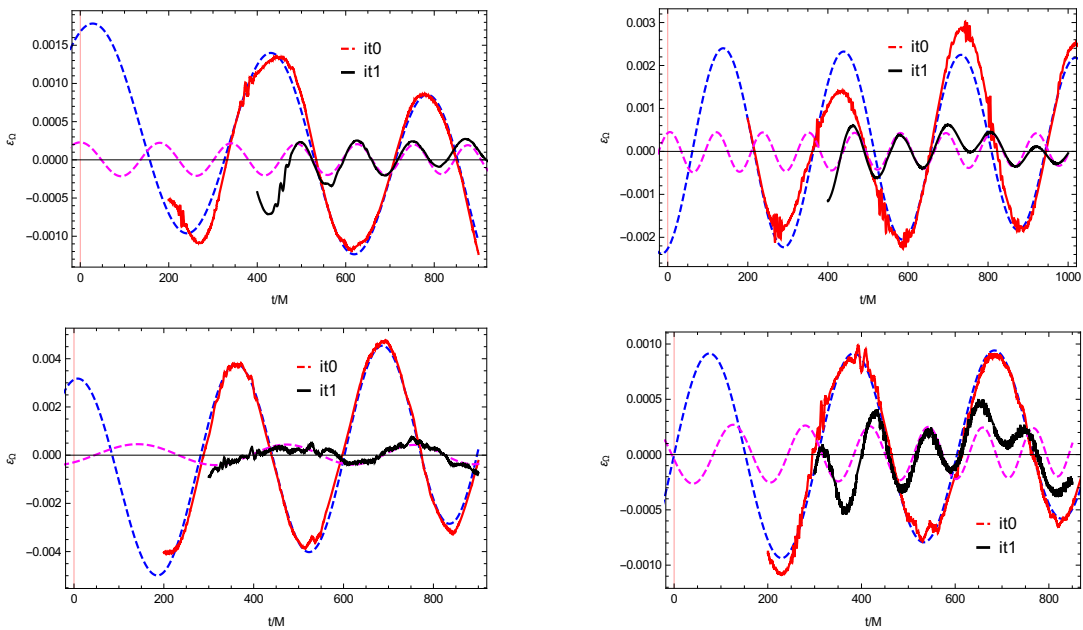
Figure 7: Time evolution of the eccentricity estimators. In the top left panel one has the configuration ID1, in the top right panel ID18, in the bottom left plot ID7 and in the bottom right picture ID23 from Table V. The red curves correspond to the data of iteration 0 and the black ones to the data of iteration 1. The dashed lines correspond to fits to the eccentricity estimators.

initial gauge transients we use a small value of the η parameter appearing in the Γ-driver shift condition, $\eta = 0.25$, as has been studied in some detail in [40]. Here we show that this method works well for a variety of cases, including precessing ones. As an alternative to measuring the eccentricity from the orbital frequency one could use the wave frequency [40], employing methods to denoise the wave frequency such as those employed in [40]. For our setup of numerical relativity simulations, abstaining from an accurate determination of the gravitational wave signal however saves computational cost for the low resolution simulations used to compute the corrected momenta or separation. The method should also apply to numerical relativity codes based on different methods and in particular coordinate gauges, e.g. the SpEC code [62]. We also hope that the simplicity of the procedure benefits extension to binary systems containing matter, in particular neutron stars or boson stars.

A coordinate dependence that is more problematic than the one for the orbital frequency arises from mapping PN momenta at some coordinate separation in the PN ADMTT gauge to the same value of the coordinate separation of the punctures in the coordinates corresponding to Bowen-York initial data, which only agree with ADMTT up to second PN order [28]. We have addressed this problem by developing two versions of our iterative scheme to correct the initial parameters of the simulation to reduce the inherent eccentricity: In the "traditional" version we correct our initial guesses for the tangential and radial momenta (p_t, p_r). In the alternative version we correct for the initial separation and p_r. The second ver-

sion, which appears logically more consistent, and is hoped to provide advantages when constructing hybrid PN-NR dynamics and waveforms, e.g. for precessing configurations, where not only the waveforms but also the spin evolutions should be glued together. This will be explored in future work.

The corrections $p_t \rightarrow \lambda_t p_t$ (3.46), $p_r \rightarrow \lambda_r p_r$ (3.47), and $r_0 \rightarrow r_0 + \delta r$ (3.57) can be applied iteratively, we find however that when combing the procedure with PC initial momenta for iteration 0, for the cases we have studied, which include mass ratios as high as 8 and also some precessing simulations, a single iteration was sufficient to obtain eccentricities below 10^{-4}. For those cases where we applied a second iteration, eccentricities dropped at least by an additional factor of 2. However, there may be parts of the parameter space, especially high mass ratios and high spins, where the initial PN formulas will produce significantly larger eccentricities of the order $O(10^{-2})$ requiring in those cases more than iteration to reach a value of the eccentricity of the order $O(10^{-4})$.

Our implementation of the eccentricity reduction procedure with analytical formulas relating the eccentricity and the correction of the momenta needed to eliminate it, provides real control in the eccentricity of a PN or NR simulation. As shown in this communication this can be used to reduce the amount of eccentricity in the simulation, but it can also be used to perform eccentric simulations. This can be used to generate eccentric NR and PN simulations, which can be glued into hybrid waveforms that are the fundamental inputs for waveform modelling.
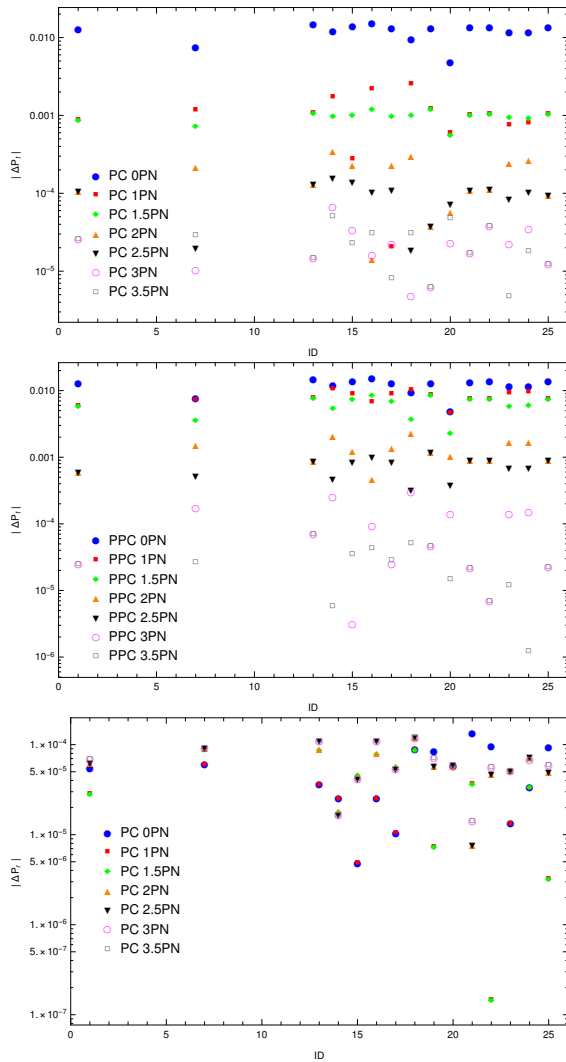
Figure 8: Absolute difference between the low eccentric tangential or radial momentum value, (p_t^{ref}, p_r^{ref}), from Table V and the momentum at a given PN order, (p_t^i, p_r^i) with $i = 0, 1, 1.5, 2, 2.5, 3, 3.5$ for the configurations of Table V. In the upper panel the absolute difference for the values of the PC tangential momentum at different PN orders are shown, in the intermediate one the absolute differences for the PPC tangential momentum, and in the lower panel the absolute differences for the radial momentum. The ID in the three plots correspond to those of Table V.

VI. ACKNOWLEDGEMENTS

Appendix A: PN initial data formulas

We present the formulas for the orbital frequency, the tangential momentum and the ADM mass as a function of the separation at 3.5PN order,

$$
M\Omega = \frac{1}{r^{3/2}} \left(1 - \frac{1}{r} \left[\frac{\left(3q^2 + 5q + 3\right)}{2(q+1)^2} \right] + \frac{1}{r^{3/2}} \left[-\frac{(3q+4)\chi_{1z}}{4(q+1)^2} - \frac{q(4q+3)\chi_{2z}}{4(q+1)^2} \right] + \frac{1}{r^2} \left[-\frac{3q^2\chi_{2x}^2}{2(q+1)^2} + \frac{3q^2\chi_{2y}^2}{4(q+1)^2} \right. \right.
$$

$$
\left. \left. + \frac{3q^2\chi_{2z}^2}{4(q+1)^2} + \frac{24q^4 + 103q^3 + 164q^2 + 103q + 24}{16(q+1)^4} - \frac{3\chi_{1x}^2}{2(q+1)^2} - \frac{3q\chi_{1x}\chi_{2x}}{(q+1)^2} + \frac{3\chi_{1y}^2}{4(q+1)^2} + \frac{3q\chi_{1y}\chi_{2y}}{2(q+1)^2} \right. \right.
$$

$$+\frac{3\chi_{1z}^2}{4(q+1)^2}+\frac{3q\chi_{1z}\chi_{2z}}{2(q+1)^2}\Bigg]+\frac{1}{r^{5/2}}\left[\frac{3\left(13q^3+34q^2+30q+16\right)\chi_{1z}}{16(q+1)^4}+\frac{3q\left(16q^3+30q^2+34q+13\right)\chi_{2z}}{16(q+1)^4}\right]$$

$$+\frac{1}{r^3}\left[\frac{\left(155q^2+180q+76\right)\chi_{1x}^2}{16(q+1)^4 r^3}+\frac{q\left(120q^2+187q+120\right)\chi_{1x}\chi_{2x}}{8(q+1)^4 r^3}-\frac{\left(55q^2+85q+43\right)\chi_{1y}^2}{8(q+1)^4 r^3}\right.$$

$$-\frac{q\left(54q^2+95q+54\right)\chi_{1y}\chi_{2y}}{4(q+1)^4 r^3}-\frac{q\left(96q^2+127q+96\right)\chi_{1z}\chi_{2z}}{16(q+1)^4 r^3}+\frac{q^2\left(76q^2+180q+155\right)\chi_{2x}^2}{16(q+1)^4 r^3}$$

$$-\frac{q^2\left(43q^2+85q+55\right)\chi_{2y}^2}{8(q+1)^4 r^3}-\frac{q^2(2q+5)(14q+27)\chi_{2z}^2}{32(q+1)^4 r^3}-\frac{(5q+2)(27q+14)\chi_{1z}^2}{32(q+1)^4 r^3}$$

$$+\frac{501\pi^2 q(q+1)^4-4\left(120q^6+2744q^5+10049q^4+14820q^3+10049q^2+2744q+120\right)}{384(q+1)^6 r^3}\bigg]+\frac{1}{r^{7/2}}\bigg[\frac{3(4q+1)q^3\chi_{2x}^2\chi_{2z}}{2(q+1)^4}$$

$$-\frac{3(4q+1)q^3\chi_{2y}^2\chi_{2z}}{8(q+1)^4}-\frac{3(4q+1)q^3\chi_{2z}^3}{8(q+1)^4}+\chi_{1x}\left(\frac{9(2q+1)q^2\chi_{2x}\chi_{2z}}{4(q+1)^4}+\frac{9(q+2)q\chi_{2x}\chi_z}{4(q+1)^4}\right)+\chi_{1y}\left(\frac{9q^2\chi_{2y}\chi_{1z}}{4(q+1)^4}+\frac{9q^2\chi_{2y}\chi_{2z}}{4(q+1)^4}\right)$$

$$+\chi_{1z}\left(\frac{9q^2(2q+3)\chi_{2x}^2}{4(q+1)^4}-\frac{9q^2(q+2)\chi_{2y}^2}{4(q+1)^4}-\frac{9q^2\chi_{2z}^2}{4(q+1)^3}-\frac{135q^5+385q^4+363q^3+377q^2+387q+168}{32(q+1)^6}\right)$$

$$-\frac{\left(168q^5+387q^4+377q^3+363q^2+385q+135\right)q\chi_{2z}}{32(q+1)^6}+\chi_{1x}^2\left(\frac{3(q+4)\chi_{1z}}{2(q+1)^4}+\frac{9q(3q+2)\chi_{2z}}{4(q+1)^4}\right)$$

$$+\chi_{1y}^2\left(-\frac{3(q+4)\chi_{1z}}{8(q+1)^4}-\frac{9q(2q+1)\chi_{2z}}{4(q+1)^4}\right)-\frac{9q\chi_{1z}^2\chi_{2z}}{4(q+1)^3}-\frac{3(q+4)\chi_{1z}^3}{8(q+1)^4}\bigg]\Bigg), \tag{A1}$$

$$p_t=\frac{q}{(1+q)^2}\frac{1}{r^{1/2}}\Bigg(1+\frac{2}{r}+\frac{1}{r^{3/2}}\left[-\frac{3\left(4q^2+3q\right)\chi_{2z}}{4(q+1)^2}-\frac{3(3q+4)\chi_{1z}}{4(q+1)^2}\right]+\frac{1}{r^2}\left[-\frac{3q^2\chi_{2x}^2}{2(q+1)^2}+\frac{3q^2\chi_{2y}^2}{4(q+1)^2}+\frac{3q^2\chi_{2z}^2}{4(q+1)^2}\right.$$

$$+\frac{42q^2+41q+42}{16(q+1)^2}-\frac{3\chi_{1x}^2}{2(q+1)^2}-\frac{3q\chi_{1x}\chi_{2x}}{(q+1)^2}+\frac{3\chi_{1y}^2}{4(q+1)^2}+\frac{3q\chi_{1y}\chi_{2y}}{2(q+1)^2}+\frac{3\chi_{1z}^2}{4(q+1)^2}+\frac{3q\chi_{1z}\chi_{2z}}{2(q+1)^2}\bigg]$$

$$+\frac{1}{r^{5/2}}\left[\frac{\left(13q^3+60q^2+116q+72\right)\chi_{1z}}{16(q+1)^4}+\frac{\left(-72q^4-116q^3-60q^2-13q\right)\chi_{2z}}{16(q+1)^4}\right]+\frac{1}{r^3}\left[\frac{\left(472q^2-640\right)\chi_{1x}^2}{128(q+1)^4}\right.$$

$$+\frac{\left(-512q^2-640q-64\right)\chi_{1y}^2}{128(q+1)^4}+\frac{\left(-108q^2+224q+512\right)\chi_{1z}^2}{128(q+1)^4}+\frac{\left(472q^2-640q^4\right)\chi_{2x}^2}{128(q+1)^4}+\frac{\left(192q^3+560q^2+192q\right)\chi_{1x}\chi_{2x}}{128(q+1)^4}$$

$$+\frac{\left(-864q^3-1856q^2-864q\right)\chi_{1y}\chi_{2y}}{128(q+1)^4}+\frac{\left(480q^3+1064q^2+480q\right)\chi_{1z}\chi_{2z}}{128(q+1)^4}+\frac{\left(-64q^4-640q^3-512q^2\right)\chi_{2y}^2}{128(q+1)^4}$$

$$+\frac{\left(512q^4+224q^3-108q^2\right)\chi_{2z}^2}{128(q+1)^4}+\frac{480q^4+163\pi^2 q^3-2636q^3+326\pi^2 q^2-6128q^2+163\pi^2 q-2636q+480}{128(q+1)^4}\bigg]$$

$$+\frac{1}{r^{7/2}}\bigg[\frac{5(4q+1)q^3\chi_{2x}^2\chi_{2z}}{2(q+1)^4}-\frac{5(4q+1)q^3\chi_{2y}^2\chi_{2z}}{8(q+1)^4}-\frac{5(4q+1)q^3\chi_{2z}^3}{8(q+1)^4}+\chi_{1x}\left(\frac{15(2q+1)q^2\chi_{2x}\chi_{2z}}{4(q+1)^4}+\frac{15(q+2)q\chi_{2x}\chi_{1z}}{4(q+1)^4}\right)$$

$$+\chi_{1y}\left(\frac{15q^2\chi_{2y}\chi_{1z}}{4(q+1)^4}+\frac{15q^2\chi_{2y}\chi_{2z}}{4(q+1)^4}\right)+\chi_{1z}\left(\frac{15q^2(2q+3)\chi_{2x}^2}{4(q+1)^4}-\frac{15q^2(q+2)\chi_{2y}^2}{4(q+1)^4}-\frac{15q^2\chi_{2z}^2}{4(q+1)^3}\right.$$

$$-\frac{103q^5+145q^4-27q^3+252q^2+670q+348}{32(q+1)^6}\bigg)-\frac{\left(348q^5+670q^4+252q^3-27q^2+145q+103\right)q\chi_{2z}}{32(q+1)^6}+\chi_{1x}^2\left(\frac{5(q+4)\chi_{1z}}{2(q+1)^4}\right.$$

$$+\frac{15q(3q+2)\chi_{2z}}{4(q+1)^4}\bigg)+\chi_{1y}^2\left(-\frac{5(q+4)\chi_{1z}}{8(q+1)^4}-\frac{15q(2q+1)\chi_{2z}}{4(q+1)^4}\right)-\frac{15q\chi_{1z}^2\chi_{2z}}{4(q+1)^3}-\frac{5(q+4)\chi_{1z}^3}{8(q+1)^4}\bigg]\Bigg), \tag{A2}$$

$$\frac{M_{ADM}}{M} = 1 - \frac{q}{2r(q+1)^2} + \frac{1}{r^2}\frac{q\left(7q^2 + 13q + 7\right)}{8(q+1)^4} + \frac{1}{r^{5/2}}\left[-\frac{(4q+3)q^2\chi_{2z}}{4(q+1)^4} - \frac{(3q+4)q\chi_{1z}}{4(q+1)^4} \right] + \frac{1}{r^3}\left[-\frac{q^3\chi_{2x}^2}{2(q+1)^4} \right.$$

$$+ \frac{q^3\chi_{2z}^2}{4(q+1)^4} - \frac{q^2\chi_{1x}\chi_{2x}}{(q+1)^4} + \frac{q^2\chi_{1y}\chi_{2y}}{2(q+1)^4} + \frac{q^2\chi_{1z}\chi_{2z}}{2(q+1)^4} + \frac{\left(9q^4 + 16q^3 + 13q^2 + 16q + 9\right)q}{16(q+1)^6} - \frac{q\chi_{1x}^2}{2(q+1)^4} + \frac{q\chi_{1y}^2}{4(q+1)^4}$$

$$\left. + \frac{q\chi_{1z}^2}{4(q+1)^4} \right] + \frac{1}{r^{7/2}}\left[-\frac{\left(q^3 + 14q^2 + 42q + 32\right)q\chi_{1z}}{16(q+1)^6} - \frac{\left(32q^3 + 42q^2 + 14q + 1\right)q^2\chi_{2z}}{16(q+1)^6} \right] + \frac{1}{r^4}\left[\frac{179q^7}{128(q+1)^8} - \frac{3497q^6}{384(q+1)^8} \right.$$

$$- \frac{18707q^5}{384(q+1)^8} - \frac{9787q^4}{128(q+1)^8} + \frac{9q^3\chi_{1x}\chi_{2x}}{8(q+1)^6} - \frac{18707q^3}{384(q+1)^8} + \frac{\left(25q^2 - 12q - 52\right)q\chi_{1x}^2}{16(q+1)^6} - \frac{3\left(4q^2 + 9q + 4\right)q^2\chi_{1y}\chi_{2y}}{4(q+1)^6}$$

$$+ \frac{3\left(10q^2 + 21q + 10\right)q^2\chi_z\chi_{2z}}{8(q+1)^6} + \frac{\left(3q^2 + 38q + 50\right)q\chi_z^2}{16(q+1)^6} - \frac{3497q^2}{384(q+1)^8} - \frac{\left(52q^2 + 12q - 25\right)q^3\chi_{2x}^2}{16(q+1)^6}$$

$$+ \frac{\left(q^2 - 17q - 15\right)q^3\chi_{2y}^2}{8(q+1)^6} + \frac{\left(-15q^3 - 17q^2 + q\right)\chi_y^2}{8(q+1)^6} + \frac{\left(50q^2 + 38q + 3\right)q^3\chi_{2z}^2}{16(q+1)^6} + \pi^2\left(\frac{81q^6}{128(q+1)^8} + \frac{81q^5}{32(q+1)^8} \right.$$

$$\left. + \frac{243q^4}{64(q+1)^8} + \frac{81q^3}{32(q+1)^8} + \frac{81q^2}{128(q+1)^8} \right) + \frac{179q}{128(q+1)^8} \right] + \frac{1}{r^{9/2}}\left[\frac{3(20q+7)q^4\chi_{2x}^2\chi_{2z}}{8(q+1)^6} - \frac{3(12q+5)q^4\chi_{2y}^2\chi_{2z}}{16(q+1)^6} \right.$$

$$- \frac{3(12q+5)q^4\chi_{2z}^3}{16(q+1)^6} + \chi_{1x}^2\left(\frac{3(22q+15)q^2\chi_{2z}}{8(q+1)^6} + \frac{3(7q+20)q\chi_{1z}}{8(q+1)^6} \right) + \chi_{1y}^2\left(-\frac{3(28q+15)q^2\chi_{2z}}{16(q+1)^6} - \frac{3(5q+12)q\chi_z}{16(q+1)^6} \right)$$

$$- \frac{3(22q+23)q^2\chi_{1z}^2\chi_{2z}}{16(q+1)^6} + \chi_{1x}\left(\frac{3(5q+3)q^3\chi_{2x}\chi_{2z}}{2(q+1)^6} + \frac{3(3q+5)q^2\chi_{2x}\chi_{1z}}{2(q+1)^6} \right) + \chi_{1y}\left(\frac{3(3-4q)q^3\chi_{2y}\chi_{2z}}{8(q+1)^6} + \frac{3(3q-4)q^2\chi_{2y}\chi_z}{8(q+1)^6} \right)$$

$$+ \chi_{1z}\left(\frac{3(15q+22)q^3\chi_{2x}^2}{8(q+1)^6} - \frac{3(15q+28)q^3\chi_{2y}^2}{16(q+1)^6} - \frac{3(23q+22)q^3\chi_{2z}^2}{16(q+1)^6} - \frac{\left(128q^5 + 181q^4 - 88q^3 + 81q^2 + 544q + 312\right)q}{64(q+1)^8} \right)$$

$$- \frac{\left(312q^5 + 544q^4 + 81q^3 - 88q^2 + 181q + 128\right)q^2\chi_{2z}}{64(q+1)^8} - \frac{3(5q+12)q\chi_z^3}{16(q+1)^6} \right]. \tag{A3}$$

In this work we have chosen to specify as initial condition the orbital separation r. Another possible choice is to specify the initial orbital frequency where we want to start our simulation. Then, equation (A1) can be inverted to obtain the relation $r(\Omega)$, and then write the separation, the tangential momentum and the ADM mass in terms of the orbital frequency. The resulting equations are,

$$\frac{r}{M} = \Omega^{-2/3} - \frac{3q^2 + 5q + 3}{3(q+1)^2} + \left[-\frac{(3q+4)\chi_{1z}}{6(q+1)^2} - \frac{q(4q+3)\chi_{2z}}{6(q+1)^2} \right]\Omega^{1/3} + \left[-\frac{\chi_{1x}^2}{(q+1)^2} - \frac{2q\chi_{2x}\chi_{1x}}{(q+1)^2} + \frac{\chi_{1y}^2}{2(q+1)^2} + \frac{q^2\chi_{2y}^2}{2(q+1)^2} \right.$$

$$\left. + \frac{\chi_{1z}^2}{2(q+1)^2} + \frac{q^2\chi_{2z}^2}{2(q+1)^2} + \frac{-18q^4 + 9q^3 + 62q^2 + 9q - 18}{72(q+1)^4} + \frac{q\chi_{1y}\chi_{2y}}{(q+1)^2} + \frac{q\chi_{1z}\chi_{2z}}{(q+1)^2} - \frac{q^2\chi_{2x}^2}{(q+1)^2} \right]\Omega^{2/3}$$

$$+ \left[\frac{q\left(3q^2 - 6q - 26\right)\chi_{1z}}{24(q+1)^4} - \frac{q\left(26q^2 + 6q - 3\right)\chi_{2z}}{24(q+1)^4} \right]\Omega + \left[\frac{\left(71q^2 + 40q - 8\right)\chi_{1x}^2}{24(q+1)^4} + \frac{q\left(36q^2 + 47q + 36\right)\chi_{2x}\chi_{1x}}{12(q+1)^4} \right.$$

$$+ \frac{q^2\left(-8q^2 + 40q + 71\right)\chi_{2x}^2}{24(q+1)^4} + \frac{\left(-27q^2 - 15q + 7\right)\chi_{1z}^2}{18(q+1)^4} + \frac{q^2\left(7q^2 - 15q - 27\right)\chi_{2z}^2}{18(q+1)^4} - \frac{q\left(11q^2 + 20q + 11\right)\chi_{1y}\chi_{2y}}{2(q+1)^4}$$

$$- \frac{\left(17q^2 + 25q + 11\right)\chi_{1y}^2}{6(q+1)^4} - \frac{q^2\left(11q^2 + 25q + 17\right)\chi_{2y}^2}{6(q+1)^4} - \frac{q\left(15q^2 + 17q + 15\right)\chi_{1z}\chi_{2z}}{9(q+1)^4} + \frac{167\pi^2 q}{192(q+1)^2}$$

$$-\frac{324q^6 + 16569q^5 + 65304q^4 + 98086q^3 + 65304q^2 + 16569q + 324}{1296(q + 1)^6}\Bigg]\Omega^{4/3} + \Bigg[\frac{(4q + 9)\chi_{2z}^3 q^3}{12(q + 1)^4} + \frac{(4q - 3)\chi_{2x}^2\chi_{2z}q^3}{3(q + 1)^4}$$

$$+\frac{(4q + 9)\chi_{2y}^2\chi_{2z}q^3}{12(q + 1)^4} + \frac{(11q + 13)\chi_{1z}^2\chi_{2z}q}{6(q + 1)^4} + \frac{\left(-72q^5 + 1629q^4 + 6731q^3 + 7197q^2 + 2331q + 81\right)\chi_{2z}q}{432(q + 1)^6} + \frac{(9q + 4)\chi_{1z}^3}{12(q + 1)^4}$$

$$+\left(\frac{(4 - 3q)\chi_{1z}}{3(q + 1)^4} + \frac{q(11q + 6)\chi_{2z}}{6(q + 1)^4}\right)\chi_{1x}^2 + \left(\frac{(9q + 4)\chi_{1z}}{12(q + 1)^4} - \frac{q(10q + 3)\chi_{2z}}{6(q + 1)^4}\right)\chi_{1y}^2 + \left(-\frac{(14q + 15)\chi_{2x}\chi_{2z}q^2}{6(q + 1)^4}\right.$$

$$-\frac{(15q + 14)\chi_{2x}\chi_{1z}q}{6(q + 1)^4}\right)\chi_{1x} + \left(\frac{(16q + 21)\chi_{2y}\chi_{2z}q^2}{6(q + 1)^4} + \frac{(21q + 16)\chi_{2y}\chi_{1z}q}{6(q + 1)^4}\right)\chi_{1y} + \left(\frac{q^2(6q + 11)\chi_{2x}^2}{6(q + 1)^4} + \frac{q^2(13q + 11)\chi_{2z}^2}{6(q + 1)^4}\right.$$

$$+\frac{81q^5 + 2331q^4 + 7197q^3 + 6731q^2 + 1629q - 72}{432(q + 1)^6}\chi_{1z}\Bigg]\Omega^{5/3}. \tag{A4}$$

$$\frac{p_t}{M} = \frac{q\Omega^{1/3}}{(q + 1)^2} + \frac{q\left(15q^2 + 29q + 15\right)\Omega}{6(q + 1)^4} + \left[-\frac{2(4q + 3)\chi_{2z}q^2}{3(q + 1)^4} - \frac{2(3q + 4)\chi_z q}{3(q + 1)^4}\right]\Omega^{4/3} + \left[\frac{\chi_{2y}^2 q^3}{2(q + 1)^4} + \frac{\chi_{2z}^2 q^3}{2(q + 1)^4} - \frac{\chi_{2x}^2 q^3}{(q + 1)^4}\right.$$

$$+\frac{\chi_{1y}\chi_{2y}q^2}{(q + 1)^4} + \frac{\chi_{1z}\chi_{2z}q^2}{(q + 1)^4} - \frac{2\chi_{1x}\chi_{2x}q^2}{(q + 1)^4} + \frac{\chi_{1y}^2 q}{2(q + 1)^4} + \frac{\chi_{1z}^2 q}{2(q + 1)^4} + \frac{\left(441q^4 + 1440q^3 + 1997q^2 + 1440q + 441\right)q}{72(q + 1)^6}$$

$$-\frac{\chi_{1x}^2 q}{(q + 1)^4}\right]\Omega^{5/3} + \left[-\frac{\left(16q^3 + 29q^2 + 22q + 7\right)\chi_{2z}q^2}{2(q + 1)^6} - \frac{\left(7q^3 + 22q^2 + 29q + 16\right)\chi_{1z}q}{2(q + 1)^6}\right]\Omega^2 + \left(\frac{\left(-116q^2 + 4q + 53\right)\chi_{2x}^2 q^3}{24(q + 1)^6}\right.$$

$$+\frac{\left(5q^2 - 41q - 31\right)\chi_{2y}^2 q^3}{12(q + 1)^6} + \frac{53\chi_{1x}\chi_{2x}q^3}{12(q + 1)^6} - \frac{\left(q^2 + 147q + 81\right)\chi_{2z}^2 q^3}{36(q + 1)^6} + \frac{161\pi^2 q^2}{192(q + 1)^4} - \frac{\left(8q^2 + 21q + 8\right)\chi_{1y}\chi_{2y}q^2}{2(q + 1)^6}$$

$$-\frac{\left(21q^2 + 67q + 21\right)\chi_{1z}\chi_{2z}q^2}{18(q + 1)^6} + \frac{\left(53q^2 + 4q - 116\right)\chi_{1x}^2 q}{24(q + 1)^6} - \frac{\left(31q^2 + 41q - 5\right)\chi_{1y}^2 q}{12(q + 1)^6} - \frac{\left(81q^2 + 147q + 1\right)\chi_{1z}^2 q}{36(q + 1)^6}$$

$$+\frac{\left(20007q^6 + 60489q^5 + 67320q^4 + 53681q^3 + 67320q^2 + 60489q + 20007\right)q}{1296(q + 1)^8}\right]\Omega^{7/3} + \left[\frac{2(2q + 3)\chi_{2z}^3 q^4}{3(q + 1)^6}\right.$$

$$+\frac{(4q - 9)\chi_{2x}^2\chi_{2z}q^4}{3(q + 1)^6} + \frac{2(2q + 3)\chi_{2y}^2\chi_{2z}q^4}{3(q + 1)^6} + \frac{(32q + 37)\chi_{1z}^2\chi_{2z}q^2}{6(q + 1)^6} + \frac{2(3q + 2)\chi_{1z}^3 q}{3(q + 1)^6} + \left(\frac{(7q + 3)\chi_{2z}q^2}{3(q + 1)^6} + \frac{(4 - 9q)\chi_{1z}q}{3(q + 1)^6}\right)\chi_{1x}^2$$

$$-\frac{\left(10656q^5 + 25560q^4 + 24235q^3 + 14853q^2 + 8550q + 2808\right)\chi_{2z}q^2}{432(q + 1)^8} + \left(\frac{2q(3q + 2)\chi_{1z}}{3(q + 1)^6} - \frac{q^2(16q + 3)\chi_{2z}}{6(q + 1)^6}\right)\chi_{1y}^2$$

$$+\left(-\frac{(22q + 21)\chi_{2x}\chi_{2z}q^3}{3(q + 1)^6} - \frac{(21q + 22)\chi_{2x}\chi_{1z}q^2}{3(q + 1)^6}\right)\chi_{1x} + \left(\frac{4(5q + 6)\chi_{2y}\chi_{2z}q^3}{3(q + 1)^6} + \frac{4(6q + 5)\chi_{2y}\chi_{1z}q^2}{3(q + 1)^6}\right)\chi_{1y}$$

$$+\left(\frac{(3q + 7)\chi_{2x}^2 q^3}{3(q + 1)^6} + \frac{(37q + 32)\chi_{2z}^2 q^3}{6(q + 1)^6} - \frac{\left(2808q^5 + 8550q^4 + 14853q^3 + 24235q^2 + 25560q + 10656\right)q}{432(q + 1)^8}\right.$$

$$-\frac{(3q + 16)\chi_{2y}^2 q^3}{6(q + 1)^6}\right)\chi_{1z}\Bigg]\Omega^{8/3} \tag{A5}$$

$$\frac{M_{ADM}}{M} = 1 - \frac{q\Omega^{-1}}{2(q + 1)^2} + \left[-\frac{(4q + 3)q^2\chi_{2z}}{4(q + 1)^4} - \frac{(3q + 4)q\chi_{1z}}{4(q + 1)^4}\right]\Omega^{-5/2} + \frac{\left(7q^2 + 13q + 7\right)q\Omega^{-2}}{8(q + 1)^4}$$

$$+\left[-\frac{\left(32q^3 + 42q^2 + 14q + 1\right)q^2\chi_{2z}}{16(q + 1)^6} - \frac{\left(q^3 + 14q^2 + 42q + 32\right)q\chi_{1z}}{16(q + 1)^6}\right]\Omega^{-7/2} + \left[-\frac{q^3\chi_{2x}^2}{2(q + 1)^4} + \frac{q^3\chi_{2y}^2}{4(q + 1)^4} + \frac{q^3\chi_{2z}^2}{4(q + 1)^4}\right.$$

$$-\frac{q^2\chi_{1x}\chi_{2x}}{(q + 1)^4} + \frac{q^2\chi_y\chi_{2y}}{2(q + 1)^4} + \frac{q^2\chi_z\chi_{2z}}{2(q + 1)^4} + \frac{\left(9q^4 + 16q^3 + 13q^2 + 16q + 9\right)q}{16(q + 1)^6} - \frac{q\chi_{1x}^2}{2(q + 1)^4} + \frac{q\chi_{1y}^2}{4(q + 1)^4} + \frac{q\chi_{1z}^2}{4(q + 1)^4}\right]\Omega^{-3}$$

$$+\left[\frac{9q^3\chi_{1x}\chi_{2x}}{8(q + 1)^6} + \frac{\left(25q^2 - 12q - 52\right)q\chi_{1x}^2}{16(q + 1)^6} - \frac{3\left(4q^2 + 9q + 4\right)q^2\chi_{1y}\chi_{2y}}{4(q + 1)^6} + \frac{3\left(10q^2 + 21q + 10\right)q^2\chi_{1z}\chi_{2z}}{8(q + 1)^6}\right.$$

$$
+ \frac{\left(3q^2 + 38q + 50\right)q\chi_{1z}^2}{16(q+1)^6} + \frac{81\pi^2 q^2}{128(q+1)^4} - \frac{\left(52q^2 + 12q - 25\right)q^3\chi_{2x}^2}{16(q+1)^6} + \frac{\left(q^2 - 17q - 15\right)q^3\chi_{2y}^2}{8(q+1)^6} + \frac{\left(-15q^3 - 17q^2 + q\right)\chi_{1y}^2}{8(q+1)^6}
$$

$$
+ \frac{\left(50q^2 + 38q + 3\right)q^3\chi_{2z}^2}{16(q+1)^6} + \frac{\left(537q^6 - 3497q^5 - 18707q^4 - 29361q^3 - 18707q^2 - 3497q + 537\right)q}{384(q+1)^8} \Bigg] \Omega^{-4}
$$

$$
+ \left[\frac{3(20q+7)q^4\chi_{2x}^2\chi_{2z}}{8(q+1)^6} - \frac{3(12q+5)q^4\chi_{2y}^2\chi_{2z}}{16(q+1)^6} - \frac{3(12q+5)q^4\chi_{2z}^3}{16(q+1)^6} + \chi_{1x}^2\left(\frac{3(22q+15)q^2\chi_{2z}}{8(q+1)^6} + \frac{3(7q+20)q\chi_{1z}}{8(q+1)^6}\right)\right.
$$

$$
+ \chi_{1y}^2\left(-\frac{3(28q+15)q^2\chi_{2z}}{16(q+1)^6} - \frac{3(5q+12)q\chi_{1z}}{16(q+1)^6}\right) - \frac{3(22q+23)q^2\chi_{1z}^2\chi_{2z}}{16(q+1)^6} + \chi_{1x}\left(\frac{3(5q+3)q^3\chi_{2x}\chi_{2z}}{2(q+1)^6} + \frac{3(3q+5)q^2\chi_{2x}\chi_{1z}}{2(q+1)^6}\right)
$$

$$
+ \chi_{1y}\left(\frac{3(3-4q)q^3\chi_{2y}\chi_{2z}}{8(q+1)^6} + \frac{3(3q-4)q^2\chi_{2y}\chi_{1z}}{8(q+1)^6}\right) + \chi_{1z}\left(\frac{3(15q+22)q^3\chi_{2x}^2}{8(q+1)^6} - \frac{3(15q+28)q^3\chi_{2y}^2}{16(q+1)^6} - \frac{3(23q+22)q^3\chi_{2z}^2}{16(q+1)^6}\right.
$$

$$
\left. - \frac{\left(128q^5 + 181q^4 - 88q^3 + 81q^2 + 544q + 312\right)q}{64(q+1)^8}\right) - \frac{\left(312q^5 + 544q^4 + 81q^3 - 88q^2 + 181q + 128\right)q^2\chi_{2z}}{64(q+1)^8}
$$

$$
- \frac{3(5q+12)q\chi_{1z}^3}{16(q+1)^6}\Bigg] \Omega^{-9/2} \tag{A6}
$$

The expression used in this paper for the gravitational wave energy flux [23, 48] is

$$
\frac{dE_{GW}}{dt} = \frac{32}{5}\eta^2\Omega^{10/3}\Bigg(1 + \left[-\frac{35\eta}{12} - \frac{1247}{336}\right]\Omega^{2/3} + \left[4\pi - \frac{5\delta}{4}\Sigma_l - 4S_l\right]\Omega + \left[\frac{65\eta^2}{18} + \frac{9271\eta}{504} - \frac{44711}{9072} - \frac{89\delta\chi_a\chi_s}{48} + \frac{287\delta\chi_a\chi_s}{48}\right.
$$

$$
+ \left(\frac{33}{16} - 8\eta\right)\chi_a^2 - \left(\frac{33}{16} - \frac{\eta}{4}\right)\chi_s^2\Bigg]\Omega^{4/3} + \left[\pi\left(-\frac{583\eta}{24} - \frac{8191}{672}\right) + \frac{43\delta\eta\Sigma_l}{4} - \frac{13\delta\Sigma_l}{16} + \frac{272\eta S_l}{9} - \frac{9S_l}{2}\right]\Omega^{5/3}
$$

$$
+ \Omega^2\Bigg[-\frac{4843497781}{69854400} - \frac{775\eta^3}{324} - \frac{94403\eta^2}{3024} + \left(\frac{8009293}{54432} - \frac{41\pi^2}{64}\right)\eta + \frac{287\pi^2}{192} + \frac{1712}{105}\left(-\gamma + \frac{35\pi^2}{107} - \frac{1}{2}\log\left(16\Omega^{2/3}\right)\right)
$$

$$
- \frac{31\pi\delta\Sigma_l}{6} - 16\pi S_l + \delta\left(\frac{611}{252} - \frac{809\eta}{18}\right)\chi_a\chi_s + \left(43\eta^2 - \frac{8345\eta}{504} + \frac{611}{504}\right)\chi_a^2 + \left(\frac{173\eta^2}{18} - \frac{2393\eta}{72} + \frac{611}{504}\right)\chi_s^2\Bigg] + \left[-\frac{31\pi\delta\Sigma_l}{6}\right.
$$

$$
- 16\pi S_l\Big]\Omega^3 + \left[\pi\left(\frac{193385\eta^2}{3024} + \frac{214745\eta}{1728} - \frac{16285}{504}\right) - \frac{1501}{36}\delta\eta^2\Sigma_l + \frac{1849\delta\eta\Sigma_l}{126} + \frac{9535\delta\Sigma_l}{336} - \frac{2810\eta^2 S_l}{27} + \frac{6172\eta S_l}{189}\right.
$$

$$
+ \frac{476645 S_l}{6804} + \delta\left(\frac{34\eta}{3} - \frac{71}{24}\right)\chi_a^3 + \delta\left(\frac{109\eta}{6} - \frac{71}{8}\right)\chi_a\chi_s^2 + \left(-\frac{104\eta^2}{3} + \frac{263\eta}{6} - \frac{71}{8}\right)\chi_a^2\chi_s + \left(-\frac{2\eta^2}{3} + \frac{28\nu}{3}\right.
$$

$$
\left. - \frac{71}{24}\right)\chi_s^3\Bigg]\Omega^{7/3} + \left[\frac{130583\pi\delta\eta\Sigma_l}{2016} - \frac{7163\pi\delta\Sigma_l}{672} + \frac{13879\pi\eta S_l}{72} - \frac{3485\pi S_l}{96}\right]\Omega^{8/3}\Bigg) \tag{A7}
$$

where we have the following definitions:

$$
\vec{\lambda} = \frac{\vec{L}}{|\vec{L}|}, \tag{A8}
$$

$$
\delta = \frac{m_2 - m_1}{m_1 + m_2}, \tag{A9}
$$

$$
\chi_1 = S_{1z}/m_1^2, \tag{A10}
$$

$$
\chi_2 = S_{2z}/m_2^2, \tag{A11}
$$

$$
\chi_a = \frac{\chi_1 - \chi_2}{2}, \tag{A12}
$$

$$
\chi_s = \frac{\chi_1 + \chi_2}{2}, \tag{A13}
$$

$$
S_l = m_1^2\chi_1 + m_2^2\chi_2, \tag{A14}
$$

$$
\Sigma_l = m_2\chi_2 - m_1\chi_1, \tag{A15}
$$

$$
S_l = (\vec{S}_1 + \vec{S}_2)\cdot\vec{\lambda}, \tag{A16}
$$

$$
\Sigma_l = (m_1 + m_2)\left(\frac{\vec{S}_2}{m_2} - \frac{\vec{S}_1}{m_1}\right)\cdot\vec{\lambda}. \tag{A17}
$$

Appendix B: Ansatz coefficients

The coefficients of the ansatz of the non-spinning fit described in Section III B are derived using the energy given by equation (2.4) and the gravitational wave energy flux given by equation (A7). The coefficients are:

$$b_1 = \frac{11\eta}{32} + \frac{743}{2688}, \tag{B1}$$

$$b_2 = \frac{1}{320}\left(-113\left[\left(\sqrt{1-4\eta}-1\right)\chi_{1z} - \left(\sqrt{1-4\eta}+1\right)\chi_{2z}\right] - 96\pi\right) - \frac{19}{80}\eta(\chi_{1z}+\chi_{2z}), \tag{B2}$$

$$b_3 = \frac{371\eta^2}{2048} + \frac{\eta\left(61236\mathrm{s}1z^2 - 119448\chi_{1z}\chi_{2z} + 61236\chi_{2z}^2 + 56975\right)}{258048} + \frac{1}{14450688}\left[1714608\left(\sqrt{1-4\eta}-1\right)\chi_{1z}^2\right.$$
$$\left. -1714608\left(\sqrt{1-4\eta}+1\right)\chi_{2z}^2 + 1855099\right], \tag{B3}$$

$$b_4 = -\frac{1}{128}17\eta^2(\chi_{1z}+\chi_{2z}) + \frac{\eta\left(117\pi - 2\left(\left(63\sqrt{1-4\eta}+1213\right)\chi_{1z} + \left(1213 - 63\sqrt{1-4\eta}\right)\chi_{2z}\right)\right)}{2304}$$
$$+\frac{-146597\left(\left(\sqrt{1-4\eta}-1\right)\chi_{1z} - \left(\sqrt{1-4\eta}+1\right)\chi_{2z}\right) - 46374\pi}{129024}, \tag{B4}$$

$$b_5 = \frac{235925\eta^3}{1769472} + \eta^2\left[\frac{335129\chi_{1z}^2}{2457600} - \frac{488071\mathrm{s}1z\chi_{2z}}{1228800} + \frac{335129\chi_{2z}^2}{2457600} - \frac{30913}{1835008}\right]$$
$$+\eta\left[\frac{\left(23281001 - 6352738\sqrt{1-4\eta}\right)\chi_{1z}^2}{68812800} + \chi_{1z}\left(\frac{1051\pi}{3200} - \frac{377345\chi_{2z}}{1376256}\right) + \frac{\left(6352738\sqrt{1-4\eta}+23281001\right)\chi_{2z}^2}{68812800}\right.$$
$$\left. +\frac{1051\pi\chi_{2z}}{3200} - \frac{451\pi^2}{2048} + \frac{25302017977}{4161798144}\right] + \frac{6127\pi\left(\sqrt{1-4\eta}-1\right)\chi_{1z}}{12800} - \frac{16928263\left(\sqrt{1-4\eta}+1\right)\chi_{2z}^2}{137625600}$$
$$+\frac{16928263\left(\sqrt{1-4\eta}-1\right)\chi_{1z}^2}{137625600} - \frac{6127\pi\left(\sqrt{1-4\eta}+1\right)\chi_{2z}}{12800} + \frac{53\pi^2}{200} - \frac{720817631400877}{288412611379200} + \frac{107}{280}\left[\gamma + \log(2\theta)\right] \tag{B5}$$

Appendix C: Numerical Relativity setup

1. BAM

Here we describe the numerical set up for NR simulations produced using the BAM code. The numerical setup is similar to the that in [40] but we present the details here for completeness. The BAM code starts with black-hole binary puncture initial data [63, 64] and evolves them using the χ-variant of the moving puncture [12, 13] version of the BSSN [55, 56] formulation of the Einstein equations. The black-hole punctures are initially placed on the y-axis at positions $y_1 = -qD/(1+q)$ and $y_2 = D/(1+q)$, where D is the coordinate distance between the two punctures and the mass ratio is $q = m_2/m_1 > 1$. The punctures are provided initial momenta $\mathbf{p} = (\mp p_t, \pm p_r, 0)$. The spin parameter of a BH is defined as $\chi_i = S_i/m_i^2$.

The code uses sixth-order spatial finite-difference derivatives, fourth-order Runge-Kutta algorithm and Kreiss-Oliger (KO) dissipation terms which converge at fifth order. Moreover, the code utilizes sixteen mesh-refinement buffer points and the base configuration consists of n_1 nested mesh-refinement boxes with N^3 points surrounding each black hole, and n_2 nested boxes with $(2N)^3$ points surrounding the entire system. On the levels where the extraction of gravitational radiation is performed $(4N)^3$ points are used in order to extract more accurately the gravitational waves emitted by the binary. These waves are computed from the Newman-Penrose scalar Ψ_4 [17]. In addition, in order to reduce gauge oscillations in the orbital quantities we set the value of the parameter η ap-

pearing in the Γ-driver shift condition to 0.25 for simulations used to reduce the eccentricity and we use $\eta = 1$ for higher resolution production simulations, that will be used in future waveform modelling and LIGO data analysis.

2. Einstein Toolkit

The Einstein Toolkit (ET) is an open source code suite for relativistic astrophysics simulations built around the Cactus framework, where individual modules are denoted *thorns*. The numerical setup of the simulations is similar to that used in [65] but we present the details here for completeness.

The simulations use standard Bowen-York initial data [63, 64] computed using the TwoPunctures thorn [66]. Time evolution is performed using the *W*-variant [67] of the BSSN formulation [55, 56] of the Einstein equations by McLachlan [68], in which the BHs are evolved using the standard moving punctures gauge conditions [12, 13]. The lapse is evolved according to the "1 + log" condition [69] and the shift evolved using the hyperbolic $\tilde{\Gamma}$-driver equation [57].

The simulations were performed using 8th order accurate finite differencing along with the appropriate KO dissipation terms. Adaptive mesh refinement is provided by Carpet, with the near zone being computed with high resolution Cartesian grids that track the motion of the BHs and the wave extraction zone being computed on spherical grids using the Llama multipatch infrastructure [65]. By using grids adapted to the spherical topology of the wave extraction zone, we are able

to efficiently compute high-accuracy waveforms at large extraction radii relative to standard Cartesian grids. The apparent horizons are computed using `AHFinderDirect` [70] and a calculation of the spins is performed in the dynamical horizon formalism using the `QuasiLocalMeasures` thorn [71]. The contrast to BAM, the two punctures are initially placed on the x-axis at positions $x_1 = D/(1 + q)$ and $x_2 = -qD/(1 + q)$, in which D is the coordinate distance separation and we assume $m_1 > m_2$. Initial momenta are chosen such that $\mathbf{p} = (\mp p_r, \pm p_t, 0)$. As with BAM, the parameter η that appears in the Γ-driver shift condition, which is denoted *BetaDriver* in

the `McLachlan` code, is set to 0.25 for low-resolution simulations and set to 1 for the higher resolution production runs.

The gravitational waves are computed using `WeylScal4` and the GW strain h calculated from Ψ_4 using fixed-frequency integration [72]. The thorns `McLachlan` and `WeylScal4` are generated using the `Kranc` [73] automated-code-generation package. The ET simulations are managed using `Simulation Factory` [74] and the analysis and post-processing of ET waveforms was performed using the open source Mathematica package `Simulation Tools` [75].

---

[1] B. P. e. a. Abbott (LIGO Scientific Collaboration and Virgo Collaboration), Phys. Rev. Lett. **116**, 061102 (2016).

[2] J. Aasi et al. (LIGO Scientific), Class. Quant. Grav. **32**, 074001 (2015).

[3] B. P. e. a. Abbott (LIGO Scientific Collaboration and Virgo Collaboration), Phys. Rev. Lett. **116**, 241103 (2016).

[4] B. P. Abbott et al. (VIRGO, LIGO Scientific), Phys. Rev. Lett. **118**, 221101 (2017), 1706.01812.

[5] B. P. Abbott et al. (Virgo, LIGO Scientific), Astrophys. J. **851**, L35 (2017), 1711.05578.

[6] B. P. Abbott et al. (Virgo, LIGO Scientific), Phys. Rev. Lett. **119**, 141101 (2017).

[7] B. P. Abbott et al. (Virgo, LIGO Scientific), Phys. Rev. Lett. **119**, 161101 (2017).

[8] B. P. Abbott et al. (Virgo, LIGO Scientific), Phys. Rev. Lett. **116**, 241102 (2016), 1602.03840.

[9] P. C. Peters and J. Mathews, Phys. Rev. **131**, 435 (1963).

[10] P. C. Peters, Phys. Rev. **136**, B1224 (1964).

[11] F. Pretorius, Phys. Rev. Lett. **95**, 121101 (2005), gr-qc/0507014.

[12] M. Campanelli, C. O. Lousto, P. Marronetti, and Y. Zlochower, Phys. Rev. Lett. **96**, 111101 (2006).

[13] J. G. Baker, J. Centrella, D.-I. Choi, M. Koppitz, and J. van Meter, Phys. Rev. Lett. **96**, 111102 (2006), gr-qc/0511103.

[14] http://www.black holes.org/waveforms (2013).

[15] J. Healy, C. O. Lousto, Y. Zlochower, and M. Campanelli, Class. Quant. Grav. **34**, 224001 (2017), 1703.03423.

[16] K. Jani, J. Healy, J. A. Clark, L. London, P. Laguna, and D. Shoemaker, Class. Quant. Grav. **33**, 204001 (2016), 1605.03204.

[17] B. Brügmann, J. A. González, M. Hannam, S. Husa, U. Sperhake, and W. Tichy, Phys. Rev. D **77**, 024027 (2008).

[18] S. Husa, S. Khan, M. Hannam, M. Pürrer, F. Ohme, X. J. Forteza, and A. Bohé, Phys. Rev. D **93**, 044006 (2016).

[19] S. Khan, S. Husa, M. Hannam, F. Ohme, M. Pürrer, X. J. Forteza, and A. Bohé, Phys. Rev. D **93**, 044007 (2016).

[20] T. Damour, A. Nagar, M. Hannam, S. Husa, and B. Brügmann, Phys. Rev. D **78**, 044039 (2008).

[21] A. Bohé, L. Shao, A. Taracchini, A. Buonanno, S. Babak, I. W. Harry, I. Hinder, S. Ossokine, M. Pürrer, V. Raymond, et al., Phys. Rev. D **95**, 044028 (2017).

[22] J. Blackman, S. E. Field, M. A. Scheel, C. R. Galley, C. D. Ott, M. Boyle, L. E. Kidder, H. P. Pfeiffer, and B. Szilágyi, Phys. Rev. D **96**, 024058 (2017).

[23] L. Blanchet, Living Reviews in Relativity **17** (2014), ISSN 1433-8351.

[24] M. Hannam, S. Husa, D. Pollney, B. Brügmann, and N. OMurchadha, Phys. Rev. Lett. **99**, 241102 (2007).

[25] M. Hannam, S. Husa, F. Ohme, B. Brügmann, and N. OMurchadha, Phys. Rev. D **78**, 064020 (2008).

[26] J. M. Bowen and J. W. York, Phys. Rev. D **21**, 2047 (1980).

[27] G. Schaefer, Annals of Physics **161**, 81 (1985).

[28] W. Tichy, B. Brügmann, M. Campanelli, and P. Diener, Phys. Rev. D **67**, 064008 (2003).

[29] N. Yunes and W. Tichy, Phys. Rev. **D74**, 064013 (2006).

[30] N. Yunes, W. Tichy, B. J. Owen, and B. Brügmann, Phys. Rev. D **74**, 104011 (2006).

[31] W. Tichy and P. Marronetti, Phys. Rev. **D83**, 024012 (2011).

[32] A. Buonanno and T. Damour, Phys. Rev. **D59**, 084006 (1999), gr-qc/9811091.

[33] S. Husa, M. Hannam, J. A. González, U. Sperhake, and B. Brügmann, Phys. Rev. D **77**, 044037 (2008).

[34] J. Healy, C. O. Lousto, H. Nakano, and Y. Zlochower, Class. Quant. Grav. **34**, 145011 (2017), 1702.00872.

[35] T. Damour and A. Nagar, Phys. Rev. **D76**, 064028 (2007), 0705.2519.

[36] T. Damour and A. Nagar, Phys. Rev. **D77**, 024043 (2008), 0711.2628.

[37] T. Damour and N. Deruelle, Ann. Inst. Henri Poincaré Phys. Théor., Vol. 43, No. 1, p. 107 - 132 (1985).

[38] G. Pratten et al (2018).

[39] H. P. Pfeiffer, D. A. Brown, L. E. Kidder, L. Lindblom, G. Lovelace, and M. A. Scheel, Class. Quant. Grav. **24**, S59 (2007), gr-qc/0702106.

[40] M. Purrer, S. Husa, and M. Hannam, Phys. Rev. **D85**, 124051 (2012), 1203.4258.

[41] A. Buonanno, Y. Chen, and T. Damour, Phys. Rev. **D74**, 104005 (2006), gr-qc/0508067.

[42] T. Damour, P. Jaranowski, and G. Schäfer, Phys. Rev. D **77**, 064032 (2008).

[43] J. Hartung and J. Steinhoff, Annalen Phys. **523**, 783 (2011), 1104.3079.

[44] J. Steinhoff, S. Hergt, and G. Schäfer, Phys. Rev. D **78**, 101503 (2008).

[45] J. Steinhoff, S. Hergt, and G. Schäfer, Phys. Rev. D **77**, 081501 (2008).

[46] M. Levi and J. Steinhoff, JHEP **06**, 059 (2015), 1410.2601.

[47] D. Brown, S. Fairhurst, B. Krishnan, R. A. Mercer, R. K. Kopparapu, L. Santamaria, and J. T. Whelan (2007), 0709.0093.

[48] K. G. Arun, A. Buonanno, G. Faye, and E. Ochsner, Phys. Rev. D **79**, 104023 (2009).

[49] A. H. Mroue, H. P. Pfeiffer, L. E. Kidder, and S. A. Teukolsky, Phys. Rev. **D82**, 124016 (2010), 1004.4697.

[50] A. Buonanno, B. R. Iyer, E. Ochsner, Y. Pan, and B. S. Sathyaprakash, Phys. Rev. D **80**, 084043 (2009).

[51] A. Buonanno, G. B. Cook, and F. Pretorius, Phys. Rev. D **75**,

124018 (2007).

[52] A. Buonanno, L. E. Kidder, A. H. Mroue, H. P. Pfeiffer, and A. Taracchini, Phys. Rev. **D83**, 104034 (2011), 1012.1549.

[53] S. Husa, J. A. Gonzalez, M. Hannam, B. Bruegmann, and U. Sperhake, Class. Quant. Grav. **25**, 105006 (2008), 0706.0740.

[54] F. Loffler et al., Class. Quant. Grav. **29**, 115001 (2012), 1111.3344.

[55] M. Shibata and T. Nakamura, Phys. Rev. D **52**, 5428 (1995).

[56] T. W. Baumgarte and S. L. Shapiro, Phys. Rev. D **59**, 024007 (1998).

[57] M. Alcubierre, B. Brügmann, P. Diener, M. Koppitz, D. Pollney, E. Seidel, and R. Takahashi, Phys. Rev. D **67**, 084023 (2003).

[58] M. Pürrer, S. Husa, and M. Hannam, Phys. Rev. D **85**, 124051 (2012).

[59] L. Santamaría, F. Ohme, P. Ajith, B. Brügmann, N. Dorband, M. Hannam, S. Husa, P. Mösta, D. Pollney, C. Reisswig, et al., Phys. Rev. D **82**, 064016 (2010).

[60] M. Boyle, Phys. Rev. **D84**, 064013 (2011).

[61] F. Ohme, M. Hannam, and S. Husa, Phys.Rev. **D84**, 064029 (2011), 1107.0996.

[62] L. T. Buchman, H. P. Pfeiffer, M. A. Scheel, and B. Szilagyi, Phys.Rev. **D86**, 084033 (2012), 1206.3015.

[63] J. M. Bowen and J. W. York, Phys. Rev. D **21**, 2047 (1980).

[64] S. Brandt and B. Brügmann, Physical Review Letters **78**, 3606

(1997), ISSN 1079-7114.

[65] D. Pollney, C. Reisswig, E. Schnetter, N. Dorband, and P. Diener, Phys. Rev. **D83**, 044045 (2011).

[66] M. Ansorg, B. Brügmann, and W. Tichy, Phys. Rev. D **70**, 064011 (2004).

[67] P. Marronetti, W. Tichy, B. Brügmann, J. González, and U. Sperhake, Phys. Rev. D **77**, 064010 (2008).

[68] D. Brown, P. Diener, O. Sarbach, E. Schnetter, and M. Tiglio, Phys. Rev. D **79**, 044023 (2009).

[69] C. Bona, J. Masso, E. Seidel, and J. Stela, Phys. Rev. Lett. **75**, 600 (1995), gr-qc/9412071.

[70] J. Thornburg, Class. Quant. Grav. **21**, 743 (2004), gr-qc/0306056.

[71] O. Dreyer, B. Krishnan, D. Shoemaker, and E. Schnetter, Phys. Rev. **D67**, 024018 (2003), gr-qc/0206008.

[72] C. Reisswig and D. Pollney, Class. Quant. Grav. **28**, 195015 (2011), 1006.1632.

[73] S. Husa, I. Hinder, and C. Lechner, Comput. Phys. Commun. **174**, 983 (2006), gr-qc/0404023.

[74] M. W. Thomas and E. Schnetter, CoRR **1008.4571** (2010), 1008.4571.

[75] I. Hinder and B. Wardell (Simulation Tools v1.1.0), URL `http://simulationtools.org`.

Chapter 5

A first exploration of spinning eccentric binary black holes

The following published article is included in this chapter:

- Antoni Ramos-Buades, Sascha Husa, Geraint Pratten, Héctor Estellés, Cecilio García-Quirós, Maite Mateu-Lucena, Marta Colleoni, Rafel Jaume. *First survey of spinning eccentric black hole mergers: numerical relativity simulations, hybrid waveforms, and parameter estimation.* Physical Review D **101**, 083015 (2020). [21 pages]

March 9, 2020

A first survey of spinning eccentric black hole mergers: numerical relativity simulations, hybrid waveforms, and parameter estimation

Antoni Ramos-Buades,[1] Sascha Husa,[1] Geraint Pratten,[1, 2] Héctor Estellés,[1]
Cecilio García-Quirós,[1] Maite Mateu-Lucena,[1] Marta Colleoni,[1] and Rafel Jaume[1]

[1]*Departament de Física, Universitat de les Illes Balears, IAC3 – IEEC, Crta. Valldemossa km 7.5, E-07122 Palma, Spain*
[2]*School of Physics and Astronomy and Institute for Gravitational Wave Astronomy,*
University of Birmingham, Edgbaston, Birmingham, B15 9TT, United Kingdom

We analyze a new numerical relativity data set of spinning but non-precessing binary black holes on eccentric orbits, with eccentricities from approximately 0.1 to 0.5, with dimensionless spins up to 0.75 included at mass ratios $q = m_1/m_2 = (1, 2)$, and further non-spinning binaries at mass ratios $q = (1.5, 3, 4)$. Comparison of the final mass and spin of these simulations with non-eccentric data extends previous results in the literature on circularisation of eccentric binaries to the spinning case. For the $(l, m) = (2, 2)$ spin-weighted spherical harmonic mode we construct eccentric hybrid waveforms that connect the numerical relativity data to a post-Newtonian description for the inspiral, and we discuss the limitations in the current knowledge of post-Newtonian theory which complicate the generation of eccentric hybrid waveforms. We also perform a Bayesian parameter estimation study, quantifying the parameter biases introduced when using three different quasicircular waveform models to estimate the parameters of highly eccentric binary systems. We find that the used aligned-spin quasicircular model including higher order modes produces lower biases in certain parameters than the non-precessing quasicircular model without higher order modes and the quasicircular precessing model.

PACS numbers: 04.25.Dg, 04.25.Nx, 04.30.Db, 04.30.Tv

I. INTRODUCTION

The detections of gravitational wave signals [1–8] have been found consistent with models of the waveform emitted from the merger of compact objects under the assumption of quasi-circularity of the binary's orbit prior to the merger. The assumption of quasicircularity motivated by the efficient circularization of binaries as a consequence of the emission of gravitational waves [9, 10] simplifies significantly the complexity of the signal and has accelerated the development of inpiral-merger-ringdown (IMR) waveform models: several mature IMR models for quasi-circular coalescences, i.e. neglecting eccentricity, are now publicly available [11–24], and are being used to search and infer the parameters of observed binary black hole systems [7].

Recently, population synthesis studies [25–28] have shown that active galactic nuclei and globular clusters can host a population of moderate and highly eccentric binaries emitting in the frequency band of ground-based detectors. Therefore, the increase in sensitivity of the detectors will increase the likelihood to detect binary systems with non-negligible eccentricities. The modelling of the gravitational waveforms from eccentric black-hole binaries complicates due to the addition of a new timescale to the binary problem, the periastron precession [29]. This new timescale induces oscillations in the waveforms due to the asymmetric emission of gravitational radiation between the apastron and periastron passages.

The orbits of eccentric black-hole binaries are typically described using the Quasi-Keplerian (QK) parametrization [30], which is currently known up to 3 Post-Newtonain (PN) order [31]. This parametrization has been proven a key element to develop inspiral PN waveforms [32–36]. The generation of IMR eccentric models relies on the connection of an ec-

centric PN inspiral with a circular merger [37, 38]. Alternatively, one can substitute the PN waveform by one produced within the Effective One Body (EOB) formalism describing an eccentric inspiral [39–41]. Some eccentric IMR waveform models show good agreement with numerical waveforms up to $e \sim 0.2$ for non-spinning configurations [37]. Recent work has shown possible extensions of the eccentric PN and EOB inspiral waveforms to include spin effects [41, 42]. A key step in the generation of IMR waveform models is the production of hybrid waveforms [43–49] between PN/EOB inspiral and Numerical Relativity (NR) waveforms. The hybridization procedure consists in smoothly attaching a PN/EOB inspiral waveform to a NR one in order to get the full description of the gravitational radiation of the binary system. The generation of data sets of hybrid waveforms has been used in the quasicircular case to calibrate and validate the accuracy IMR waveform models [16–18, 22, 23].

In this paper we present the input data and some key tools required for the development of an IMR eccentric waveform model calibrated to eccentric hybrid PN-NR waveforms. In Sec. II we first present our Numerical Relativity (NR) catalog of non-spinning and spinning eccentric binaries, computed with the private BAM code [50] and the open source EinsteinToolkit (ET) [51, 52]. This includes a discussion of our procedure to specify the initial parameters of the eccentric simulations in subsection II B, a study of the remnant quantities in Sec. II C, and a new method to measure the eccentricity of NR waveforms with arbitrarily high eccentricity in Sec. II D. We find that the final spin and mass are consistent within the error estimates with the quasicircular case, which extends the study in [53] to the eccentric spinning case. We hybridize the dominant gravitational waveform $(l = 2, m = 2)$ mode between numerical relativity and post-Newtonian wave-

forms in Sec. III. This will provide the input data for future work on constructing waveform models that contain the inspiral, merger and ringdown, and allows us to perform injections into detector noise which contain a long inspiral phase. In Sec. IV we use such injections of hybrid waveforms, as well as of pure numerical relativity waveforms, to study the parameter biases introduced when using quasi-circular waveform models to estimate the parameters of highly eccentric spinning systems. Unless explicitly noted, we are working in geometric units $G = c = 1$. To simplify expressions we will also set the total mass of the system $M = 1$ in Secs. II and III. We define the mass ratio $q = m_1/m_2$ with the choice $m_1 > m_2$, so that $q > 1$. We also introduce the symmetric mass ratio $\eta = q/(1 + q)^2$, and we will denote the black hole's dimensionless spin vectors by $\vec{\chi}_i = \vec{S}_i/m_i^2$, for $i = 1, 2$.

II. NUMERICAL RELATIVITY DATA SET

A. Overview

We present a catalog of 60 eccentric NR simulations performed with the non-public BAM code [50] and the open-source ET code [51, 52] with the multipatch `Llama` infrastructure [54]. The numerical setup of both codes is the same as in [55]. Most of the simulations are run with the ET code using the Llama module due to its ability to extract the waves at larger extraction radii. The different simulations and their initial conditions are described in Table IV of Appendix A. In Figure 1 we show our choices of mass ratio q, initial eccentricity e_0, and effective spin parameter, $\chi_{\text{eff}} = (m_1\chi_{1,z} + m_2\chi_{2,z})/(m_1 + m_2)$. We have also added 20 public eccentric SXS simulations presented in [38].
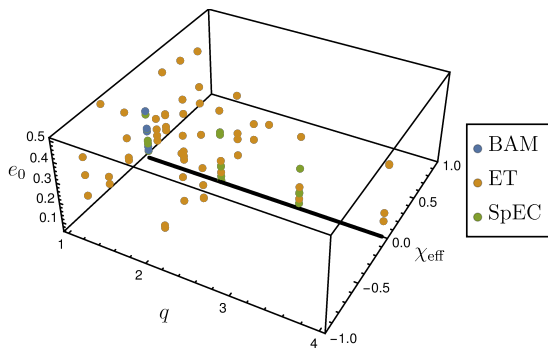

Figure 1: Initial eccentricity e_0, mass ratio q and effective spin parameter $\chi_{\text{eff}} = (m_1\chi_{1,z} + m_2\chi_{2,z})/(m_1 + m_2)$ for the Numerical Relativity simulations generated with the BAM, EinsteinToolkit and SpEc [56] codes. The thick black line represents the cases with $\chi_{\text{eff}} = 0$.

B. Initial parameters of eccentric NR simulations

We use conformally flat Bowen-York initial data [57] in the center of mass frame, where the free parameters are the spins

and masses of the two black holes, the separation, and the momentum of one of the two black holes (the momentum of the second black hole is then equal in magnitude but opposite in direction). We first choose the masses and spins as displayed in Fig. 1. In order to be able to construct hybrid waveforms, the minimal separation, i.e. the separation at periastron, has to be large enough such that the PN approximation is still roughly valid. We then use a simple PN approximation as discussed below to compute the apastron separation required to achieve a chosen value of the eccentricity, and a further PN approximation to compute the appropriate value of the momentum corresponding to this value of the eccentricity. Due to the simplicity, i.e. low order, of the PN approximations used, neither the periastron separation, nor the measured eccentricity will exactly coincide with the specified values. In this study we choose our initial choice for the approximate periastron separation as $r_{\text{min}} \sim 9M$, with slightly different values in order to account for mass ratio and spin effects which can significantly increase the computational cost of the simulations. We start our simulations at the apastron, where the PN approximation employed to specify the initial momentum and the agreement with the PN data we use for hybridization, will be more accurate than during other points of the orbit.

Larger choices of eccentricity for the same configuration of masses and spins thus lead to a larger merger time and number of orbits, as one can see in Table IV of Appendix A. For instance, focusing on simulations with IDs 34, 35 and 36 one observes an increase in the merger time when increasing the initial eccentricity. This increase in merger time also implies an increase in the computational cost of the simulation.

Using the QK parametrization at Newtonian order one can relate the initial minimum and maximum separations by

$$r_{\text{min}} = r_{\text{max}} \frac{1 - e}{1 + e}. \qquad (2.1)$$

As stated above, for our simulations we choose $r_{\text{min}} \sim 9M$ such that the PN approximation is still roughly valid. Then for $e_0 = 0.1, 0.2, 0.5$ Eq. (2.1) implies that $r_{\text{max}} = 11M$, $13.5M$, $27M$, respectively. These values of r_{max} are rough estimates based on a Newtonian order calculation, in practice, we slightly modify those values of initial separations in order to account for the increase of computational cost depending on the mass ratio and the spins of the simulations as observed in Table IV. For instance, in the case of negative spin components the merger time is significantly reduced [58], thus, we increase r_{max} for $e = 0.1, 0.2$ cases in order to produce longer NR waveforms which are easier to hybridize afterwards.

In order to produce initial data for a desired eccentricity we then make use of Eq. (3.25) of [55] to perturb the initial tangential momentum of the black holes by a factor λ_t from its quasicircular value. The expression for λ_t in terms of the eccentricity at 1PN order is

$$\lambda_t(r, e_0, \eta, \text{sign}) = 1 + \frac{e_0}{2} \times \text{sign} \times \left[1 - \frac{1}{r}(\eta + 2)\right], \qquad (2.2)$$

where η is the symmetric mass ratio, r is the orbital separation and sign $= \pm 1$ depends on the initial phase of the eccentricity

estimator [55]. We refer the reader to Sec. III D of [55] for an explicit derivation of Eq. (2.2). Taking Eq. (2.2) we compute the correction factor applied to the momentum as the mean between the inverse of the expression with the plus sign plus the expression with the minus sign,

$$
\begin{aligned}
\bar{\lambda}_t^0(r, e_0, \eta) &= \frac{1}{2} \left[\lambda_t(r, e_0, \eta, +1)^{-1} + \lambda_t(r, e_0, \eta, -1) \right] \\
&= \frac{8r^2 - e_0^2(\eta - r + 2)^2}{4r(e_0(-\eta + r - 2) + 2r)}.
\end{aligned} \tag{2.3}
$$

We use the combination of factors in Eq. (2.3) because we have experimentally tested that it works more accurately than just specifying a value of $\lambda_t(r, e, \text{sign})$ with a given sign. In Table IV one can compare the value of the desired initial eccentricity, e_0, specified in Eq. (2.3), and the actually measured initial eccentricity, e_ω, from the orbital motion of the simulation. Both quantities are also displayed in Fig. 10 of App. A, where we have differentiated among non-spinning, positive and negative spin simulations. The results point out that the use of Eq. (2.3) produces differences of less than 10% between e_ω and e_0 in non-spinning cases at low eccentricities of the order of 0.1. However, when spins are present or the eccentricities are higher, the inaccuracy of the formula becomes manifest, with differences of the order of $20 - 30\%$, this is due to the fact that Eq. (2.2) was derived assuming a non-spinning binary in the low eccentric limit. Additionally, one can check in Table IV and Fig. 10 that the differences between e_ω and e_0 are smaller for the cases with positive spins than in cases with negative spins because in Eq. (2.2) the radiation reaction effects, which are more significant for negative spins, are also not taken into account.

C.   Final state of spinning eccentric systems

We compare the final state of the eccentric NR simulations with the predicted final mass and final spin of the QC NR fits [59] as an indicator of circularisation of the coalescence process as the binary merges. This is basically an extension of [53] to the eccentric spinning case with more moderate values of the eccentricity, but with longer NR evolutions.

The final mass and final spin of the simulations are computed using the apparent horizon (AH) of the remnant black hole and are shown in Table IV. The magnitude S of the angular momentum of the final black hole can be computed from the integral

$$
S = \frac{1}{8\pi} \oint_{\text{AH}} K_{ij} n^i \phi^j dA, \tag{2.4}
$$

see the discussion in [60, 61]. Here for the BAM code [50] the vector ϕ^j is a coordinate-based approximation to the (approximate) axial Killing vector of the black hole horizon as in [60], and for the Einstein Toolkit code the `QuasiLocalMeasures` module is used, which constructs an approximate Killing vector with rotational symmetry around the spin axis as in [62, 63]. The vector n^i is a spacelike unit normal to the horizon surface and K_{ij} is the extrinsic curvature. The final mass

can be computed from the Christodoulou formula in terms of the BH angular momentum and AH area A as

$$
M_f = \sqrt{M_{irr}^2 + \frac{S^2}{4M_{irr}^2}}, \quad M_{irr} = \sqrt{\frac{A}{16\pi}}. \tag{2.5}
$$

where M_{irr} is the irreducible mass. The dimensionless final spin can then be computed as $\chi_f = S/M_f^2$.

In Fig. 2 we have computed the absolute and relative errors between the eccentric simulations and the quasicircular NR final mass and final spin fitting formulas [59],

$$
\Delta X = \left| \frac{X^{NR}}{X^{QC}} - 1 \right| \times 100, \quad X = M_f \text{ or } \chi_f. \tag{2.6}
$$

The results in Fig. 2 show that the differences in the final spin are generally higher than for the final mass. However, the differences with respect to the quasicircular fitting values are as high as $\sim 1\%$ which is entirely consistent with numerical errors and gauge artifacts in the apparent horizon surfaces and inaccuracies in the fits. Hence, we can conclude that within the current knowledge of systematic errors (compare [59]), the final state of the eccentric simulations up to the values of eccentricity studied here, is consistent with the quasicircular values. Identifying small physical deviations between the quasicircular and eccentric final states will require numerical simulations with improved error estimates.

D.   Measuring the eccentricity of highly eccentric systems

This subsection aims to extend the discussion on the measurement of the eccentricity in NR presented in [55] to highly eccentric systems. An eccentricity parameter is chosen to describe the non-circularity of orbits, such that for bound orbits its value ranges between 0 and 1, corresponding to circular and extremely elliptical configurations, respectively. Such an eccentricity can only be defined naturally in Newtonian gravity, whereas in general relativity the eccentricity is a gauge dependent quantity. In order to measure the eccentricity in NR data one defines quantities known as eccentricity estimators, which estimate the eccentricity from the relative oscillations of a certain combination of dynamical quantities such as the orbital separation or orbital frequency, or wave quantities like the amplitude or frequency of the $(l, m) = (2, 2)$ mode. All these different estimators are usually defined such that they agree in the Newtonian limit and in the low eccentricity limit.

In [55], where we studied the reduction of residual eccentricity in initial data sets, we choose our eccentricity estimator based on the orbital frequency as

$$
e_\omega(t) = \frac{\omega(t) - \omega(e = 0)}{2\omega(e = 0)} \equiv \frac{\omega(t) - \omega^{\text{fit}}(t)}{2\omega^{\text{fit}}(t)}, \tag{2.7}
$$

where $\omega(t)$ is the orbital frequency of the simulation and $\omega(e = 0)$ is the orbital frequency in the quasicircular limit. We note that when dealing with numerical simulations, the quasicircular frequency in Eq. (2.7) is typically replaced by a fit,
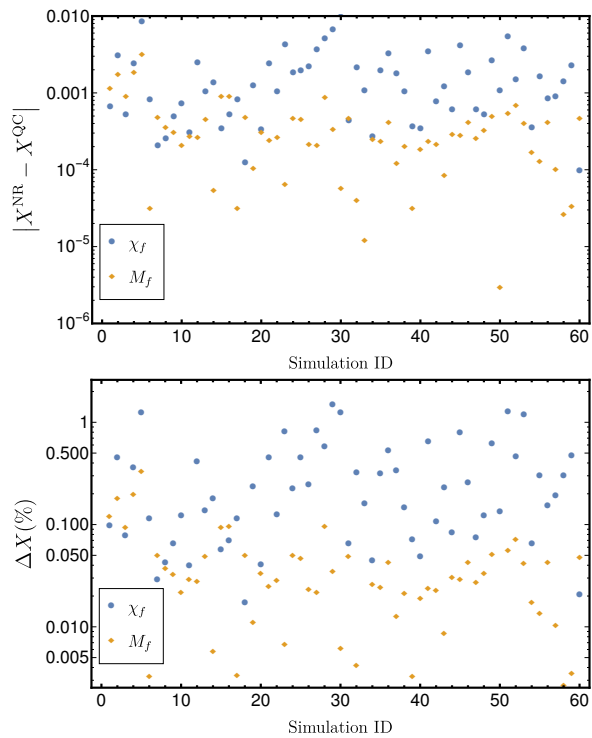
Figure 2: In the top panel the absolute difference between the final mass and spin of the simulations and the QC NR fits as a function of the ID of the simulations in Table IV. In the bottom plot the absolute relative error for the phase and amplitude, $\Delta X = |X^{NR}/X^{QC} - 1| \times 100$ for $X = M_f, \chi_f$, relative error of the final mass and final spin of the simulations against the QC NR fits as a function of the ID of the simulations in Table IV.

$\omega^{\text{fit}}(t)$, of the non-oscillatory part of the frequency [55]. This eccentricity estimator is largely used to measure the residual eccentricity of NR simulations of quasicircular black-hole binaries. We remark that while in Eq. (2.7) we decide to use the orbital frequency calculated from the BH motion, one can also use the gravitational wave frequency extracted from the waves as discussed below. Furthermore, gauge effects can impact the eccentricity measurement from the orbital frequency of NR codes as extensively discussed in the small eccentricity limit in [64, 65]. Here, we follow the practice of the literature [55, 64–66] to avoid contamination of the eccentricity measurement through the gauge quantities, like the choice of the value of the η-parameter in the Gamma driver condition [67], which can lead to residual oscillations in the orbital frequency complicating the determination of the eccentricity.

In [55], we argue that the procedure shown there, based on Eq. (2.7), to measure the eccentricity is limited to values as high as $e \sim 0.1$ due to the lack of an accurate ansatz to fit the higher order contributions beyond the sinusoidal contribution. While the lack of an ansatz for high eccentricities is a clear limitation, the use of (2.7) biases the eccentricity measurement due to its reliance on a non-eccentric fit of the orbital
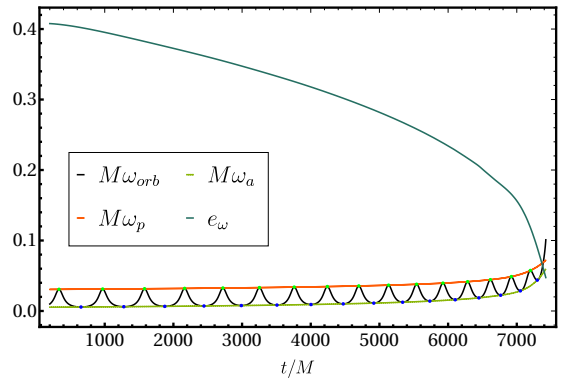

Figure 3: Time evolution of the orbital frequency, $M\omega_{orb}$, the orbital frequency at apastron, $M\omega_a$, the orbital frequency at periastron $M\omega_p$ and the eccentricity estimator, e_ω, defined in Eq. (2.8).

frequency and due to the fact that Eq. (2.7) for high eccentricities does not reduce to the common definition of eccentricity in the Newtonian limit.

Therefore, we decide to change to another estimator [68], constructed also from the orbital frequency,

$$e_\omega(t) = \frac{\omega_p^{1/2} - \omega_a^{1/2}}{\omega_p^{1/2} + \omega_a^{1/2}}, \qquad (2.8)$$

where ω_a, ω_p are the orbital frequency at apastron and periastron, respectively. The eccentricity estimator in (2.8) does not depend on any non-eccentric fit of the orbital frequency. Furthermore, as shown in Appendix B the eccentricity estimator from (2.7) in the Newtonian limit at high eccentricities does not reduce to the eccentricity parameter and it is not normalized, while the eccentricity estimator from (2.8) fulfills all these conditions.

We measure the eccentricity from the maxima and minima of the orbital frequency corresponding to the periastron and apastron passages, respectively. Additionally, we produce an interpolated function from the maxima, ω_p, and the minima ω_a, and substitute them into Eq. (2.8), so that one can estimate the evolution of the eccentricity from those points. The interpolation is calculated using the Hermite method implemented in the function `Interpolation` in Mathematica [69]. The new procedure to measure the eccentricity is shown in Fig. 3, where the time evolution of the orbital frequency, the interpolated functions of the maxima and minima of the orbital frequency and the eccentricity are shown for the configuration with ID 60 from Table IV. As expected the eccentricity is a monotonically decaying function, whose value at $t = 200M$, after the burst of junk radiation, is $e_\omega = 0.415 \pm 0.005$. The error in the eccentricity, δe_ω, is computed using error propagation: from Eq. (2.8) we obtain

$$\delta e_\omega = \frac{\delta\omega}{\left(\omega_a^{1/2} + \omega_p^{1/2}\right)^2} \left[\frac{\omega_a^{1/2}}{\omega_p^{1/2}} + \frac{\omega_p^{1/2}}{\omega_a^{1/2}}\right], \qquad (2.9)$$

where we have assumed $\delta\omega_a = \delta\omega_p = \delta\omega$. Motivated by the results of the error in the convergence analysis of the orbital

frequency in [70] we have taken as a conservative estimate for $\delta\omega = 0.0001$. The error estimate of Eq. (2.9) is the statistical error associated with eccentricity measurement taking into account the error of the orbital frequency from different resolutions of NR simulations. We remark that this error does not take into account systematics coming from the use of a different eccentricity estimator, neither contributions from the interpolation error when the number of minima and maxima is small due to the short length of the simulations. Due to the difficulties in quantifying the systematics associated with the choice of the eccentricity estimator estimator and the fact that the interpolation error is a subdominant effect for most of the simulations here, we restrict for simplicity our eccentricity error calculation to Eq. (2.9).

The main drawback of this method is that when the simulations are so short that there is only one minimum and one maximum it becomes inefficient and inaccurate. Furthermore, one could choose the frequency of the $(l, m) = (2, 2)$ mode and compute the orbital frequency as $\omega_{orb} \approx \omega_{22}/2$, and employ the same method as discussed in this section. Nevertheless, as pointed out in [64] the usage of the orbital frequency from the $(2, 2)$-mode requires additional post-processing of the data due to the presence of high frequency noise when taking a time derivative of the phase of the $(2, 2)$-mode. As a conclusion, if one has long enough highly eccentric simulations, the method introduced in this section allows one to measure the eccentricity as a monotonically decaying function for the whole inspiral, which is a key tool to be used to construct a time domain eccentric waveform model.

III. HYBRIDIZATION OF ECCENTRIC WAVEFORMS

In the eccentric case the hybrization of the PN-NR waveforms is a challenging problem. The higher the eccentricity the stronger is the interaction between the binary components at each periastron passage, which can break the post-Newtonian, weak-field and low velocity, approximation and generate a secular dephasing between both waveforms. Moreover, the lack of a general description in PN theory of eccentric black-hole binary systems poses the main difficulty. Therefore, we briefly review the status of the PN theory for eccentric systems in Sec. III A. In Sec. III B we show an example of our procedure to hybridize eccentric PN-NR waveforms.

A. Review of eccentric post-Newtonian theory

As far as the authors know by the time of writing this communication, the orbital averaged gravitational wave energy flux for eccentric binaries is know up to 3PN order [71] using the 3PN QK parametrization [31]. Our strategy consists in evolving the 3.5PN Hamilton's equations of motion in ADMTT gauge[72–74] for a point particle binary,

$$\frac{d\boldsymbol{X}}{dt} = \frac{\partial \mathcal{H}}{\partial \boldsymbol{P}}, \quad \frac{d\boldsymbol{P}}{dt} = -\frac{\partial \mathcal{H}}{\partial \boldsymbol{X}} + \boldsymbol{F}, \quad \frac{d\boldsymbol{S}_i}{dt} = \frac{\partial \mathcal{H}}{\partial \boldsymbol{S}_i} \times \boldsymbol{S}_i, \quad i = 1, 2.$$
(3.1)

with $\boldsymbol{X}, \boldsymbol{P}$ and $\boldsymbol{S}_i$ the position, momentum and spin vectors in the center-of-mass frame, $\mathcal{H}$ the Hamiltonian described in Sec. II of [55] and $\boldsymbol{F}$ the radiation reaction force described in [75] enhanced with the eccentric contribution to the energy flux from [71]. The eccentric term in the flux is expressed in the QK parametrization and depends only on the orbital frequency ω, which is computed while evolving the system, and the eccentricity e_t, for which we use its 3PN expression in terms of the orbital energy and the angular momentum of the system, which are variables computed at each time step.

The solution of the PN point particle equations, Eqs. (3.1), can be used to compute the gravitational radiation emitted by the system. Here, the lack of general PN expressions for the waveforms of point particles evolving on quasi-elliptical orbits sets a strong limitation. The instantaneous terms of the waveform multipoles are known up to 3PN order for general non-spinning systems with arbitrary eccentricity [76]. Recently, the complete description of the 3PN non-spinning multipoles has been computed including tail, tail-of-tails and memory terms within the QK parametrization for low eccentricities [77, 78]. At this point only using the 3PN instantaneous terms [76] introduces more error than the quadrupole order, due to the missing tail and tail-of-tails terms that enter at 1.5PN, 2.5PN and 3PN orders, respectively. Additionally, the translation of the generic solution we obtain from solving Eqs. (3.1) to the QK form of the waveform modes in [77, 78] is more involved due to the fact that they split the dynamical variables into adiabatic and post-adiabatic contributions. Therefore, we will restrict here to the quadrupole formula to generate the $(l, m) = (2, 2)$ mode and leave for future work the generation of full 3PN waveforms, which will additionally allow us to construct multimode eccentric hybrids.

B. Hybridization example

The hybridization of PN and NR waveforms consists in determining the time shift and phase offset which minimizes the difference between both waveforms in a certain time window. This hybridization procedure is well-established in the quasi-circular case [43, 48, 49, 79, 80]. The time shift is usually computed by minimizing a suitable quantity that measures disagreement of the two waveforms, such as an overlap integral [48, 80], or the deviation between phase or frequency of the $(2, 2)$-mode [49]. However, in the eccentric case the calculation of the time shift requires alignment of the peaks due to eccentricity of both waveforms in the hybridization window. This alignment is complicated to obtain with the phase because the peaks corresponding to each periastron passage are not very pronounced and they are difficult to estimate. One could use the frequency of the $(2, 2)$ mode. However, it is a quantity obtained from a time derivative of the phase, which for NR waveforms tends to be noisy. As a consequence, for simplicity we use the amplitude of the $(2, 2)$ mode to determine the time shift of the waveform because it is a clean quantity with clearly defined peaks. We remark that aligning the oscillations of the amplitude of PN and NR waveforms in a certain hybridization window is equivalent to minimiz-

ing their difference as the maximum agreement between both quantities is obtained when both are aligned at the eccentric peaks.

As an example, we take the NR simulation with ID 60 of Table IV, which is a mass ratio $q = 4$ non-spinning configuration with an initial eccentricity of $e_\omega^0 = 0.415 \pm 0.005$ and initial orbital separation at apastron $D_0 = 27.5M$. We take the initial conditions of the NR simulation defined by the initial position vector, momenta (velocities in the case of SpEc waveforms) and dimensionless spin vectors: $\{X, P/V, S_1, S_2\}_{t=0}$. The fact that PN and NR coordinates for the initial data agree up to 1.5PN order [81–83] makes this identification a good approximation. However, we have checked that the differences between PN and NR initial conditions can produce discrepancies between the NR and PN waveforms of the order of 10%.

In order to leverage these differences we decide to modify the initial condition vector of the PN evolution by modifying the initial separation by a δr such that the difference in the amplitude of the Newman-Penrose scalar, ψ_4, for the $(2, 2)$-mode between PN and NR is minimal. In our example we obtained $\delta r = 0.08$. The outcome of such a calculation can be observed in the top panel of Fig. 4, where the time domain amplitude of the PN and NR waveforms are shown. We do not show the full time domain range of the hybrid waveform in the top panel of Fig. 4 to better display the matching PN/NR region. The procedure is also applied to eccentric aligned-spin configurations. We find that initial highly eccentric configurations require larger δr than low eccentric ones, and that the hybridization errors for high negative spins, where radiation reaction plays a dominant role, are one order of magnitude higher than for non-spinning or low spins due to the lack of expressions for PN spinning eccentric waveforms.

The procedure to construct the hybrid waveform is similar to the one presented in [49]. We first choose the matching region to be after the junk radiation burst, in our particular case we take $t/M \in (275, 375)$, which corresponds to less than one gravitational wave cycle as shown in the top panel of Fig. 4. In order to understand the choice of this short hybridization window for eccentric waveforms, we first explain the criteria for hybridizing quasicircular ones following [103]. Quasicircular waveforms are hybridized over several cycles as the low frequency approximant, typically EOB, is very accurate and resembles faithfully the NR behavior during the late inspiral. Furthermore, hybridization over several cycles is required to accurately compute the time-alignment between waveforms by averaging out residual oscillations due to eccentricity and high frequency numerical noise coming from NR. In the eccentric case, the time-alignment is much easier to compute as the peaks in the GW frequency ease such an alignment, so there is no need to use several cycles. Moreover, the inaccuracy of the current low frequency eccentric approximants sets also a clear limitation to faithfully reproduce the NR waveforms along several cycles. Hence, we have chosen a small hybridization window to ensure small errors in the GW amplitude and frequency between PN and NR. Choices of hybridization window including several cycles make that error increase to 10% or larger depending on the case, due to the inaccuracy of the PN approximant. We have also checked that

the election of different peaks for hybridization in the GW amplitude (in the inspiral regime), does not change significantly the errors maintaining them below 1% as quoted in the low panel of Fig. 4.

After choosing the hybridization region, we have to compute the time shift, τ, and phase offset, φ_0, which reduce the difference between the PN and NR waveforms in the matching window,

$$h^{PN}(t) = e^{i\varphi_0} h^{NR}(t + \tau). \qquad (3.2)$$

In order to align the waveforms in time we choose τ such that it minimizes the amplitude difference along the matching window. For the phase offset we decide to align the phases at the beginning of the the window, $\varphi_0 = \phi^{NR}(t_0 - \tau) - \phi^{PN}(t_0)$, where t_0 is the initial time of the window. Once τ and φ_0 are calculated the hybrid waveform is constructed as a piecewise function

$$h^{hyb}(t) = \begin{cases} e^{i\varphi_0} h^{PN}(t + \tau) & \text{if } t < t_1 \\ w^-(t) e^{i\varphi_0} h^{PN}(t + \tau) + w^+(t) h^{NR}(t) & \text{if } t_1 < t < t_2 \\ h^{NR}(t) & \text{if } t > t_2 \end{cases}$$
$$(3.3)$$

where $t_1 = 275M$ and $t_2 = 375M$. The functions $w^\pm(t)$ denote the blending functions defined in the interval $[t_1, t_2]$ that monotonically go from 0 to 1 and from 1 to 0, respectively,

$$w^+(t)_{[t_1,t_2]} = \frac{t - t_1}{t_2 - t_1}, \quad w^-(t)_{[t_1,t_2]} = 1 - w^+(t). \qquad (3.4)$$

The result of the application of such a hybridization procedure can be observed in the bottom panel of Fig. 4, where the absolute value of the relative error between the hybrid and NR amplitude and frequency are shown. The quantity ΔX is defined as $\Delta X = |X^{hyb}/X^{NR} - 1| \times 100$ for $X = A_{22}, \omega_{22}$. The errors in the gravitational wave frequency and amplitude are both below 1%, being those for the amplitude slightly smaller due to the choice of the amplitude as the quantity with which to minimize the agreement between PN and NR waveforms.

Finally, note that the PN waveform used to produce the hybrid is evolved backwards in time from $D_0/M = 27.5$ to $D_f/M = 60$. This makes the initial eccentricity to increase with respect to the NR waveform. Next, we explicitly show the systematics affecting the measurement of the initial eccentricity of the hybrid. We display in Fig. 5 the time evolution of the orbital frequency for the same hybrid waveform of Fig. 4, $\omega_{orb} \approx \dot\phi_{22}/2$, computed from the phase of the $(2, 2)$ mode of the Newman-Penrose scalar and the strain computed using Fixed-Frequency Integration (FFI) algorithm [84]. We also compute the orbital frequency from the PN dynamics as,

$$\omega = \left| \frac{v \times r}{r^2} \right| \qquad (3.5)$$

where $r = |r|$, and v, r are the velocity and the position vectors in the center of mass frame. The curves from Fig. 5 indicate that the orbital frequency computed from ψ_4 and h overestimate and underestimate, respectively, the values of eccentricity with respect to the ones from the dynamics. This is confirmed from the values for the initial eccentricity one obtains
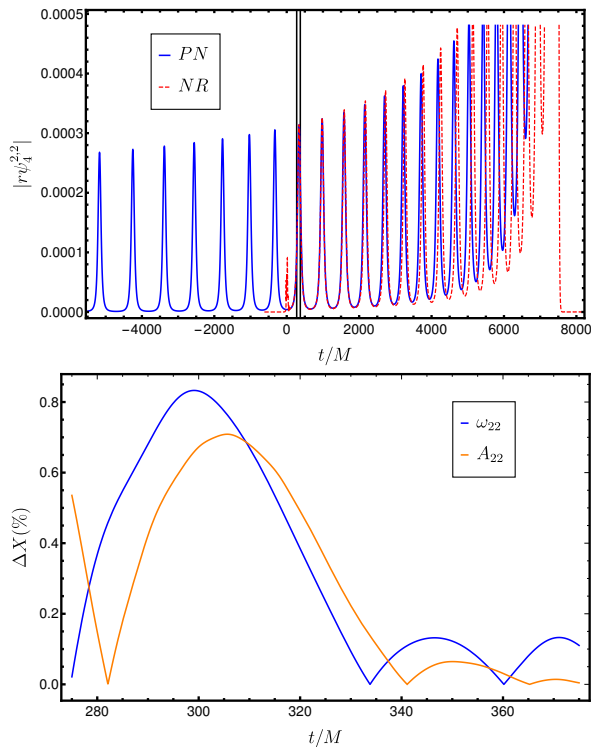
Figure 4: In the top panel the time domain amplitude of the $|r\psi_4^{2,2}|$ mode. The blue thick and the red dashed curves represent the PN and NR waveforms, respectively, and the vertical black lines highlight the hybridization window. In the bottom plot the absolute value of the relative error for the gravitational wave frequency and amplitude, $\Delta X = |X^{hyb}/X^{NR} - 1| \times 100$ for $X = \phi_{22}, A_{22}$, of the hybrid against the NR waveform in the matching region is displayed.

Figure 5: Time evolution of the orbital frequency, $M\omega_{orb}$ computed from the phase of $r\psi_4^{2,2}$, the orbital frequency computed from the dynamics, $\omega = |\frac{v \times r}{r^2}|$, and from the phase of the strain $h^{2,2}$.

that we choose not to integrate backwards in time too far in the past of the binary due to the inaccuracy of the eccentric PN fluxes which make the solutions inaccurate for extremely high eccentricities and the inaccuracy of the PN expressions for the waveform which also become more and more inaccurate for high eccentricities.

IV. PARAMETER ESTIMATION WITH ECCENTRIC SIGNALS

In this section we employ the waveforms introduced in Secs. II and III for data analysis studies. First, we analyze the impact of the eccentricity when computing overlaps against quasicircular models. Second, we perform parameter estimation studies injecting eccentric NR and hybrid waveforms into detector noise and compute parameter biases using three different IMR quasicircular models available in the LIGO Libraries, LALSUITE [85].

A. Match calculation

A generic black-hole binary evolving in a quasi-elliptical orbit is described by 17 parameters. The intrinsic parameters are the individual masses of the binary m_1, m_2, the 6 components of the two spin vectors, $\vec{S}_1$ and $\vec{S}_2$, the orbital eccentricity e and the argument of the periapsis Ω. The extrinsic parameters describing the sky position of the binary with respect to the detector are: the distance from the detector to the source r, the coalescence time t_c, the inclination ι, the azimuthal angle φ, the right ascension (ϕ), declination (θ) and polarization angle (ψ). All these parameters together describe the strain induced in a detector from a passing gravitational wave [86]

$$h(t, \zeta, \Theta) = [F_+(\theta, \phi, \psi)h_+(t - t_c; \iota, \varphi, \zeta) \\ + F_\times(\theta, \phi, \psi)h_\times(t - t_c; \iota, \varphi, \zeta)]. \tag{4.1}$$

from the orbital frequency of the strain, ψ_4 and the dynamics, $e_0^h = 0.55 \pm 0.01$, $e_0^{\psi_4} = 0.84 \pm 0.03$ and $e_0^{dyn} = 0.65 \pm 0.01$, respectively. These three values of eccentricity are measured at the same initial time, $t = 600M$. These results lead to the conclusion that the eccentricity measured from the frequency of the $(2, 2)$ mode is higher for ψ_4 than for h, this can be understood from the fact that $h \approx \int \int \psi_4 dt' dt$, therefore, h is a smoother function than ψ_4. As shown in Fig. 5 this is not a particular result of our procedure to measure the eccentricity, but a general fact which can be reproduced by any method to measure the eccentricity based on the oscillations of the frequency of the $(2, 2)$ mode. We have decided to show the orbital frequency from the PN dynamics as it contains more cycles and eases the visualization of the effect, but the same effect can be obtained with the orbital frequency from the BH motion of a NR simulation. Moreover, we remark that these differences have also been noted in [64], where they explicitly computed the factor between the eccentricity estimator calculated from the gravitational wave frequency of h and ψ_4 in the low eccentric limit. Thus, one expects to see these discrepancies even augmented as the eccentricity increases as it is the case of the waveforms studied in this article. We also note
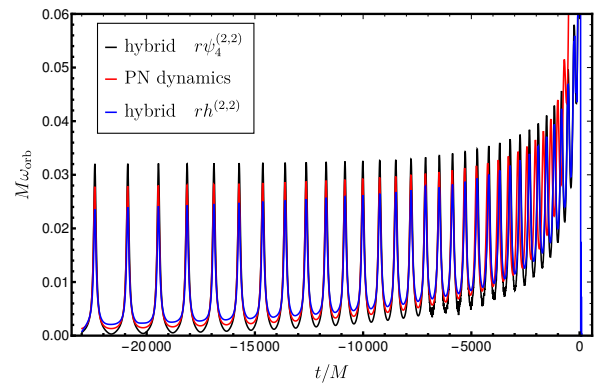
Where $\Theta = \{t_c, r, \theta, \phi, \iota, \varphi, \psi\}$ is the set of extrinsic parameters, $\zeta = \{m_1, m_2, \vec{S}_1, \vec{S}_2, e, \Omega\}$ are the intrinsic parameters and $F_+, F_\times$ are the antenna patterns functions defined in [86] . The detector response is written in terms of the waveform polarizations $(h_+, h_\times)$ which combine to define the complex waveform strain

$$h(t) = h_+ - ih_\times = \sum_{l=2}^{\infty} \sum_{m=-l}^{l} Y_{lm}^{-2}(\iota, \varphi) h_{lm}(t - t_c; \zeta), \quad (4.2)$$

where $Y_{lm}^{-2}(\iota, \varphi)$ are spin-weighted -2 spherical harmonics and h_{lm} refers to the (l, m) waveform mode. The comparison between two waveforms is usually quantified by an overlap integral, which is a noise-weighted inner product between signals [87], and which can be maximised over subsets or all of the parameters of the signal. Given a real-valued detector response, the inner product between the signal, $h_{resp}^S(t)$, and the model, $h_{resp}^M(t)$, is defined as

$$\langle h_{resp}^S | h_{resp}^M \rangle = 4\text{Re} \int_0^{+\infty} \frac{\tilde{h}_{resp}^S(f) \tilde{h}_{resp}^{M*}(f)}{S_n(|f|)} df, \quad (4.3)$$

where $\tilde{h}$ denotes the Fourier transform of h, h^* the complex conjugate of h and $S_n(|f|)$ is the one sided noise Power Spectral Density (PSD) of the detector.

The normalized match optimized over a relative time shift and the initial orbital phase can be written as

$$\mathcal{M}(\iota_S, \varphi_{0_S}) = \max_{t_c, \varphi_{0_S}} \left[\frac{\langle h_{resp}^S | h_{resp}^M \rangle}{\sqrt{\langle h_{resp}^S | h_{resp}^S \rangle \langle h_{resp}^M | h_{resp}^M \rangle}} \right]. \quad (4.4)$$

The match is close to 1 when the model is able to faithfully reproduce the signal, while values of the match close to 0 indicate large disagreement between the two waveforms. In Eq. (4.4) the match is computed for given values of the angles (ι_S, φ_{0_S}) of the signal and maximizing over phase and time shifts. We will take only the h_{22} mode of the eccentric hybrids and a quasicircular (QC) waveform model and compute single mode mismatches maximized over a time shift, t_0, and a phase offset, ϕ_0, as

$$\mathcal{MM} = \max_{t_0, \phi_0} \left[\frac{\langle h_{22}^{\text{hyb}} | h_{22}^{\text{QC}} \rangle}{\sqrt{\langle h_{22}^{\text{hyb}} | h_{22}^{\text{hyb}} \rangle \langle h_{22}^{\text{QC}} | h_{22}^{\text{QC}} \rangle}} \right]. \quad (4.5)$$

To simplify the comparisons we introduce the mismatch, $1 - \mathcal{MM}$. Values of the mismatch close to zero indicate good agreement between the signal and the model, while the higher the mismatch the larger the difference between both waveforms, indicating that the model is not able to accurately represent the signal.

Having set the notation for the calculation of the mismatch, we compute the mismatch between the eccentric (2, 2) mode hybrids computed in Sec. III and the quasicircular model PhenomX [22, 23], which is an upgrade of the aligned-spin PhenomD model [12, 88], with calibration to a larger NR data set and also to extreme-mass ratio waveforms. We employ

the Advanced LIGO' "zero detuned high power" PSD [89] to compute the overlap in Eq. (4.3). The integral of Eq. (4.3) is evaluated between a frequency range of 20 and 2000 Hz. The non-monotonic behaviour of the GW frequency of eccentric systems complicates the determination of the frequency range of a signal in the detector band. The ideal case would be the one in which the initial apastron and periastron frequencies are below 20Hz. This would mean that the whole waveform starts before the cutoff frequencies of the detectors and one observes the complete eccentric inspiral of the binary. Another possibility is that both frequencies are above 20 Hz, then the signal is very short and much of the inspiral waveform is lost. Finally, it is also possible that during some part of the waveform the periastron frequencies are above 20 Hz and apastron frequencies are below 20Hz. The latter is typically the case of our hybrid waveforms.
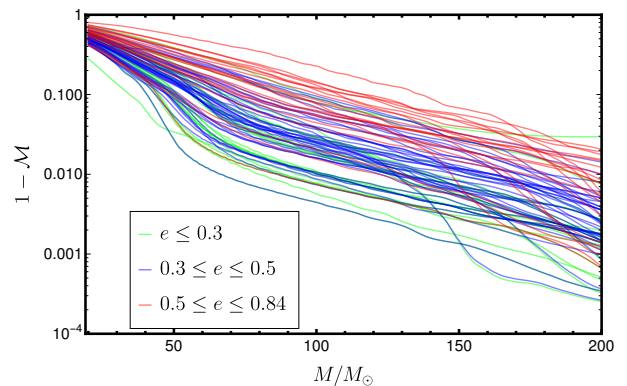
Figure 6: Mismatches for the $(l, m) = (2, 2)$ mode between the eccentric hybrid waveforms corresponding to the cases presented in Table IV of Appendix A and the quasicircular PhenomX waveform model as a function of the total mass of the system. The green, blue, black and red lines correspond to eccentric PN-NR hybrid waveforms with initial eccentricities $e \le 0.3$, $0.3 \le e \le 0.5$ and $0.5 \le e \le 0.84$, respectively.

In Fig. 6 we show the single mode mismatches between the eccentric hybrids and PhenomX for a range of total mass of the system between $M_T \in \{20, 200\} M_\odot$. As expected, for larger total masses of the system most of the waveform in the frequency band of the detector is in the merger and ringdown parts and the mismatches are even below the 3% threshold. This is consistent with the results obtained in Sec. II C, which show the agreement for the final state between the eccentric simulations and the quasicircular fits. However, the lower the total mass the higher the mismatch, this is due to the fact that at low frequencies there is more inspiral part of the waveform in the frequency band, and therefore, the inability of the quasicircular model to resemble the eccentric inspiral becomes notorious. One can also appreciate in Fig. 6 that generally the higher the initial eccentricity the higher the mismatch for the whole mass range.

B. Eccentric Injections into detector noise

In this section we show some applications of the eccentric waveform data set to parameter estimation. We inject eccentric hybrids into Gaussian noise realization recolored to match the spectral density of the Advanced LIGO and Virgo detectors at design sensitivity. All simulations with the same injected signal are performed with the same noise realization. We do not address the challenge of detecting eccentric signals and instead assume that the signal has been detected by standard CBC search pipelines [90]. We perform parameter estimation using the python-based `BILBY` code [91]. Of the numerous stochastic samplers implemented in `BILBY`, we employ the nested sampler `CPNEST` [92] and use waveform approximants implemented in `LALSUITE` [85] as the model templates. The eccentric hybrids make use of the Numerical Relativity injection infrastructure [93, 94].

At the time of writing, the state of the art non-spinning eccentric IMR models [37–40] were not yet implemented in `LALSUITE`. The only eccentric waveform models in `LALSUITE` are inspiral non-spinning frequency domain approximants [32, 95, 96]. We decide not to use such inspiral waveform models to avoid biases induced by the sharp cutoff at the end of the waveform [97]. For a study of the eccentricity measurement using such inspiral approximants see [98, 99]. We restrict to IMR quasicircular approximants and perform parameter estimation analysis on the injected eccentric signals sampling on the 15 parameters of a quasicircular black-hole binary.

ID	Simulation	q	$\chi_{1,z}$	$\chi_{2,z}$	D/M	$e_\omega \pm \delta e_\omega$
61	`SXS:BBH:1355`	1.	0.	0.	12.97	0.090 ± 0.003
62	`SXS:BBH:1359`	1.	0.	0.	15.73	0.146 ± 0.003
63	`SXS:BBH:1361`	1.	0.	0.	16.69	0.209 ± 0.003

Table I: Summary of the injected NR simulations. The first column denotes the identifier of the simulation, the second column indicates the name of the simulation as presented in [38]. Next columns show the mass ratio, z-component of the dimensionless spin vectors, the initial orbital separation and the initial orbital eccentricity as measured using the procedure detailed in Sec. II D.

We inject three NR equal mass non-spinning simulations described in Table I into a network of gravitational wave detectors composed of the LIGO-Hanford, LIGO-Livingston [100] and Virgo interferometers [101], each operating at design sensitivity. We set a reference frequency of $f_{\rm ref}$ = 20 Hz, where the waveforms start. Some injected parameters are displayed in Table II, while the declination is δ = −1.21 rad, the right ascension α = 1.37 rad and the coalescence phase ϕ = 0 rad. From these simulations, the $\{(l,m) = (2,\pm2),(3,\pm2),(4,\pm4),(5,\pm4),(6,\pm6)\}$ modes are used, we do not inject odd m modes because they are zero by symmetry. For the injected signal we choose the luminosity distance, D_L = 430 Mpc, similar to the first detection of a gravitational wave signal, GW150914 [7], which produces a high network signal-to-noise ratio (SNR) as shown in Tables II, III.

We employ a uniform-in-volume prior on the luminosity distance, $p(D_L|H) \propto D_L^2$, between 50 and 1500 Mpc. The inclination and polarization angles have both uniform priors between $(0, \pi)$. We use the standard priors for the extrinsic variables, as in Table I of [91]. Instead of sampling in the component masses we sample in mass ratio, q, and chirp mass, $\mathcal{M}_c$, with a range $(0.05, 1)$ and $(15, 60)M_\odot$, respectively. The spin priors are set differently according to the approximant. If the approximant is non-precessing, we set the option of `aligned_spin=True` in the `BBHPriorDict` function of `Bilby` which samples in the dimensionless spin z-components between -0.8 and +0.8. While for precessing approximants, we sample in the tilt angles, (θ_1, θ_2), the angle between the spin vectors, ϕ_{12}, the angle between **J** and **L**, ϕ_{JL} and the dimensionless spin magnitudes (a_1, a_2). The priors for $a_1, a_2, \theta_1, \theta_2, \phi_{JL}$ and ϕ_{12} are the same as in Table I of [91]. We also define a uniform prior for the coalescence time of two seconds centered at the injection time.

We take three quasicircular models as approximants: 1) IMRPhenomD [12, 88], non-precessing model with only the $(2,\pm2)$ modes, 2) IMRPhenomHM [15], non-precessing model including higher order modes, and 3) IMRPhenomPv2 [13], effective precessing model.

We plot the posterior probability distribution for the chirp mass, mass ratio, effective spin parameter and luminosity distance for the PhenomD approximant in Fig. 7 with 90% credible intervals specified by the dashed vertical lines and the injected values by the magenta thick vertical lines. As a control case we show in Fig. 7 also the posterior distribution of an equal mass non-spinning zero eccentricity injection performed using the hybridized surrogate model NRHybSur3dq8 [19] with the same injected parameters as in Table II and recovered with the PhenomD model. The NRHybSur3dq8 injected waveform contains all higher order modes up to $l = 4$, which in this case seems to cause the small bias one observes in the luminosity distance when recovering with the PhenomD model which only contains the $(2,|2|)$ modes. For the rest of the parameters, like the mass ratio, chirp mass and the effective spin parameter, we obtain results consistent with the accuracy of the PhenomD model for parameter estimation of injected signals as shown in [22].

The posterior distributions for the rest of approximants are shown in Fig. 13 of App. C. The same information is summarized in Fig. 8, where the median and the error bars corresponding to the 90% credible intervals of the posterior distribution are shown as a function of the initial eccentricity. Note that the bars corresponding to the same initial eccentricity but different approximants have been separated by a small amount to ease the visualization of the results. For the lowest initial eccentricity, $e_0 = 0.09$ the results for the four quantities are pretty different. The chirp mass and the effective spin parameter produce similar distributions for the three approximants, while for the mass ratio and the luminosity distance, PhenomHM distributions are closer to the injected values than PhenomD and PhenomPv2.

Furthermore, for $e_0 = 0.14$ and $e_0 = 0.2$ we observe increasing poorer agreement with the injected values, except for the mass ratio where the lowest initial eccentricity signal pro-

duces wider distributions than the ones with higher initial eccentricity. This can also be checked in Table II, where the recovered parameters, median values and 90% credible intervals, are compared to the injected values. Regarding the effective spin parameter and the chirp mass, the increase of initial eccentricity in the injected signal shifts the posteriors for the three quasicircular models, while for the mass ratio the increase of initial eccentricity reduces the bias on the measurement of the mass ratio, probably as a consequence of the shift in the chirp mass distribution, as displayed in Fig. 11 of App. C for the all the injections recovered with the PhenomD model.

One observes also that PhenomHM recovers better the injected parameters than PhenomD and PhenomPv2. For the luminosity distance the probability densities tend to flatten and be closer to the prior distributions for high initial eccentricities, one notes again that PhenomHM has less parameter bias than PhenomD and PhenomPv2. Injected values of the sky position like the right ascension $\alpha = 1.375$ rad and $\delta = -1.21$ rad are well recovered for all the nine runs, probably due to the expensive PE settings described in App. C : $\alpha = 1.37^{+0.01}_{-0.01}$ rad and $\delta = -1.21^{+0.01}_{-0.01}$ rad.

Furthermore, we have computed the recovered matched-filter SNR for the detector network, ρ_{Match}, for each simulation. This quantity, ρ_{Match}, is computed calculating the matched filter between the detector data with the eccentric signal injected and the waveform of the approximant waveform model with the parameters corresponding to the highest log-likelihood value of the posterior distribution. The results of such a calculation are shown in Table I. As expected, we observe that the zero eccentricity injection recovers much more SNR than the eccentric injections, with decreasing values of the recovered SNR with increasing eccentricity.

Additionally, we display the values of the log Bayes factor for each simulation. The Bayes factor is computed here as the ratio between the signal and null evidences (see Eq. 13 of [102]). One can observe that both the recovered matched-filter SNR and the log Bayes factor decrease the higher the initial eccentricity of the injected signal. The matched-filter SNR produces similar values between models for simulations with the same initial eccentricity. However, the log Bayes factor tends to be slightly higher for aligned-spin waveform models, PhenomD and PhenomHM, for the lowest initial eccentric injected signal, while for higher initial eccentricities the precessing model IMRPhenomPv2 shows slightly greater log Bayes factors than the aligned-spin ones. The highest log Bayes factor is obtained for the zero-eccentricity injection.

We repeat the same procedure injecting a hybrid waveform, including only the $(l, m) = (2, \pm2)$ modes, of an eccentric spinning waveform with ID 8 of Table IV. This is an equal mass with the z-component of the dimensionless spin vectors $\chi_{1z} = \chi_{2z} = -0.25$ and initial eccentricity $e_0 = 0.420 \pm 0.006$. The posterior distribution for the chirp mass, mass ratio, luminosity distance and χ_{eff} are shown in Fig. 9 for the IMRPhenomD, IMRPhenomHM and IMRPhenomPv2 as waveform models. In this case, the parameter biases are much higher than in the previous injection study mainly due to the fact that the injected signal has a much higher initial eccentricity.

The values of the recovered parameters as well as the injected values are shown in Table III. The injected values of the sky position like the right ascension $\alpha = 1.375$ rad and $\delta = -1.21$ rad are again well recovered parameters for the three runs $\alpha = 1.37^{+0.01}_{-0.01}$ rad and $\delta = -1.21^{+0.01}_{-0.01}$ rad. The bias in the chirp mass is $\sim 4M_\odot$ for the three models. Here one observes again the correlation between chirp mass and mass ratio, the shift in chirp mass posteriors with respect to the injected value translates into a better determined mass ratio distribution, which is clearly the case for PhenomHM which performs unexpectedly well recovering the mass ratio parameter, while PhenomD and PhenomPv2 show much wider distributions and much larger credible intervals.

The posteriors of the luminosity distance show also large error bars for the three models, where again PhenomHM reduces the bias with respect to PhenomD and PhenomPv2. The recovered effective spin parameter is completely off with respect to the injected value for the three approximants. The recovered χ_{eff} is positive while the injected one is negative, the bias in the effective spin parameter is approximately -0.3 for the three models, indicating the inability of the quasicircular models to estimate the spin parameter of highly eccentric spinning binaries with quasicircular models. Regarding the recovered matched-filter SNR and the log Bayes factor displayed in Table III one can observe that while the SNR provides comparable values among models, the values of the log Bayes factor indicate that PhenomPv2 fits scarcely better the data than PhenomHM and PhenomD.

This section shows examples of the kind of study that one is able to perform with the current eccentric waveform data set. We have shown the limitations of the current IMR quasicircular to estimate the parameters of moderately eccentric waveforms including a moderately spinning case. For the cases studied in this section we have found that although the use of quasicircular models to estimate parameters of eccentric signals leads to inevitable biases, aligned spin quasicircular models with higher order modes leverage the impact of this biases for the mass ratio and the luminosity distance when compared to aligned spin models with only the $(2, \pm2)$ modes or precessing models. Due to the computational cost of the PE runs and the amount of eccentric waveforms available we leave for future work a detailed study of the whole data set using not only quasicircular models, but also eccentric waveform approximants.

V. SUMMARY AND CONCLUSIONS

In this paper we have presented the first parameter study of numerical relativity simulations of eccentric spinning black-hole binaries. We have presented a simple procedure to set up the initial parameters of eccentric simulations. The higher the initial eccentricity of the simulation the longer the initial separation has to be in order to avoid the immediate plunge of the binary due to the strong interactions at the periastron. This increases the computational cost of the simulations of Table IV with $e_0 \sim 0.4$ which is roughly double the one with $e_0 \sim 0.2$ as can be observed in their merger times. Additionally, longer

e_0	Model	$m_1/M_\odot$	$m_2/M_\odot$	$\mathcal{M}_c/M_\odot$	q	D_L/Mpc	$\chi_{\rm eff}$	ψ (rad)	ι (rad)	$\rho_{\rm Match}$	$\log\mathcal{B}$
	PhenomD	$35.06^{+2.55}_{-1.92}$	$31.29^{+1.10}_{-1.33}$	$28.40^{+0.17}_{-0.17}$	$0.87^{+0.10}_{-0.17}$	384^{+49}_{-82}	$0.00^{+0.02}_{-0.02}$	$1.60^{+1.28}_{-1.34}$	$0.54^{+0.32}_{-0.32}$	89.40	3463.79
0.09	PhenomHM	$34.05^{+2.14}_{-1.16}$	$31.79^{+0.69}_{-1.17}$	$28.38^{+0.16}_{-0.16}$	$0.92^{+0.07}_{-0.11}$	429^{+16}_{-33}	$-0.01^{+0.02}_{-0.02}$	$2.01^{+0.97}_{-1.82}$	$0.28^{+0.21}_{-0.17}$	89.28	3463.78
	PhenomPv2	$35.26^{+2.97}_{-2.06}$	$31.28^{+1.18}_{-1.53}$	$28.44^{+0.21}_{-0.18}$	$0.86^{+0.11}_{-0.13}$	412^{+24}_{-66}	$0.00^{+0.02}_{-0.02}$	$1.65^{+1.32}_{-1.32}$	$0.39^{+0.32}_{-0.22}$	89.19	3459.54
	PhenomD	$34.03^{+1.34}_{-0.72}$	$32.63^{+0.44}_{-0.73}$	$28.86^{+0.15}_{-0.15}$	$0.95^{+0.04}_{-0.07}$	407^{+53}_{-84}	$0.02^{+0.02}_{-0.02}$	$1.58^{+1.21}_{-1.23}$	$0.54^{+0.32}_{-0.32}$	84.87	3288.25
0.14	PhenomHM	$33.76^{+0.96}_{-0.54}$	$32.73^{+0.35}_{-0.56}$	$28.82^{+0.16}_{-0.14}$	$0.96^{+0.03}_{-0.05}$	408^{+46}_{-52}	$0.02^{+0.02}_{-0.02}$	$1.91^{+0.46}_{-0.58}$	$0.54^{+0.19}_{-0.25}$	84.74	3283.61
	PhenomPv2	$34.22^{+1.48}_{-0.89}$	$32.54^{+0.54}_{-0.82}$	$28.87^{+0.19}_{-0.21}$	$0.94^{+0.05}_{-0.08}$	389^{+33}_{-60}	$0.01^{+0.02}_{-0.03}$	$1.70^{+1.09}_{-1.07}$	$0.64^{+0.25}_{-0.18}$	85.08	3302.37
	PhenomD	$35.65^{+1.52}_{-0.85}$	$34.01^{+0.51}_{-0.82}$	$30.13^{+0.16}_{-0.16}$	$0.94^{+0.05}_{-0.07}$	420^{+72}_{-109}	$0.07^{+0.02}_{-0.02}$	$1.57^{+1.36}_{-1.18}$	$0.61^{+0.41}_{-0.37}$	81.88	3102.70
0.2	PhenomHM	$35.47^{+1.36}_{-0.78}$	$33.97^{+0.46}_{-0.72}$	$30.06^{+0.16}_{-0.15}$	$0.95^{+0.04}_{-0.07}$	438^{+43}_{-47}	$0.06^{+0.02}_{-0.02}$	$0.42^{+0.90}_{-0.29}$	$0.54^{+0.16}_{-0.20}$	81.97	3101.79
	PhenomPv2	$37.13^{+2.11}_{-1.76}$	$33.20^{+1.00}_{-1.12}$	$30.12^{+0.21}_{-0.22}$	$0.87^{+0.09}_{-0.09}$	414^{+41}_{-69}	$0.06^{+0.02}_{-0.02}$	$1.62^{+0.98}_{-1.29}$	$0.66^{+0.25}_{-0.18}$	82.05	3112.97
0	PhenomD	$34.07^{+2.05}_{-1.29}$	$30.91^{+1.24}_{-1.77}$	$28.24^{+0.16}_{-0.16}$	$0.91^{+0.07}_{-0.10}$	375^{+48}_{-75}	$0.0^{+0.02}_{-0.02}$	$1.58^{+1.28}_{-1.24}$	$0.53^{+0.33}_{-0.32}$	173.16	3632.19
	Injected	32.5	32.5	28.29	1.	430	0.	0.33	0.3		

Table II: Black hole binary recovered parameters for the three NR simulations from Table I. The last row corresponds to the injected parameters. In the penultimate row we show the recovered parameters of the zero eccentricity injection performed with NRHybSur3dq8 model. The first column describes the initial eccentricity of the injected signal, then we specify the approximant, the component masses, the chirp mass, mass ratio, luminosity distance, effective spin parameter, polarization angle, inclination, the recovered matched-filter SNR for the detector network and the log of the Bayes factor.
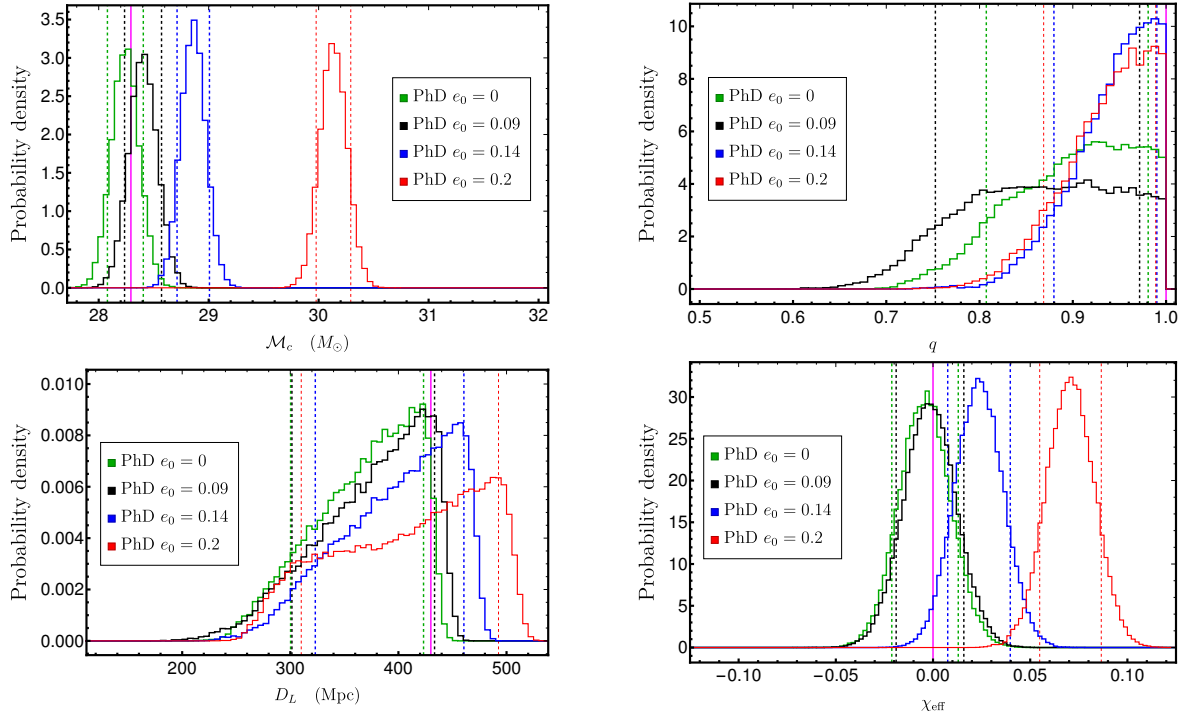
Figure 7: Posterior probability distributions for the injected NR simulations of Table I and a zero eccentricity injection using the NRHybSur3dq8 model. The vertical dashed lines correspond to 90% credible regions. The magenta thick vertical line represents the injected value. The green, black, blue and red curves represent distributions sampled using the IMRPhenomD approximant with injected initial eccentricities, $e_0 = 0.0, 0.09, 0.14, 0.2$, respectively.
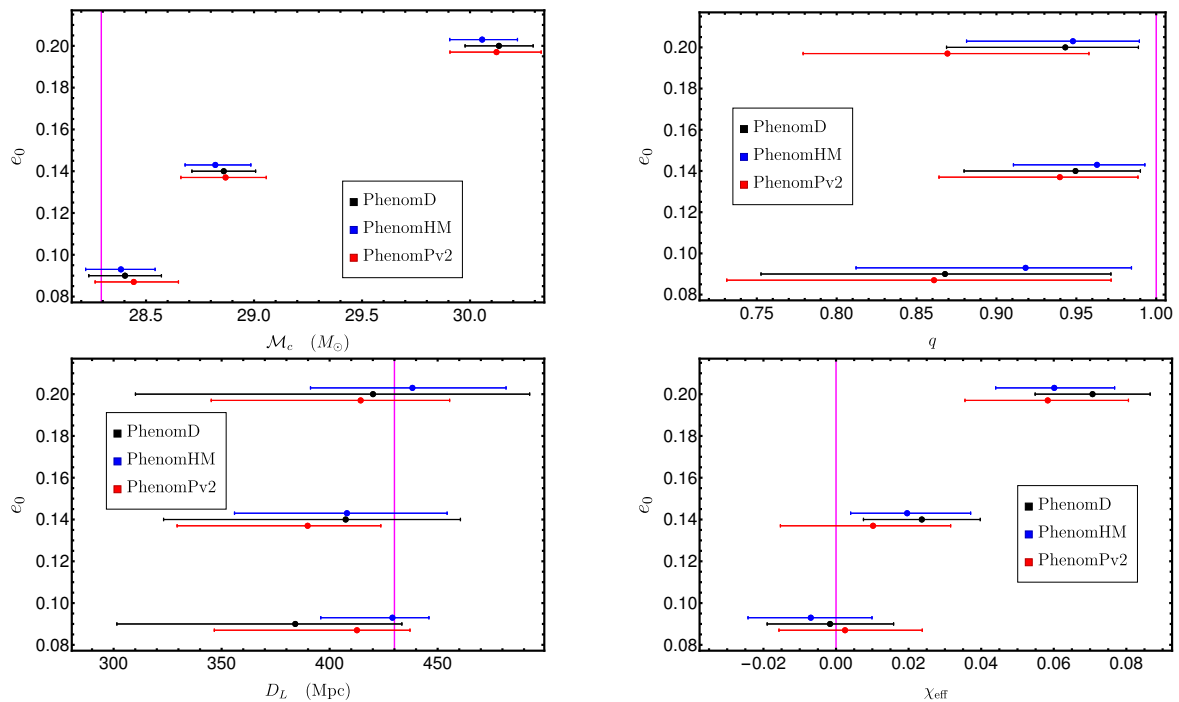
Figure 8: Median values and error bars corresponding to 90% credible regions of the posterior probability distributions for the injected NR simulations of Table I. The vertical magenta line represents the injected value. The black, blue and red segments represent the median values and errors bars of the distributions sampled using the IMRPhenomD, IMRPhenomHM and IMRPhenomPv2 approximants, respectively. The cases are represented for three initial eccentricities of the injected signal, $e_0 = 0.09, 0.14, 0.2$. To ease the visualization of the horizontal bars, cases with the same initial eccentricity and run with different approximants have been separated a $\Delta e = 0.003$.

e_0	Model	$m_1/M_\odot$	$m_2/M_\odot$	$\mathcal{M}_c/M_\odot$	q	D_L/Mpc	χ_{eff}	ψ (rad)	ι (rad)	ρ_{Match}	$\log \mathcal{B}$
	PhenomD	$37.52^{+1.30}_{-0.76}$	$36.04^{+0.49}_{-0.73}$	$31.86^{+0.19}_{-0.2}$	$0.95^{+0.04}_{-0.06}$	474^{+62}_{-101}	$0.06^{+0.02}_{-0.02}$	$2.60^{+0.31}_{-0.33}$	$1.54^{+1.22}_{-1.19}$	82.68	2895.91
0.42	PhenomHM	$37.23^{+0.95}_{-0.37}$	$36.62^{+0.30}_{-0.81}$	$32.07^{+0.18}_{-0.23}$	$0.98^{+0.02}_{-0.06}$	384^{+54}_{-45}	$0.08^{+0.02}_{-0.02}$	$2.28^{+0.18}_{-0.16}$	$1.04^{+1.12}_{-0.26}$	82.54	2894.17
	PhenomPv2	$39.15^{+2.08}_{-1.62}$	$35.20^{+0.84}_{-1.06}$	$31.87^{+0.23}_{-0.26}$	$0.88^{+0.07}_{-0.08}$	413^{+77}_{-110}	$0.05^{+0.03}_{-0.03}$	$2.33^{+0.33}_{-0.44}$	$1.46^{+1.36}_{-0.45}$	82.62	2910.28
	Injected	32.5	32.5	28.29	1.	430	-0.25	0.33	0.3		

Table III: Black hole binary recovered parameters for the spinning hybrid waveform from Fig. 9. The last row corresponds to the injected parameters. The first column describes the initial eccentricity of the injected signal, then we specifiy the approximant, the component masses, the chirp mass, mass ratio, luminosity distance, effective spin parameter, polarization angle, inclination,the recovered matched-filter SNR for the detector network and the log of the Bayes factor.

initial separations produce long enough waveforms which allow to avoid the breakdown of the post-Newtonian approximation and ease the posterior construction of PN-NR hybrid waveforms. As part of the post-processing step, we have computed the final mass and final spin of the 60 new simulations presented in Table IV. We have compared the final mass and final spin of those simulations with quasicircular NR fits [59] and found that relative differences are as high as 1%, which is completely consistent with the inaccuracies of the fitting formulae and gauge transient in the apparent horizon quantities. Therefore, we have extended previous work [53] on the circularization of eccentric non-spinning Numerical Relativ-

ity simulations to the eccentric spinning case. Note that the eccentricities of the simulations presented in this communication have more moderate values than the ones presented in [53], although ours are much longer and include spins.

Crucial part of these work has been to extend the low eccentric procedure to measure the eccentricity in NR [55] to the arbitrary high eccentric limit. We have shown that eccentricity estimator used in [55] cannot be used for high eccentricities because it does not reduce to the Newtonian definition of the eccentricity. Additionally, its reliance on a non-eccentric fit makes it numerically inaccurate and it can produce eccentricity values higher than 1. As a consequence, we have de-
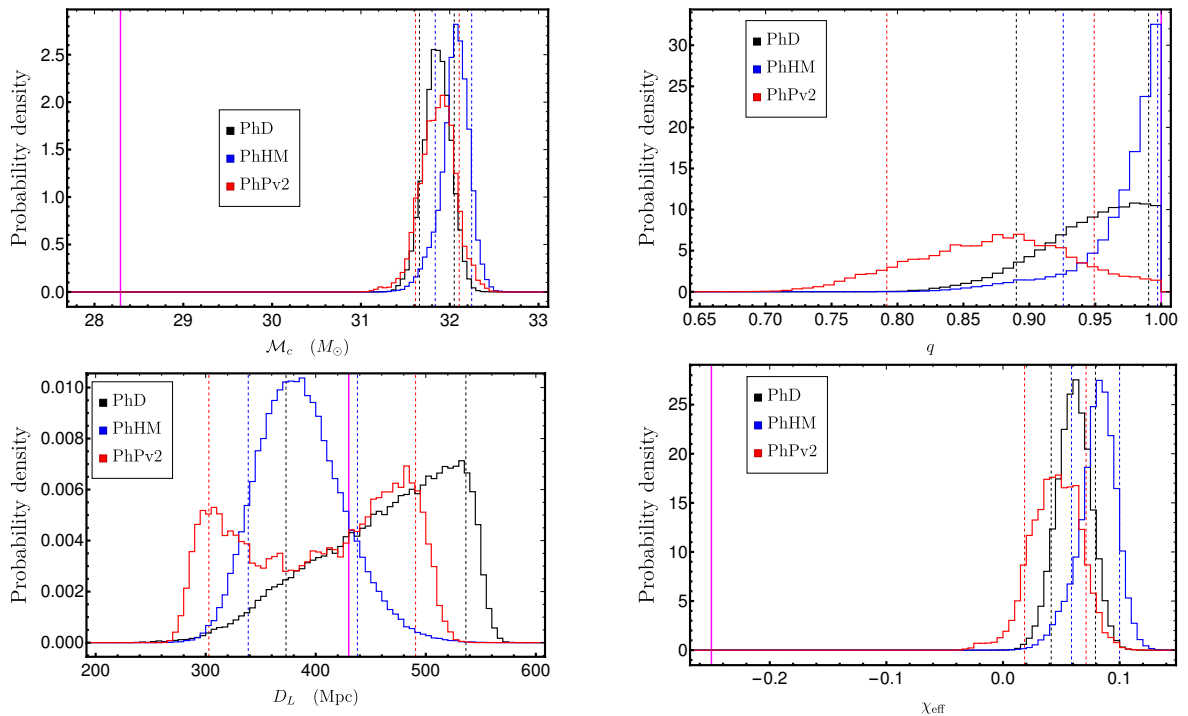
Figure 9: Posterior probability distributions for the injected spinning eccentric hybrid waveform, with initial eccentricity $e_0 = 0.420 \pm 0.006$. The vertical dashed lines correspond to 90% credible regions. The magenta thick vertical line represents the injected value. The black, blue and red curves represent distributions sampled using the IMRPhenomD, IMRPhenomHM and IMRPhenomPv2 approximants, respectively.

cided to use another eccentricity estimator [68] constructed also upon the orbital frequency and which does not rely on any non-eccentric fit. This eccentricity estimator reduces to the Newtonian definition of eccentricity for arbitrarily high eccentricities. We have shown that with this eccentricity estimator we are able to robustly measure the eccentricity for the whole evolution, which will be a key result to generate a future eccentric waveform model.

We have then taken the NR waveforms and hybridized the $(2, 2)$ mode with PN waveforms. The production of the eccentric PN waveforms has required to solve the point particle 3.5PN equations of motion in ADMTT coordinates [55] enhanced with the eccentric contribution to the energy flux from [71]. The absence of complete generic PN expressions for the waveform modes has caused the inaccuracy of the PN waveforms to dominate the error in the hybridization procedure. The use of the instantaneous terms at 3PN order [76] produces inaccurate waveforms due to the lack of the low order tail terms, while the full 3PN expressions in [77] are restricted to the QK parametrization and rely on a certain decomposition of the dynamical variables which complicates their combination with the generic numerical solution of the equations of motion (3.1). Therefore, we have restricted to the use of the quadrupole formula with a correction procedure for the initial orbital separation. We have developed a procedure which corrects the initial orbital separation of the PN evolution code for a certain δr, such that it minimizes the difference in amplitude

between the PN and NR $(2, 2)$ waveforms modes. We have shown that with that procedure we are left with relative errors in the amplitude and phase below 1% in the hybridization region. These errors in amplitude and phase are high compared to the quasicircular ones [103], where the PN knowledge is wider. Therefore, we expect that in the future an improvement in the knowledge of the post-Newtonian waveforms will allow us to construct more accurate hybrid waveforms, not only for the $(2, 2)$ mode, but also for the higher order modes.

We have also compared the hybrid waveforms with quasicircular IMR waveform models. This has been done first computing the mismatch of the eccentric hybrid data set against the quasicircular non-precessing PhenomX model [22, 23]. We find that the mismatches become much higher than 3% for binaries with a total mass lower than $100M_\odot$, while for total masses higher than $150M_\odot$, the mismatch lowers below 3% due to the fact that most of the eccentric waveform in the frequency band of the detector is in the merger-ringdown parts, which as shown in Sec. II C, due to circularization agrees really well with the quasicircular model.

Additionally, we have made a set of injection into gaussian detector noise colored to match the LIGO and Virgo design detector sensitivities. We have studied the parameter biases on recovered parameters when using quasicircular models as approximants. We have used three different quasicircular models to recover the parameters and shown that, although the use of quasicircular models leads to inevitable biases in pa-

rameters like the effective spin parameter or the chirp mass, where the biases are similar among the three models, others like the mass ratio and the luminosity distance present lower biases when using quasicircular aligned spin models including higher order modes. Another important feature is the correlation between chirp mass and mass ratio, the better the measurement of the chirp mass the worse the determination of the mass ratio and viceversa, and this can be clearly observed in Figs. 9 and 13 where for initial eccentricities 0.09 the chirp mass is well measured for the three models, but the mass ratio distributions are not and as the initial eccentricity increases so does the shift in the chirp mass distribution and generally the better the mass ratio is determined. In the case of the spinning eccentric hybrid the high initial eccentricity produces clear biases in all the quantities and unexpectedly PhenomHM recovers well the injected value of the mass ratio and performs the best for the luminosity distance. The study of this phenomenology for the different cases that we have available is ongoing and we leave for a future communication the extension of these results to the whole parameter space.

The work presented in this communication is a natural extension of [55]. We have set up the current infrastructure of our group for quasicircular waveform modelling to the eccentric case. As shown in this paper, we have developed new methods to produce a set of spinning eccentric hybrid waveforms which can actually be used for data analysis purposes. The next natural step is to use this hybrid data set to produce a calibrated eccentric IMR waveform, which can be used for detection and parameter estimation of eccentric black-hole binaries.

Appendix A: Numerical Relativity Simulations

The numerical set up for the BAM and the EinsteinToolkit codes is the same described in Appendix C of [55]. We present in Table IV the NR simulations we have produced for this publication. In Table IV we show the main properties of the NR simulations: from left to the right we start providing an identifier to the simulations, the simulation name, the mass ratio $q = m_1/m_2 \geq 1$, the code used to produce it, the z-component of the dimensionless spin vectors, $\chi_{1,z}, \chi_{2,z}$, of each black hole, the initial orbital separation D/M, where M is the total mass of the system, the initial eccentricity e_0 corresponding to the eccentricity value used in Eq. (2.3) to compute the perturbation factors of the initial linear momenta of the simulations, the initial orbital eccentricity, e_ω, measured with Eq. (2.8) from the orbital frequency computed from the motion of the black holes, an eccentricity error estimate, δe_ω, computed using Eq. (2.9), the time to merger, T_{merger}/M, calculated as the time elapsed from the start of the simulation until the peak of the amplitude of the $(l,m) = (2,2)$ mode, the number of orbits, $N_{\mathrm{orbits}} = \phi_{22}^M/(4\pi)$, where ϕ_{22}^M is the value of the phase of the $(2,2)$ mode at merger, the final mass, M_f, as defined in Eq. (2.5) and the magnitude of the dimensionless final spin, $\chi_f = S/M_f$, where S is specified in Eq. (2.4).

In Fig. 10 we display the values of the eccentricity measured from the orbital frequency, e_ω, defined in Eq. (2.8), and the value of the eccentricity, e_0, used in Eq. (2.3) to compute the perturbation factors of the initial linear momenta of the simulations in Table IV. Moreover, we distinguish for e_ω with blue, red and green colors non-spinning, positive and negative spin simulations, respectively. As expected, we observe an increase in the differences between e_ω and e_0 with higher initial eccentricities and with high spins as the formula for $\lambda_t(r, e_0, \eta, \mathrm{sign})$ where e_0 is used, Eq. (2.2), is a 1PN expression derived for non-spinning binaries in the low eccentricity limit. In order to obtain better control on the initial eccentricity of the NR simulations for high eccentricities, higher order corrections, including spin effects, should be taken into account in the derivation of the correction factors for the initial linear momenta of the black holes. We leave for future work an extension of the current PN formulas to the high eccentricity limit.

Appendix B: Eccentricity estimators in highly eccentric systems

In this section we briefly show the form of the eccentricity estimators of Eqs. (2.7) and (2.8) in the Newtonian limit. We start analyzing the eccentricity estimator

$$e_\omega(t) = \frac{\omega(t) - \omega(e = 0)}{2\omega(e = 0)}. \tag{B1}$$

ID	Simulation	Code	q	$\chi_{1,z}$	$\chi_{2,z}$	χ_{eff}	D/M	e_0	$e_\omega \pm \delta e_\omega$	T_{merger}/M	N_{orbits}	M_f	χ_f
1	q1.__0.__0.__et0.1__D12.23	BAM	1.	0.	0.	0.	12.23	0.1	0.114 ± 0.002	1256.42	4.5	0.9527	0.6871
2	q1.__0.__0.__et0.2__D15	BAM	1.	0.	0.	0.	15.0	0.2	0.210 ± 0.002	1682.01	5.2	0.9533	0.6895
3	q1.__0.__0.__et0.1__D15	BAM	1.	0.	0.	0.	15.0	0.1	0.095 ± 0.002	2961.01	8.3	0.9525	0.6869
4	q1.__0.__0.__et0.2__D17	BAM	1.	0.	0.	0.	17.0	0.2	0.195 ± 0.003	2917.42	8.2	0.9535	0.6889
5	q1.__0.__0.__et0.3__D20	BAM	1.	0.	0.	0.	20.0	0.3	0.301 ± 0.001	497.48	1.5	0.9548	0.6950
6	Eccq1.__0.__0.25__et0.1__D14	ET	1.	0.	0.25	0.125	14.0	0.1	0.100 ± 0.002	2319.85	6.4	0.9480	0.7249
7	Eccq1.__0.__0.25__et0.2__D16	ET	1.	0.	0.25	0.125	16.0	0.2	0.217 ± 0.003	2449.84	5.8	0.9474	0.7243
8	Eccq1.__-0.25__-0.25__et0.1__D12	ET	1.	−0.25	−0.25	−0.25	12.0	0.1	0.148 ± 0.002	939.87	2.8	0.9579	0.6080
9	Eccq1.__0.25__0.25__et0.1__D12	ET	1.	0.25	0.25	0.25	12.0	0.1	0.131 ± 0.002	1347.59	4.8	0.9440	0.7605
10	Eccq1.__-0.25__-0.25__et0.1__D14	ET	1.	−0.25	−0.25	−0.25	14.0	0.1	0.134 ± 0.002	1897.26	5.3	0.9573	0.6091
11	Eccq1.__0.25__0.25__et0.1__D14	ET	1.	0.25	0.25	0.25	14.0	0.1	0.112 ± 0.003	2464.75	7.6	0.9440	0.7607
12	Eccq1.__-0.25__-0.25__et0.2__D14	ET	1.	−0.25	−0.25	−0.25	14.0	0.2	0.249 ± 0.002	1067.25	3.8	0.9578	0.6109
13	Eccq1.__0.25__0.25__et0.2__D14	ET	1.	0.25	0.25	0.25	14.0	0.2	0.194 ± 0.002	1499.92	5.0	0.9432	0.7620
14	Eccq1.__0.25__0.25__et0.2__D16	ET	1.	0.25	0.25	0.25	16.0	0.2	0.199 ± 0.003	2599.90	8.9	0.9437	0.7624
15	Eccq1.__-0.25__-0.25__et0.5__D26	ET	1.	−0.25	−0.25	−0.25	26.0	0.5	0.38 ± 0.004	3287.31	7.7	0.9566	0.6080
16	Eccq1.__0.25__0.25__et0.5__D26	ET	1.	0.25	0.25	0.25	26.0	0.5	0.418 ± 0.004	4613.02	11.3	0.9428	0.7604
17	Eccq1.__0.25__0.__et0.1__D14	ET	1.	0.25	0.	0.125	14.0	0.1	0.128 ± 0.003	2302.69	7.2	0.9480	0.7249
18	Eccq1.__0.25__0.__et0.2__D16	ET	1.	0.25	0.	0.125	16.0	0.2	0.161 ± 0.002	2411.27	7.4	0.9474	0.7242
19	Eccq1.__-0.5__-0.5__et0.1__D13	ET	1.	−0.5	−0.5	−0.5	13.0	0.1	0.143 ± 0.002	1131.58	3.2	0.9623	0.5286
20	Eccq1.__0.5__0.5__et0.1__D13	ET	1.	0.5	0.5	0.5	13.0	0.1	0.116 ± 0.002	2071.02	7.3	0.9323	0.8309
21	Eccq1.__-0.5__-0.5__et0.2__D15	ET	1.	−0.5	−0.5	−0.5	15.0	0.2	0.104 ± 0.001	1170.51	3.3	0.9624	0.5298
22	Eccq1.__0.5__0.5__et0.2__D15	ET	1.	0.5	0.5	0.5	15.0	0.2	0.194 ± 0.002	2290.43	7.7	0.9329	0.8323
23	Eccq1.__-0.5__-0.5__et0.5__D26	ET	1.	0.5	0.5	0.5	26.0	0.5	0.505 ± 0.005	2675.44	6.1	0.9622	0.5230
24	Eccq1.__0.5__0.5__et0.5__D26	ET	1.	0.5	0.5	0.5	26.0	0.5	0.400 ± 0.004	5307.53	13.4	0.9322	0.8294
25	Eccq1.__-0.75__-0.75__et0.1__D13	ET	1.	−0.75	−0.75	−0.75	13.0	0.1	0.144 ± 0.002	907.44	2.5	0.9654	0.4458
26	Eccq1.__0.75__0.75__et0.1__D13	ET	1.	0.75	0.75	0.75	13.0	0.1	0.089 ± 0.002	2307.95	8.3	0.9156	0.8934
27	Eccq1.__-0.75__-0.75__et0.2__D15	ET	1.	−0.75	−0.75	−0.75	15.0	0.2	0.249 ± 0.002	902.561	2.6	0.9657	0.4475
28	Eccq1.__0.75__0.75__et0.2__D15	ET	1.	0.75	0.75	0.75	15.0	0.2	0.181 ± 0.002	2629.47	9.5	0.9149	0.8904
29	Eccq1.__-0.75__-0.75__et0.5__D26	ET	1.	−0.75	−0.75	−0.75	26.0	0.5	0.339 ± 0.003	2079.87	4.1	0.9655	0.4506
30	Eccq1.__0.75__0.75__et0.5__D26	ET	1.	0.75	0.75	0.75	26.0	0.5	0.373 ± 0.004	5907.6	15.1	0.9158	0.8843
31	Eccq1.5__0.__0.__et0.1__D13	ET	1.5	0.	0.	0.	13.0	0.1	0.108 ± 0.002	1606.33	5.2	0.9552	0.6651
32	Eccq1.5__0.__0.__et0.2__D13.5	ET	1.5	0.	0.	0.	13.5	0.2	0.126 ± 0.001	1142.56	3.8	0.9553	0.6619
33	Eccq1.5__0.__0.__et0.2__D15	ET	1.5	0.	0.	0.	15.0	0.2	0.245 ± 0.002	1809.34	5.4	0.9548	0.6636
34	Eccq2.__0.__0.__et0.1__D13	ET	2.	0.	0.	0.	13.0	0.1	0.106 ± 0.002	1738.71	5.3	0.9610	0.6232
35	Eccq2.__0.__0.__et0.2__D16	ET	2.	0.	0.	0.	16.0	0.2	0.167 ± 0.002	2499.02	7.5	0.9610	0.6249
36	Eccq2.__0.__0.__et0.5__D26	ET	2.	0.	0.	0.	26.0	0.5	0.422 ± 0.004	4380.33	10.4	0.9609	0.6262
37	Eccq2.__-0.25__-0.25__et0.1__D12	ET	2.	−0.25	−0.25	−0.25	12.0	0.1	0.138 ± 0.002	1026.39	3.2	0.9664	0.5283
38	Eccq2.__0.25__0.25__et0.1__D12	ET	2.	0.25	0.25	0.25	12.0	0.1	0.103 ± 0.002	1435.07	5.1	0.9544	0.7170
39	Eccq2.__-0.25__-0.25__et0.1__D14	ET	2.	−0.25	−0.25	−0.25	14.0	0.1	0.130 ± 0.002	2001.7	5.6	0.9663	0.5261
40	Eccq2.__0.25__0.25__et0.1__D14	ET	2.	0.25	0.25	0.25	14.0	0.1	0.103 ± 0.002	2707.25	8.3	0.9544	0.7155
41	Eccq2.__-0.25__-0.25__et0.2__D14	ET	2.	−0.25	−0.25	−0.25	14.0	0.2	0.072 ± 0.001	1123.58	3.5	0.9660	0.5300
42	Eccq2.__0.25__0.25__et0.2__D14	ET	2.	0.25	0.25	0.25	14.0	0.2	0.219 ± 0.002	1708.92	5.6	0.9548	0.7151
43	Eccq2.__-0.25__-0.25__et0.2__D16	ET	2.	−0.25	−0.25	−0.25	16.0	0.2	0.225 ± 0.003	2085.67	5.8	0.9663	0.5253
44	Eccq2.__0.25__0.25__et0.2__D16	ET	2.	0.25	0.25	0.25	16.0	0.2	0.188 ± 0.003	2847.34	8.3	0.9549	0.7165
45	Eccq2.__-0.25__-0.25__et0.5__D26	ET	2.	−0.25	−0.25	−0.25	26.0	0.5	0.392 ± 0.003	3628.05	8.4	0.9665	0.5308
46	Eccq2.__0.25__0.25__et0.5__D26	ET	2.	0.25	0.25	0.25	26.0	0.5	0.411 ± 0.004	5203.86	12.5	0.9542	0.7140
47	Eccq2.__0.5__0.5__et0.1__D14	ET	2.	0.5	0.5	0.5	14.0	0.1	0.095 ± 0.002	2985.28	9.1	0.9448	0.8052
48	Eccq2.__-0.5__-0.5__et0.1__D14	ET	2.	−0.5	−0.5	−0.5	14.0	0.1	0.158 ± 0.003	1714.88	4.2	0.9698	0.4279
49	Eccq2.__-0.5__-0.5__et0.2__D16	ET	2.	−0.5	−0.5	−0.5	16.0	0.2	0.277 ± 0.003	1712.98	4.2	0.9696	0.4300
50	Eccq2.__0.5__0.5__et0.2__D16	ET	2.	0.5	0.5	0.5	16.0	0.2	0.180 ± 0.003	3294.21	10.5	0.9451	0.8035
51	Eccq2.__-0.5__-0.5__et0.5__D27	ET	2.	−0.5	−0.5	−0.5	27.0	0.5	0.393 ± 0.004	3522.66	7.2	0.9696	0.4328
52	Eccq2.__-0.75__-0.75__et0.1__D14	ET	2.	−0.75	−0.75	−0.75	14.0	0.1	0.137 ± 0.002	1386.95	3.2	0.9725	0.3273
53	Eccq2.__-0.75__-0.75__et0.2__D16	ET	2.	−0.75	−0.75	−0.75	16.0	0.2	0.125 ± 0.002	1353.72	3.4	0.9728	0.3297
54	Eccq3.__0.__0.__et0.1__D13	ET	3.	0.	0.	0.	13.0	0.1	0.104 ± 0.002	1978.55	6.1	0.9713	0.5414
55	Eccq3.__0.__0.__et0.2__D15	ET	3.	0.	0.	0.	15.0	0.2	0.166 ± 0.002	2156.21	6.2	0.9710	0.5401
56	Eccq3.__0.__0.__et0.5__D26	ET	3.	0.	0.	0.	26.0	0.5	0.416 ± 0.004	5029.06	11.5	0.9710	0.5385
57	Eccq4.__0.__0.__et0.1__D12	ET	4.	0.	0.	0.	12.0	0.1	0.134 ± 0.002	1609.06	5.3	0.9780	0.4725
58	Eccq4.__0.__0.__et0.2__D15	ET	4.	0.	0.	0.	15.0	0.2	0.176 ± 0.002	2412.73	7.4	0.9779	0.4731
59	Eccq4.__0.__0.__et0.5__D27	ET	4.	0.	0.	0.	27.0	0.5	0.412 ± 0.004	6698.64	15.2	0.9779	0.4739
60	Eccq4.__0.__0.__et0.5__D27.5	ET	4.	0.	0.	0.	27.5	0.5	0.415 ± 0.005	7422.59	16.4	0.9784	0.4717

Table IV: Summary of the eccentric NR simulations used in this work. In the first column we indicate the identifier of the simulation. Additionally, each simulation is specified by its mass ratio $q = m_1/m_2 \geq 1$, the code with it was produced, the z-component of the dimensionless spin vectors, $\chi_{1,z}$, $\chi_{2,z}$, the orbital separation D/M, the desired initial eccentricity e_0 used in Eq. (2.3) and the actual measured initial orbital eccentricity, e_ω and its error, δe_ω, the time to merger, T_{merger}/M, the number of orbits, N_{orbits}, the final mass, M_f and the magnitude of the dimensionless final spin, χ_f.
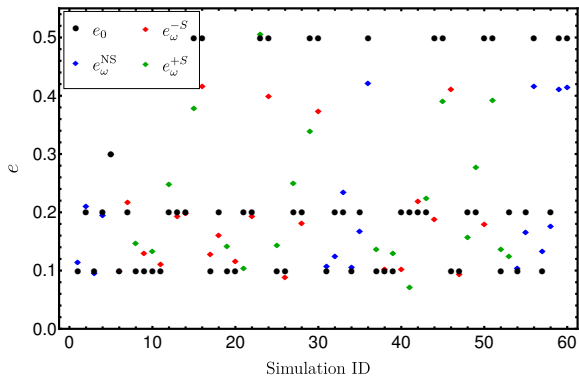
Figure 10: Eccentricity measured from the orbital frequency, e_ω^X with $X = \mathrm{NS}, -S, +S$ corresponding to non-spinning, positive and negative spin simulations, for all the simulations in Table IV compared to the PN eccentricity, e_0, specified in Eq. (2.3) to compute the perturbation factors to the initial linear momentum of the simulations. The black dots represent e_0, the eccentricity value prescribed in Eq. (2.3), while the diamonds represent the actual measured eccentricity e_ω^X. For e_ω^X we distinguish non-spinning (X=NS), positive spin (X=+S) and negative spin (X=-S) simulations with blue, red and green colors, respectively.

In the Keplerian parametrization the orbital frequency can be written as:

$$\omega(t) = \frac{n_t \sqrt{1 - e^2}}{(1 - e \cos u)^2}, \tag{B2}$$

where $n_t = 2\pi/T_{\mathrm{orb}}$ is the mean motion, T_{orb} is the orbital period, e is the eccentricity and u is the eccentric anomaly. In the low eccentric limit, Eq. (B1) reduces to

$$\omega(t) \approx n_t \left[1 + 2e \cos u\right] + O\left(e^2\right). \tag{B3}$$

Replacing Eq. (B3) in Eq. (B1) one obtains $e_\omega = e$. However, if one substitutes Eq. (B2) in Eq. (B1) one gets

$$e_\omega(t) = \frac{1}{2}\left(\frac{\sqrt{1 - e^2}}{[e \cos(u) - 1]^2} - 1\right), \tag{B4}$$

which does not reduce to the Newtonian definition of eccentricity. Moreover, one can show that the estimator of Eq. (B4) is not normalized for a certain combination of values of u and e. For example, if u vanishes, then

$$e_\omega \geq 1 \quad \text{for} \quad e \geq 0.455212. \tag{B5}$$

This shows that the eccentricity estimator given by Eq. (B1) has to be taken with caution in the high eccentric limit because it can go above 1. On the other hand, the eccentricity estimator

$$e_{\Omega_{a,p}}(t) = \frac{\omega_p^{1/2} - \omega_a^{1/2}}{\omega_p^{1/2} + \omega_a^{1/2}}, \tag{B6}$$

where ω_a, ω_p are the orbital frequency at the apastron and periastron, respectively. This eccentricity estimator has the

property that even for high eccentricities it reduces to the Newtonian definition of eccentricity, i.e., $e_{\Omega_{a,p}} = e$.

Appendix C: Posterior distributions

In this Appendix we show further information about the parameter estimation methods used and posterior distributions of several relevant quantities. The settings of the CPNEST sampler [92] are a number of live points $N_{\mathrm{live}} = 16824$ and a maximum number of Markov-Chain Monte Carlo (MCMC) steps to take max-mcmc = 5000. We refer the reader to [104] for details on the meaning of those parameters in the context of nested sampling. This is a computationally expensive setup aiming to ensure an accurate sampling of the likelihood given the complexity of the signal.

We show in Fig. 11 a contour plot of the mass ratio and chirp mass posterior distributions for the injected eccentric NR simulations of Table I and the zero eccentricity injection with the NRHybSur3dq8 model recovered with PhenomD. This plot explicitly exhibits the correlation between the bias in the measurement of the chirp mass and the narrowing of the posterior for the mass ratio with increasing initial eccentricity.

For completion we also show in Fig. 12 the posterior distribution of the χ_p parameter for the NR simulations of Fig. 1 run with IMRPhenomPv2. This parameter, defined in [105], accounts for the spin components orthogonal to the direction of the orbital angular momentum vector of the system. Therefore, for non-precessing configurations $\chi_p = 0$ and for precessing configurations it ranges between 0 and 1. In Fig. 12 one can observe an increase in χ_p with increasing initial eccentricity of the injected signal. This result means that the precessing waveform IMRPhenomPv2 is trying to compensate the inability to reproduce the eccentric signal incrementing the value of the χ_p parameter, i.e., increasing the precession.

In Fig. 13 we display the posterior probability distributions of the chirp mass, mass ratio, effective spin parameter and luminosity distance for the eccentric injected NR simulations of Table I recovered with the IMRPhenomD, IMRPhenomHM and IMRPhenomPv2 approximants with 90% credible intervals specified by the dashed lines and the injected values by the magenta thick vertical lines. The fainter the colour of the posterior distributions the lower the initial eccentricity ($e_0 = 0.09, 0.14, 0.20$).
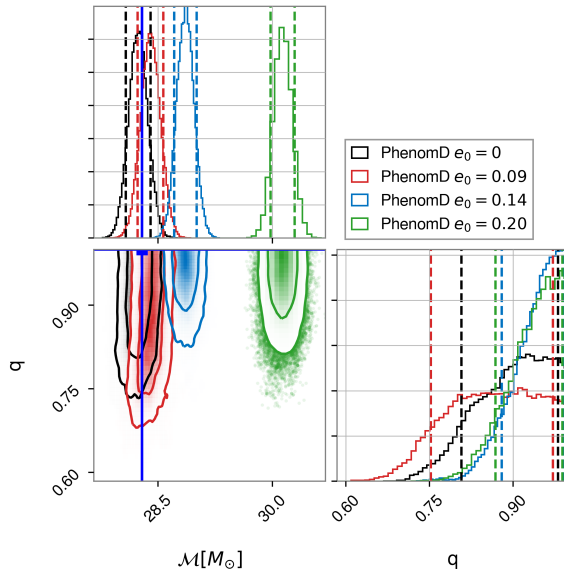
Figure 11: Posterior probability distributions of the mass ratio and the chirp mass for the injected eccentric NR simulations of Table I and the zero eccentricity injection with the NRHybSur3dq8 model, using IMRPhenomD as approximant. The vertical dashed lines correspond to 90% credible regions. The dark blue thick vertical line represents the injected value. The black, red, blue and green curves represent injections with initial eccentricities, $e_0 = 0, 0.09, 0.14, 0.2$, respectively.
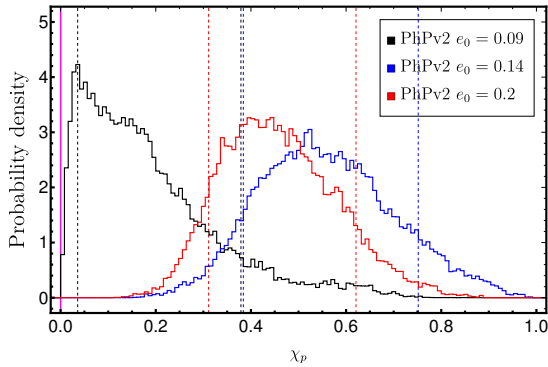
Figure 12: Posterior probability distributions of χ_p for the injected NR simulations of Table I. The vertical dashed lines correspond to 90% credible regions. The magenta thick vertical line represents the injected value. The black, blue and red curves represent injections with initial eccentricities, $e_0 = 0.09, 0.14, 0.2$. All cases are sampled using as approximant IMRPhenomPv2.
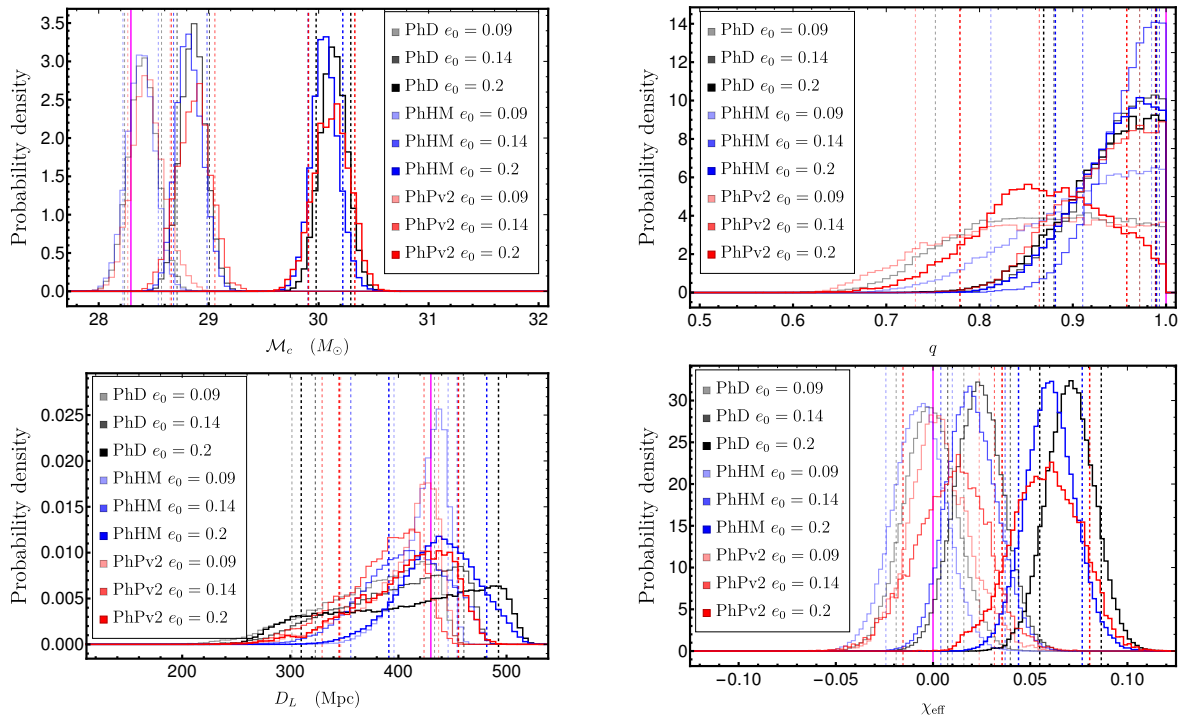
Figure 13: Posterior probability distributions for the eccentric injected NR simulations of Table I. The vertical dashed lines correspond to 90% credible regions. The magenta thick vertical line represents the injected value. The black, blue and red curves represent distributions sampled using the IMRPhenomD, IMRPhenomHM and IMRPhenomPv2 approximants, respectively. With increasingly higher opacity are represented injections with initial eccentricities, $e_0 = 0.09, 0.14, 0.2$.

[1] B. P. Abbott *et al.* (LIGO Scientific Collaboration and Virgo Collaboration), Phys. Rev. Lett. **116**, 061102 (2016).

[2] B. P. Abbott *et al.* (LIGO Scientific Collaboration and Virgo Collaboration), Phys. Rev. Lett. **116**, 241103 (2016).

[3] B. P. Abbott *et al.* (VIRGO, LIGO Scientific), Phys. Rev. Lett. **118**, 221101 (2017), arXiv:1706.01812 [gr-qc] .

[4] B. P. Abbott *et al.* (Virgo, LIGO Scientific), Astrophys. J. **851**, L35 (2017), arXiv:1711.05578 [astro-ph.HE] .

[5] B. P. Abbott *et al.* (Virgo, LIGO Scientific), Phys. Rev. Lett. **119**, 141101 (2017).

[6] B. P. Abbott *et al.* (Virgo, LIGO Scientific), Phys. Rev. Lett. **119**, 161101 (2017).

[7] B. P. Abbott *et al.* (LIGO Scientific, Virgo),   (2018), arXiv:1811.12907 [astro-ph.HE] .

[8] I. M. Romero-Shaw, P. D. Lasky, and E. Thrane, (2019), arXiv:1909.05466 [astro-ph.HE] .

[9] P. C. Peters and J. Mathews, Phys. Rev. **131**, 435 (1963).

[10] P. C. Peters, Phys. Rev. **136**, B1224 (1964).

[11] S. Husa, S. Khan, M. Hannam, M. Pürrer, F. Ohme, F. Jiménez Forteza, and A. Bohé, (2015).

[12] S. Khan, S. Husa, M. Hannam, F. Ohme, M. Pürrer, X. J. Forteza, and A. Bohé, Phys. Rev. D **93**, 044007 (2016).

[13] M. Hannam, P. Schmidt, A. Bohé, L. Haegel, S. Husa, F. Ohme, G. Pratten, and M. Pürrer, Phys. Rev. Lett. **113**, 151101 (2014).

[14] A. Bohé, L. Shao, A. Taracchini, A. Buonanno, S. Babak, I. W. Harry, I. Hinder, S. Ossokine, M. Pürrer, V. Raymond, T. Chu, H. Fong, P. Kumar, H. P. Pfeiffer, M. Boyle, D. A. Hemberger, L. E. Kidder, G. Lovelace, M. A. Scheel, and B. Szilágyi, Phys. Rev. D **95**, 044028 (2017).

[15] L. London, S. Khan, E. Fauchon-Jones, C. García, M. Hannam, S. Husa, X. Jiménez-Forteza, C. Kalaghatgi, F. Ohme, and F. Pannarale, Phys. Rev. Lett. **120**, 161102 (2018).

[16] R. Cotesta, A. Buonanno, A. Bohé, A. Taracchini, I. Hinder, and S. Ossokine, Phys. Rev. D **98**, 084028 (2018).

[17] J. Blackman, S. E. Field, M. A. Scheel, C. R. Galley, D. A. Hemberger, P. Schmidt, and R. Smith, Phys. Rev. **D95**, 104023 (2017), arXiv:1701.00550 [gr-qc] .

[18] V. Varma, S. E. Field, M. A. Scheel, J. Blackman, D. Gerosa, L. C. Stein, L. E. Kidder, and H. P. Pfeiffer, Phys. Rev. Research **1**, 033015 (2019).

[19] V. Varma, S. E. Field, M. A. Scheel, J. Blackman, L. E. Kidder, and H. P. Pfeiffer, Phys. Rev. D **99**, 064045 (2019).

[20] S. Khan, K. Chatziioannou, M. Hannam, and F. Ohme, (2018), arXiv:1809.10113 [gr-qc] .

[21] S. Khan, F. Ohme, K. Chatziioannou, and M. Hannam, (2019), arXiv:1911.06050 [gr-qc] .

[22] G. Pratten, S. Husa, C. García-Quirós, M. Colleoni, A. Ramos-Buades, H. Estellés, and R. Jaume, (2020), arXiv:2001.11412 [gr-qc] .

[23] C. García-Quirós, M. Colleoni, S. Husa, H. Estellés, G. Pratten, A. Ramos-Buades, M. Mateu-Lucena, and R. Jaume, (2020), arXiv:2001.10914 [gr-qc] .

[24] H. Estellés, A. Ramos-Buades, S. Husa, C. García-Quirós, and L. Haegel, (2020), in preparation.

[25] K. Belczynski, D. E. Holz, T. Bulik, and R. O'Shaughnessy, Nature **534**, 512 (2016), arXiv:1602.04531 [astro-ph.HE] .

[26] D. Park, C. Kim, H. M. Lee, Y.-B. Bae, and K. Belczynski, Mon. Not. Roy. Astron. Soc. **469**, 4665 (2017), arXiv:1703.01568 [astro-ph.HE] .

[27] J. Samsing, Phys. Rev. D **97**, 103014 (2018).

[28] J. Samsing, M. MacLeod, and E. Ramirez-Ruiz, Astrophys. J. **784**, 71 (2014), arXiv:1308.2964 [astro-ph.HE] .

[29] T. Damour and N. Deruelle, Ann. Inst. Henri Poincaré Phys. Théor., Vol. 43, No. 1, p. 107 - 132 (1985).

[30] T. Damour, A. Gopakumar, and B. R. Iyer, Phys. Rev. D **70**, 064028 (2004).

[31] R.-M. Memmesheimer, A. Gopakumar, and G. Schäfer, Phys. Rev. D **70**, 104011 (2004).

[32] S. Tanay, M. Haney, and A. Gopakumar, Phys. Rev. D **93**, 064031 (2016).

[33] B. Moore, T. Robson, N. Loutrel, and N. Yunes, Class. Quant. Grav. **35**, 235006 (2018), arXiv:1807.07163 [gr-qc] .

[34] B. Moore and N. Yunes, Class. Quant. Grav. **36**, 185003 (2019), arXiv:1903.05203 [gr-qc] .

[35] N. Loutrel, S. Liebersbach, N. Yunes, and N. Cornish, Class. Quant. Grav. **36**, 025004 (2019), arXiv:1810.03521 [gr-qc] .

[36] B. Moore and N. Yunes, Classical and Quantum Gravity **36**, 185003 (2019).

[37] E. A. Huerta, C. J. Moore, P. Kumar, D. George, A. J. K. Chua, R. Haas, E. Wessel, D. Johnson, D. Glennon, A. Rebei, A. M. Holgado, J. R. Gair, and H. P. Pfeiffer, Phys. Rev. D **97**, 024031 (2018).

[38] I. Hinder, L. E. Kidder, and H. P. Pfeiffer, Phys. Rev. D **98**, 044015 (2018).

[39] Z. Cao and W.-B. Han, Phys. Rev. D **96**, 044028 (2017).

[40] T. Hinderer and S. Babak, Phys. Rev. D **96**, 104048 (2017).

[41] D. Chiaramello and A. Nagar, (2020), arXiv:2001.11736 [gr-qc] .

[42] A. Klein, Y. Boetzel, A. Gopakumar, P. Jetzer, and L. de Vittori, Phys. Rev. D **98**, 104043 (2018).

[43] L. Santamaría, F. Ohme, P. Ajith, B. Brügmann, N. Dorband, M. Hannam, S. Husa, P. Mösta, D. Pollney, C. Reisswig, E. L. Robinson, J. Seiler, and B. Krishnan, Phys. Rev. D **82**, 064016 (2010).

[44] F. Ohme, Classical and Quantum Gravity **29**, 124002 (2012).

[45] F. Ohme, M. Hannam, and S. Husa, Phys. Rev. D **84**, 064029 (2011).

[46] I. MacDonald, S. Nissanke, and H. P. Pfeiffer, Classical and Quantum Gravity **28**, 134002 (2011).

[47] P. Ajith, M. Boyle, D. A. Brown, B. Brügmann, L. T. Buchman, L. Cadonati, M. Campanelli, T. Chu, Z. B. Etienne, S. Fairhurst, M. Hannam, J. Healy, I. Hinder, S. Husa, L. E. Kidder, B. Krishnan, P. Laguna, Y. T. Liu, L. London, C. O. Lousto, G. Lovelace, I. MacDonald, P. Marronetti, S. Mohapatra, P. Mösta, D. Müller, B. C. Mundim, H. Nakano, F. Ohme, V. Paschalidis, L. Pekowsky, D. Pollney, H. P. Pfeiffer, M. Ponce, M. Pürrer, G. Reifenberger, C. Reisswig, L. Santamaría, M. A. Scheel, S. L. Shapiro, D. Shoemaker, C. F. Sopuerta, U. Sperhake, B. Szilágyi, N. W. Taylor, W. Tichy, P. Tsatsin, and Y. Zlochower, Classical and Quantum Gravity **29**, 124001 (2012).

[48] M. Boyle, Phys. Rev. D **84**, 064013 (2011).

[49] J. C. Bustillo, A. Bohé, S. Husa, A. M. Sintes, M. Hannam, and M. Pürrer, (2015), arXiv:1501.00918 [gr-qc] .

[50] B. Brügmann, J. A. González, M. Hannam, S. Husa, U. Sperhake, and W. Tichy, Phys. Rev. D **77**, 024027 (2008).

[51] F. Loffler *et al.*, Class. Quant. Grav. **29**, 115001 (2012), arXiv:1111.3344 [gr-qc] .

[52] M. Babiuc-Hamilton *et al.*, "The Einstein Toolkit," (2019), to find out more, visit http://einsteintoolkit.org.

[53] I. Hinder, B. Vaishnav, F. Herrmann, D. M. Shoemaker, and

P. Laguna, Phys. Rev. D **77**, 081502 (2008).

[54] D. Pollney, C. Reisswig, E. Schnetter, N. Dorband, and P. Diener, Phys. Rev. **D83**, 044045 (2011).

[55] A. Ramos-Buades, S. Husa, and G. Pratten, Phys. Rev. D **99**, 023003 (2019).

[56] S. collaboration, "https://www.black-holes.org/SpEC.html," .

[57] J. M. Bowen and J. W. York, Phys. Rev. D **21**, 2047 (1980).

[58] J. Healy and C. O. Lousto, Phys. Rev. D **97**, 084002 (2018).

[59] X. Jiménez-Forteza, D. Keitel, S. Husa, M. Hannam, S. Khan, and M. Pürrer, Phys. Rev. D **95**, 064024 (2017).

[60] M. Campanelli, C. O. Lousto, Y. Zlochower, B. Krishnan, and D. Merritt, Phys. Rev. D **75**, 064030 (2007).

[61] O. Dreyer, B. Krishnan, D. Shoemaker, and E. Schnetter, Phys. Rev. D **67**, 024018 (2003).

[62] J. Thornburg, Phys. Rev. D **54**, 4899 (1996).

[63] J. Thornburg, Class. Quant. Grav. **21**, 743 (2004), arXiv:gr-qc/0306056 [gr-qc] .

[64] M. Purrer, S. Husa, and M. Hannam, Phys. Rev. **D85**, 124051 (2012), arXiv:1203.4258 [gr-qc] .

[65] A. H. Mroué, H. P. Pfeiffer, L. E. Kidder, and S. A. Teukolsky, Phys. Rev. D **82**, 124016 (2010).

[66] A. Buonanno, L. E. Kidder, A. H. Mroué, H. P. Pfeiffer, and A. Taracchini, Phys. Rev. D **83**, 104034 (2011).

[67] M. Alcubierre, B. Bruegmann, P. Diener, M. Koppitz, D. Pollney, E. Seidel, and R. Takahashi, Phys. Rev. **D67**, 084023 (2003), arXiv:gr-qc/0206072 [gr-qc] .

[68] T. Mora and C. M. Will, Phys. Rev. D **66**, 101501 (2002).

[69] W. R. Inc., "Mathematica, Version 12.0," Champaign, IL, 2019.

[70] S. Husa *et al.*, (2019).

[71] K. G. Arun, L. Blanchet, B. R. Iyer, and S. Sinha, Phys. Rev. D **80**, 124018 (2009).

[72] R. Arnowitt, S. Deser, and C. W. Misner, Phys. Rev. **116**, 1322 (1959).

[73] S. Deser, R. Arnowitt, and C. W. Misner, J. Math. Phys. **1**, 434 (1960).

[74] R. Arnowitt, S. Deser, and C. W. Misner, Phys. Rev. **117**, 1595 (1960).

[75] A. Buonanno, Y. Chen, and T. Damour, Phys. Rev. **D74**, 104005 (2006).

[76] C. K. Mishra, K. G. Arun, and B. R. Iyer, Phys. Rev. D **91**, 084040 (2015).

[77] Y. Boetzel, C. K. Mishra, G. Faye, A. Gopakumar, and B. R. Iyer, (2019), arXiv:1904.11814 [gr-qc] .

[78] M. Ebersold, Y. Boetzel, G. Faye, C. K. Mishra, B. R. Iyer, and P. Jetzer, Phys. Rev. D **100**, 084043 (2019).

[79] I. MacDonald, S. Nissanke, and H. P. Pfeiffer, *Theory meets data analysis at comparable and extreme mass ratios. Proceedings, Conference, NRDA/CAPRA 2010, Waterloo, Canada, June 20-26, 2010*, Class. Quant. Grav. **28**, 134002

(2011), arXiv:1102.5128 [gr-qc] .

[80] I. MacDonald, A. H. Mroué, H. P. Pfeiffer, M. Boyle, L. E. Kidder, M. A. Scheel, B. Szilágyi, and N. W. Taylor, Phys. Rev. D **87**, 024009 (2013).

[81] W. Tichy, B. Brugmann, M. Campanelli, and P. Diener, Phys. Rev. **D67**, 064008 (2003).

[82] N. Yunes and W. Tichy, Phys. Rev. **D74**, 064013 (2006).

[83] N. Yunes, W. Tichy, B. J. Owen, and B. Brugmann, Phys. Rev. D **74**, 104011 (2006).

[84] C. Reisswig and D. Pollney, Class. Quant. Grav. **28**, 195015 (2011), arXiv:1006.1632 [gr-qc] .

[85] LIGO Scientific Collaboration, (2018), 10.7935/GT1W-FZ16.

[86] L. S. Finn and D. F. Chernoff, Phys. Rev. D **47**, 2198 (1993).

[87] P. Jaranowski and A. Królak, Living Reviews in Relativity **15**, 4 (2012).

[88] S. Husa, S. Khan, M. Hannam, M. Pürrer, F. Ohme, X. J. Forteza, and A. Bohé, Phys. Rev. D **93**, 044006 (2016).

[89] "https://dcc.ligo.org/LIGO-T0900288/public." .

[90] D. A. Brown and P. J. Zimmerman, Phys. Rev. D **81**, 024007 (2010).

[91] G. Ashton *et al.*, Astrophys. J. Suppl. **241**, 27 (2019), arXiv:1811.02042 [astro-ph.IM] .

[92] J. Veitch and W. D. Pozzo, "CPNEST," 10.5281/zenodo.322819 (2017).

[93] C. R. Galley and P. Schmidt, (2016), arXiv:1611.07529 [gr-qc] .

[94] P. Schmidt, I. W. Harry, and H. P. Pfeiffer, (2017), arXiv:1703.01076 [gr-qc] .

[95] M. Favata, Phys. Rev. Lett. **112**, 101101 (2014).

[96] E. A. Huerta, P. Kumar, S. T. McWilliams, R. O'Shaughnessy, and N. Yunes, Phys. Rev. D **90**, 084016 (2014).

[97] I. Mandel, C. P. L. Berry, F. Ohme, S. Fairhurst, and W. M. Farr, Class. Quant. Grav. **31**, 155005 (2014), arXiv:1404.2382 [gr-qc] .

[98] M. E. Lower, E. Thrane, P. D. Lasky, and R. Smith, Phys. Rev. D **98**, 083028 (2018).

[99] B. Moore and N. Yunes, (2019), arXiv:1910.01680 [gr-qc] .

[100] J. Aasi *et al.* (LIGO Scientific), Class. Quant. Grav. **32**, 074001 (2015).

[101] F. Acernese *et al.* (VIRGO), Class. Quant. Grav. **32**, 024001 (2015), arXiv:1408.3978 [gr-qc] .

[102] E. Thrane and C. Talbot, Publications of the Astronomical Society of Australia **36** (2019), 10.1017/pasa.2019.2.

[103] S. Husa *et al.*, (2020), in preparation.

[104] J. Skilling *et al.*, Bayesian analysis **1**, 833 (2006).

[105] P. Schmidt, F. Ohme, and M. Hannam, Phys. Rev. D **91**, 024043 (2015).

Chapter 6

Analysis of approximations for modelling precessing binaries with numerical relativity

The following published article is included in this chapter:

- Antoni Ramos-Buades, Patricia Schmidt, Geraint Pratten, Sascha Husa. *Validity of common modelling approximations for precessing binary black holes with higher-order modes.* Physical Review D **101**, 103014 (2020). [26 pages]

Validity of common modelling approximations for precessing binary black holes with higher-order modes

Antoni Ramos-Buades,[1] Patricia Schmidt,[2] Geraint Pratten,[2, 1] and Sascha Husa[1]

[1]*Departament de Física, Universitat de les Illes Balears, IAC3 – IEEC, Crta. Valldemossa km 7.5, E-07122 Palma, Spain*
[2]*School of Physics and Astronomy and Institute for Gravitational Wave Astronomy,*
University of Birmingham, Edgbaston, Birmingham, B15 9TT, United Kingdom
(Dated: March 12, 2020)

The current paradigm for constructing waveforms from precessing compact binaries is to first construct a waveform in a non-inertial, co-precessing binary source frame followed by a time-dependent rotation to map back to the physical, inertial frame. A key insight in the construction of these models is that the co-precessing waveform can be effectively mapped to some equivalent aligned spin waveform. Secondly, the time-dependent rotation implicitly introduces *m*-mode mixing, necessitating an accurate description of higher-order modes in the co-precessing frame. We assess the efficacy of this modelling strategy in the strong field regime using Numerical Relativity simulations. We find that this framework allows for the highly accurate construction of $(2, \pm 2)$ modes in our data set, while for higher order modes, especially the $(2, |1|), (3, |2|)$ and $(4, |3|)$ modes, we find rather large mismatches. We also investigate a variant of the approximate map between co-precessing and aligned spin waveforms, where we only identify the slowly varying part of the time domain co-precessing waveforms with the aligned-spin one, but find no significant improvement. Our results indicate that the simple paradigm to construct precessing waveforms does not provide an accurate description of higher order modes in the strong-field regime, and demonstrate the necessity for modelling mode asymmetries and mode-mixing to significantly improve the description of precessing higher order modes.

PACS numbers: 04.25.Dg, 04.30.Db, 04.30.Tv

I. INTRODUCTION

The first observation of gravitational waves (GWs) from colliding black holes by Advanced LIGO [1, 2] marked the beginning of a new era in astronomy. Since then, GWs from twelve coalescing compact binaries such binary black holes (BBHs) and binary neutron stars (BNSs) have been detected confidently [3, 4] by Advanced LIGO (aLIGO) and Virgo [5], and many more GW candidates have been recorded since the start of the third observing run [6]. For all confident BBH detections, the emitted signal was found to be consistent with predictions from General Relativity [7, 8] and consistent with compact binaries whose spins are aligned with the orbital angular momentum **L** [3]. The GW signal of such aligned-spin binaries is well described by the current generation of semi-analytic waveform models [9–13] governing the inspiral, merger and ringdown. More recent work [14–17] has focused on extending these waveform models to incorporate subdominant harmonics beyond the dominant quadrupolar $(2, |2|)$ modes.

Generic BBHs, however, can have arbitrarily oriented spin configurations, i.e., the spins are not (anti-)parallel to the orbital angular momentum. Relativistic couplings between the orbital and spin angular momenta induce precession of the spins and the orbital plane [18, 19], resulting in complex amplitude and phase modulations of GW signal. This complicates waveform modelling efforts and impedes brute force Numerical Relativity (NR) studies as the parameter space grows from three intrinsic parameters to seven for quasi-spherical binaries [20]. Recent attempts, guided by reduced order modelling strategies [21, 22], have been successful in accurately modelling precessing waveforms in very restricted domains of the parameter space [23–25].

In recent years, a number of key breakthroughs in waveform modelling enabled the development of the first inspiral-merger-ringdown (IMR) waveforms for precessing compact binaries [26–31]. A key insight was the observation that the waveform of precessing binaries can be greatly simplified when transformed to an effectively co-precessing, non-inertial frame that tracks the leading-order precession of the orbital plane [26, 27, 32]. This general framework has since been used to produce several IMR waveform models of precessing binaries [23, 24, 33–36]. A second crucial insight was the realisation that a co-precessing waveform can be approximately mapped to a some equivalent aligned-spin waveform [26, 30, 37]. This identification is predicated on an approximate decoupling between the spin components parallel to the orbital angular momentum **L** and the spin components perpendicular to **L** (in-plane spins) [30]. Schematically, we can construct an approximate precessing waveform using a time-dependent rotation of the co-precessing waveform given a model of the precessional motion of the orbital plane [26, 29]. Within this general framework, several approximations are commonly made, though different waveform models use different approximations. Here, we focus on the *phenomenological* waveform family, a key tool for LIGO data analysis due to its computational efficiency. Precessing phenomenological waveform models [33, 36, 38, 39] are constructed using three independent pieces: 1) an aligned-spin waveform model, 2) a model for the Euler angles describing the time-dependent rotation of the orbital plane, and 3) a modification of the final state that captures spin-precession effects. The most commonly for GW analysis used model IM-RPhenomPv2 [33, 38], has recently been upgraded to include double-spin effects in the inspiral [36], and to incorporate (uncalibrated) subdominant spherical harmonic modes in the

2

co-precessing frame [39], while a forthcoming phenomenological waveform model will include the calibration of these modes [40].

Precessing phenomenological waveform models are constructed based on a set of simplifying approximations. Each of these approximations will introduce systematic modelling errors. While current observations are dominated by the statistical uncertainty in the measurement, advances in the detector sensitivity will reveal systematic errors. We thus need to understand the impact of various modelling approximations to guide the model development for the coming years. Due to the dimensionality of the precessing parameter space, systematic studies are sparse. Here, we make a first attempt at scrutinizing two main approximations made in the phenomenological modelling paradigm:

1. (APX1) The identification between co-precessing and aligned-spin waveform modes.
2. (APX2) The choice of subdominant harmonic modes used in constructing the co-precessing waveform modes, i.e., the number of aligned-spin modes used to generate the approximate precessing modes.

In particular, we focus on the limitations of these two approximations when extended to higher order mode for both individual modes as well as the strain. We note that in the analyses presented here, we neglect modifications to the final state and compute the Euler angles directly from the precessing NR simulations.

The paper is organised as follows: In Sec. II we briefly summarise the general framework used to model precessing binaries. In Sec. III we present the data set of NR waveforms used in this study, afterwards we present our results on the validity of (APX1) and (APX2) in Sec. V. In Sec. VI we discuss caveats and possible improvements of (APX1). We conclude in Sec. VII. In Appendices A-D we present details of the NR data set, additional results and supporting analyses.

Throughout we use geometric units $G = c = 1$. To simplify expressions we set the total mass of the system to $M = m_1 + m_2 = 1$ unless stated otherwise. We define the mass ratio as $q = m_1/m_2 \geq 1$ with $m_1 \geq m_2$. We also introduce the symmetric mass ratio $\eta = q/(1+q)^2$, and we will denote the black holes' dimensionless spin vectors by $\boldsymbol{\chi}_i = \boldsymbol{S}_i/m_i^2$, for $i = 1, 2$.

II. MODELLING PRECESSING BINARIES

The orbital precession dynamics of a binary system is encoded in three time-dependent Euler angles $\{\beta(t), \alpha(t), \varepsilon(t)\}$ [26], where β is the angle between the total angular momentum $\boldsymbol{J}$ and $\mathbf{L}$ and α is the azimuthal orientation of $\mathbf{L}$. These two angles track the direction of the maximal radiation axis, which is approximately normal to the orbital plane [41]. The final angle, ε, corresponds to a rotation around the maximal radiation axis given by enforcing the minimal rotation condition [42], $\varepsilon = -\int \dot{\alpha}(t) \cos\beta(t) \, dt$, which is related to the precession rate of the binary.

A coordinate frame, which tracks the orbital precession is referred to as co-precessing. In any such co-precessing frame, the waveform modes $h_{\ell m}^{\text{co-prec}}$ can be obtained by an active ro-

tation applied to the modes $h_{\ell m}^{\text{prec}}$ obtained in an inertial coordinate system [26, 29]:

$$h_{\ell m}^{\text{co-prec}}(t) = \sum_{k=-\ell}^{\ell} \mathbf{R}_{\ell m k}(\beta, \alpha, \varepsilon) \, h_{\ell k}^{\text{prec}}(t), \qquad (2.1)$$

where $\mathbf{R}_{k\ell m}(\beta, \alpha, \varepsilon)$ is the $k\ell m$-element of the rotation operator which describes the inertial motion, adopting the (z, y, z)-convention. It follows that the inverse transformation permits the generation of precessing waveform modes, i.e., given the modes in the co-precessing frame, we find

$$h_{\ell m}^{\text{prec}} = \sum_{k=-\ell}^{\ell} \mathbf{R}_{\ell m k}^{-1}(\beta, \alpha, \varepsilon) \, h_{\ell k}^{\text{co-prec}}(t). \qquad (2.2)$$

While all available precessing IMR waveform models use this general framework, they make different assumptions about the RHS of Eq. (2.2). In particular, phenomenological waveform models [33, 36, 41] identify the co-precessing waveform modes in Eq. (2.2) with aligned-spin (AS) modes obtained from a binary with the same mass ratio and spin component parallel to $\mathbf{L}$, i.e.,

$$\bar{h}_{\ell m}^{\text{prec}}(t; q, \boldsymbol{S}_1, \boldsymbol{S}_2) = \sum_{k=-l}^{l} \mathbf{R}_{\ell m k}^{-1}(\beta, \alpha, \varepsilon) \, h_{lk}^{\text{AS}}(t; q, S_{1\|}(t_0), S_{2\|}(t_0)), \qquad (2.3)$$

where $\bar{h}_{lk}^{\text{prec}}$ and h_{lk}^{AS} denote the approximate precessing and AS waveform modes, respectively. Given an appropriate description of the rotation operator, the identification between $h_{\ell m}^{\text{co-prec}} \simeq h_{\ell m}^{\text{AS}}$ (APX1) provides a straightforward procedure to construct approximate precessing waveforms.

One key aspect of precessing waveforms that is not captured by this identification are mode asymmetries [43]. For time domain aligned-spin waveforms the negative-m modes are given by complex conjugation, i.e.,

$$h_{\ell, -m}^{\text{AS}} = (-1)^{\ell} \left(h_{\ell m}^{\text{AS}} \right)^*, \qquad (2.4)$$

where the symbol $*$ denotes complex conjugation. This relation is no longer true for precessing waveforms, which is neglected in the identification $h_{\ell m}^{\text{co-prec}} \simeq h_{\ell m}^{\text{AS}}$. We investigate in detail the effect of neglecting these mode-asymmetries in Sec. V A.

III. NUMERICAL RELATIVITY DATASET

The set of NR simulations used in this study includes publicly available waveforms from the SXS Collaboration [44], as well as non-public waveforms generated with BAM [45, 46] and the open-source Einstein Toolkit [47, 48]. The simulations employed here, including their properties are listed in Tab. A of App. A. Throughout the main text we will highlight results for three precessing cases: IDs 10, 28 and 36. Their parameters are listed in Tab. I. We choose these three cases due to the presence of particular features which we discuss in detail in Sec. V A.

ID	Simulation	Code	q	χ_1	χ_2	χ_{eff}	D/M	$M\Omega_0$	$e_0 \cdot 10^{-3}$
10	`SXS:BBH:0023`	SpEC	1.5	$(0.5, 0.05, 0.)$	$(0.08, -0.49, 0.)$	0.	16.	0.0145	0.28
36	`SXS:BBH:0058`	SpEC	5.	$(0.5, 0.03, 0.)$	$(0., 0., 0.)$	0.	15.	0.0158	2.12
28	`q3._0.56_0.56_0._0.6_0._0._T_80_400`	BAM	3	$(0.75, -0.27, 0.)$	$(0.3, 0.52, 0.)$	0	8.83	0.0329	2.94

Table I. Parameters of three precessing simulations highlighted in various analyses. The full list of NR simulations and further details for all simulations can be found in Tab. A.

From all available NR simulations we pair the precessing and AS waveforms whose initial dimensionless spin vector projected onto the initial orbital angular momentum $\hat{L}_0$ coincide, i.e.,

$$\hat{L}_0^{\text{AS}} \cdot \chi_{0,i}^{\text{AS}} \equiv \hat{L}_0^{\text{prec}} \cdot \chi_{0,i}^{\text{prec}}, \quad i = 1, 2, \qquad (3.1)$$

where $\hat{L}_0 = L_0/\|L_0\|$ is the unit orbital angular momentum vector after junk radiation. Note that satisfying Eq. (3.1) exactly is very difficult when working with NR simulations. We have thus chosen a tolerance of 10^{-3}. Applying this criterion we obtain 36 unique precessing simulations with an AS counterpart. Figure 1 shows the distribution of the mass ratio q as well as two spin parameters for the 36 NR simulations: (i) the effective inspiral spin parameter χ_{eff} [49, 50] given by

$$\chi_{\text{eff}} = \frac{m_1 \chi_{1L} + m_2 \chi_{2L}}{m_1 + m_2}, \qquad (3.2)$$

where $\chi_{iL} = \chi_i \cdot \hat{L}$ with $i = 1, 2$, and (ii) the effective precession spin parameter χ_p [30] defined as

$$\chi_p := \frac{S_p}{A_2 m_2^2}, \quad S_p = \max(A_1 S_{1\perp}, A_2 S_{2\perp}), \qquad (3.3)$$

where $A_1 = 2 + 3q/2$, $A_2 = 2 + 3/(2q)$, and $S_{i\perp}$, with $i = 1, 2$, is the norm of the spin components perpendicular to L (in-plane spin components). The effective spin parameter is a mass weighted combination of the spin components aligned with L, which predominantly affects the inspiral rate [51]. It is the best constrained spin parameter to date [3]. The in-plane spin components source the precession of the binary system. The average precession exhibited by the binary is approximated by χ_p.

The NR simulations have been selected according to the following criteria:

1) *Waveform accuracy*. When multiple resolutions of a simulation are available, we use the highest resolution and the waveforms extracted at largest extraction radius. For SXS waveforms we choose the second order extrapolation to future-null infinity.

2) *NR code*. We only compare simulations produced with the same NR code to avoid systematics coming from the different numerical methods and ambiguities due to the use of different gauges.

3) *Length requirements*. Due to the lack of a robust hybridization procedure between precessing NR and post-Newtonian inspiral waveforms as well as the introduction of additional systematics, we restrict this study to NR waveforms only. We select NR waveforms long
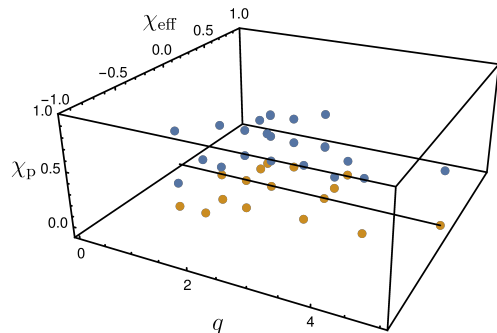
Figure 1. Parameter space distribution in mass ratio, q, and effective spin parameters, χ_{eff} and χ_p, of the NR simulations from Table A. The black thick line corresponds to $\chi_{\text{eff}} = 0$. The blue (yellow) dots represent precessing (aligned-spin) simulations. The simulations span the following parameter ranges: $q \in [1, 5]$, $\chi_{\text{eff}} \in [-0.5, 0.38]$ and $\chi_p \in [0, 0.8]$.

enough to cover a total mass below 100 $M_\odot$ at 20 Hz for all the considered (ℓm) modes, except for one BAM case, ID 28, whose length is shorter but it is interesting as it has a high value of $\chi_p = 0.8$.

4) *Residual eccentricity*. We only select NR simulations that have a residual initial eccentricity $e \leq 3 \times 10^{-3}$. The low-eccentricity initial parameters of the ET simulations have been computed using the method developed in [52].

IV. METHODOLOGY

A. Quadrupole Alignment

Several ways have been put forward to compute the waveform modes in a co-precessing frame [26–28]. We choose the method developed in [26] referred to as *quadrupole-alignment*, henceforth abbreviated QA. It is based on finding the coordinate frame that maximises the mean magnitude of the $(2, \pm 2)$ modes [26–30].

Once the three time-dependent Euler angles that define this frame have been computed, each precessing waveform mode can be rotated to this QA frame through Eq. (2.1). Conversely, given AS modes, these can be rotated through Eq. (2.3) into an inertial frame where they resemble precessing modes.

Furthermore, in order to minimize the effect of the difference between the inertial frames of the rotated AS and the

precessing simulations, we perform an additional global rotation of the (ℓm) modes specified by the three Euler angles which rotate the z-axis onto the direction of the final spin of the black-hole. The direction of the final spin is computed from the data of the apparent horizon of the simulations, while its magnitude is computed using two different procedures, from the apparent horizon of the simulations and from fits to the ringdown orbital frequency as in [53]. Note that another approximated fixed direction for a precessing system is the asymptotic total angular of the system [41], which one could in principle compute from the initial total angular momentum of the system read from the NR simulations and evolve it backwards in time using PN equations of motion. However, this is a difficult procedure due to the gauge differences between PN and NR. We have also tested that the differences between the directions of the initial and final angular momentum of the system are small ($\sim 1°$) for the cases discussed here, thus, the choice of one or the other does not modify the subsequent analysis.

B. Match calculation

The GW signal of a quasicircular binary black hole system with arbitrary spins is described by 15 parameters [54]. Some of these parameters are properties intrinsic to the GW emitting source: the total mass and mass ratio of the binary as well as the six components of the two spin vectors. The remaining parameters are extrinsic and describe the relation between the binary source frame and the observer; they are: the luminosity distance d_L, the coalescence time t_c, the inclination ι, the azimuthal angle φ, the right ascension ϕ, declination θ and polarization angle ψ.

The real-valued GW strain observed in a detector is given by [55]

$$h_{resp}(t;\zeta,\Theta) = F_+(\theta,\phi,\psi)h_+(t-t_c,d_L,\iota,\varphi,\zeta)$$
$$+ F_\times(\theta,\phi,\psi)h_\times(t-t_c,d_L,\iota,\varphi,\zeta), \quad (4.1)$$

where $\Theta = \{t_c,d_L,\theta,\varphi,\alpha,\delta,\psi\}$ and $\zeta = \{M,q,\boldsymbol{S}_1,\boldsymbol{S}_2\}$ are the set of extrinsic and intrinsic parameters, respectively. The two waveform polarisations $h_+,h_\times$ are defined as

$$h(t) = h_+ - ih_\times = \sum_{l=2}^{\infty}\sum_{m=-l}^{l} {}^{-2}Y_{\ell m}(\iota,\varphi)h_{\ell m}(t-t_c;\zeta), \quad (4.2)$$

where ${}^{-2}Y_{\ell m}$ denotes the spin-weighted spherical harmonics of spin weight -2.

The comparison between two waveforms is commonly quantified by the match – the noise-weighted inner product between the signals [56]. Given a real-valued detector response, the inner product between the signal $h_{resp}^S(t)$ and a model $h_{resp}^M(t)$, is defined as

$$\langle h_{resp}^S|h_{resp}^M\rangle = 2\int_{-\infty}^{\infty} \frac{\tilde{h}_{resp}^S(f)\tilde{h}_{resp}^{M*}(f)}{S_n(|f|)}df, \quad (4.3)$$

where $\tilde{h}$ denotes the Fourier transform of h, h^* the complex conjugate of h and $S_n(|f|)$ is the one-sided noise power spectral density (PSD) of the detector.

In order to reduce the dimensionality of the parameter space we can combine declination, right ascension and polarization angle (θ,ϕ,ψ) into an effective polarization angle κ defined as [57]

$$\kappa(\theta,\phi,\psi) := \arctan\left(\frac{F_\times}{F_+}\right), \quad \mathcal{A}(\theta,\phi) = \sqrt{F_\times^2 + F_+^2}. \quad (4.4)$$

The detector response can then be rewritten in terms of the effective polarization angle κ as

$$h_{resp}(t) = \frac{\mathcal{A}}{d_L}[h_+(t)\cos\kappa + h_\times(t)\sin\kappa]. \quad (4.5)$$

The normalized match is then defined as the inner product optimized over a relative time shift, the initial orbital phase and the polarization angle given by

$$\mathcal{M} = \max_{t_0^M,\varphi_0^M,\kappa^M}\left[\frac{\langle h_{resp}^S|h_{resp}^M\rangle}{\sqrt{\langle h_{resp}^S|h_{resp}^S\rangle\langle h_{resp}^M|h_{resp}^M\rangle}}\right], \quad (4.6)$$

where the values of the signal angles $(\iota^S,\varphi_0^S,\kappa^S)$ are fixed. The procedure to compute the match is described in detail in App. B of [30]. A match $\mathcal{M}\simeq 1$ indicates good agreement between the signal and the model, while $\mathcal{M}\simeq 0$ indicates orthogonality between the two waveforms.

We perform an analytical maximization over κ^M and compute numerically the maximum for t_0^M and φ_0^M through an inverse Fourier transform and numerical maximization. To ease the comparisons we introduce the mismatch, $1-\mathcal{M}$.

C. Radiated energy

In addition to the commonly used mismatch calculation to quantify the disagreement between two waveforms, we also compute the radiated energy per (ℓm)-mode,

$$E_{\ell m} = \frac{1}{16\pi}\int_{t_0}^{t_f} d\tau\left|\dot{h}_{\ell m}(\tau)\right|^2, \quad (4.7)$$

where t_0 is the relaxed time after the burst of junk of radiation, t_f is the final time of the simulation, $\dot{h}_{\ell m}(\tau) \equiv dh_{\ell m}(\tau)/d\tau$. This quantity is more sensitive to discrepancies in the amplitude of the waveforms than the mismatch, which is more sensitive to phase differences. We will use this measure in particular as a diagnostic tool to quantify mode asymmetries. Note that given the fact that we have set set the scale of the total mass to 1, the radiated energy scales consistently with that choice.

V. TESTING THE ACCURACY OF MODELLING APPROXIMATIONS

We quantify and discuss the impact of the two approximations (APX1) and (APX2) used in the phenomenological

framework to model precessing binaries including higher order modes. The higher order modes analyzed in this paper are $(\ell, m) = \{(2,|2|), (2,|1|), (3,|2|), (3,|3|), (4,|3|), (4,|4|)\}$. These modes can be grouped in three subsets: the $\ell = 2$ modes, where at least for the $(2,|2|)$ we expect high accuracy of the approximations, the $(3,|2|), (4,|3|)$ modes for which poor accuracy is expected due to the significant mode-mixing [58] which the approximations are not able to reproduce, and the $(4,|4|)$ and $(3,|3|)$ modes as the next dominant higher order modes.

The analyses are carried out in two different coordinate frames, the non-inertial co-precessing frame and the inertial precessing frame. We discuss the interpretation of the results in both frames and show the suitability of one or another to assess the accuracy of the approximations.

A.   Co-precessing waveforms: QA vs. AS

We first study the validity of the identification of AS and co-precessing waveforms (APX1), where the latter are constructed via the QA method described in Sec. IV A. For this comparison we use all available waveform modes of each simulation in order to generate the QA modes, i.e., we take all terms in the sum of Eq. (2.1). For instance, we generate the QA (2,2) and (3,3) modes as follows:

$$h_{22}^{\text{QA}}(t) = \mathbf{R}_{222} h_{22}^{\text{prec}}(t) + \mathbf{R}_{22,-2} h_{2,-2}^{\text{prec}}(t) + \mathbf{R}_{22,0} h_{2,0}^{\text{prec}}(t)$$
$$+ \mathbf{R}_{221} h_{21}^{\text{prec}}(t) + \mathbf{R}_{22,-1} h_{2,-1}^{\text{prec}}(t). \tag{5.1}$$

$$h_{33}^{\text{QA}}(t) = \mathbf{R}_{333} h_{33}^{\text{prec}}(t) + \mathbf{R}_{33,-3} h_{3,-3}^{\text{prec}}(t) + \mathbf{R}_{33,0} h_{3,0}^{\text{prec}}(t)$$
$$+ \mathbf{R}_{332} h_{32}^{\text{prec}}(t) + \mathbf{R}_{32,-2} h_{3,-2}^{\text{prec}}(t)$$
$$+ \mathbf{R}_{331} h_{31}^{\text{prec}}(t) + \mathbf{R}_{33,-1} h_{3,-1}^{\text{prec}}(t). \tag{5.2}$$

The qualitative behavior of (APX1) is illustrated in Fig. 2, where we show a selection of higher-order modes in the co-precessing frame with the corresponding AS modes for the configuration with ID 36. We observe the well-known hierarchy between the amplitudes of the AS higher-order modes[59], which is also reproduced by the QA modes. Furthermore, we see clear asymmetries between positive and negative m QA modes at merger.

Note that in Fig. 2 there is not only an amplitude discrepancy but also a time shift between positive and negative m QA modes. This is due to the fact that for the strain, which is two time derivatives of the Newman-Penrose scalar ψ_4, the amplitude discrepancies in the $\psi_{4,\ell m}$ modes translate also into time-shifts in the $h_{\ell m}$ modes. However, only amplitude asymmetries are relevant for the subsequent analysis as the mismatch calculation maximizes over possible time-shifts between waveforms by performing an inverse Fourier transform. These amplitude asymmetries are not captured by (APX1), and reduce the accuracy of the QA-AS identification, especially for higher order modes, where these effects are exacerbated (see Fig. 2).

We now quantify the agreement between the QA and AS modes by calculating the mismatch between individual modes
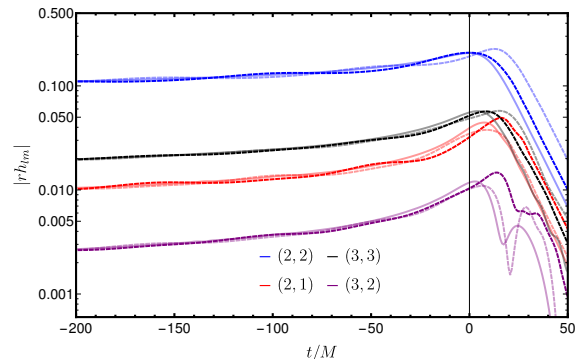

Figure 2.   Time-domain amplitude of the strain for the $\{(2,\pm2),(2,\pm1),(3,\pm3),(3,\pm2))\}$ modes. The solid lines with low opacity represent the amplitude of the AS (ℓ, m) mode, while the dashed lines with high (low) opacity represent the QA (ℓ, m) $((\ell, -m))$ modes for the configuration with ID 36 from Table A of App. A.

optimized over a time shift and phase offset for all pairs of NR simulations in Tab. A. The integral in Eq. (4.3) is evaluated between 20 Hz and a maximum frequency below 2000 Hz which varies depending on the total mass of the system and the length of the NR waveform. We use the Advanced LIGO design sensitivity PSD [1, 60].

Figure 3 shows the mismatch between single QA modes and AS ones for the $\{\ell, m\} = \{(2,\pm2)$ (top panel) and $\{\ell, m\} = (2,\pm1)\}$ modes (bottom panel) as a function of the total mass compatible with the length of the NR waveforms. The results for the other modes can be found in Fig. 9 in App. B. In each panel of Figures 3 and 9 we mark with horizontal lines the 1%, 3% and 10% values of the mismatch. Moreover, we highlight two cases with IDs 10 (red) and 36 (blue): ID 10 is selected as a representative of the bulk of available NR waveforms, with a small mass ratio, $q = 1.5$, and moderate precession spin, $\chi_p = 0.5$, while the case ID 36 has the highest mass ratio in our data set of NR waveforms, $q = 5$.

For the $(2,\pm2)$-modes, top panel in Fig. 3, we observe mismatches well below 3%, except for the $(2,2)$ mode of the case with ID 28. This configuration has a moderate mass ratio, $q = 3$, and high values of the in-plane spin components $\chi_{1\perp} = 0.8, \chi_{2\perp} = 0.6$ on both BHs. A closer look (see Fig. 14 in App. B) reveals that while the $(2,2)$-QA mode resembles the AS $(2,2)$-mode reasonably well during the inspiral, at merger the amplitude of the QA-mode is significantly higher than for the AS-mode. Additionally, we identify a clear asymmetry between the $(2,2)$ and $(2,-2)$ QA modes. In order to quantify this asymmetry between positive and negative m-modes, as well as the difference between AS and QA modes, we also compute the radiated energy per (ℓ, m)-mode for this case. The amount of energy radiated per m-mode is given in Tab. II. We also calculate the ratio of radiated energy between positive and negative m-modes. The large differences in radiated energy between positive and negative m-modes translate into great differences in the peak of the waveforms, which is the cause of the high mismatch for this particular case.
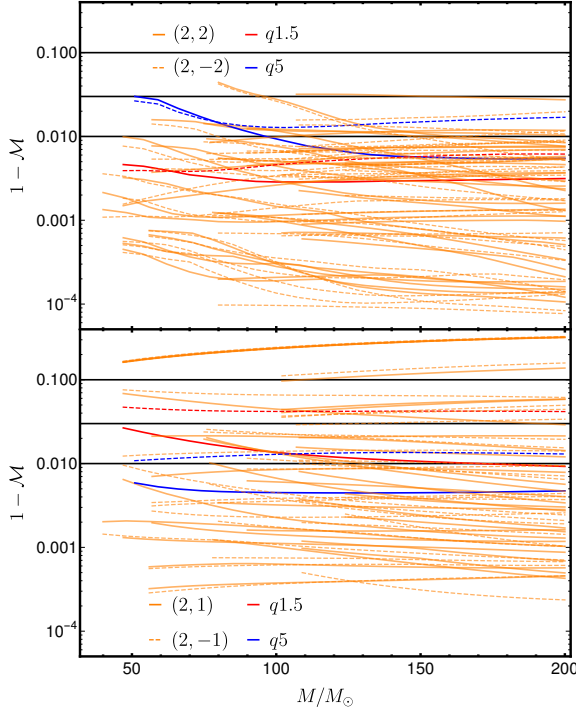
6

Figure 3. Mode by mode mismatches between QA and AS modes for all NR configurations in Table A as a function of the total mass of the system. Top: Results for the $(2,\pm2)$; Bottom: Result for the $(2,\pm1)$ modes. The configurations with IDs 10 (red) and 36 (blue) are highlighted. The solid and dashed curves correspond to positive and negative m-modes, respectively. The horizontal lines mark mismatches of 1%, 3% and 10%. Configurations with PI symmetry (IDs 1, 2, 3 and 4) have been removed from the bottom panel.

$(\ell,\lvert m\rvert)$ 10^{-3}	$E_{\ell,m}^{AS}$	$E_{\ell,m}^{QA}$	$E_{\ell,-m}^{AS}$	$E_{\ell,-m}^{QA}$	$E_{\ell,m}^{QA}/E_{\ell,-m}^{QA}$
$(2,2)$	8.912	13.619	8.912	8.083	1.68
$(2,1)$	0.104	0.098	0.104	0.192	0.51
$(3,2)$	0.012	0.026	0.012	0.049	0.53
$(3,3)$	0.852	1.124	0.852	1.003	1.21
$(4,3)$	0.005	0.008	0.005	0.016	0.52
$(4,4)$	0.164	0.201	0.164	0.195	1.03

Table II. Radiated energy in the $(2,\lvert2\rvert)$, $(2,\lvert1\rvert)$, $(3,\lvert2\rvert)$, $(3,\lvert3\rvert)$, $(4,\lvert3\rvert)$, $(4,\lvert4\rvert)$ modes of the AS and QA configurations for the case with ID 28 in Table A.

This picture changes quite significantly for the $(2,\pm1)$ modes, bottom panel of Fig. 3: We identify five configurations with a mass averaged mismatch larger than 10%: ID 4, which is an equal mass, equal spin binary; IDs 9, 10 and 12, which correspond to a series of $q = 1.5$ simulations with the same χ_{1L} but differently oriented in-plane spin components for the smaller black hole; and ID 20, a $q = 2$ simulation. For those cases we find that the QA-mode is not represented well by the corresponding AS-mode (see App. C for details). We note that odd-m modes, in particular the $(2,1)$-mode, are very sensitive to asymmetries in the binary, which may be reflected in the values of the final recoil of the system [61]. Thus, we have computed the recoil velocity for all available simulations in Tab. A. However, we do not find a direct correlation between the recoil velocity and large mismatches. We observe that some configurations with mass ratios 1.5 and 2, the same χ_{eff} but different in-plane spin components have mismatches $< 3\%$, while others have mismatches $\geq 10\%$.

Furthermore, there are also four cases with mass averaged mismatches $\langle 1 - \mathcal{M} \rangle$ between 5% and 10%, corresponding to the simulations with IDs 1, 15, 16 and 21. Simulation with ID 1 is an equal mass equal, spin configuration with PI symmetry, hence, with mathematically vanishing odd m modes, while IDs 15, 16 and 21 are $q = 2$ simulations with $\chi_{\text{eff}} = 0$ and $\chi_{\text{eff}} = -0.33$, respectively, and small AS $(2,1)$ modes. Further discussion can be found in App. C. For the remaining simulations, i.e., 75% of the NR data set, we find mass averaged mismatches $\langle 1 - \mathcal{M} \rangle \leq 3\%$.

We have also investigated the QA-AS correspondence for other higher-order modes. Overall, we find that the number of cases with $\langle 1 - \mathcal{M} \rangle \leq 3\%$ is significantly smaller than for the quadrupolar modes. This indicates a clear degradation of (APX1) for higher order modes. We identify the QA mode asymmetries as well as strongly pronounced residual oscillations due to nutation as the cause. See Fig. 9 in App. B for the details. We further remark that the $(3,\lvert2\rvert)$ and $(4,\lvert3\rvert)$ modes are affected strongly by mode mixing, which requires a transformation to a spheroidal harmonic basis. In addition, all higher order modes suffer from more numerical noises in comparison to the quadrupolar mode, which necessarily impacts the mismatch. Possible ways to address such limitations are discussed in Sec. VI B.

B.   Approximate precessing waveforms: Impact of higher-order modes

We are now turning our attention to (APX2), analyzing the impact of the number of AS higher order modes used in the construction of approximate precessing waveforms in the inertial frame. To do so, we use the inverse QA-transformation. In contrast to the previous section, where all available higher-order modes were taken into account (see Eqs. (5.1) and (5.2)), in this section we restrict the number of available AS modes in the sum of Eq. (2.3) to the same set of modes used in current Phenom/EOB waveform models [15, 16]: $(\ell,m) = \{(2,\pm2),(2,\pm1),(3,\pm2),(3,\pm3),(4,\pm3),(4,\pm4)\}$. The impact of these higher order modes in the map between the

co-precessing and the inertial frame is assessed via truncating different terms in the sum. For instance, in the case of the approximate precessing $(2,2)$ mode, we calculate it taking into account either only the AS $(2,\pm2)$ modes or the AS $(2,\pm2),(2,\pm1)$ modes, i.e.,

$$h_{22}^{\mathrm{P,k:}\{\pm2\}}(t) = \mathbf{R}_{222}^{-1}h_{22}^{\mathrm{AS}}(t) + \mathbf{R}_{22,-2}^{-1}h_{2,-2}^{\mathrm{AS}}(t), \qquad (5.3)$$

$$\begin{aligned} h_{22}^{\mathrm{P,k:}\{\pm2,\pm1\}}(t) = {}& \mathbf{R}_{222}^{-1}h_{22}^{\mathrm{AS}}(t) + \mathbf{R}_{22,-2}^{-1}h_{2,-2}^{\mathrm{AS}}(t) \\ &+ \mathbf{R}_{221}^{-1}h_{21}^{\mathrm{AS}}(t) + \mathbf{R}_{22,-1}^{-1}h_{2,-1}^{\mathrm{AS}}(t). \end{aligned} \qquad (5.4)$$

The notation $h_{\ell m}^{\mathrm{P,k:}\{\pm r,\pm s\}}$ refers to the approximate precessing (ℓ,m) waveform mode constructed with the AS $(\ell,\pm r)$, $(\ell,\pm s)$ modes.

The agreement between fully precessing and approximate precessing modes is first quantified via single-mode mismatches following the same procedure as in Sec. V A. The results for the $(2,\pm2)$ and $(2,\pm1)$ modes are shown in Fig. 4, the results for the other modes in Fig. 10. Solid and dashed lines represent the mismatches calculated with two AS modes, as per Eq. (5.3), or with four AS modes, as per Eq. (5.4), respectively. The configurations with IDs 10 (blue) and 36 (red) are again highlighted; horizontal lines indicate mismatches of 1%, 3% and 10%.

The precessing $(2,2)$-mode mismatches (top panel of Fig. 4) are below 3% for all cases except for the case with ID 28, which shows mismatches > 3% for all total masses. This outlier configuration is the same as in Sec. V A when testing (APX1) for the $(2,2)$-mode and it corresponds to a short BAM simulation with $q = 3$ and $\chi_p = 0.8$, the highest value in our NR data set. We identify an amplitude asymmetry as the underlying cause (see App. C for details).

In Tab. III the percentages of cases with a mass average mismatch within different threshold values are shown. For the $(2,2)$ mode 97.2% of the cases in our data set have an average mismatch below the 3%. The addition of the AS $(2,\pm1)$ modes does not change the percentage of simulations with an average mismatch below 3%. This indicates that the inclusion of the AS $(2,\pm1)$ modes in the construction of the approximate precessing $(2,2)$ mode has little impact, although we generally observe improved mismatches (see top panel of Fig. 10).

The bottom panel of Fig. 4 shows the results for the precessing $(2,1)$ mode; we see a higher number of cases with mismatches above 3% than for the $(2,2)$ mode. In particular, we find that the inclusion of the AS $(2,\pm1)$ decreases the total percentage of simulations with mismatched below 3% as shown in Table III, see e.g. the red and blue curves in the bottom panel of Fig. 4. We attribute this decrease to the less accurate identification between the QA and AS $(2,1)$ mode. For the configuration ID 10 we see in the right panel of Fig. 14 that the approximate precessing $(2,1)$-mode constructed with four AS modes, although it reproduces more accurately the shape of the precessing mode during the inspiral, it has larger errors at merger than the one built with only two AS modes. This error at merger dominates the value of the mismatch and it also indicates the inability of the approximation to accurately reproduce the merger part of the precessing $(2,1)$-mode for this

P Mode	AS Modes	$N_{3\%\leq\langle 1-\mathcal{M}\rangle}$	$N_{3\%\leq\langle 1-\mathcal{M}\rangle\leq10\%}$	$N_{\langle 1-\mathcal{M}\rangle\geq10\%}$
$(2,2)$	$(2,\pm2)$	97.2%	2.8%	0%
	$(2,\pm2),(2,\pm1)$	97.2%	2.8%	0%
$(2,1)$	$(2,\pm2)$	77.8%	13.9%	8.3%
	$(2,\pm2),(2,\pm1)$	63.9%	22.2%	13.9%
$(3,2)$	$(3,\pm3)$	8.3%	13.9%	77.8%
	$(3,\pm3),(3,\pm2)$	25.%	33.3%	41.7%
$(3,3)$	$(3,\pm3)$	86.1%	5.6%	8.3%
	$(3,\pm3),(3,\pm2)$	88.9%	8.3%	2.8%
$(4,3)$	$(4,\pm4)$	27.8%	33.3%	38.9%
	$(4,\pm4),(4,\pm3)$	27.8%	30.6%	41.7%
$(4,4)$	$(4,\pm4)$	83.3%	16.7%	0%
	$(4,\pm4),(4,\pm3)$	83.3%	16.7%	0%

Table III. Distribution of single mode mismatches shown in Figs. 4 and 10. The notation $N_{X\%\leq\langle 1-\mathcal{M}\rangle\leq Y}$ refers to the percentage of cases in the NR data set, with a mismatch averaged over the mass range between the $X\%$ and $Y\%$. The first column indicates the precessing (ℓ,m)−mode for which the mismatches are calculated; the second column the AS modes used to constructed the approximate precessing mode; the remaining columns give the percentage of cases in our NR data set with an average mismatch $\leq 3\%$, between 3% and 10%, and $\geq 10\%$, respectively.

case. Further, high mismatches for the $(2,\pm1)$ modes are also obtained for configurations for which the $(2,|1|)$-modes have a particularly small amplitude. This poses a challenge for NR codes to resolve such small signals. We discuss possible systematics for the AS $(2,\pm1)$ mode in Sec. VI A.

The mismatches for the remaining higher order modes $\{(3,3),(3,2),(4,4),(4,3)\}$ are shown in Fig. 10 of App. B and summarized in Table III. We observe a clear difference between the higher order modes affected by mode-mixing, $(3,2)$ and $(4,3)$ modes, which show poor mismatches with less than 30% of cases below the 3% mismatch; the next dominant higher order modes, $(3,3)$ and $(4,4)$ modes, which are not affected significantly by mode-mixing and have 80% of configurations with mass-averaged mismatches below the 3% mismatch. Note that the mismatches of the $(3,2)$ and $(4,3)$ modes are higher in the inertial frame than in the co-precessing, indicating that the effects of mode-mixing become more relevant in the former due to the more complicated structure caused by the precession of the orbital plane of the binary. Generally, the addition of the AS $(3,\pm2)$ or the $(4,\pm3)$ modes tends to improve the mismatches. However, for a non-negligible subset of configurations their inclusion increases the mismatch, see e.g. the blue and red curves in the left panels of Fig. 10. This indicates the necessity to disentangle the effects of the two sources of mode-mixing in the approximate precessing waveforms, the one coming from using different AS modes in the map between the co-precessing and inertial frame, and the one from the contribution of approximate precessing higher order modes with the same m index. One possible approach to that problem would be to study the map between inertial and co-precessing frames with the spheroidal harmonic basis
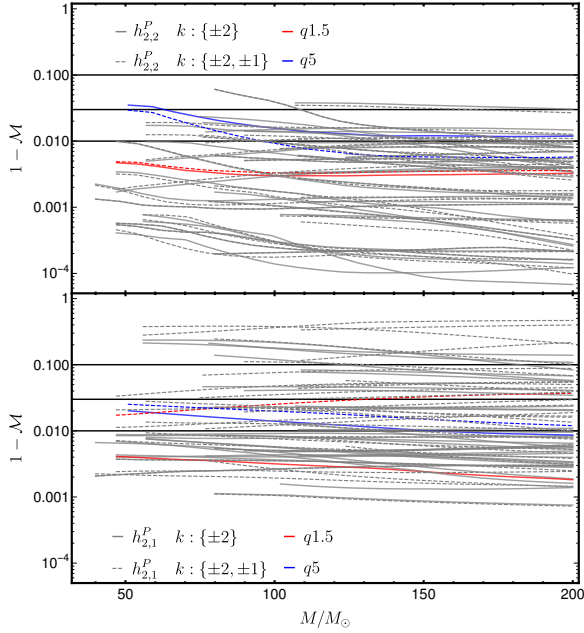
Figure 4. Mode by mode mismatches between precessing and approximate precessing modes in the inertial frame for all NR configurations from Table A as a function of the total mass of the system. In the top and bottom panels we show the results for the $(2,2)$ and $(2,1)$ modes, respectively. The thick and dashed lines correspond to taking two, Eq. (5.3), and four AS modes, Eq. (5.4), to generate the approximate precessing waveforms, respectively. The letter k represents the index of the rotation operator given in Eq. (2.3). In addition, configurations with IDs 10 and 36 are highlighted with red and blue colors, respectively. The horizontal lines mark a mismatch of 1%, 3% and 10% respectively.

for the ringdown part of the waveform for these modes, which we leave for future work.

We also compute mismatches for negative m modes in Fig. 11. Computing the average mismatch for each configuration, we find similar results to the positive m-modes.

The analysis of the single mode mismatches indicates that the inclusion of more AS higher order modes can lower the mismatch between the precessing and approximate precessing waveforms quite significantly. Therefore, it is not necessarily optimal to include an arbitrary number of AS modes when constructing approximate precessing waveform modes.

However, this analysis concerns only the individual modes, thus neglects the geometric coefficients which reweight the modes depending on the orientation of the source. Therefore, we now take this into account and compute mismatches between the detector response (Eq. (4.5)) constructed from the precessing NR modes and the approximate precessing modes calculated with either two or four AS modes as per Eqs. (5.3) and (5.4). When computing the mismatches for the detector response we optimize over time shifts and phase offsets as

in the case of the single mode mismatches, but we also optimize analytically over the effective polarization angle of the template, κ_t, following the procedure described in [30]. The mismatches are calculated using the same number of (ℓ, m) modes in the signal and the template. For instance, when using only the approximate precessing $(2, \pm 2)$ modes in the complex strain,

$$h^{P,k:\{\pm 2\}}(t) = Y_{22}^{-2}(\iota, \varphi) h_{22}^{P,k:\{\pm 2\}} + Y_{2,-2}^{-2}(\iota, \varphi) h_{2,-2}^{P,k:\{\pm 2\}}, \quad (5.5)$$

and the AS $(2, \pm 2)$ modes in the rotation operator as in Eq. (5.3), we use the label $(\ell, m) = (2, \pm 2)/\text{AS} : \{(\ell, \pm \ell)\}$. Figures 5 and 15 show contour plots of the mismatches between precessing and approximate precessing waveforms averaged over κ_S for the configuration with ID 36 as a function of inclination and azimuthal angle for a total mass of $M = 65 M_\odot$.

In the top right panel of Fig. 5 the mismatches for the strain computed with the $(\ell, m) = (2, \pm 2)/\text{AS} : \{(\ell, \pm \ell)\}$ modes are displayed. The mismatches increase above 3% in a range of inclinations $67.5° < \iota_S < 112.5°$. In addition close to $\iota_S = 90°$ (edge-on configuration) the values reach a maximum of $\sim 15\%$ value. On the left panel, where the AS $(2, \pm 1)$ modes have been included in the calculation of the approximate precessing modes, the maximum value at $\iota_S = 90°$ has decreased to $\sim 2\%$. For small inclinations the benefit of adding the AS $(2, \pm 1)$ modes is more moderate. Hence, the inclusion of the AS $(2, \pm 1)$ modes significantly improves the description of the strain constructed with the $(2, \pm 2)$ modes, especially for edge-on configurations.

In the mid panels the $(2, \pm 1)$ modes are added to the complex strain. The right mid panel, where only the AS $(2, \pm 2)$ modes are taken into account, displays mismatches above the 3% in small regions around $\iota_S = \{45°, 135°\}$, while the left mid panel, where the AS $(2, \pm 2), (2, \pm 1)$ modes are taken into account, shows mismatch values below 3% for all orientations. Therefore, the inclusion of the $(2, \pm 1)$ AS modes reduces the mismatch with respect to the case where only the $(2, \pm 2)$ AS modes are available. This result also indicates that the improvement in the $(2, \pm 2)$ approximate precessing modes, due to the inclusion of the $(2, \pm 1)$ AS modes, is higher than the degradation of the single $(2, \pm 1)$ approximate precessing modes as observed in the bottom panel of Fig. 4. The choice of an inertial frame where the $(2, \pm 2)$ modes have more power than the $(2, \pm 1)$ modes alleviates the inaccuracy in the description of the precessing $(2, \pm 1)$ modes.

In the bottom panels of Fig. 5 the strain is constructed from the $(2, \pm 2), (2, \pm 1), (3, \pm 3)$ modes. The bottom right panel, which uses the AS $(2, \pm 2), (3, \pm 3)$ modes to generate the approximate precessing waveforms, shows higher mismatches than the left panel, which employs the AS $(2, \pm 2), (2, \pm 1), (3, \pm 3), (3, \pm 2)$ modes. The results show an overall increase in the mismatch due to the addition of the $(3, \pm 3), (3, \pm 2)$ modes whose inaccuracy, as shown in the single mode mismatches of Fig. 10 of App. B, is higher than for the $(2, \pm 2), (2, \pm 1)$ modes.

In Fig. 15 of App. B strain mismatch contour plots between precessing and approximate precessing waveforms in the inertial frame for the same configuration as in Fig. 5 with more higher order modes in the sum

of the complex strain are shown. In the top, middle and bottom panels the $(2, \pm2), (2, \pm1), (3, \pm3), (4, \pm4)$; $(2, \pm2), (2, \pm1), (3, \pm3), (3, \pm2), (4, \pm4)$ and $(2, \pm2), (2, \pm1)$, $(3, \pm3), (3, \pm2), (4, \pm4), (4, \pm3)$ modes are taken into account in the sum of the complex strain, respectively. In the left and right panels the $(\ell, |\ell|), (\ell, |\ell - 1|)$ AS modes are taken into account, respectively. The mismatches tend to increase slightly when adding more higher order modes in the sum of the complex strain, consistent with the single mode mismatches of Figs. 4 and 10, while the inclusion of more AS higher order tends to lower the mismatch, although its effect is restricted due to the small power of the AS higher order modes. Note that the results of Figs. 5 and 15, although different quantities, are consistent with the signal-to-noise ratio weighted mismatches of references [36, 39].

We conclude that the inclusion of AS higher order modes in the construction of approximate precessing waveforms tends to decrease the mismatches when the full strain is considered. However, individual modes are not always better described when adding more AS modes due to the inaccuracy of (APX1) for higher order modes, especially those significantly affected by mode-mixing like the $(3, |2|)$ and $(4, |3|)$ modes. Furthermore, the analysis showed that the inclusion of AS higher order modes, like the $(2, \pm1)$, in the precessing strain can reduce the mismatches by up to an order of magnitude. We stress, however, that the addition of even more higher order modes can also have a negative impact, especially when modes, where (APX1) is clearly not applicable, are included.

VI.   CAVEATS AND POSSIBLE IMPROVEMENTS

A.   Systematic errors and $(2, 1)$-amplitude minima

Let us now discuss possible sources of systematic errors in the NR waveforms which can affect our results.

The first systematic error source we consider is the quantity used to calculate the Euler angles that encode the precession of the orbital plane. For the SXS simulations we compute the angles from the gravitational radiation extrapolated to infinite radius [62], while for the ET and BAM simulations we use the Newman-Penrose scalar [63], ψ_4, at the outermost extraction radius available in the simulation. Alternatively, we could also integrate ψ_4 twice in time to obtain the strain and calculate the angles from it. However, integrating twice in time can add extra oscillations in the waveforms which can be as large as those coming from the difference between using ψ_4 or the strain. Therefore, we restrict to compute the angles from the ψ_4 in the case of the BAM and ET simulations.

Aligned-spin configurations with PI symmetry, i.e. the two black holes can be exchanged under a reflection in the orbital plane, have vanishing odd m-modes, which reduce to noise in NR simulations. Naturally, this poses a clear limitation to the identification between AS and QA modes. In our data set simulations with IDs 1-4 show this particular feature. From those four we note that the non-spinning configuration ID 1 has a small AS spin amplitude with respect to the precessing counterpart leading to higher mismatches than the spinning

configurations IDs 2, 3 and 4. We discuss this point in more detail in App. C.

Another known issue concerns the occurrence of minima in the amplitude of the AS $(2, \pm1)$, which are not observed in the corresponding QA modes. In order to obtain some insight into these minima, we have reproduced the AS configuration `q2._0.6_-0.6_pcD12` simulation from Tab. I of Ref. [16] with the Einstein Toolkit (ID 37 in our data set). In addition, we also produced two precessing simulations to test not only the existence of the minimum with a finite difference code, but also to check its relevance for the QA approximation. We summarize the properties of these three simulations in Tab. IV.

Figure 6 shows the time domain amplitudes of the $(2, 1)$ mode of ψ_4 for the three simulations of Tab. IV. We clearly identify a minimum in the AS $(2, 1)$ mode shortly before $t = 0$. The minimum occurs at an orbital frequency of $\Omega_{\min}^{ET} = 0.19$, which is slightly different from the one obtained from the original SpEC simulation, $\Omega_{\min}^{SpEC} = 0.17$. This small difference could be due to differences in the initial data and numerical errors, such as the inaccuracies in the wave extraction or in the double time integration of ψ_4 to obtain the strain. Additionally, we also display the approximate precessing $(2, 1)$ modes constructed from all available AS modes, and the corresponding QA modes. We see that the QA $(2, 1)$ modes do not accurately resemble the AS $(2, 1)$ modes. The mismatches between the $(2, 1)$-modes are of the order of 15(20)% for configuration 38 (39), while the mismatches between the $(2, 2)$-AS and $(2, 2)$-QA modes are 0.2(0.04)%, respectively. Furthermore, the precessing $(2, 2)[(2, 1)]$ modes are faithfully reproduced by the approximate precessing ones with mismatches of 0.2(0.04)[0.2(0.2)]% for simulation with ID 38 (39). The agreement of the precessing modes is due to the negligible contribution of the rather small AS $(2, 1)$-mode in comparison to the large AS $(2, 2)$ mode, while the poor recovery of the AS mode by the QA mode confirms the inability of the AS-QA identification to reproduce the amplitude minima observed in the AS $(2, 1)$-mode.

B.   Waveform decomposition in the co-precessing frame

We have seen previously that the identification between QA and AS modes does not capture mode asymmetries as well as residual modulations due to nutation. This can ultimately lead to a poor reconstructions of the fully precessing GW strain. We now study an extension to (APX1), following the strategy adopted by the precessing surrogate models NRSur4d2s and NRSur7dq2 [64, 65], where the time domain co-precessing waveforms are decomposed into slowly-varying functions and small oscillatory ones such that

$$A_{\ell,m}^{\pm}(t) = \frac{1}{2}\left[A_{\ell,m}(t) \pm A_{\ell,-m}(t)\right], \quad m > 0, \tag{6.1}$$

$$\phi_{\ell,m}^{\pm}(t) = \frac{1}{2}\left[\phi_{\ell,m}(t) \pm \phi_{\ell,-m}(t)\right], \quad m > 0, \tag{6.2}$$

where $A_{\ell,m} = |h_{\ell,m}^{\text{co-prec}}(t)|$ and $\phi_{\ell,m} = \arg\left(h_{\ell,m}^{\text{co-prec}}(t)\right)$. The symmetric amplitude $A_{\ell,m}^{+}$ and the antisymmetric phase $\phi_{\ell,m}^{-}$ are
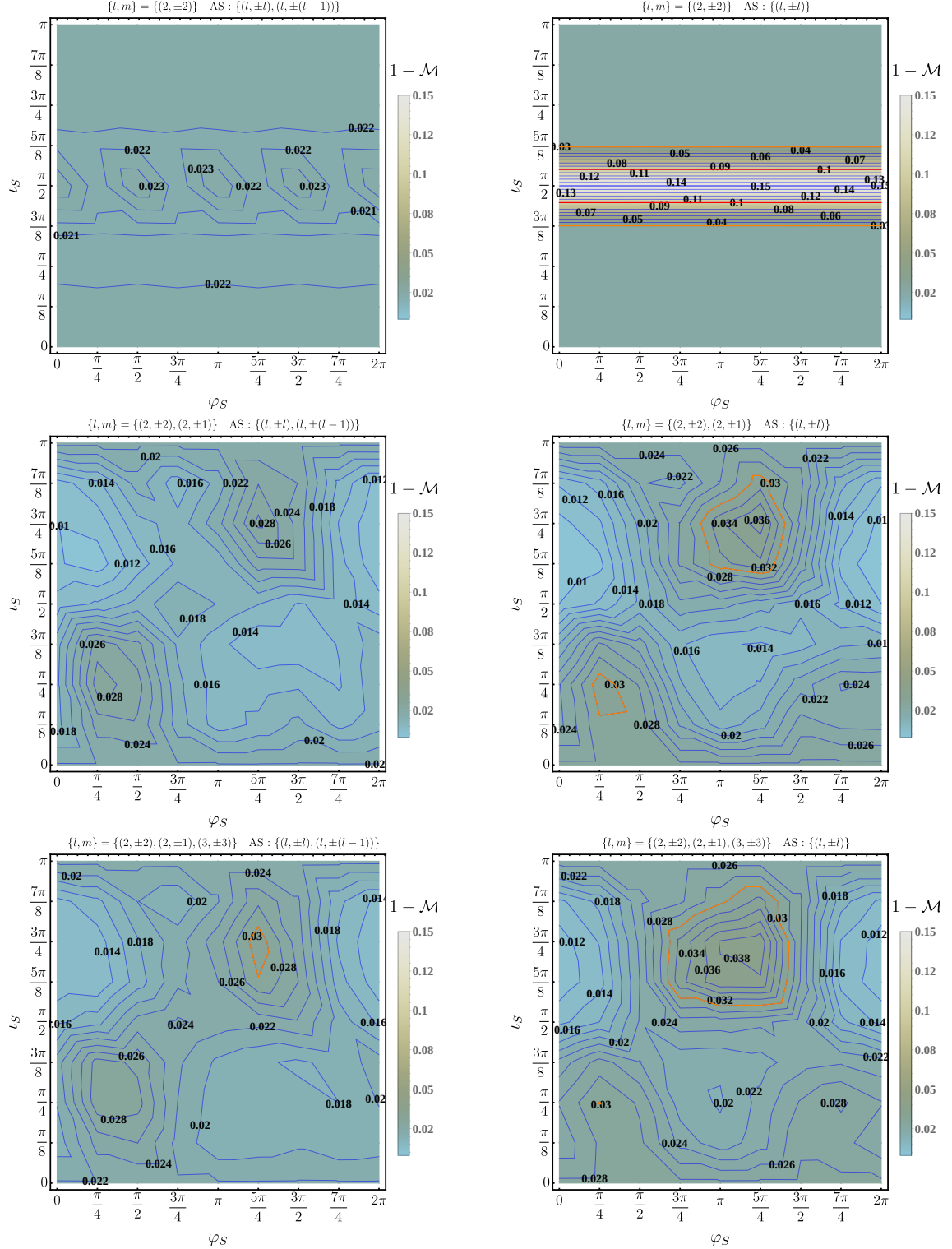
Figure 5. Strain mismatch between precessing and approximate precessing waveforms in the inertial frame averaged over the angle κ_S for a total mass of 65 $M_\odot$ for the configuration with ID 36 as a function of the inclination and the azimuthal angle of the signal (precessing waveform). In the plot labels $\{\ell, m\}$ denotes the modes used in the sum of the complex strain given in Eq. (4.2), while AS represent the aligned-spin modes taken into account in Eq. (2.3). In addition, the 3% and 10% mismatch values are highlighted with orange and red curvess, respectively.

ID	Simulation	Code	q	χ_1	χ_2	D/M	$M\Omega_0$	$e_0 \cdot 10^{-3}$
37	q2._0.6_-0.6__pcD12	ET	2	$(0.,0.,0.6)$	$(0.,0.,-0.6)$	11.72	0.022	1.17
38	q2.__0.4_0._0.6_0._0._-0.6__pcD12	ET	2	$(0.4,0.,0.6)$	$(0.,0.,-0.6)$	11.68	0.022	1.47
39	q2.__0._0._0.6_0.4_0._-0.6__pcD12	ET	2	$(0.,0.,0.6)$	$(0.4,0.,-0.6)$	11.71	0.022	1.08

Table IV. Summary of the properties of the simulations used for the analysis of the impact of the $(2,1)$ minimum. Each simulation is specified by its mass ratio $q = m_1/m_2 \geq 1$, the initial dimensionless spin vectors, χ_1, χ_2, the orbital separation D/M, the orbital frequency Ω_0 and the orbital eccentricity, e_0, at the relaxation time.
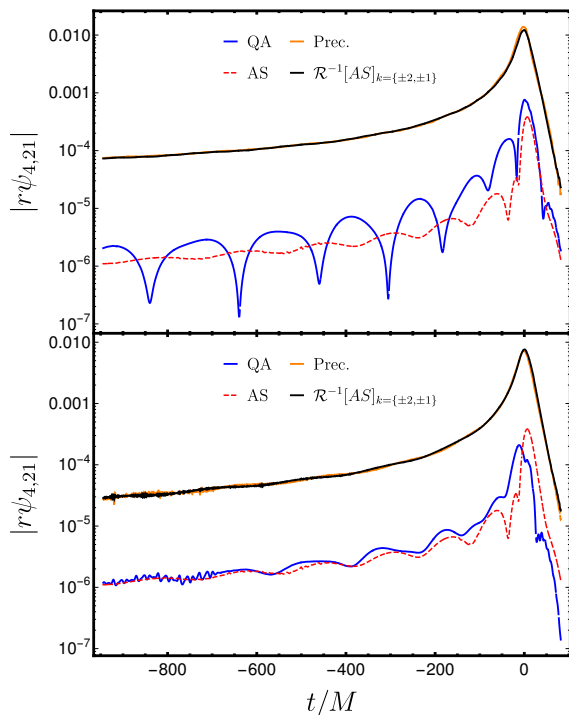
Figure 6. Time domain amplitude of the $r\psi_4$ for the $(2,1)$ mode of the aligned-spin (AS), quadrupole-aligned (QA), precessing (Prec.) and approximate precessing ($\mathcal{R}^{-1}[AS]_{k=\{\pm 2,\pm 1\}}$) configurations. In the upper plot we compare simulations with ID 37 and 38, and in the bottom panel we compare simulations with ID 37 and 39 of Table IV.

Figure 7. Single mode mismatches between the AS modes, $h_{\ell,m}^{AS}$, and the symmetric QA modes, $h_{\ell m}^+$, for all the configurations in Table A as a function of the total mass of the system. In the top and bottom panels we show the results for the $(2,2)$ and $(2,1)$ modes, respectively. The configurations with IDs 10 and 36 are highlighted with red and blue colors, respectively. The horizontal lines mark the 1%, 3% and 10% value of the mismatch.

monotonic functions similar to aligned-spin waveforms, while the antisymmetric amplitude, $A_{\ell,m}^-$ and the symmetric phase $\phi_{\ell,m}^+$ are small real-valued oscillatory functions whose modelling is challenging. In Ref. [23] apply a Hilbert transform is applied to $A_{\ell,m}^-$ and $\phi_{\ell,m}^+$ to convert them into slowly-varying functions easier to model.

We pursue to assess the identification between what we call the symmetric waveform, constructed with the symmetric amplitude and the antisymmetric phase, i.e., $h_{\ell m}^+ = A_{\ell,m}^+ e^{i\phi_{\ell,m}^-}$, and the aligned-spin modes. In order to quantify that comparison we calculate single mode mismatches following the procedure

of Sec. V A. In Fig. 7 we show the single mode mismatches between the $h_{\ell m}^+$ and $h_{\ell m}^{AS}$ for the $(2,2)$ and $(2,1)$ modes. The mismatches for higher order modes are displayed in Fig. 12 of App. B. For odd-m modes we have removed the cases with PI symmetry. The results of Fig. 7 suggest that for the $(2,\pm 2)$ modes the identification between $h_{2,\pm 2}^+$ and $h_{2,\pm 2}^{AS}$ is an outstanding approximation as all the mismatches are below 3%. For higher order modes the mismatches increase one or two orders of magnitude for some particular cases as shown in Fig. 12 of App. B, although the bulk of cases are below 3%.

Given this, which suggests a good approximation between

the symmetric QA and the AS waveforms, we can also study the impact of constructing the QA waveform modes replacing $A_+^{\ell,m}$ and $\phi_-^{\ell,m}$ with the AS the amplitude and phases, $A_{\ell,m}^{AS}$, $\phi_{\ell,m}^{AS}$,

$$A_{l,\pm m}^{QA} = A_{\ell,m}^+ \pm A_{\ell,-m}^- \quad \rightarrow \quad \hat{A}_{l,\pm m}^{QA} \approx A_{\ell,m}^{AS} \pm A_{\ell,-m}^-, \quad (6.3)$$

$$\phi_{l,\pm m}^{QA} = \phi_{\ell,m}^+ \pm \phi_{\ell,-m}^- \quad \rightarrow \quad \hat{\phi}_{l,\pm m}^{QA} \approx \phi_{\ell,m}^+ \pm \phi_{\ell,-m}^{AS}. \quad (6.4)$$

Therefore, one can compute an approximate QA waveform as $\hat{h}_{\ell m}^{QA} = \hat{A}_{l,m}^{QA} e^{i\hat{\phi}_{l,m}^{QA}}$. Once, this waveform is constructed we quantify the difference between the QA modes, $h_{\ell m}^{QA}$, and the approximate ones, $\hat{h}_{\ell m}^{QA}$ via single mode mismatches. In Fig. 8 one observes that $\hat{h}_{\ell m}^{QA}$ produces lower mismatches than $h_{\ell m}^{AS}$. This indicates that the approximation of the symmetric amplitude and asymmetric phase by the AS amplitude and phase can be used with high accuracy for the $(2, \pm 2)$ modes, while for higher order modes, especially the weak $(2, \pm 1), (3, \pm 2)$ and $(4, \pm 3)$ modes this approximation degrades as shown in Fig. 13. This degradation is mainly due to the fact that the small difference between $A_{\ell,m}^{AS}$ and $A_{\ell,m}^+$ is a significant fraction of the power of the modes.

These results suggest a modification to the modelling strategy of precessing waveforms as follows: Instead of directly identifying the QA with corresponding AS modes, one should use the symmetric amplitude and antisymmetric phases constructed from the AS modes as per Eqs. (6.3) and (6.4).

VII.   SUMMARY AND CONCLUSIONS

We have assessed and quantified the accuracy of two main approximations commonly used to construct phenomenological inspiral-merger-ringdown waveforms from precessing BBHs. The first approximation (APX1) is the identification between aligned-spin and co-precessing waveforms [26–29]. The second approximation (APX2) concerns the inclusion of higher-order aligned-spin modes in the construction of approximate precessing modes.

Focusing exclusively on the late inspiral and merger regime, we use NR waveforms from the first SXS catalog [44] and additional waveforms produced with the private BAM code and the open-source Einstein Toolkit. Our analysed NR data set consists of a total of 36 pairs of AS and precessing configurations, and we restrict our analyses to comparisons of waveforms generated with the same NR code to avoid the introduction of systematics due to numerical errors. We note that during the preparation of this manuscript a much larger SXS catalog [66] was released. This allows for the extension of the presented analyses to a larger parameter space, which we leave for future work.

We first quantified the efficacy of the QA-AS mapping (APX1) via single-mode mismatches and the radiated energy per mode. We find that this approximation yields mismatches below 3% for the $(2, \pm 2)$ modes for the majority of configurations in our sample. However, the picture changes dramatically for higher-order modes. For modes that are prone to

mode-mixing such as the $(3, |2|)$ and $(4, |3|)$ mode, the approximation is particularly poor, but the matches drop significantly also for the $(2, |1|)$-modes.

Furthermore, we find that the QA-AS map breaks down for configurations with highly asymmetric energy content between the $+m$ and $-m$ modes as quantified by the radiated energy per mode. The mode asymmetries are one of the clear limitations of this approximate mapping due to the tight symmetry condition of the AS waveforms which is not fulfilled by precessing and therefore the QA waveforms. We conclude that it will become increasingly important to correctly model these mode asymmetries in order to improve the accuracy of waveform models, which will particularly important in the coming years as ground-based GW detectors are set to improve their sensitivity [67–71].

To alleviate some of the shortcomings of (APX1), we have investigated a modification used in surrogate models [23, 25], where rather than identifying the co-precessing modes with AS modes, a combination of slowly varying amplitude and phase functions is used to model the co-precessing modes. We find that the symmetric amplitude and antisymmetric phase of the co-precessing modes can be identified with the amplitude and phase of the AS modes to high accuracy for the $(2, \pm 2)$ modes. For certain higher order modes such as the $(3, \pm 3)$ and $(4, \pm 4)$ we find comparable results, but the weakest modes such as $(2, \pm 1)$, $(3, \pm 2)$ and $(4, \pm 3)$ still have significantly larger mismatches.

Our study of (APX2) shows that the addition of the AS $(2, \pm 1)$ modes to construct the approximate precessing $(2, \pm 2)$ modes, does not significantly impact the mode accuracy. Again, we find that the opposite is true for higher order modes, where the inclusion of higher order AS modes improves the accuracy of the approximate precessing modes. And similarly to (APX1), we find that the $(2, |1|), (3, |2|)$ and $(4, |3|)$ modes are most strongly affected.

Beyond the individual modes, we have also analyzed the GW strain, which takes into account the different contributions from higher order modes depending on the orientation of the binary. Similarly, we find that the inclusion of AS higher order modes to construct approximate precessing waveforms improves the mismatches by an order of magnitude for edge-on configurations. However, care needs to be taken as the inclusion of even more higher order modes in the strain can increase the mismatch due to the accumulation of approximation errors when summing up the individual modes to construct the strain.

To highlight some additional error sources, we have studied a particular configuration which shows a minimum in the aligned-spin $(2, 1)$ mode. We find that while the QA $(2, 1)$ mode is not able to resemble the AS mode accurately, the precessing $(2, 1)$ is hardly affected since the main contribution in its construction stems from the AS $(2, 2)$ mode. Nevertheless, we have also seen that the inclusion of higher order modes in the construction of approximate precessing waveforms does matter for the majority of cases and therefore their accuracy is crucial.

Overall, our results show larger mismatches than what has previously been found for precessing phenomenological and
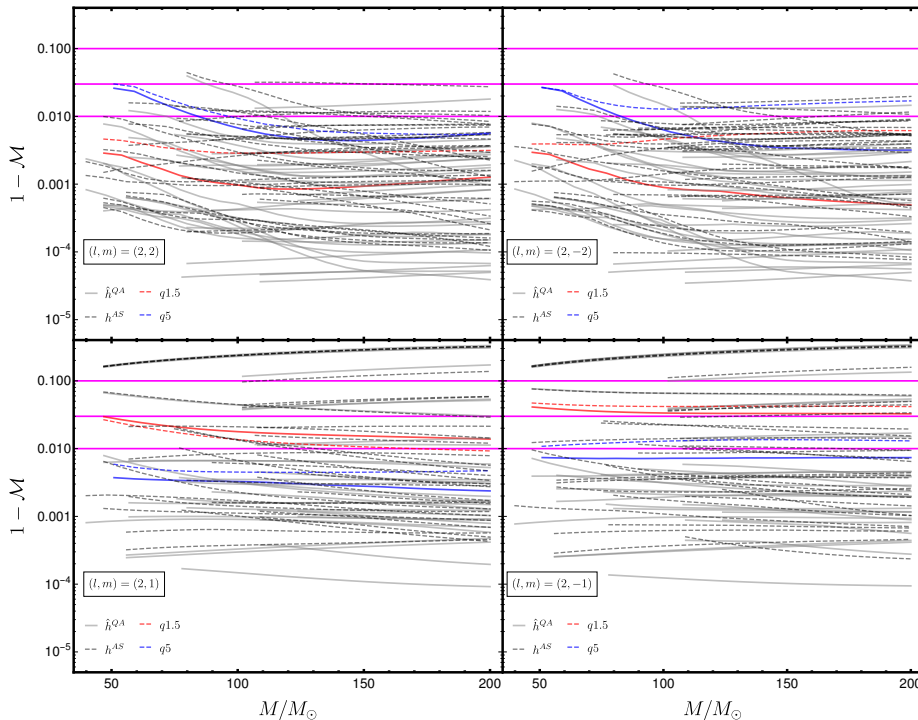
Figure 8. Single mode mismatches between the QA modes, $h^{QA}_{\ell m}$, and the approximate QA, $\hat{h}^{QA}_{\ell m}$, and the AS, $h^{AS}_{\ell m}$, modes; for all the configurations in Table A of App. A as a function of the total mass of the system. In the top [bottom] left and right panels we show the results for the $(2,\pm 2)$ $[(2,\pm 1)]$, respectively. The thick gray (dashed black) lines correspond to mismatches between $h^{QA}_{\ell m}$ and $\hat{h}^{QA}_{\ell m}$ ($h^{AS}_{\ell m}$). In addition, configurations with IDs 10 and 36 are highlighted with red and blue colors, respectively. The horizontal lines mark the 1%, 3% and 10% value of the mismatch.

EOB models [36, 72]. We attribute this difference to the impact of NR errors in our waveforms, which are much higher than those described in [36, 38, 72] due to the inclusion of higher order modes, although the strain mismatches in Sec. V B are consistent with those obtained in [39] for the same configurations. We also note that we neglect modifications to the final state that capture spin precession effects. However, we have verified using other phenomenological waveform models [9, 10, 73] that such modifications are a subdominant effect in the whole framework. Hence, the intrinsic limitations of the two modelling approximation (APX1) and (APX2), combined with the impact of NR errors for higher order modes are responsible for the reduced accuracy pf precessing higher order modes produced in this paradigm.

Our studies show that in order to produce accurate phenomenological precessing waveform models necessary to facilitate the maximal science return from future GW observations, modifications to the simple paradigm that take into account mode asymmetries and subdominant effects will be crucial.

Appendix A: Numerical Relativity Simulations

The `Einstein Toolkit` (ET) [47, 48] is an open source NR code built around the Cactus framework [74, 75]. The numerical setup of our simulations is similar to that used in [76], though we present the details here for completeness.

We use standard Bowen-York initial data [77, 78] computed using the `TwoPunctures` thorn [79], in which the punctures are initially placed on the x-axis at positions $x_1 = D/(1 + q)$ and $x_2 = -qD/(1 + q)$, where D is the coordinate separation and we assume $m_1 \geq m_2$. The initial momenta are chosen such that $\mathbf{p} = (\mp p_r, \pm p_t, 0)$. We use low-eccentricity initial data following the prescription detailed in [52].

The time evolution is performed using the *W*-variant [80] of the BSSN formulation [81, 82] of the Einstein field equations as implemented by `McLachlan` [83]. The black holes are evolved using the standard moving punctures gauge conditions [84, 85] with the lapse being evolved according to the "1 + log" condition [86] and the shift being evolved using a hyperbolic $\tilde{\Gamma}$-driver equation [87].

The simulations were performed using 8th order accurate finite differencing and Kreiss-Oliger dissipation [88]. Adaptive mesh refinement is provided by `Carpet` [89–91], with the near zone being computed with high resolution Cartesian grids that track the motion of the BHs, while the wave extraction zone uses spherical grids provided the `Llama` multipatch infrastructure [76]. By using grids adapted to the spherical topology of the wave extraction zone, we are able to efficiently compute high-accuracy waveforms at large extraction radii relative to standard Cartesian grids. The apparent horizons are computed using `AHFinderDirect` [92] and a calculation of the spins is performed in the dynamical horizon formalism using the `QuasiLocalMeasures` thorn [93].

The gravitational waves are computed using the `WeylScal4` thorn and the GW strain h is calculated from Ψ_4 via fixed-frequency integration [94]. The thorns `McLachlan` and `WeylScal4` are generated by the automated-code-generation package `Kranc` [95, 96]. The ET simulations are managed using `Simulation Factory` [97] and the analysis and post-processing of ET waveforms was performed using the open source `Mathematica` package `Simulation Tools` [98].

The SXS waveform data used here are described in detail in [66, 99] and can be obtained from [100].

The BAM simulations use the same numerical setup as described in App. C 1 of [52]. In brief, the BAM code [45] evolves black-hole binary initial data [101, 102] using the χ-variant version of the moving puncture [84, 85] version of the

BSSN formulation [81, 82] of the Einstein equations. The black-hole punctures are initially located on the y-axis at positions $y_1 = -qD/(1 + q)$ and $y_2 = D/(1 + q)$, where D is the coordinate distance between the two punctures and the mass ratio is $q = m_2/m_1 > 1$. The code uses sixth-order spatial finite-difference derivatives, fourth-order Runge-Kutta algorithm and Kreiss-Oliger dissipation terms [88] which converge at fifth order. Furthermore, the code uses sixteen mesh-refinement buffer points and the base configuration consists of n_1 nested mesh-refinement boxes with N^3 points surrounding each black hole, and n_2 nested boxes with $(2N)^3$ points surrounding the entire system. On the levels where the extraction of gravitational radiation is performed, $(4N)^3$ points are used in order to extract more accurately the gravitational waves emitted by the binary. These waves are computed from the Newman-Penrose scalar Ψ_4 [45] and converted into strain via fixed-frequency integration [94].

Table A summarizes some key properties of the main set of NR simulations used for this work. We arrange the simulations in pairs, each pair consisting of a different precessing simulation and its corresponding aligned-spin counterpart following Eq. (3.1).

Appendix B: Mismatches of higher order modes

Complementary to Sec. V here we present the results of single mode mismatches for the remaining higher order modes.

Figure 9 shows the results for the mismatches between QA and AS modes following Sec. V A. From top to bottom, the plots refer to the $(3, |3|)$, $(4, |4|)$, $(3, |2|)$, and $(4, |3|)$ modes. Additionally, mismatches for the configurations with IDs 10 and 36 are highlighted with red and blue colors, respectively. The horizontal lines mark the 1%, 3% and 10% value of the mismatch. We find overall increase in the mismatch values in the two lowest panels, corresponding to $(3, |2|)$ and $(4, |3|)$ modes compared to the $(3, |3|)$, $(4, |4|)$ modes (top two panels). As discussed in the main text, this increase is caused by the strong mode-mixing effect in the $(3, |2|)$ and $(4, |3|)$ modes which is not captured properly by (APX1).

Single mode mismatches between approximate precessing and precessing waveforms for the higher order modes $\{\ell, m\} = \{(3, 2), (3, 3), (4, 3), (4, 4)\}$ are shown in Fig. 10. The top left and right panels correspond to the $(3, 3)$ and $(4, 4)$ modes; the bottom left and right panels show the results for the $(3, 2)$ and $(4, 3)$ modes. The configurations with IDs 10 and 36 are highlighted with red and blue colors, respectively. The thick and dashed lines correspond to taking 2 and 4 AS waveforms to generate the approximate precessing waveforms, respectively. For instance, in the case of the $(3, 2)$ mode the thick lines correspond to taking the AS $(3, \pm 3)$ modes, while the dashed lines to taking the AS $(3, \pm 3)$ and $(3, \pm 2)$ modes into account in the construction (see Sec. V B for details). For the higher order modes, we find that the modes affected by mode-mixing, $(3, |2|)$ and $(4, |3|)$, have high mismatches with less than 30% of cases below 3% (see Tab. III). The other subdominant modes, $(3, 3)$ and $(4, 4)$, have mismatches below 3% for more than 80% of cases. Furthermore, the inclusion of more AS modes,

15

Table A. Summary of NR simulations used in this work. Each simulation is specified by its mass ratio $q = m_1/m_2 \geq 1$, the initial dimensionless spin vectors, $\vec{\chi}_1$, $\vec{\chi}_2$, the orbital separation D/M, the orbital frequency Ω_0, and the orbital eccentricity, e_0, at the relaxation time, final dimensionless spin vector, χ_f, its magnitude χ_f, final recoil vector $\boldsymbol{v}_f$ (km/s) and its magnitude v_f (km/s).

ID	Simulation	Code	q	$\boldsymbol{\chi}_1$	$\boldsymbol{\chi}_2$	$\chi_{\rm eff}$	D/M	$M\Omega_0$	$e_0\cdot10^{-3}$	M_f	$\boldsymbol{\chi}_f$	χ_f	$\boldsymbol{v}_f(km/s)$	$v_f(km/s)$
1	q1.__0.2_0.1__0.5__0.1_0.2_-0.5__pcD12	ET	1.	(0.2,0.1,-0.5)	(0.1,0.2,-0.5)	-0.5	11.38	0.0232	2.14	0.9618	(0.047,0.036,0.533)	0.536	(3.88,-34.97,-157.09)	160.98
	q1.__0.5__0.5__pcD12	ET	1.	(0.,0.,-0.5)	(0.,0.,-0.5)	-0.5	11.38	0.0232	2.31	0.9621	(0.,0.,0.527)	0.527	(-0.94,0.81,0.00)	1.24
2	q1.__-0.5_0.5__0.5__0.5_-0.5_-0.5__pcD12	ET	1.	(-0.5,0.5,-0.5)	(0.5,-0.5,-0.5)	-0.5	11.38	0.0232	1.59	0.9595	(0.,0.,0.517)	0.517	(-3.15,2.78,1693.88)	1693.89
	q1.__0.5__0.5__pcD12	ET	1.	(0.,0.,-0.5)	(0.,0.,-0.5)	-0.5	11.38	0.0232	2.31	0.9621	(0.,0.,0.527)	0.527	(-0.94,0.81,0.)	1.24
3	q1.__0.5_0.5_-0.5__0.5_0.5_-0.5__pcD12	ET	1.	(0.5,0.5,-0.5)	(0.5,0.5,-0.5)	-0.5	11.25	0.0233	1.21	0.9576	(0.194,0.144,0.567)	0.618	(-1.71,-1.31,3.79)	4.36
	q1.__0.5__0.5__pcD12	ET	1.	(0.,0.,-0.5)	(0.,0.,-0.5)	-0.5	11.38	0.0232	2.31	0.9621	(0.,0.,0.527)	0.527	(-0.94,0.81,0.)	1.24
4	SXS:BBH:0003	SpEC	1.	(0.5,0.05,0.)	(0.,0.,0.)	0.	19.	0.0113	0.26	0.9511	(0.066,0.009,0.691)	0.6947	(122.91,6.75,697.04)	707.82
	SXS:BBH:0001	SpEC	1.	(0.,0.,0.)	(0.,0.,0.)	0.	18.	0.0113	0.17	0.9516	(0.,0.,0.686)	0.686	(0.,0.,0.)	0.00
5	q1.5_0.__0.5_0.__-0.5_0.__pcD11	ET	1.5	(0.,-0.5,0.)	(0.,0.,0.5)	0.2	10.44	0.0260	1.50	0.9487	(-0.007,-0.129,0.710)	0.722	(-73.58,-266.64,1539.6)	1564.25
	q1.5_0.5_0.__pcD11	ET	1.5	(0.,0.,0.5)	(0.,0.,0.)	0.2	10.46	0.0260	1.10	0.9506	(0.,0.,0.707)	0.707	(-122.89,-89.37,0.)	151.95
6	q1.5_0.__-0.5_0.__0.5_0.__pcD12	ET	1.5	(0.,0.,-0.5)	(0.5,0.,0.)	-0.3	11.47	0.0229	1.30	0.9621	(0.052,0.0,0.54)	0.542	(-62.27,208.92,-644.27)	680.15
	q1.5_-0.5_0.__pcD12	ET	1.5	(0.,0.,-0.5)	(0.,0.,0.)	-0.3	11.49	0.0229	1.51	0.9624	(0.,0.,0.540)	0.540	(-6.32,221.25,0.)	221.34
7	q1.5_0.__0.5_-0.5_0.__0.__-0.5_0.5__pcD12	ET	1.5	(0.,0.5,-0.5)	(0.,0.,-0.5)	-0.5	11.42	0.0230	2.60	0.9643	(0.001,0.090,0.514)	0.522	(-113.37,-72.82,-321.97)	349.03
	q1.5_-0.5_-0.5__pcD12	ET	1.5	(0.,0.,-0.5)	(0.,0.,-0.5)	-0.5	11.43	0.0230	2.03	0.9651	(0.,0.,0.491)	0.491	(-108.15,112.94,0.)	156.37
8	SXS:BBH:0015	SpEC	1.5	(0.5,0.06,0.)	(0.,0.,0.)	0.	18.	0.0123	0.34	0.9548	(0.115,-0.014,0.675)	0.685	(119.5,65.27,324.21)	351.64
	SXS:BBH:0007	SpEC	1.5	(0.,0.,0.)	(0.,0.,0.)	0.	18.	0.0123	0.43	0.9552	(0.,0.,0.664)	0.664	(103.38,-1.,0.)	103.38
9	SXS:BBH:0020	SpEC	1.5	(0.,0.,0.5)	(0.49,0.07,0.)	0.3	16.	0.0144	0.12	0.9450	(0.045,0.009,0.788)	0.79	(-14.38,-25.56,20.23)	35.63
	SXS:BBH:0013	SpEC	1.5	(0.,0.,0.5)	(0.,0.,0.)	0.3	16.	0.0144	0.14	0.9446	(0.,0.,0.781)	0.781	(-58.40,27.41,0.01)	64.51
10	SXS:BBH:0023	SpEC	1.5	(0.5,0.05,0.)	(0.08,-0.49,0.)	0.	16.	0.0145	0.28	0.9535	(0.1,-0.046,0.675)	0.684	(156.67,101.15,968.07)	985.87
	SXS:BBH:0007	SpEC	1.5	(0.,0.,0.)	(0.,0.,0.)	0.	18.	0.0123	0.43	0.9552	(0.,0.,0.664)	0.664	(103.38,-1.,0.)	103.38
11	SXS:BBH:0024	SpEC	1.5	(0.5,0.05,0.)	(-0.08,0.49,0.)	0.	16.	0.0145	0.21	0.9550	(0.092,0.053,0.68)	0.688	(-161.54,73.31,-129.14)	219.42
	SXS:BBH:0007	SpEC	1.5	(0.,0.,0.)	(0.,0.,0.)	0.	18.	0.0123	0.43	0.9552	(0.,0.,0.664)	0.664	(103.38,-1.,0.)	103.38
12	SXS:BBH:0026	SpEC	1.5	(0.,0.,0.5)	(-0.49,-0.07,0.)	0.3	16.	0.0144	0.12	0.9450	(-0.046,-0.009,0.788)	0.789	(-15.01,-25.75,-20.12)	35.90
	SXS:BBH:0013	SpEC	1.5	(0.,0.,0.5)	(0.,0.,0.)	0.3	16.	0.0144	0.14	0.9446	(0.,0.,0.781)	0.781	(-58.40,27.41,0.01)	64.51
13	SXS:BBH:0027	SpEC	1.5	(0.5,0.05,0.)	(-0.49,-0.07,0.)	0.	16.	0.0145	0.07	0.9545	(0.044,0.004,0.673)	0.675	(105.94,251.68,1128.58)	1161.14
	SXS:BBH:0007	SpEC	1.5	(0.,0.,0.)	(0.,0.,0.)	0.	18.	0.0123	0.43	0.9552	(0.,0.,0.664)	0.664	(103.38,-1.,0.)	103.38
14	SXS:BBH:0028	SpEC	1.5	(0.,0.,0.5)	(0.08,-0.49,0.)	0.3	16.	0.0144	0.18	0.9435	(0.009,-0.041,0.785)	0.786	(-42.34,-32.47,-41.01)	67.30
	SXS:BBH:0013	SpEC	1.5	(0.,0.,0.5)	(0.,0.,0.)	0.3	16.	0.0144	0.14	0.9446	(0.,0.,0.781)	0.781	(-58.40,27.41,0.01)	64.51
15	SXS:BBH:0029	SpEC	1.5	(0.5,0.05,0.)	(0.49,0.07,0.)	0.	16.	0.0145	0.47	0.9536	(0.151,-0.001,0.678)	0.694	(107.59,120.27,474.1)	500.81
	SXS:BBH:0007	SpEC	1.5	(0.,0.,0.)	(0.,0.,0.)	0.	18.	0.0123	0.43	0.9552	(0.,0.,0.664)	0.664	(103.38,-1.,0.)	103.38
16	q2.__-0.35_0.35_0.5__0._0._0.__pcD10.8	ET	2.	(-0.35,0.35,0.5)	(0.,0.,0.)	0.333	10.28	0.0265	1.11	0.9476	(-0.126,0.120,0.785)	0.804	(-104.70,95.90,551.66)	569.64
	q2.__0._0._0.5__pcD11	ET	2.	(0.,0.,0.5)	(0.,0.,0.)	0.333	10.55	0.0257	0.96	0.9494	(0.,0.,0.778)	0.778	(37.33,-43.68,0.)	57.46
17	q2.__-0.35_0.35_0.__0._0._0.__pcD10.8	ET	2.	(-0.35,0.35,0.)	(0.,0.,0.)	0.	10.24	0.0270	0.78	0.9602	(-0.095,0.114,0.641)	0.658	(96.36,-159.30,-93.83)	208.48
	q2.__0._0.__pcD11	ET	2.	(0.,0.,0.)	(0.,0.,0.)	0.	10.52	0.0261	1.34	0.9612	(0.,0.,0.623)	0.623	(111.94,89.01,0.)	143.02

16

(Continued)

| ID	Simulation	Code	q	χ_1	χ_2	χ_{eff}	D/M	$M\Omega_0$	$e_0\cdot10^{-3}$	M_f	χ_f	χ_f	$\boldsymbol{v_f}(km/s)$	$v_f(km/s)$
18	q2._-0.35_0.35_-0.5_0._0._0._0._pcD10.8	ET	2.	(-0.35,0.35,-0.5)	(0.,0.,0.)	-0.333	10.06	0.0277	2.65	0.9674	(-0.115,0.071,0.489)	0.507	(308.13,95.87,0.04)	322.70
	q2._0._-0.5_pcD11	ET	2.	(0.,0.,-0.5)	(0.,0.,0.)	-0.333	10.37	0.0267	1.88	0.9683	(0.,0.,0.460)	0.460	(-239.88,91.74,0.)	256.82
19	q2._-0.35_0.35_-0.5_0._0._0._0._pcD10.8	ET	2.	(0.35,0.35,-0.5)	(0.,0.,0.)	-0.333	10.06	0.0277	1.51	0.9669	(0.071,0.116,0.486)	0.505	(-5.13,-207.31,-758.34)	786.18
	q2._0._-0.5_pcD11	ET	2.	(0.,0.,-0.5)	(0.,0.,0.)	-0.333	10.37	0.0267	1.88	0.9683	(0.,0.,0.460)	0.460	(-239.88,91.74,0.)	256.82
20	q2._-0.35_0.35_0.5_0._0._0._0._pcD10.8	ET	2.	(0.35,0.35,0.5)	(0.,0.,0.)	0.333	10.28	0.0265	0.24	0.9464	(0.119,0.125,0.783)	0.802	(-356.8,-141.84,-1279.92)	1336.27
	q2._0._0.5_pcD11	ET	2.	(0.,0.,0.5)	(0.,0.,0.)	0.333	10.55	0.0257	0.96	0.9494	(0.,0.,0.778)	0.778	(37.33,-43.68,0.)	57.46
21	q2._-0.18_0.18_0.5_0._0._0._0._pcD10.8	ET	2.	(-0.18,0.18,0.5)	(0.,0.,0.)	0.333	10.31	0.0265	0.27	0.9490	(-0.062,0.060,0.780)	0.785	(-79.86,34.08,308.69)	320.67
	q2._0._0.5_pcD11	ET	2.	(0.,0.,0.5)	(0.,0.,0.)	0.333	10.55	0.0257	0.96	0.9494	(0.,0.,0.778)	0.778	(37.33,-43.68,0.)	57.46
22	q2._-0.18_0.18_0._0._0._0._0._pcD10.8	ET	2.	(-0.18,0.18,0.)	(0.,0.,0.)	0.	10.25	0.027	1.47	0.9609	(-0.045,0.053,0.628)	0.632	(-28.97,-139.95,-294.76)	327.58
	q2._0._0._pcD11	ET	2.	(0.,0.,0.)	(0.,0.,0.)	0.	10.52	0.0261	1.34	0.9612	(0.,0.,0.623)	0.623	(111.94,89.01,0.)	143.02
23	q2._-0.18_0.18_0._0._0._0._0._pcD10.8	ET	2.	(0.18,0.18,0.)	(0.,0.,0.)	0.	10.25	0.0270	0.50	0.9608	(0.053,0.046,0.627)	0.631	(-48.56,-95.22,388.39)	402.83
	q2._0._0._pcD11	ET	2.	(0.,0.,0.)	(0.,0.,0.)	0.	10.52	0.0261	1.34	0.9612	(0.,0.,0.623)	0.623	(111.94,89.01,0.)	143.02
24	q2._-0.49_0.49_0._0._0._0._0._pcD10	ET	2.	(-0.49,0.49,0.)	(0.,0.,0.)	0.	10.2	0.0270	1.62	0.9591	(-0.141,0.168,0.654)	0.69	(171.54,-157.08,-108.77)	256.77
	q2._0._0._pcD11	ET	2.	(0.,0.,0.)	(0.,0.,0.)	0.	10.52	0.0261	1.34	0.9612	(0.,0.,0.623)	0.623	(111.94,89.01,0.)	143.02
25	q2._-0.49_0.49_0._0._0._0._0._pcD10.8	ET	2.	(0.49,0.49,0.)	(0.,0.,0.)	0.	10.19	0.0270	0.20	0.9575	(0.167,0.139,0.649)	0.684	(179.99,243.12,1436.06)	1467.57
	q2._0._0._pcD11	ET	2.	(0.,0.,0.)	(0.,0.,0.)	0.	10.52	0.0261	1.34	0.9612	(0.,0.,0.623)	0.623	(111.94,89.01,0.)	143.02
26	q2._0._0._0.7_0._0._0._pcD11.5	ET	2.	(0.7,0.,0.)	(0.,0.,0.)	0.	11.03	0.0241	1.87	0.9578	(0.227,-0.022,0.645)	0.684	(-303.04,18.28,-1281.16)	1316.64
	q2._0._0._pcD11	ET	2.	(0.,0.,0.)	(0.,0.,0.)	0.	10.52	0.0261	1.34	0.9612	(0.,0.,0.623)	0.623	(111.94,89.01,0.)	143.02
27	q3._-0.5_0._-0.3_0._0._-0.3_pcD12	ET	3.	(0.5,0.,-0.3)	(0.,0.,-0.3)	-0.3	11.66	0.0226	1.47	0.9744	(0.169,0.019,0.450)	0.481	(-135.64,-283.05,-426.4)	529.46
	q3._-0.3_-0.3_pcD12	ET	3.	(0.,0.,-0.3)	(0.,0.,-0.3)	-0.3	11.73	0.0226	1.19	0.9757	(0.,0.,0.396)	0.396	(-6.63,-205.79,0.)	205.90
28	q3._0._56.0._0._6.0._0._T_80_400	BAM	3.	(0.75,-0.27,0.)	(0.3,0.52,0.)	0	8.83	0.0329	2.94	0.9675	(0.299,-0.135,0.561)	0.650	(-471.57,54.81,-896.04)	1014.04
	q3._0._0._T_80_400	BAM	3.	(0.,0.,0.)	(0.,0.,0.)	0.	10.	0.0177	2.12	0.9721	(0.,0.,0.541)	0.541	(-64.48,-124.91,0.)	140.57
29	SXS:BBH:0035	SpEC	3.	(0.5,0.03,0.)	(0.,0.,0.)	0.	17.	0.0132	0.44	0.9704	(0.167,0.023,0.581)	0.605	(144.12,216.96,186.26)	320.21
	SXS:BBH:0030	SpEC	3.	(0.,0.,0.)	(0.,0.,0.)	0.	14.	0.0177	2.12	0.9710	(0.,0.,0.541)	0.541	(149.78,90.38,0.)	174.94
30	SXS:BBH:0048	SpEC	3.	(0.,0.,0.5)	(0.47,0.16,0.)	0.375	14.	0.0175	0.20	0.9607	(0.023,-0.002,0.755)	0.755	(2.83,-78.51,-235.65)	248.40
	SXS:BBH:0174	SpEC	3.	(0.,0.,0.5)	(0.47,0.,0.)	0.375	17.	0.0132	0.36	0.9607	(0.,0.,0.756)	0.756	(-100.76,21.66,0.)	103.07
31	SXS:BBH:0050	SpEC	3.	(0.49,0.07,0.)	(0.47,0.18,0.)	0.	14.	0.0175	0.18	0.9695	(0.243,0.003,0.561)	0.611	(-397.86,211.53,-819.3)	935.03
	SXS:BBH:0030	SpEC	3.	(0.,0.,0.)	(0.,0.,0.)	0.	14.	0.0177	2.12	0.971	(0.,0.,0.541)	0.541	(149.78,90.38,0.)	174.94
32	SXS:BBH:0051	Spec	3.	(0.,0.,0.5)	(-0.47,-0.16,0.)	0.375	14.	0.0174	0.16	0.9607	(-0.023,0.002,0.755)	0.755	(6.,-78.14,231.09)	244.02
	SXS:BBH:0174	SpEC	3.	(0.,0.,0.5)	(0.,0.,0.)	0.375	17.	0.0132	0.36	0.9607	(0.,0.,0.756)	0.756	(-100.76,21.66,0.)	103.07
33	SXS:BBH:0053	SpEC	3.	(0.49,0.07,0.)	(-0.46,-0.18,0.)	0.	14.	0.0176	0.20	0.9707	(0.201,-0.006,0.562)	0.597	(-201.97,216.74,-405.19)	501.94
	SXS:BBH:0030	SpEC	3.	(0.,0.,0.)	(0.,0.,0.)	0.	14.	0.0177	2.12	0.9710	(0.,0.,0.541)	0.541	(149.78,90.38,0.)	174.94
34	q4._0.5_0._-0.3_0._0._0.5_-0.3_pcD12	ET	4.	(0.5,0.0,-0.3)	(0.,0.5,-0.3)	-0.3	11.75	0.0225	2.82	0.9807	(0.216,0.054,0.380)	0.44	(-171.36,46.93,-242.82)	300.88
	q4._-0.3_-0.3_pcD12	ET	4.	(0.,0.,-0.3)	(0.,0.,-0.3)	-0.3	11.85	0.0225	0.95	0.9814	(0.,0.,0.305)	0.305	(50.33,-175.04,0.)	182.13
35	q4._0.5_0._-0.3_0._0._0.5_-0.3_pcD12	ET	4.	(0.,0.5,-0.3)	(0.,0.5,-0.3)	-0.3	11.81	0.0224	1.41	0.9804	(-0.033,0.232,0.386)	0.452	(28.33,-215.29,-310.75)	379.10
	q4._-0.3_-0.3_pcD12	ET	4.	(0.,0.,-0.3)	(0.,0.,-0.3)	-0.3	11.85	0.0225	0.95	0.9814	(0.,0.,0.305)	0.305	(50.33,-175.04,0.)	182.13
36	SXS:BBH:0058	SpEC	5.	(0.5,0.03,0.)	(0.,0.,0.)	0.	15.	0.0158	2.12	0.9815	(0.287,0.014,0.455)	0.538	(274.63,-163.17,210.99)	382.84
	SXS:BBH:0056	SpEC	5.	(0.,0.,0.)	(0.,0.,0.)	0.	15.	0.0159	0.50	0.9824	(0.,0.,0.417)	0.417	(-68.11,-122.09,0.)	139.81
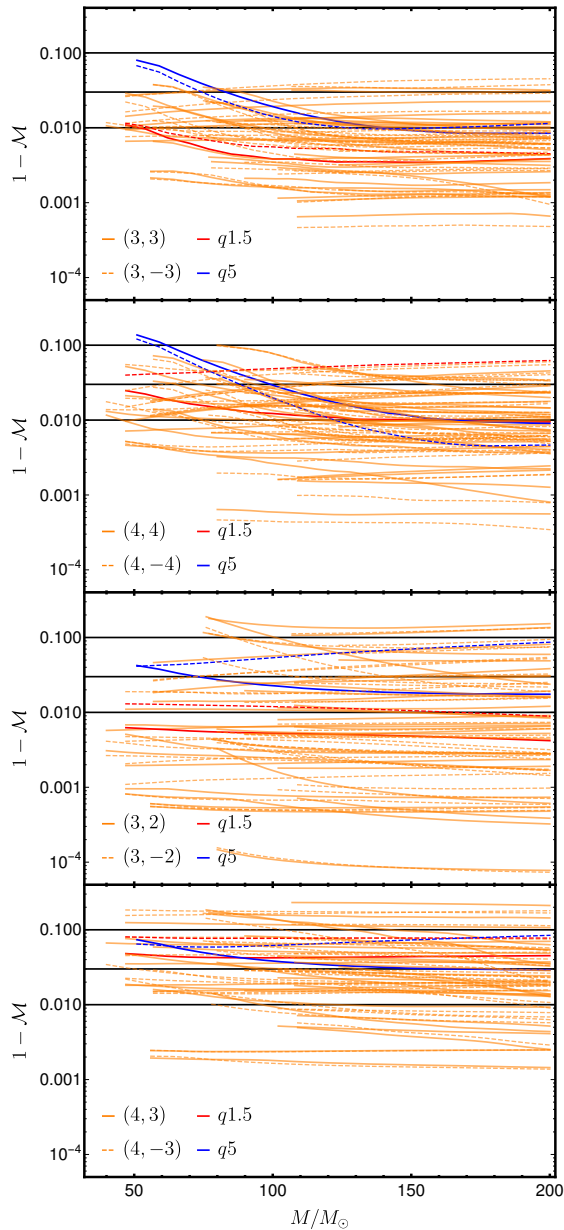
Figure 9. Mode by mode mismatches between QA and AS modes for all NR configurations as a function of the total mass of the system. From the top to the bottom we show the results for the $(3, \pm 3)$, $(4, \pm 4)$, $(3, \pm 2)$,$(4, \pm 3)$ modes, respectively. The configurations with IDs 10 and 36 are highlighted with red and blue colors, respectively. The thick and dashed curves correspond to positive and negative m modes, respectively. The horizontal lines mark the 1%, 3% and 10% value of the mismatch.

although it has a moderate impact, tends to improve the mismatches.

Figure 11 shows the results for single mode mismatches between the approximate precessing and precessing negative *m*-modes $\{\ell,m\} = \{(2,-2),(2,-1),(3,-2),(3,-3),(4,-3),(4,-4)\}$ for all NR pairs as a function of the total mass of the system. Comparing Fig. 4 and 11 we identify some asymmetries between the positive and negative *m*-modes. For instance, focusing on the highlighted configurations, IDs 36 and 10, we find slightly smaller mismatches for the negative *m*-modes than for the positive ones.

In Sec. VI B we have further investigated the time domain decomposition of co-precessing waveforms used by precessing surrogate models [23, 65]. We show the results of this analysis for higher order modes in Figs. 13 and 12. The identification between AS and the slowly varying part of the QA modes, referred to as symmetric QA modes defined as $h_{\ell m}^+ = A_{\ell m}^+ e^{i\phi_{\ell m}^-}$, is quantified through mismatches displayed in Fig. 13. Overall, we find that this approximation gets worse for higher order modes, especially for the modes affected significantly by mode mixing. Given this first approximation, we then constructed approximate QA modes (see Sec. VI B for details), $\hat{h}_{\ell m}^{QA}$, replacing the slowly-varying part of the QA modes by the AS amplitude and phase. The mismatches between the approximate QA and the QA modes for higher order modes are shown in Fig. 12. Similarly to the first approximation, we find an increase in mismatch, in particular for the modes affected by mode-mixing.

Appendix C: PI symmmetry and waveform systematics

In Sec. V we found (APX1) to be particularly poor for certain binary configurations. Once such case is the configuration with ID 28 in Tab. A. The time domain amplitude of $rh_{\ell m}$ for the AS and QA $\{\ell,m\} = \{(2,2),(2,-2)\}$ are shown in the left panel Fig. 14. The solid and dashed lines represent the positive and negative m modes, respectively. In this particular case, the QA $(2,2)$-mode has more power at merger than the corresponding AS mode, which causes the mismatch to rise above the 3%. However, the QA $(2,-2)$ mode accurately reproduces the AS mode through merger and ringdown. The mode asymmetry is inherent to precession and is exacerbated by the high χ_p value of this particular precessing configuration.

In contrast to Fig. 2, we do not observe time shifts between the QA and AS modes as the QA modes shown in Fig. 14 have been constructed from $\psi_{4,\ell m}$ via fixed frequency integration [94], therefore reducing the amount of time-shift. Note also that these time shifts do not affect the result of the mismatch calculations as they are computed taking into account time shifts between waveforms by performing an inverse Fourier transform.

The right panel of Fig. 14 shows the $(2,1)$-modes for the configuration with ID 10, a case with a mass averaged mismatch above 10% (see In Sec. V A). We observe a clear difference between the QA (purple) and AS (brown) amplitudes, demonstrating that (APX1) is unable to capture the strong in-
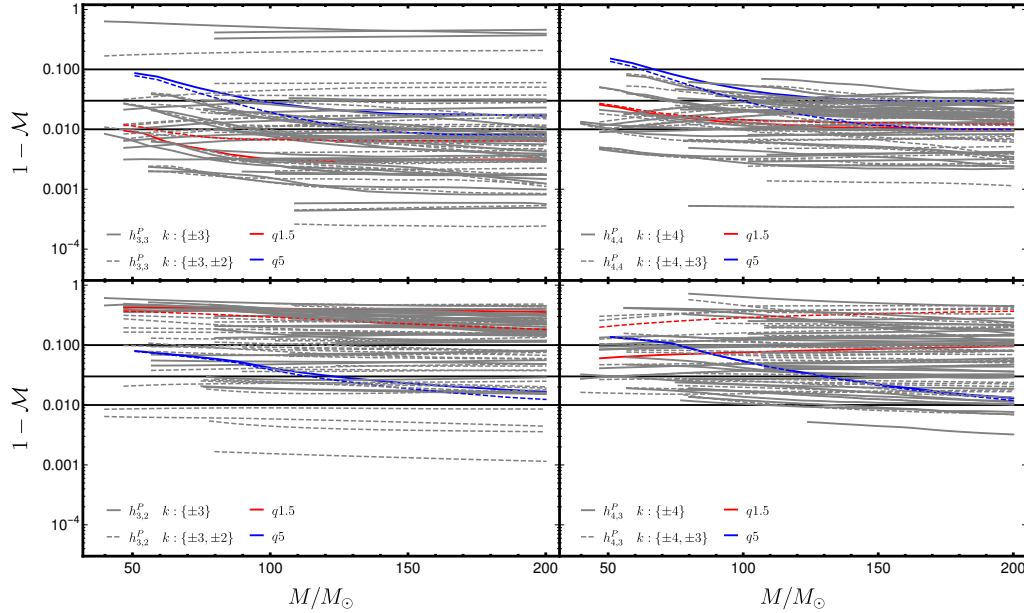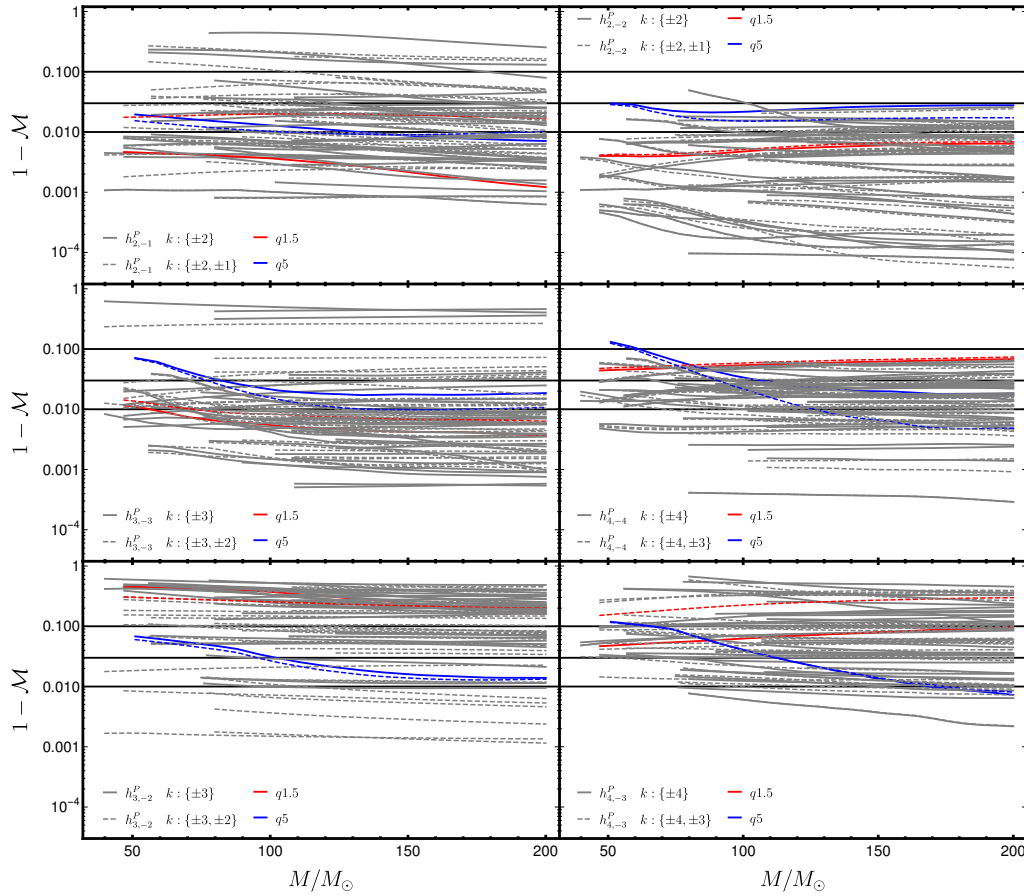
Figure 10. Mode by mode mismatches between precessing and approximate precessing modes for all configurations in Tab. A as a function of the total mass of the system. The top left and right panels show the results for the (3, 3) and (4, 4) modes; the bottom left and right plots for the (3, 2) and (4, 3) modes. The thick and dashed lines correspond to taking two or four aligned-spin waveforms to generate the approximate precessing waveforms, respectively. The letter k represents the index of the rotation operator given in Eq. (2.3). In addition, configurations with IDs 10 and 36 are highlighted with red and blue colors, respectively. The horizontal lines mark the 1%, 3% and 10% value of the mismatch.

teraction at merger for this configuration. The approximate precessing waveform generated with the either two or four AS modes, resembles the precessing (2, 1)-mode (blue) better but still not accurately throughout the late inspiral but in particular during the merger. These large differences are the source of the high mismatch.

We have found in Sec. V A that the case with ID 4 has a very high mismatch for the odd m-modes due to the PI symmetry exhibited by equal mass equal spin black holes. For configurations with PI symmetry the odd m-modes vanish identically, however, in NR simulations these modes are not zero due to numerical error, although they are extremely small compared to the even m-modes. For precessing configuration, however, this symmetry is broken and the odd m QA modes will not vanish. As a consequence, the mismatches between the QA and AS odd m-modes for such configurations are high. From the four configurations with PI symmetry, IDs 1,2,3 show lower mismatches than ID 4 due to fact that the negative aligned spin component diminishes the difference in the amplitude between the modes resulting in a much lower mismatch when compared to the one of ID 4 ($\chi_{\mathrm{eff}} = 0$). This also poses a clear limitation when rotating the (2, 1) precessing mode to form the QA (2, 1) because the mode mixing in the rotation leaves the QA with more power than the corresponding AS mode. Moreover, it is also a tight constraint in the inverse transformation because the approximate precessing modes can only be generated with the information of the even m modes. This is a clear limitation of (APX1).

Finally, in Sec. V B when analyzing the single mode mismatches of the (2, 2)-mode (top panel of Fig. 4) we found a case, ID 28, with the mismatch curve above the 3% threshold. The configuration with ID 28 is the same as in the co-precessing frame has a mismatch slightly above 3%. In the inertial frame it occurs the same situation as in Fig. 14. The asymmetries between positive and negative m precessing modes are not accurately reproduced by the approximate precessing waveforms. As a consequence, the mismatch of the (2, 2) mode is much higher than the mismatch of the (2, −2) mode, which is below the 3% horizontal line as seen in the top right panel of Fig. 11.

Appendix D: Contour Plots matches including higher order modes

Figure 15 contour plots of the strain mismatches between precessing and approximate precessing waveforms, averaged over the angle κ_S for a total mass of 65 $M_\odot$ for the configuration with ID 36. In the figure, the label $\{\ell, m\}$ refers to the modes used in the sum of the complex strain of Eq. (4.2), while AS represents the aligned-spin modes taken into account in Eq. (2.3). In addition, the 3% and 10% mismatch values are highlighted with orange and red curves, respectively. In the top, middle and bottom panels the (2, ±2), (2, ±1), (3, ±3), (4, ±4); (2, ±2), (2, ±1), (3, ±3), (3, ±2), (4, ±4) and (2, ±2), (2, ±1),

Figure 11. Mode by mode mismatches between negative *m* precessing and approximate precessing modes for all NR configurations as a function of the total mass of the system. We show results for the following modes: $(2, -1)$ (top left), $(2, -2)$ (top right), $(3, -3)$ (middle left), $(4, -4)$ (middle right), $(3, -2)$ (bottom left) and $(4, -3)$ (bottom right). The thick and dashed lines correspond to taking two and four aligned-spin waveforms to generate the approximate precessing waveforms, respectively. The letter *k* represents the index of the rotation operator given in Eq. (2.3). Configurations with IDs 10 and 36 are highlighted in red and blue, respectively. The horizontal lines mark mismatches of 1%, 3% and 10%.

$(3, \pm 3)$, $(3, \pm 2)$, $(4, \pm 4)$, $(4, \pm 3)$ modes are taken into account in the sum of the complex strain, respectively. In the left and right panels the $(\ell, |\ell|), (\ell, |\ell - 1|)$ AS modes are taken into account, respectively. The results are similar to the bottom panels of Fig. 5. The addition of higher order modes in the complex strain increases the mismatch overall for all inclinations, while the inclusion of more AS higher order modes tends to lower the mismatches.

20
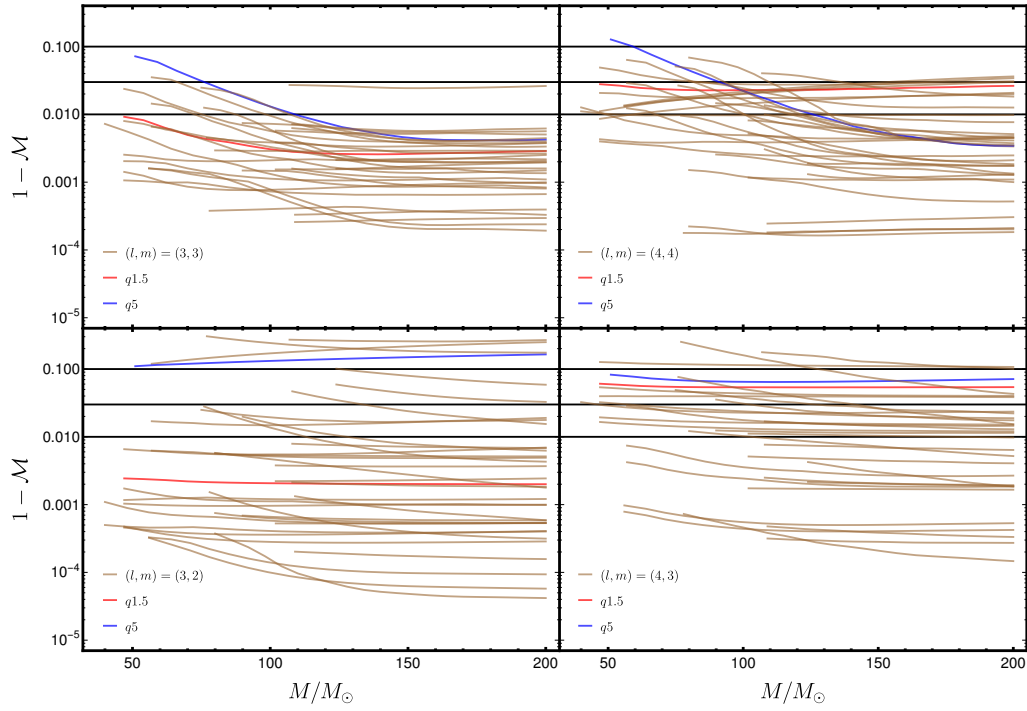
Figure 12. Single mode mismatches between the AS modes, $h_{\ell m}^{AS}$, and the symmetric QA modes, $h_{\ell m}^{+}$, as a function of the total mass of the system for all configurations in Tab. A. Top row: Results for the $(3,3)$ (left) and $(4,4)$ modes (right). Bottom row: Result for the $(3,2)$ (left) and $(4,3)$ modes (right). The configurations with IDs 10 and 36 are highlighted with red and blue colors, respectively. The horizontal lines mark the 1%, 3% and 10% value of the mismatch.
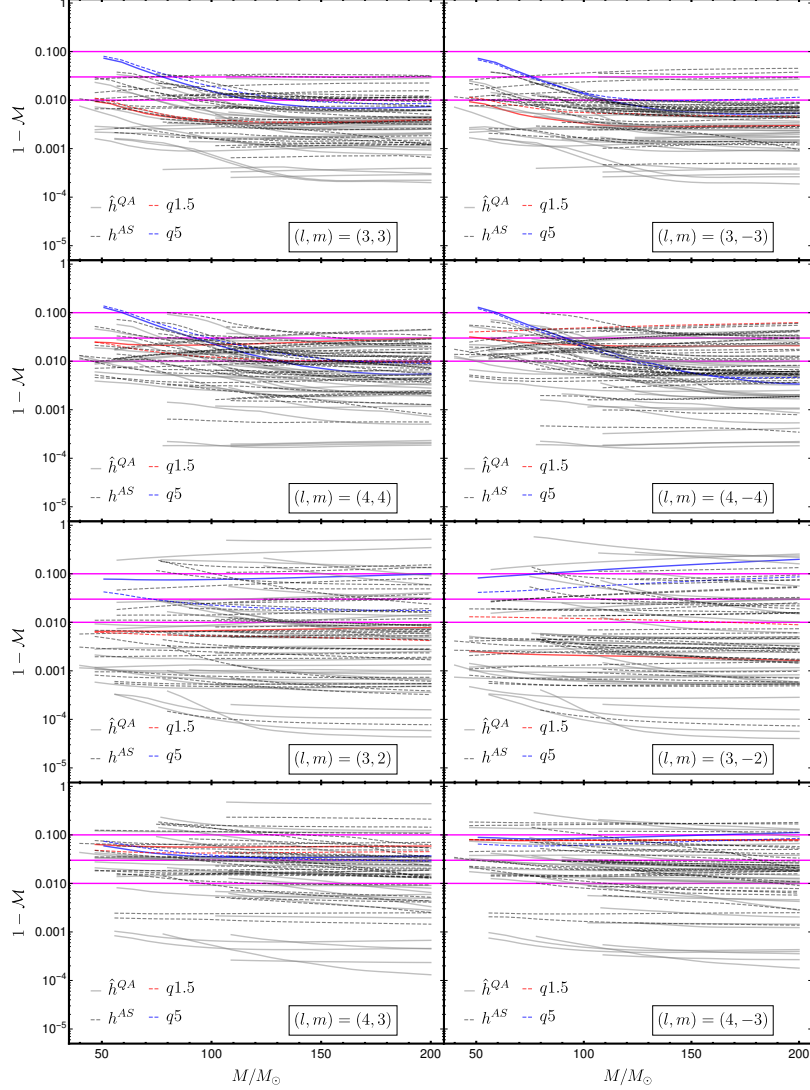
Figure 13. Single mode mismatches between the QA modes, $h_{\ell m}^{QA}$, the approximate QA modes, $\hat{h}_{\ell m}^{QA}$, and the AS modes, $h_{\ell m}^{AS}$, as a function of the total mass of the system for all NR configurations. In the left [right] panels from top to bottom we show the results for the {(3,3), (4,4),(3,2),(4,3)} [{(3,−3), (4,−4), (3,−2),(4,−3)}] modes. The thick gray (dashed black) lines correspond to mismatches between $h_{\ell m}^{QA}$ and $\hat{h}_{\ell m}^{QA}$ ($h_{\ell m}^{AS}$). In addition, configurations with IDs 10 and 36 are highlighted with red and blue colors, respectively. The horizontal lines mark the 1%, 3% and 10% value of the mismatch. In the odd-m panels the cases with PI symmetry have been removed
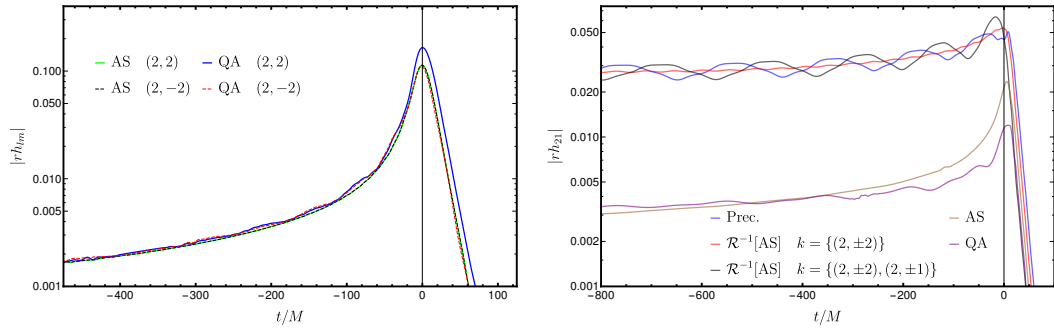
Figure 14. Left: Time domain amplitudes of the $\{\ell, m\} = \{(2,2),(2,-2)\}$-modes for the configuration with ID 28 in Tab. A. Right: Time domain amplitude of the aligned-spin (AS, brown), quadrupole-aligned (QA, purple), precessing (Prec., blue) and approximate precessing ($\mathcal{R}^{-1}[AS]$, red and black) $(2,1)$-mode for the configuration with ID 10. In both panels Tthe vertical line indicates the peak of the AS $(2,2)$-mode.
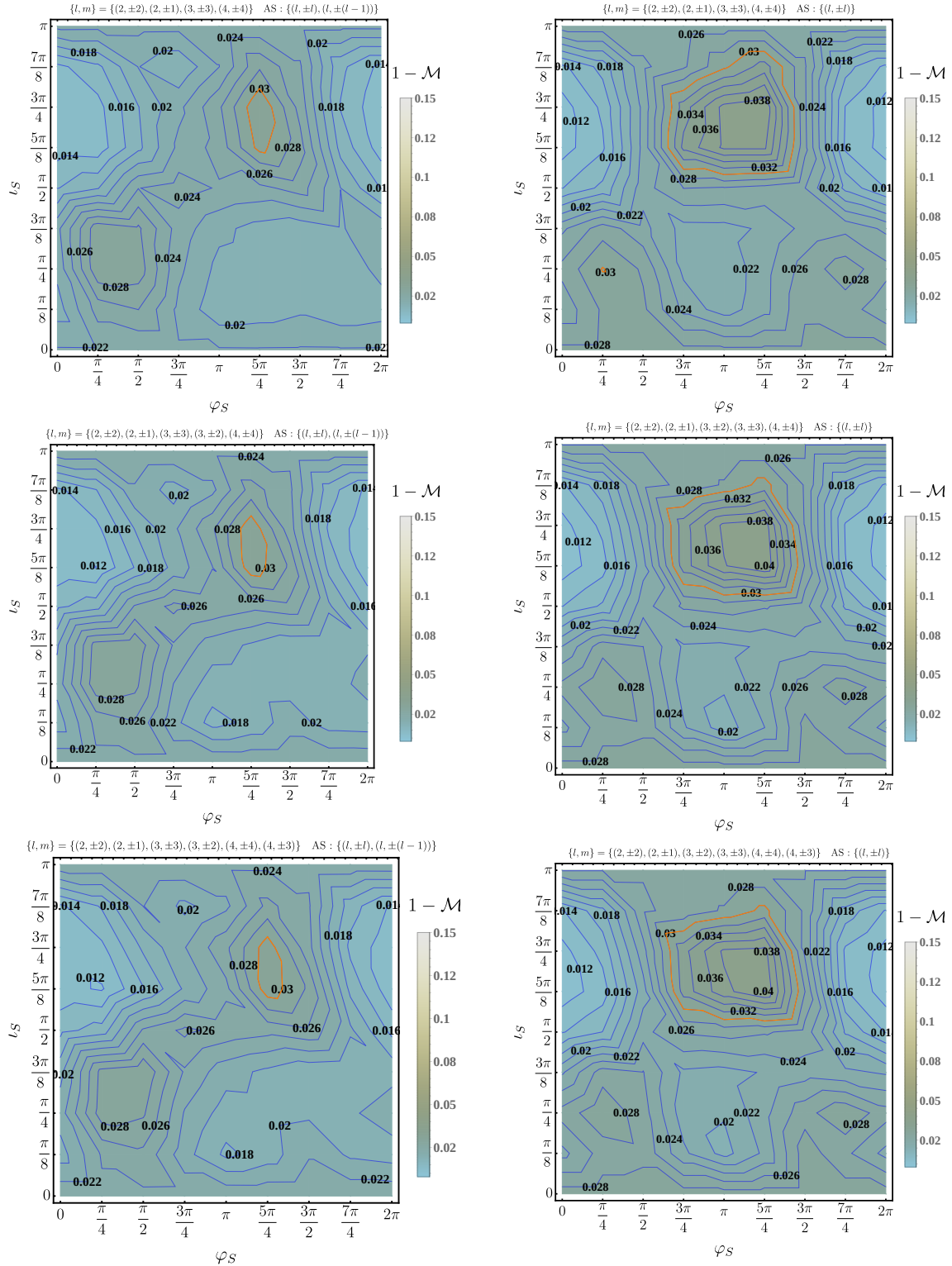
Figure 15. Strain mismatch between precessing and approximate precessing waveforms in the inertial frame averaged over the angle κ_S for a total mass of 65 $M_\odot$ for the configuration with ID 36 as a function of the inclination and the azimuthal angle of the signal (precessing waveform). In the plot labels $\{\ell,m\}$ denotes the modes used in the sum of the complex strain given in Eq. (4.2), while AS represent the aligned-spin modes taken into account in Eq. (2.3). In addition, the 3% and 10% mismatch values are highlighted with orange and red curvess, respectively.

[1] J. Aasi *et al.* (LIGO Scientific), "Advanced LIGO," Class. Quant. Grav. **32**, 074001 (2015).

[2] B. P. et al Abbott (LIGO Scientific Collaboration and Virgo Collaboration), "Observation of gravitational waves from a binary black hole merger," Phys. Rev. Lett. **116**, 061102 (2016).

[3] B. P. Abbott *et al.* (LIGO Scientific, Virgo), "GWTC-1: A Gravitational-Wave Transient Catalog of Compact Binary Mergers Observed by LIGO and Virgo during the First and Second Observing Runs," Phys. Rev. **X9**, 031040 (2019), arXiv:1811.12907 [astro-ph.HE].

[4] B. P. Abbott *et al.* (LIGO Scientific, Virgo), "GW190425: Observation of a Compact Binary Coalescence with Total Mass ∼ 3.4$M_⊙$," (2020), arXiv:2001.01761 [astro-ph.HE].

[5] F. Acernese *et al.* (VIRGO), "Advanced Virgo: a second-generation interferometric gravitational wave detector," Class. Quant. Grav. **32**, 024001 (2015).

[6] "https://gracedb.ligo.org/superevents/public/O3/," .

[7] "Tests of General Relativity with the Binary Black Hole Signals from the LIGO-Virgo Catalog GWTC-1," (2019), arXiv:1903.04467 [gr-qc].

[8] B. P. Abbott *et al.* (LIGO Scientific, Virgo), "Tests of General Relativity with GW170817," (2018), arXiv:1811.00364 [gr-qc].

[9] Sascha Husa, Sebastian Khan, Mark Hannam, Michael Pürrer, Frank Ohme, Xisco Jiménez Forteza, and Alejandro Bohé, "Frequency-domain gravitational waves from nonprecessing black-hole binaries. i. new numerical waveforms and anatomy of the signal," Phys. Rev. D **93**, 044006 (2016).

[10] S. Khan, S. Husa, M. Hannam, F. Ohme, M. Pürrer, F. Jiménez Forteza, and A. Bohé, "Frequency-domain gravitational waves from non-precessing black-hole binaries. II. A phenomenological model for the advanced detector era," (2015).

[11] Yi Pan, Alessandra Buonanno, Andrea Taracchini, Lawrence E. Kidder, Abdul H. Mroué, Harald P. Pfeiffer, Mark A. Scheel, and Béla Szilágyi, "Inspiral-merger-ringdown waveforms of spinning, precessing black-hole binaries in the effective-one-body formalism," Phys. Rev. D **89** (2014), 10.1103/physrevd.89.084006.

[12] Alejandro Bohé *et al.*, "Improved effective-one-body model of spinning, nonprecessing binary black holes for the era of gravitational-wave astrophysics with advanced detectors," Phys. Rev. **D95**, 044028 (2017), arXiv:1611.03703 [gr-qc].

[13] Geraint Pratten, Sascha Husa, Cecilio García-Quirós, Marta Colleoni, Antoni Ramos-Buades, Héctor Estellés, and Rafel Jaume, "Setting the cornerstone for the IMRPhenomX family of models for gravitational waves from compact binaries: The dominant harmonic for non-precessing quasi-circular black holes," (2020), arXiv:2001.11412 [gr-qc].

[14] Cecilio García-Quirós, Marta Colleoni, Sascha Husa, Héctor Estellés, Geraint Pratten, Antoni Ramos-Buades, Maite Mateu-Lucena, and Rafel Jaume, "IMRPhenomXHM: A multi-mode frequency-domain model for the gravitational wave signal from non-precessing black-hole binaries," (2020), arXiv:2001.10914 [gr-qc].

[15] Lionel London, Sebastian Khan, Edward Fauchon-Jones, Cecilio García, Mark Hannam, Sascha Husa, Xisco Jiménez-Forteza, Chinmay Kalaghatgi, Frank Ohme, and Francesco Pannarale, "First higher-multipole model of gravitational waves from spinning and coalescing black-hole binaries," Phys. Rev. Lett. **120**, 161102 (2018).

[16] Roberto Cotesta, Alessandra Buonanno, Alejandro Bohé, Andrea Taracchini, Ian Hinder, and Serguei Ossokine, "Enriching the symphony of gravitational waves from binary black holes by tuning higher harmonics," Phys. Rev. D **98**, 084028 (2018).

[17] Vijay Varma, Scott E. Field, Mark A. Scheel, Jonathan Blackman, Lawrence E. Kidder, and Harald P. Pfeiffer, "Surrogate model of hybridized numerical relativity binary black hole waveforms," Phys. Rev. D **99**, 064045 (2019).

[18] Theocharis A. Apostolatos, Curt Cutler, Gerald J. Sussman, and Kip S. Thorne, "Spin-induced orbital precession and its modulation of the gravitational waveforms from merging binaries," Phys. Rev. D **49**, 6274–6297 (1994).

[19] Lawrence E. Kidder, "Coalescing binary systems of compact objects to (post)$^{5/2}$-newtonian order. v. spin effects," Phys. Rev. D **52**, 821–847 (1995).

[20] Mark Hannam, "Modelling gravitational waves from precessing black-hole binaries: Progress, challenges and prospects," Gen. Rel. Grav. **46**, 1767 (2014), arXiv:1312.3641 [gr-qc].

[21] Scott E. Field, Chad R. Galley, Jan S. Hesthaven, Jason Kaye, and Manuel Tiglio, "Fast prediction and evaluation of gravitational waveforms using surrogate models," Phys.Rev. **X4**, 031006 (2014), arXiv:1308.3565 [gr-qc].

[22] Jonathan Blackman, Bela Szilagyi, Chad R. Galley, and Manuel Tiglio, "Sparse Representations of Gravitational Waves from Precessing Compact Binaries," Phys. Rev. Lett. **113**, 021101 (2014), arXiv:1401.7038 [gr-qc].

[23] Jonathan Blackman, Scott E. Field, Mark A. Scheel, Chad R. Galley, Daniel A. Hemberger, Patricia Schmidt, and Rory Smith, "A Surrogate Model of Gravitational Waveforms from Numerical Relativity Simulations of Precessing Binary Black Hole Mergers," Phys. Rev. **D95**, 104023 (2017), arXiv:1701.00550 [gr-qc].

[24] Jonathan Blackman, Scott E. Field, Mark A. Scheel, Chad R. Galley, Christian D. Ott, Michael Boyle, Lawrence E. Kidder, Harald P. Pfeiffer, and Béla Szilágyi, "Numerical relativity waveform surrogate model for generically precessing binary black hole mergers," Phys. Rev. **D96**, 024058 (2017), arXiv:1705.07089 [gr-qc].

[25] Vijay Varma, Scott E. Field, Mark A. Scheel, Jonathan Blackman, Davide Gerosa, Leo C. Stein, Lawrence E. Kidder, and Harald P. Pfeiffer, "Surrogate models for precessing binary black hole simulations with unequal masses," Phys. Rev. Research **1**, 033015 (2019).

[26] Patricia Schmidt, Mark Hannam, Sascha Husa, and P. Ajith, "Tracking the precession of compact binaries from their gravitational-wave signal," Phys. Rev. D **84**, 024046 (2011).

[27] R. O'Shaughnessy, B. Vaishnav, J. Healy, Z. Meeks, and D. Shoemaker, "Efficient asymptotic frame selection for binary black hole spacetimes using asymptotic radiation," Phys. Rev. D **84**, 124002 (2011).

[28] Michael Boyle, Robert Owen, and Harald P. Pfeiffer, "Geometric approach to the precession of compact binaries," Phys. Rev. D **84**, 124011 (2011).

[29] Patricia Schmidt, Mark Hannam, and Sascha Husa, "Towards models of gravitational waveforms from generic binaries: A simple approximate mapping between precessing and non-precessing inspiral signals," Phys. Rev. D **86**, 104063 (2012).

[30] Patricia Schmidt, Frank Ohme, and Mark Hannam, "Towards models of gravitational waveforms from generic binaries: Ii. modelling precession effects with a single effective precession

parameter," Phys. Rev. D **91**, 024043 (2015).

[31] Alessandra Buonanno, Yanbei Chen, and Michele Vallisneri, "Detecting gravitational waves from precessing binaries of spinning compact objects: Adiabatic limit," Phys. Rev. D **67**, 104025 (2003).

[32] Michael Boyle, "Uncertainty in hybrid gravitational waveforms: Optimizing initial orbital frequencies for binary black-hole simulations," Phys. Rev. **D84**, 064013 (2011).

[33] Mark Hannam, Patricia Schmidt, Alejandro Bohé, Leïla Haegel, Sascha Husa, Frank Ohme, Geraint Pratten, and Michael Pürrer, "Simple model of complete precessing black-hole-binary gravitational waveforms," Phys. Rev. Lett. **113**, 151101 (2014).

[34] Yi Pan, Alessandra Buonanno, Andrea Taracchini, Lawrence E. Kidder, Abdul H. Mroué, Harald P. Pfeiffer, Mark A. Scheel, and Béla Szilágyi, "Inspiral-merger-ringdown waveforms of spinning, precessing black-hole binaries in the effective-one-body formalism," Phys. Rev. **D89**, 084006 (2014), arXiv:1307.6232 [gr-qc].

[35] Jonathan Blackman, Scott E. Field, Chad R. Galley, Bela Szilagyi, Mark A. Scheel, *et al.*, "Fast and accurate prediction of numerical relativity waveforms from binary black hole mergers using surrogate models," (2015).

[36] Sebastian Khan, Katerina Chatziioannou, Mark Hannam, and Frank Ohme, "Phenomenological model for the gravitational-wave signal from precessing binary black holes with two-spin effects," Phys. Rev. D **100**, 024059 (2019).

[37] L. Pekowsky, R. O'Shaughnessy, J. Healy, and D. Shoemaker, "Comparing gravitational waves from nonprecessing and precessing black hole binaries in the corotating frame," Phys. Rev. **D88**, 024040 (2013), arXiv:1304.3176 [gr-qc].

[38] A. Bohé *et al.*, *PhenomPv2 - Technical Notes for LAL Implementation*, Tech. Rep. LIGO-T1500602 (2016).

[39] Sebastian Khan, Frank Ohme, Katerina Chatziioannou, and Mark Hannam, "Including higher order multipoles in gravitational-wave models for precessing binary black holes," (2019), arXiv:1911.06050 [gr-qc].

[40] Geraint Pratten et al, (2020), in preparation.

[41] Patricia Schmidt, Mark Hannam, and Sascha Husa, "Towards models of gravitational waveforms from generic binaries: A simple approximate mapping between precessing and non-precessing inspiral signals," Phys. Rev. **D86**, 104063 (2012), arXiv:1207.3088 [gr-qc].

[42] Michael Boyle, Robert Owen, and Harald P. Pfeiffer, "A geometric approach to the precession of compact binaries," Phys. Rev. **D84**, 124011 (2011), arXiv:1110.2965 [gr-qc].

[43] Michael Boyle, Lawrence E. Kidder, Serguei Ossokine, and Harald P. Pfeiffer, "Gravitational-wave modes from precessing black-hole binaries," (2014), arXiv:1409.4431 [gr-qc].

[44] Abdul H. Mroué, Mark A. Scheel, Béla Szilágyi, Harald P. Pfeiffer, Michael Boyle, Daniel A. Hemberger, Lawrence E. Kidder, Geoffrey Lovelace, Serguei Ossokine, Nicholas W. Taylor, Anıl Zenginoğlu, Luisa T. Buchman, Tony Chu, Evan Foley, Matthew Giesler, Robert Owen, and Saul A. Teukolsky, "Catalog of 174 binary black hole simulations for gravitational wave astronomy," Phys. Rev. Lett. **111**, 241104 (2013).

[45] Bernd Bruegmann, Jose A. Gonzalez, Mark Hannam, Sascha Husa, Ulrich Sperhake, and Wolfgang Tichy, "Calibration of Moving Puncture Simulations," Phys. Rev. **D77**, 024027 (2008), arXiv:gr-qc/0610128 [gr-qc].

[46] Sascha Husa, Jose A. Gonzalez, Mark Hannam, Bernd Bruegmann, and Ulrich Sperhake, "Reducing phase error in long numerical binary black hole evolutions with sixth order finite differencing," Class. Quant. Grav. **25**, 105006 (2008),

arXiv:0706.0740 [gr-qc].

[47] Frank Loffler *et al.*, "The Einstein Toolkit: A Community Computational Infrastructure for Relativistic Astrophysics," Class. Quant. Grav. **29**, 115001 (2012), arXiv:1111.3344 [gr-qc].

[48] Maria Babiuc-Hamilton *et al.*, "The Einstein Toolkit," (2019), to find out more, visit http://einsteintoolkit.org.

[49] P. Ajith, M. Hannam, S. Husa, Y. Chen, B. Brügmann, N. Dorband, D. Müller, F. Ohme, D. Pollney, C. Reisswig, and et al., "Inspiral-merger-ringdown waveforms for black-hole binaries with nonprecessing spins," Physical Review Letters **106** (2011), 10.1103/physrevlett.106.241101.

[50] Étienne Racine, "Analysis of spin precession in binary black hole systems including quadrupole-monopole interaction," Phys. Rev. D **78**, 044021 (2008).

[51] P. Ajith, M. Hannam, S. Husa, Y. Chen, B. Brügmann, N. Dorband, D. Müller, F. Ohme, D. Pollney, C. Reisswig, L. Santamaría, and J. Seiler, "Inspiral-merger-ringdown waveforms for black-hole binaries with nonprecessing spins," Phys. Rev. Lett. **106**, 241101 (2011).

[52] Antoni Ramos-Buades, Sascha Husa, and Geraint Pratten, "Simple procedures to reduce eccentricity of binary black hole simulations," Phys. Rev. D **99**, 023003 (2019).

[53] Xisco Jiménez-Forteza, David Keitel, Sascha Husa, Mark Hannam, Sebastian Khan, and Michael Pürrer, "Hierarchical data-driven approach to fitting numerical relativity data for nonprecessing binary black holes with an application to final spin and radiated energy," Phys. Rev. D **95**, 064024 (2017).

[54] K. G. Arun, Alessandra Buonanno, Guillaume Faye, and Evan Ochsner, "Higher-order spin effects in the amplitude and phase of gravitational waveforms emitted by inspiraling compact binaries: Ready-to-use gravitational waveforms," Phys. Rev. D **79**, 104023 (2009).

[55] Lee Samuel Finn and David F. Chernoff, "Observing binary inspiral in gravitational radiation: One interferometer," Phys. Rev. D **47**, 2198–2219 (1993).

[56] Piotr Jaranowski and Andrzej Królak, "Gravitational-wave data analysis. formalism and sample applications: The gaussian case," Living Reviews in Relativity **15**, 4 (2012).

[57] Collin Capano, Yi Pan, and Alessandra Buonanno, "Impact of higher harmonics in searching for gravitational waves from nonspinning binary black holes," Phys. Rev. D **89**, 102003 (2014).

[58] Emanuele Berti and Antoine Klein, "Mixing of spherical and spheroidal modes in perturbed kerr black holes," Phys. Rev. D **90**, 064012 (2014).

[59] James Healy, Pablo Laguna, Larne Pekowsky, and Deirdre Shoemaker, "Template mode hierarchies for binary black hole mergers," Phys. Rev. D **88**, 024034 (2013).

[60] "https://dcc.ligo.org/LIGO-T0900288/public." .

[61] Bernd Brügmann, José A. González, Mark Hannam, Sascha Husa, and Ulrich Sperhake, "Exploring black hole superkicks," Phys. Rev. D **77**, 124047 (2008).

[62] Michael Boyle and Abdul H. Mroué, "Extrapolating gravitational-wave data from numerical simulations," Phys. Rev. D **80**, 124045 (2009).

[63] Bernd Brügmann, José A. González, Mark Hannam, Sascha Husa, Ulrich Sperhake, and Wolfgang Tichy, "Calibration of moving puncture simulations," Phys. Rev. D **77** (2008), 10.1103/physrevd.77.024027.

[64] Jonathan Blackman, Scott E. Field, Mark A. Scheel, Chad R. Galley, Daniel A. Hemberger, Patricia Schmidt, and Rory Smith, "A surrogate model of gravitational waveforms from numerical relativity simulations of precessing binary black

hole mergers," Phys. Rev. D **95**, 104023 (2017).

[65] Jonathan Blackman, Scott E. Field, Mark A. Scheel, Chad R. Galley, Christian D. Ott, Michael Boyle, Lawrence E. Kidder, Harald P. Pfeiffer, and Béla Szilágyi, "Numerical relativity waveform surrogate model for generically precessing binary black hole mergers," Phys. Rev. D **96**, 024058 (2017).

[66] Michael Boyle *et al.*, "The SXS Collaboration catalog of binary black hole simulations," (2019), arXiv:1904.04831 [gr-qc].

[67] John Miller, Lisa Barsotti, Salvatore Vitale, Peter Fritschel, Matthew Evans, and Daniel Sigg, "Prospects for doubling the range of advanced ligo," Phys. Rev. D **91**, 062005 (2015).

[68] "https://dcc.ligo.org/LIGO-T1800042/public," .

[69] M Punturo *et al.*, "The einstein telescope: a third-generation gravitational wave observatory," Classical and Quantum Gravity **27**, 194002 (2010).

[70] S Hild *et al.*, "Sensitivity studies for third-generation gravitational wave observatories," Classical and Quantum Gravity **28**, 094013 (2011).

[71] B P Abbott *et al.*, "Exploring the sensitivity of next generation gravitational wave detectors," Classical and Quantum Gravity **34**, 044001 (2017).

[72] Stanislav Babak, Andrea Taracchini, and Alessandra Buonanno, "Validating the effective-one-body model of spinning, precessing binary black holes against numerical relativity," Phys. Rev. D **95**, 024010 (2017).

[73] Héctor Estellés, Antoni Ramos-Buades, Sascha Husa, Cecilio García-Quirós, and Leila Haegel, "IMRPhenomTP: A phenomenological time domain model for dominant quadrupole gravitational wave signal of coalescing binary black holes," (2020), in preparation.

[74] Cactus Computational Toolkit, "," http://www.cactuscode.org.

[75] Tom Goodale *et al.*, "The cactus framework and toolkit: Design and applications," in *High Performance Computing for Computational Science — VECPAR 2002*, edited by José M. L. M. Palma, A. Augusto Sousa, Jack Dongarra, and Vicente Hernández (Springer Berlin Heidelberg, Berlin, Heidelberg, 2003) pp. 197–227.

[76] Denis Pollney, Christian Reisswig, Erik Schnetter, Nils Dorband, and Peter Diener, "High accuracy binary black hole simulations with an extended wave zone," Phys. Rev. **D83**, 044045 (2011).

[77] Jeffrey Bowen and James York, "Time-asymmetric initial data for black holes and black-hole collisions," Phys. Rev. D **21**, 2047–2056 (1980).

[78] Steven Brandt and Bernd Brügmann, "A simple construction of initial data for multiple black holes," Physical Review Letters **78**, 3606–3609 (1997).

[79] Marcus Ansorg, Bernd Brügmann, and Wolfgang Tichy, "Single-domain spectral method for black hole puncture data," Phys. Rev. D **70** (2004), 10.1103/physrevd.70.064011.

[80] Pedro Marronetti, Wolfgang Tichy, Bernd Bruegmann, Jose Gonzalez, and Ulrich Sperhake, "High-spin binary black hole mergers," Phys. Rev. **D77**, 064010 (2008), arXiv:0709.2160 [gr-qc].

[81] Masaru Shibata and Takashi Nakamura, "Evolution of three-dimensional gravitational waves: Harmonic slicing case," Phys. Rev. D **52**, 5428–5444 (1995).

[82] Thomas W. Baumgarte and Stuart L. Shapiro, "On the numerical integration of Einstein's field equations," Phys. Rev. **D59**, 024007 (1999).

[83] J. David Brown, Peter Diener, Olivier Sarbach, Erik Schnetter, and Manuel Tiglio, "Turduckening black holes: An Analytical and computational study," Phys. Rev. **D79**, 044023 (2009),

arXiv:0809.3533 [gr-qc].

[84] John G. Baker, Joan Centrella, Dae-Il Choi, Michael Koppitz, and James van Meter, "Gravitational wave extraction from an inspiraling configuration of merging black holes," Phys. Rev. Lett. **96**, 111102 (2006), arXiv:gr-qc/0511103 [gr-qc].

[85] Manuela Campanelli, C. O. Lousto, P. Marronetti, and Y. Zlochower, "Accurate evolutions of orbiting black-hole binaries without excision," Phys. Rev. Lett. **96**, 111101 (2006).

[86] Carles Bona, Joan Masso, Edward Seidel, and Joan Stela, "A New formalism for numerical relativity," Phys. Rev. Lett. **75**, 600–603 (1995), arXiv:gr-qc/9412071 [gr-qc].

[87] Miguel Alcubierre, Bernd Bruegmann, Peter Diener, Michael Koppitz, Denis Pollney, Edward Seidel, and Ryoji Takahashi, "Gauge conditions for long term numerical black hole evolutions without excision," Phys. Rev. **D67**, 084023 (2003), arXiv:gr-qc/0206072 [gr-qc].

[88] Kreiss, Heinz Otto and Oliger, Joseph, *Methods for the approximate solution of time dependent problems* (World Meteorological Organization, International Council of Scientic Unions, 1973).

[89] "Carpet: Adaptive mesh refinement for the Cactus framework," http://www.carpetcode.org (2011).

[90] Erik Schnetter, Scott H. Hawley, and Ian Hawke, "Evolutions in 3-D numerical relativity using fixed mesh refinement," Class. Quant. Grav. **21**, 1465–1488 (2004), arXiv:gr-qc/0310042 [gr-qc].

[91] Erik Schnetter, Peter Diener, Ernst Nils Dorband, and Manuel Tiglio, "A Multi-block infrastructure for three-dimensional time-dependent numerical relativity," Class. Quant. Grav. **23**, S553–S578 (2006), arXiv:gr-qc/0602104 [gr-qc].

[92] Jonathan Thornburg, "A Fast apparent horizon finder for three-dimensional Cartesian grids in numerical relativity," Class. Quant. Grav. **21**, 743–766 (2004), arXiv:gr-qc/0306056 [gr-qc].

[93] Olaf Dreyer, Badri Krishnan, Deirdre Shoemaker, and Erik Schnetter, "Introduction to isolated horizons in numerical relativity," Phys. Rev. **D67**, 024018 (2003), arXiv:gr-qc/0206008 [gr-qc].

[94] Christian Reisswig and Denis Pollney, "Notes on the integration of numerical relativity waveforms," Class. Quant. Grav. **28**, 195015 (2011), arXiv:1006.1632 [gr-qc].

[95] Sascha Husa, Ian Hinder, and Christiane Lechner, "Kranc: A Mathematica application to generate numerical codes for tensorial evolution equations," Comput. Phys. Commun. **174**, 983–1004 (2006), arXiv:gr-qc/0404023 [gr-qc].

[96] Kranc: Kranc assembles numerical code, http://kranccode.org.

[97] Michael W. Thomas and Erik Schnetter, "Simulation factory: Taming application configuration and workflow on high-end resources," CoRR **1008.4571** (2010), arXiv:1008.4571.

[98] Ian Hinder and Barry Wardell, "Simulation Factory: Taming Application Configuration and Workflow on High-End Resources," (Simulation Tools v1.1.0).

[99] Abdul H. Mroué, Mark A. Scheel, Bela Szilagyi, Harald P. Pfeiffer, Michael Boyle, *et al.*, "A catalog of 174 binary black-hole simulations for gravitational-wave astronomy," Phys.Rev.Lett. **111**, 241104 (2013), arXiv:1304.6077 [gr-qc].

[100] Simulating Extreme Spacetimes (SXS), http://black-holes.org.

[101] Steven Brandt and Bernd Brügmann, "A simple construction of initial data for multiple black holes," Phys. Rev. Lett. **78**, 3606–3609 (1997).

[102] Jeffrey M. Bowen and James W. York, "Time-asymmetric initial data for black holes and black-hole collisions," Phys. Rev. D **21**, 2047–2056 (1980).

Chapter 7

Impact of eccentricity on the gravitational wave searches for binary black holes

In this chapter I include the draft of a paper performed in collaboration with Drs. Shubhanshu Tiwari and Maria Haney from the university of Zurich, and my supervisor Dr. Sascha Husa, where we analyze the sensitivity of two search pipelines to the full signal of eccentric binary black holes. The results presented in this section are preliminary as the article is not public by the time of submission, but in a mature enough form to include it as a part of the original results of this thesis.

May 10, 2020

Impact of eccentricity on the gravitational wave searches for binary black holes: High mass case

Antoni Ramos-Buades,[1] Shubhanshu Tiwari,[2] Maria Haney,[2] and Sascha Husa[1]

[1]*Departament de Física, Universitat de les Illes Balears, IAC3 – IEEC, Crta. Valldemossa km 7.5, E-07122 Palma, Spain*
[2]*Physik-Institut, Universität Zürich, Winterthurerstrasse 190, 8057 Zürich, Switzerland*

The formation of stellar-mass binary black holes through dynamical interactions in dense stellar environments predicts the existence of binaries with non-negligible eccentricity in the frequency band of ground-based gravitational wave detectors; the detection of binary black hole mergers with measurable orbital eccentricity would validate the existence of this formation channel. Waveform templates currently used in the matched-filter gravitational-wave searches of LIGO-Virgo data neglect effects of eccentricity which is expected to reduce their efficiency to detect eccentric binary black holes. Meanwhile, the sensitivity of coherent unmodeled gravitational-wave searches (with minimal assumptions about the signal model) have been shown to be largely unaffected by the presence of even sizable orbital eccentricity. In this paper, we compare the performance of two state-of-the-art search algorithms recently used by LIGO and Virgo to search for binary black holes in the second Observing Run (O2), quantifying their search sensitivity by injecting numerical-relativity simulations of inspiral-merger-ringdown eccentric waveforms into O2 LIGO data. Our results show that the matched-filter search PyCBC performs better than the unmodeled search cWB for the high chirp mass ($> 20 M_\odot$) and low eccentricity region ($e_{30Hz} < 0.25$) of parameter space. For moderate eccentricities and low chirp mass, on the other hand, the unmodeled search is more sensitive than the modeled search.

PACS numbers: 04.25.Dg, 04.25.Nx, 04.30.Db, 04.30.Tv

I. INTRODUCTION

The number of detections of gravitational wave (GW) signals has steeply increased from the first and second Observing runs (O1/O2) of Advanced LIGO and Advanced Virgo [1] to the third Observing run (O3), where tens of GW candidates have already been recorded [2]. So far, all GW detections of binary black holes (BBHs) are consistent with signals emitted from quasicircular binaries [3, 4].

Generally, two main scenarios can be considered regarding possible formation channels for BBH mergers: 1) isolated binary evolution [5–8], during which BBHs shed their formation eccentricity through GW emission and have circularized by the time they enter the frequency band of the ground-based detectors [9, 10]; 2) binaries dynamically formed in dense stellar environments like globular clusters and active galactic nuclei (AGNs) [11–15], which may still retain a significant eccentricity by the time they enter the frequency band of the Advanced LIGO [16] and Advanced Virgo [17] detectors. Although both formation channels (and their different astrophysical scenarios) predict BBH mergers with distinct distributions of masses and spins [18–21], the model uncertainties —as well as the low statistics due to the limited number of GW detections —do not permit to set tight constraints on BBH formation scenarios from the mass and spin distributions alone.

Dynamical BBH formation, hoewever, is distinctly characterized by the potential existence of binaries with non-negligible eccentricity in the frequency band of the ground-based detectors, which were formed through dynamical capture at very close separations (without time to circularize before merger) or through a dynamical process that increased the eccentricity of the binary (e.g. Kozai-Lidov oscillations [22, 23]). The detection of a GW signal with an unambiguous

signature of non-negligible orbital eccentricity would therefore confirm the dynamical formation channel for BBHs and provide information about possible formation mechanisms and the astrophysical environments of such sources.

In order to be able to confidently detect eccentric binary black hole signals it is necessary to assess the sensitivity of the pipelines used to search for such signals. As a consequence several studies have analysed the sensitivity of different search pipelines to eccentric compact binary mergers over data from O1 and O2 Advanced LIGO and Advanced Virgo observing runs [24–26].

In this paper we quantify the sensitivity of two different gravitational-wave search pipelines to eccentric inspiral-merger-ringdown (IMR) signals calculated from numerical relativity (NR) simulations. The two search pipelines are: 1) the template-based PyCBC algorithm [27, 28], and 2) the un-modeled coherent WaveBurst (cWB) algorithm [29, 30]. We study the sensitivity of the pipelines with increasing eccentricity of the signal for three different mass ratios $q = 1, 2, 4$, with $q = m_1/m_2 > 1$ and m_1, m_2 the component masses of the binary. Furthermore, for mass ratio $q = 1$ we inject eccentric simulations with increasing dimensionless component spins $|\vec{\chi}_i| \leq 0.75$ (aligned with the orbital angular momentum of the system), where $\vec{\chi}_i = \vec{S}_i/m_i^2$ and $\vec{S}_i$ the spin vector of the i-component, with $i = 1, 2$. Due to the restricted length of the NR simulations the waveforms are injected at $30Hz$, and the eccentricity is consistently defined at that frequency according to the procedure detailed in Sec. II.

The paper is organised as follows: In Sec. II we provide details about the NR IMR eccentric waveforms used in this work. In Sec. III we briefly summarize the two search algorithms considered in this study, the template-based search PyCBC and the un-modeled search, cWB. We present in Sec. IV the results of the sensitivity estimates of both studied pipelines. We conclude in Sec. V discussing the results ob-

tained and reporting our conclusions.

II. ECCENTRIC BINARY BLACK HOLES

The gravitational wave signal emitted from a generic binary black hole is described by 17 parameters [31]. The parameters of a binary can be separated into 10 intrinsic parameters, i.e. properties of the emitting source, and 7 extrinsic parameters, describing the position of the source in the detector sky. The intrinsic parameters are the two component masses m_i, the six dimensionless spin vectors $\vec{\chi}_i = \vec{S}_i/m_i^2$, the eccentricity parameter e, and the argument of the periapsis Ω. Another useful mass parameter in gravitational wave data analysis is the chirp mass $\mathcal{M}$ of a binary with masses m_1 and m_2, which is defined as $\mathcal{M} \equiv (m_1 m_2)^{3/5}(m_1 + m_2)^{-1/5}$. The extrinsic parameters are the luminosity distance d_L, the azimuthal angle φ, the inclination ι, the time of coalescence t_c, the polarization angle ψ, the right ascension ϕ and the declination θ. The strain induced in a gravitational wave detector can be written in terms of these parameters as [32, 33]

$$h(t, \zeta, \Theta) = [F_+(\theta, \phi, \psi)h_+(t - t_c; \iota, \varphi, \zeta) \\ + F_\times(\theta, \phi, \psi)h_\times(t - t_c; \iota, \varphi, \zeta)], \qquad (2.1)$$

where F_+, $F_\times$ are the antenna pattern functions, and $\Theta = \{t_c, r, \theta, \varphi, \psi, \iota, \varphi\}$ and $\zeta = \{m_1, m_2, \vec{S}_1, \vec{S}_2, e, \Omega\}$ represent the sets of extrinsic and intrinsic parameters, respectively. The gravitational wave polarizations $(h_+, h_\times)$ appearing in the detector response can be expressed as a complex waveform strain

$$h(t) = h_+ - ih_\times = \sum_{l=2}^{\infty} \sum_{m=-l}^{l} Y_{lm}^{-2}(\iota, \varphi)h_{lm}(t - t_c; \zeta), \qquad (2.2)$$

where h_{lm} are the (l, m) waveform modes and $Y_{lm}^{-2}(\iota, \varphi)$ the spin-weighted -2 spherical harmonics.

A. Numerical Relativity data set

In this work we inject eccentric numerical relativity (NR) waveforms produced with the open-source EinsteinToolkit (ET) code [34, 35] and the SpEc code [36]. The ET waveforms were presented in [37], and the SXS ones in [38]. The injected waveforms are displayed in Table I, where we show for each simulation its identifier (ID, an integer number), the simulation name, mass ratio, z-components of the dimensionless spin vectors $(\chi_{1,z}, \chi_{2,z})$ and the initial eccentricity measured with the method developed in [37].

The injected data set is chosen with the following criteria: simulations with IDs $1 - 4$ are equal mass non-spinning cases which serve as control cases because eccentric equal mass non-spinning binaries have already been studied in the literature [39], while simulations with IDs $5 - 10$ extend the equal mass case to the spinning sector. Finally, simulations sets $11 - 14$ and $15 - 17$ allow to test the efficiency of the pipelines at higher mass ratios.

ID	Simulation	q	$\chi_{1,z}$	$\chi_{2,z}$	e_0^{NR}
1	SXS:BBH:1356	1.	0.	0.	0.09
2	SXS:BBH:1360	1.	0.	0.	0.15
3	SXS:BBH:1363	1.	0.	0.	0.23
4	Eccq1._0._0._et0.5_D27	1.	0.	0.	0.30
5	Eccq1._-0.25_-0.25_et0.1_D14	1.	−0.25	−0.25	0.07
6	Eccq1._-0.5_-0.5_et0.1_D13	1.	−0.5	−0.5	0.07
7	Eccq1._-0.75_-0.75_et0.1_D13	1.	−0.75	−0.75	0.08
8	Eccq1._0.25_0.25_et0.2_D16	1.	0.25	0.25	0.12
9	Eccq1._0.5_0.5_et0.2_D15	1.	0.5	0.5	0.12
10	Eccq1._0.75_0.75_et0.2_D15	1.	0.75	0.75	0.12
11	SXS:BBH:1365	2.	0.	0.	0.06
13	Eccq2._0._0._et0.2_D16	2.	0.	0.	0.14
12	SXS:BBH:1369	2.	0.	0.	0.20
14	Eccq2._0._0._et0.5_D26	2.	0.	0.	0.30
15	Eccq4._0._0._et0.1_D12	4.	0.	0.	0.07
16	Eccq4._0._0._et0.2_D15	4.	0.	0.	0.14
17	Eccq4._0._0._et0.5_D27.5	4.	0.	0.	0.30

Table I: Summary of the injected NR simulations. The first column denotes the identifier of the simulation, the second column indicates the name of the simulation as presented in [37, 38]. Next columns show the mass ratio, z-component of the dimensionless spin vectors and the initial NR eccentricity as measured using the procedure detailed in [37].

The eccentricity parameter describes the ellipticity of the binary's orbit, values close to 0 indicate a quasi-circular evolution while values close to 1 represent an almost head-on collision. In general relativity the eccentricity is a gauge dependent quantity. As a consequence, a plethora of eccentricity estimators have been developed to measure the eccentricity in numerical relativity simulations [40–46]. Eccentricity estimators are combinations of dynamical or wave quantities, like the orbital frequency of the binary, the orbital separation, the gravitational wave frequency of the $(2, 2)$ mode, etc., measuring the relative oscillations in those quantities due to eccentricity. In this work we measure the eccentricity from the gravitational wave frequency of the h_{22} mode, ω_{22}, following the procedures of [37]. We remark that the eccentricities presented in Table I are measured from the gravitational wave frequency and their values differ from those presented in [37] as they were calculated there using the orbital frequency computed from the motion of the black holes.

In the top panel of Fig. 1 we show the time evolution of the eccentricity of the simulation with ID 17 in Table I. Moreover, we choose the end of the inspiral given by the minimum energy circular orbit (MECO) [47], and explicitly set the eccentricity to zero from the MECO time onwards as at that point the eccentricity is so small which is practically zero.

In this study we are interested in injecting the waveforms presented in Table I at a certain detector frequency and for a certain total mass distribution. The modification of the total mass of the system implies a change in length of the waveform within the frequency band of the detector, as a conse-

quence different total masses imply also different initial eccentricities, as one can appreciate from the top panel of Fig. 1, which shows the eccentricity as a monotonically decaying function as the binary evolves. One possible solution might be to express the eccentricity measured from the NR simulation as a function of gravitational wave frequency of the 22-mode scaled by the total mass of the system, $2\pi M f_{22} = M\omega_{22}$, approximate the value of the injection frequency by the frequency of the 22-mode, $f_{22} \approx f_{GW}$, and construct a function $e(M f_{GW})$ which would provide the value of the eccentricity at a certain total mass for a given injection frequency. However, in the eccentric case the gravitational wave frequency is a non-monotonic function due to the asymmetric gravitational interaction along the orbit of the binary as one can observe in the mid panel of Fig. 1, where the time domain frequency of the 22-mode for the eccentric simulation with ID 17 from Table I and the frequency of the quasicircular IMRPhenomT [48] waveform model for the same configuration are displayed. We note that after the MECO time both curves converge indicating circularization of the eccentric system at merger.

One possibility for the definition of the eccentricity as a function of a monotonically increasing frequency is to consider the Radiation Reaction (RR) equations [49] for $x = \omega^{2/3}$ and e_t, replace e_t by the eccentricity measured from the NR simulation and solve the differential equation for $\dot{x}$. However, we find that this procedure does not work satisfactorily, as we have checked that the RR equations show a divergent behavior before the MECO time in some cases indicating the breakdown of the post-Newtonian approximation. Therefore, we decide to take the gravitational wave frequency of IMRPhenomT and combine it with the eccentricity measured from the simulation to construct the function $e_{NR}(M f_{22})$. The outcome of such a calculation for the simulation with ID 17 in Table I is shown in the bottom plot of Fig. 1. Hence, given an injection with total mass M_T and an injection frequency of f_{GW}, we can compute the eccentricity at that frequency and total mass as

$$e_{\text{inj}} = e_{NR}(M_T f_{GW}). \qquad (2.3)$$

We note that we focus only on the eccentricity parameter as the initial argument of the periapsis (also initial mean anomaly in the quasi-Keplerian parametrization [50]) in the non-precessing case acts as an initial phase during the inspiral and its main impact is in the morphology of the waveform at plunge, whose detailed study would require going beyond the high total mass regime ($M_T > 100 M_\odot$) considered in this communication.

Finally, in Fig. 2 we plot the time evolution of the GW polarization state $h_x(t)$ for non-spinning, eccentric stellar-mass binary black holes with total mass $m_{tot} = 50 M_\odot$ and mass ratio $q = 2$, provided by numerical-relativity simulations. The characteristic orbital eccentricity of the system —defined at a reference frequency of $30 Hz$ —is estimated to be 0.05 (in blue, simulation ID 11) and 0.23 (in orange, simulation ID 14), respectively. The time-domain waveforms clearly demonstrate the effects of increasing initial orbital eccentricity: rapid dephasing, as well as pronounced amplitude modulations due to the advance of periastron.
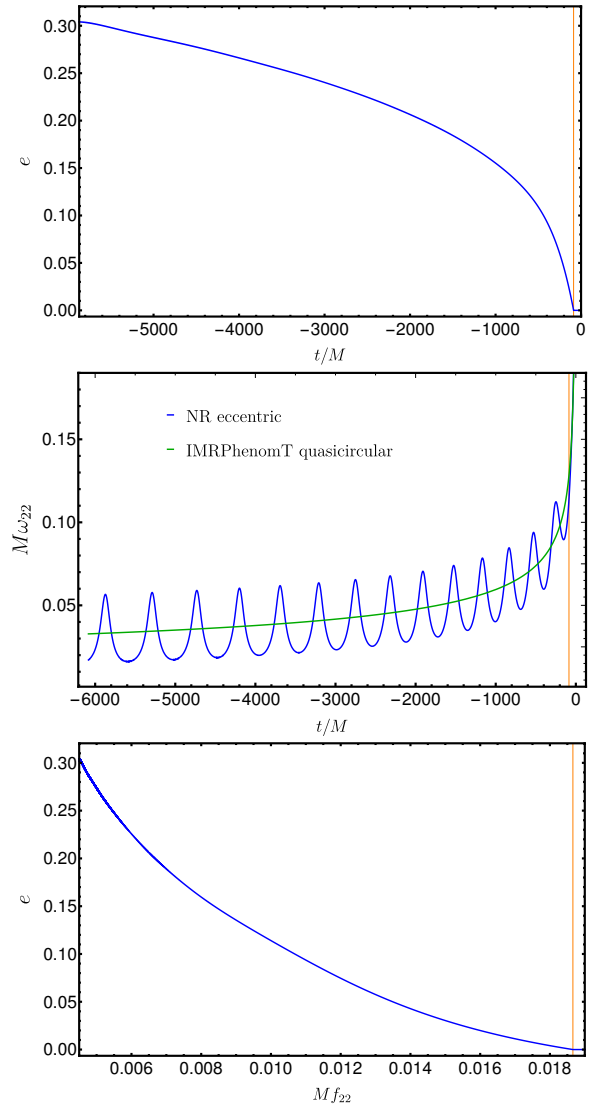

Figure 1: Top panel: Time domain evolution of the eccentricity estimated from the eccentric NR simulation with ID 17 in Table I. Mid panel: Time domain 22-mode gravitational wave frequencies of the eccentric case with ID 17 from Table I and of the quasicircular IMRPhenomT waveform model, highlighted in blue and green colors respectively. Bottom panel: Eccentricity as a function of the gravitational frequency of the (2, 2) mode for the same configuration as in the upper panel. With vertical lines in the top and bottom plots we have highlighted the MECO time and frequency, respectively.

III. ANALYSIS

A. Data

The data set used to conduct this study is part of the O2 Data Release through the Gravitational Wave Open Science Center
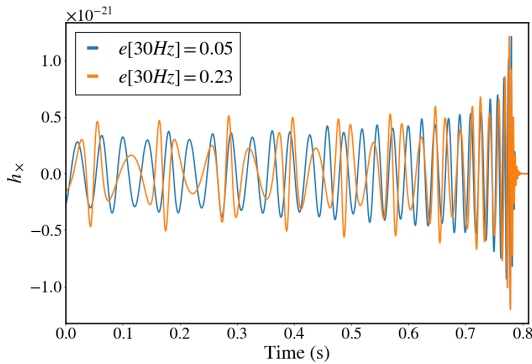
Figure 2: Temporal evolution of the GW polarization state $h_x(t)$ for non-spinning, eccentric stellar-mass binary black holes with total mass $m_{tot} = 50 M_\odot$ and mass ratio $q = 2$, provided by numerical-relativity simulations. The characteristic orbital eccentricity of the system —defined at a reference frequency of $30 Hz$ —is estimated to be 0.05 (in blue, simulation ID 11) and 0.23 (in orange, simulation ID 14), respectively.

[51]. This covers approximately ≈ 5 days of the coincident data between LIGO Livingston and LIGO Hanford between UTC Interval 2017-02-28 16:30:00 - 2017-03-10 13:35:00. Times with significant instrumental disturbances have been removed from the time period considered here [52, 53]. We consider two search algorithms, pyCBC and cWB, with the same search configurations that were used for the first catalogue of gravitational waves transients GWTC-1 [1] for these algorithms.

B. PyCBC : The matched filter algorithm

PyCBC is a search pipeline devised to detect GWs from compact binary coalescences using the PyCBC software package [54]. In this work we have employed the PyCBC search algorithm in the exact same configuration as was used for GWTC-1 [1].

The analysis uses a template bank of waveforms to perform match filtering over the data to compute the signal-to-noise ratio (SNR) for each combination of detector, coalescence time and template waveforms [55]. Triggers are generated by the pipeline according to excesses of matched-filter SNR over a predetermined threshold of 5.5 in each detector. Furthermore, signal consistency tests between the data and the template, like the χ^2 veto [56], are applied to suppress noise transient artefacts ('glitches') . Then, a single-detector rank ϱ is computed for each single-detector trigger using the SNR, the weighting vetoes, and a fitting and smoothing procedure intended to ensure an approximately constant rate of single-detector triggers across the search parameter space [57].

PyCBC performs also a coincidence test on the remaining triggers [28] requiring that the signals observed by the LIGO Hanford and LIGO Livingston detectors have to be seen within a time difference of 15 ms ($\sim$10 ms travel time between detector +5 ms for timing errors). Coincident triggers are assigned a ranking statistic which assesses their statistical significance and approximates the likelihood of obtaining the trigger parameters in the presence of a GW signal versus in the case of only noise [57].

In the PyCBC analysis presented here the template bank described in [58] is used. This bank covers binary systems with a total mass between $2 M_\odot$ and $500 M_\odot$ and mass ratios $q < 98$. Binary components with masses below $2 M_\odot$ are assumed to be neutron stars with a maximum dimensionless spin magnitude of 0.05; otherwise, the maximum dimensionless spin magnitude is 0.998. This template bank includes no effects of eccentric orbits.

In a previous study it has been found that a quasi-circular bank does not provide a good match for searching binaries with eccentric orbits [59]. Furthermore, it is known that the signal morphology of the eccentric BBH is orthogonal to the aligned-spin quasi-circular BBH [60]. As a consequence the quasi-circular, dominant harmonic and aligned spin template bank renders ineffective for searching eccentric BBH for high eccentricities.

The way eccentricity affects the matched-filter search by a quasi-circular template bank is two fold, *first* the collection of matched filtered SNR is reduced as a function of eccentricity (this can be quantified by studying the overlap of eccentric and quasi-circular waveforms), *second* the signal-based χ^2 veto used for weighting the single detector SNR to compute the rank also penalizes the final detection statistics of the search.

C. cWB : The un-modeled search algorithm

The unmodeled search pipeline cWB [24, 29] is a search algorithm designed to detect and reconstruct short-lived signals which are weakly modeled or unmodeled using a network of detectors networks of GW detectors [30], but also signals with a known morphology as is the case of BBH events reported in GWTC-1 [1]. The configuration of cWB used in this work is the same as used in the GWTC-1 catalog. The lack of a template bank for binary black holes in eccentric orbits which could be use by matched filtering pipelines motivated the use of cWB as robust tool to search eccentric BBH signals during the first and second observing runs of the LIGO and Virgo detectors [25].

cWB is devised to search for transient signals without requiring the use of a specific waveform model for the source. The detection process is based on the identification of a coherent excess power in multi-resolution time-frequency representations of the detectors strain data, for signal frequencies up to 1 kHz and duration up to a few seconds. In the case of binary black holes the collection of excess power in the time-frequency plane is is performed assuming monotonically increasing frequency for a better collection of the signal energy. Then, the pipeline identifies events which are coherent in multiple detectors and reconstructs the source sky location and signal waveform by using a constrained maximum likelihood method [30].

The cWB detection statistic ρ is based on the coherent energy E_c obtained by cross-correlating the signal waveform reconstructed in the network of detectors, which in turn it is proportional to the coherent network signal-to-noise ratio. Moreover, this detection statistic takes into account the quality of the reconstructed chirp by fitting the time-frequency pixels with the Newtonian chirp mass formula [61]. The estimation of statistical significance of an event is assessed by ranking the quantity ρ computed for the event against the ρ distribution for the background events obtained by repeating the analysis on time-shifted data. The applied time shifts are chosen much larger than the expected signals observed by the LIGO Hanford and LIGO Livingston detectors, ~ 15 ms (~ 10 ms travel time between detector + 5 ms for timing errors), in order to exclude astrophysical events from the background sample.

The robustness of the pipeline against non-stationary detector noise is increased by applying signal independent vetoes. This motivates the definition of the network correlation coefficient [30]

$$c_c = E_c/(E_c + E_n), \tag{3.1}$$

where E_n is the residual noise energy estimated after the reconstructed signal pixels are subtracted from the data. Then, gravitational-wave signals are expected to have $c_c \approx 1$, while for noise artefacts $c_c \ll 1$. Events with $c_c < 0.7$ are rejected.

The cWB search pipeline performs worse than matched-filter pipelines in the case the signal is well recovered by the template bank as matched-filtering is a near optimal method for searching well modeled signals. Nonetheless, the sensitivity of cWB improves at parts of the parameter space where the template bank does not faithfully reproduces the incoming signal. The cWB search in its earlier version was found to have almost no dependency of the search sensitivity as a function of eccentricity [24]. This was also confirmed in the latest results for observing run 1 and 2 of LIGO and Virgo detectors [25]. Also being a weakly modelled search cWB is affected more by the background noise and hence has a lower sensitivity as compared to the optimal matched filter searches. But to detect signals which are outside the template bank of matched filter search cWB provides a valuable complementarity.

IV. SEARCH SENSITIVITY

A. Injection set

The injection set used in this study is composed of the NR waveforms detailed in Table I. As a consequence, injections have fixed spin vectors and mass ratio values corresponding to those of the NR waveforms, although the total mass of the system acts a scale parameter which can be freely specified consistent with the length of the NR waveforms such that the injected signals are in the frequency band of the detectors. Due to the length limitations of the NR waveforms we set the reference frequency of the injection set to $30Hz$.

The injection set is constructed using a uniform distribution in distance scaled by the chirp mass [62]. The total mass val-
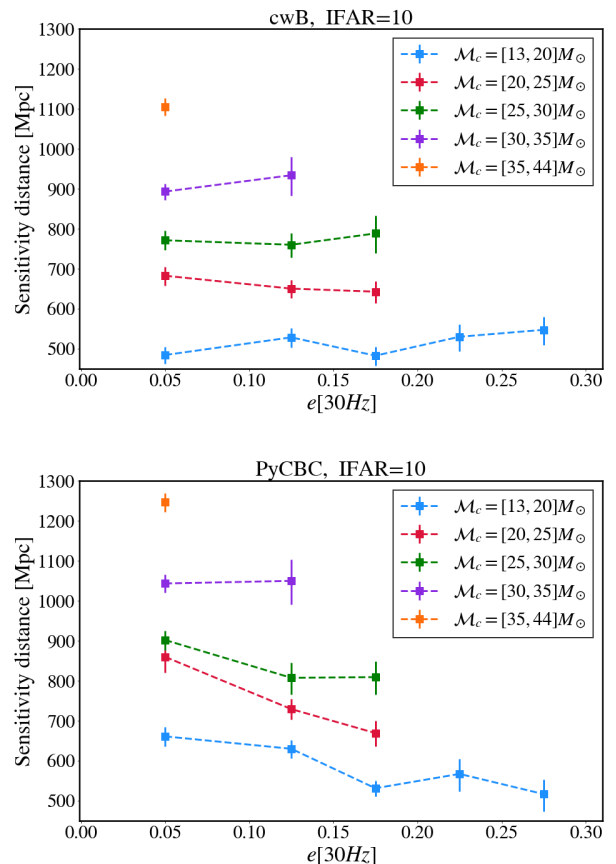

Figure 3: The upper (lower) panel shows the sensitivity range for the cWB (PyCBC) search pipeline for various chirp mass bins as a function of eccentricity defined at $30Hz$ at an IFAR > 10 years is shown. The plot markers are placed in the center of the eccentricity bins.

ues are uniformly distributed from a minimum value consistent with the length of the NR waveforms (between $30-50M_\odot$ for our dataset) to a maximum total mass of $100M_\odot$.

The orbital eccentricity of the individual injections, defined at a reference frequency of $30Hz$ is estimated through Eq. (2.3). We note that with this method the maximum eccentricity at $30Hz$ of a given injected NR waveform is given by the values of the last column of Table I, as these values are measured at the start of the NR waveforms.

The moderate values of eccentricity considered here are well-suited for a first study of sensitivity to the full inspiral-merger-ringdown (IMR) signal to the gravitational waves searches. Furthermore, many astrophysical models for eccentric binary black hole coalescences in the frequency band of ground-based detectors predict similar eccentricity values as those used here [63–66].

B. Visible range

The visible range for a given source parameters is calculated by injecting simulated waveform in the data as explained in Sec. III. Each recovered signal is assigned an inverse False Alarm rate (IFAR) according to its detection statistic. Then, one can compute for each bin of the source parameters the visible volume over a certain IFAR threshold. For a generic binary, the sensitive volume V of a network of detectors with a given sensitivity can be defined as

$$V(\xi) = \int_0^\infty f(z|\xi) \frac{dV_c}{dz} \frac{1}{1+z} \, dz, \qquad (4.1)$$

where $f(z|\xi)$ is the detection probability of a binary with a given parameter set ξ at redshift z, averaged over the extrinsic binary orientation parameters [67]. In Eq. (4.1) the sensitivity is assumed to be constant over the observing time, T_{obs}, which is why we have chosen the chunk of O2 data where sensitivity was almost uniform.

Given a population with parameters θ, the total observed volume can be computed as

$$V_\theta = \int_\xi p(\xi|\theta) V(\xi) \, d\xi, \qquad (4.2)$$

where $p(\xi|\theta)$ describes the underlying distribution of the intrinsic parameters. The visible range can be then estimated as the radius of the visible volume.

The sensitivity of GW detectors is a strongly dependent function of the binary chirp masses and distance, and also varies with spin. We also note that the eccentricity can be a relevant factor depending on the pipeline used to conduct the search. Thus, we have mainly chosen chirp mass binning to study the impact of eccentricity on visible range as it shows more clearly the dependence of the search sensitivity than other parameters, like the total mass.

C. Effect of eccentricity on search sensitivities

We now turn to discussing the visible range at an IFAR threshold of 10 years for both search pipelines and the same injection set. Although matched-filter searches are an optimal method to search for signals of known morphologies, in the case of eccentric BBHs computationally efficient waveform models describing the full GW signal of eccentric BBH coalescences have not yet been developed. For this reason it is expected that the quasi-circular template bank used by PyCBC will not be able to detect eccentric BBH events with orbital eccentricities beyond a certain threshold. On the other hand, cWB does not require signal models for detection and should be equally sensitive to eccentric BBH signals more or less throughout parameter space. It should be noted, however, that cWB is not an optimal method to detect BBH merger events and thus has lower sensitivity than PyCBC for regions of parameter space which are either explicitly covered by the PyCBC template bank or where the signal is otherwise 'mimicked' by templates in the bank.

In Figure 3 we exhibit the visible ranges of the PyCBC and cWB pipelines binned in chirp mass and eccentricity for all the injected signals. The results show a reduction in visible range of PyCBC with increasing eccentricity. The steepness of the reduction of visible range becomes more apparent when one goes to lower chirp masses; this is due to the fact that for high chirp masses the number of cycles visible in the sensitivity band of the LIGO detectors (and hence the inspiral part of the signal where eccentricity effects are pronounced) is rather short. One can conclude that for high chirp mass events with moderate to low eccentricities the PyCBC search and its quasi-circular template bank does not lose much visible range. This behaviour is contrary to the low chirp mass case with moderate eccentricities, where the loss in visible range is substantial.

Regarding cWB, previous work [25] found that the search pipeline is almost independent of eccentricity for a given chirp mass bin. However, the waveforms used in that investigation were significantly less accurate than the NR simulations used here. We note an interesting feature in the dependency of the range as a function of eccentricity for cWB for the lowest chirp mass bin. The range increases slightly as a function of eccentricity. This can probably be attributed to the power content in higher harmonics in eccentric BBH signals which is enhanced when the eccentricity increases; cWB captures the total radiated power and therefore can observe eccentric BBH events at larger range. For completeness we also show in Fig. 5 the analogous to Fig. 3 at an IFAR threshold of 100 years, where one observes the expected overall decrease of the sensitivity of both pipelines with increasing IFAR.

In our NR simulations we only have waveforms with moderate eccentricities ($e_{30Hz} < 0.3$). We note that the addition of spins to to mildly eccentric signals does not change significantly the detection efficiency for both pyCBC and cWB searches. We leave the study of a large parameter space of the eccentric non-precessing spin sector, as well as eccentric spin-precessing systems, to future work.

D. Comparisons of search sensitivities and astrophysical implications

In Figure 4 we show the comparison of the visible volumes of PyCBC and cWB at an IFAR threshold of 10 years. Within our injection set PyCBC almost always performs better than or similar to cWB in terms of visible volume. In the case of low chirp mass and high eccentricity the situation is reversed: PyCBC loses sensitivity and cWB becomes more sensitive.

These comparison results can also be viewed in the light of coalescence rate. Suppose the coalescence rate of eccentric BBH mergers with eccentricities between $(0, 0.3)$ at 30 Hz is R_{eBBH}; then the number of visible events will be simply $N_{events} = R_{eBBH} \times V_{iFAR} \times T_{obs}$. The relative difference in the number of detected events will be the same as the relative difference between the visible volume for the two search algorithms that we have considered. From this, we can conclude that cWB will see $\sim 10\%$ more events than pyCBC if the chirp mass is between $[13M_\odot, 20M_\odot]$ and the eccentricity
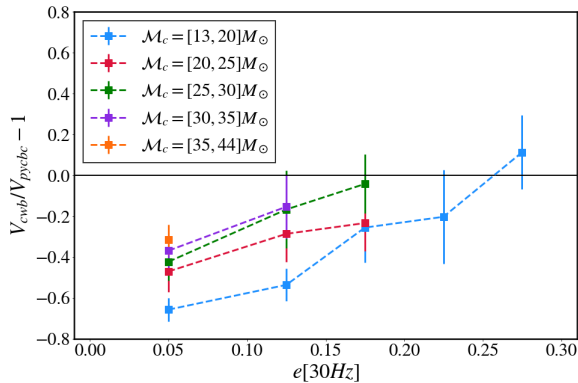
Figure 4: Relative difference in sensitivity volume between the search sensitivity of pyCBC and cWB for various chirp mass bins is presented as function of eccentricity at an iFAR > 10 years. The plot markers are placed in the center of the eccentricity bins.

at 30 Hz is between [0.25-0.3].

V.   CONCLUSIONS

In this paper we have quantified for the first time the sensitivities of GW search algorithms to eccentric BBH signals, using NR simulations of eccentric BBH mergers. The effect of eccentricity on matched filtered searches has only been studied for inspiral-only waveforms until now [59]; we have extended those studies to complete IMR signals. The search range of unmodeled searches for eccentric signals has been previously investigated with a particular IMR waveform model [25]; however, that waveform model is far less accurate than the NR simulations used here.

We have employed two different gravitational waves searches for BBH to compare the search sensitivity in terms of visible volume. The matched filter search PyCBC performs better than the unmodeled search cWB in most parts of the limited parameter space that we have considered. Only in the parameter space region of low chirp mass and high eccentricity does cWB perform better than PyCBC. It should also be noted that the parameter space that is covered by our NR injections is rather small. Due to the restricted length of the NR simulations, the parameter space of low chirp mass ($\mathcal{M}_c <$ 13) and high eccentricity $e_{30Hz} > 0.3$ is not yet probed in this work. This, however, is the most interesting part of parameter space for eccentric BBHs, with waveform morphologies that are substantially different than those of quasicircular BBHs. We plan to investigate this part of parameter space in subsequent work, with eccentric hybrid waveforms that combine NR data with an analytic description of the inspiral, or with future waveform models for the full IMR signal.

The two search pipelines used here —very different algorithms as described in Sec. III —offer a complementary way

to search for BBH mergers in different parts of the source parameter space. Constructing a template-based search for eccentric BBH will be challenging as the rate of background triggers increases with the increase of template bank parameters. In the light of astrophysical considerations, most of the BBH events observable by LIGO and Virgo are expected to have eccentricities lower than 0.2 at 30 Hz; this region of parameter space has been demonstrated to be well-covered by the PyCBC search, even with a quasi-circular template bank. Certain astrophysical scenarios suggest LIGO-Virgo relevant BBH events with higher eccentricities: for such sources the cWB search provides decent coverage.

With the expected availability of computationally efficient and accurate eccentric IMR BBH waveforms models (and/or eccentric hybrids) in the near future it will be interesting to probe the low chirp mass and high eccentricity part of the parameter space, where the modelled search is penalized due to substantial dephasing between the quasicircular template bank and the signal.

With future upgrades, the detectors' low-frequency sensitivity (in the range $24 - 100$ Hz) is expected to improve significantly; this will in turn allow a significant gain in SNR during the inspiral even for BBH systems with relatively high masses, adding more prominence to detectable inspiral features like eccentricity and penalizing the matched-filter searches for eccentric BBH even further. With future improvements at low frequencies, the role of un-modeled searches is therefore expected to become important also for the part of parameter space which is well-covered by matched-filter searches at current detector configuration.

8

Islands. The authors are grateful for computational resources provided by the LIGO Laboratory and supported by National Science Foundation Grants PHY-0757058 and PHY-0823459. MH acknowledges support from Swiss National Science Foundation (SNSF) grant IZCOZ0-177057. ARB is grateful to the Pauli Center for Theoretical Studies at ETHZ which provided valuable travel support during stages of this work. S. T. is supported by the Swiss National Science Foundation and a Forschungskredit of the University of Zurich. This research has made use of data, software and/or web tools obtained from the Gravitational Wave Open Science Center (https://www.gw-openscience.org), a service of LIGO Laboratory, the LIGO Scientific Collaboration and the Virgo Collaboration. LIGO is funded by the U.S. National Science Foundation. Virgo is funded by the French Centre National de Recherche Scientifique (CNRS), the Italian Istituto Nazionale della Fisica Nucleare (INFN) and the Dutch Nikhef, with contributions by Polish and Hungarian institutes. The authors gratefully acknowledge the support of the NSF CIT cluster for the provision of computational resources for pyCBC and cWB runs.

Appendix A: Effect of increasing the IFAR in the searches

In Sec. IV C we have discussed the effect of eccentricity in PyCBC and cWB at an IFAR threshold of 10 years. For completeness we present here results at an IFAR threshold of 100 years. The outcome of such a calculation is shown in Fig. 5, where one observes comparing to Fig. 3 the expected overall decrease of the sensitivity distance of both pipelines with increasing IFAR.
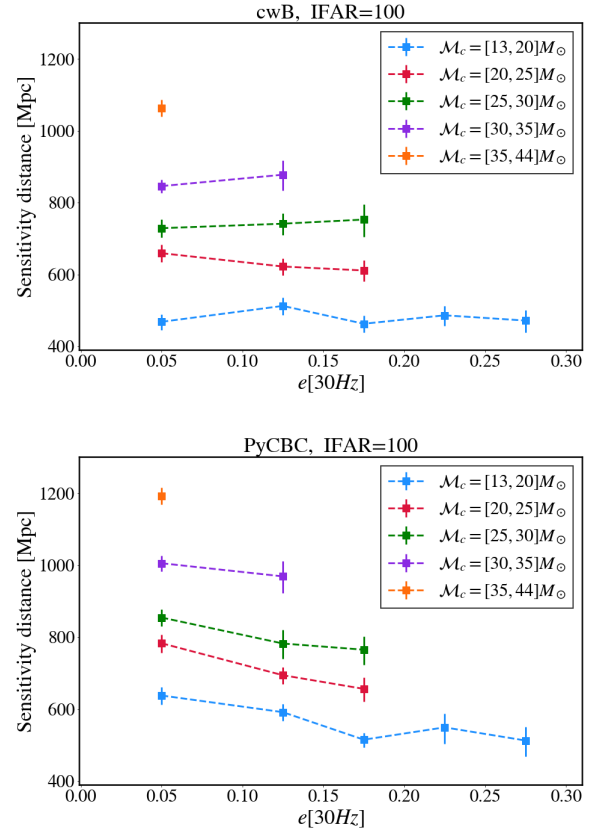

Figure 5: The upper (lower) panel shows the sensitivity range for the cWB (PyCBC) search pipeline for various chirp mass bins as a function of eccentricity defined at $30Hz$ at an IFAR > 100 years is shown. The plot markers are placed in the center of the eccentricity bins.

[1] B. P. Abbott et al. GWTC-1: A Gravitational-Wave Transient Catalog of Compact Binary Mergers Observed by LIGO and Virgo during the First and Second Observing Runs. *Phys. Rev.*, X9(3):031040, 2019.

[2] https://gracedb.ligo.org/superevents/public/O3/.

[3] B. P. Abbott et al. Search for Eccentric Binary Black Hole Mergers with Advanced LIGO and Advanced Virgo during their First and Second Observing Runs. 2019.

[4] Isobel M. Romero-Shaw, Paul D. Lasky, and Eric Thrane. Searching for Eccentricity: Signatures of Dynamical Formation in the First Gravitational-Wave Transient Catalogue of LIGO and Virgo. *Mon. Not. Roy. Astron. Soc.*, 490(4):5210–5216, 2019.

[5] Hans A. Bethe and G. E. Brown. Evolution of binary compact objects which merge. *Astrophys. J.*, 506:780–789, 1998.

[6] Krzysztof Belczynski, Vassiliki Kalogera, and Tomasz Bulik. A comprehensive study of binary compact objects as gravitational wave sources: Evolutionary channels, rates, and physical properties. *The Astrophysical Journal*, 572(1):407–431, jun 2002.

[7] Matthias U Kruckow, Thomas M Tauris, Norbert Langer, Michael Kramer, and Robert G Izzard. Progenitors of gravitational wave mergers: binary evolution with the stellar grid-based code ComBinE. *Monthly Notices of the Royal Astronomical Society*, 481(2):1908–1949, 08 2018.

[8] Jim W. Barrett, Sebastian M. Gaebel, Coenraad J. Neijssel, Alejandro Vigna-Gómez, Simon Stevenson, Christopher P. L. Berry, Will M. Farr, and Ilya Mandel. Accuracy of inference on the physics of binary evolution from gravitational-wave observations. *Mon. Not. Roy. Astron. Soc.*, 477(4):4685–4695, 2018.

[9] P. C. Peters and J. Mathews. Gravitational radiation from point masses in a keplerian orbit. *Phys. Rev.*, 131:435–440, Jul 1963.

[10] P. C. Peters. Gravitational radiation and the motion of two point masses. *Phys. Rev.*, 136:B1224–B1232, Nov 1964.

[11] Ryan M. O'Leary, Frederic A. Rasio, John M. Fregeau, Natalia Ivanova, and Richard O'Shaughnessy. Binary mergers and growth of black holes in dense star clusters. *The Astrophysical Journal*, 637(2):937–951, feb 2006.

[12] Johan Samsing. Eccentric black hole mergers forming in globular clusters. *Phys. Rev. D*, 97:103014, May 2018.

[13] Giacomo Fragione and Bence Kocsis. Black hole mergers from quadruples. *Mon. Not. Roy. Astron. Soc.*, 486(4):4781–4789, 2019.

[14] Jun Kumamoto, Michiko S. Fujii, and Ataru Tanikawa. Gravitational-Wave Emission from Binary Black Holes Formed in Open Clusters. *Mon. Not. Roy. Astron. Soc.*, 486(3):3942–3950, 2019.

[15] Ryan M. O'Leary, Bence Kocsis, and Abraham Loeb. Gravitational waves from scattering of stellar-mass black holes in galactic nuclei. *Mon. Not. Roy. Astron. Soc.*, 395(4):2127–2146, 2009.

[16] J. Aasi et al. Advanced LIGO. *Class. Quant. Grav.*, 32:074001, 2015.

[17] F. Acernese et al. Advanced Virgo: a second-generation interferometric gravitational wave detector. *Class. Quant. Grav.*, 32(2):024001, 2015.

[18] B. P. Abbott et al. Binary Black Hole Population Properties Inferred from the First and Second Observing Runs of Advanced LIGO and Advanced Virgo. *Astrophys. J.*, 882(2):L24, 2019.

[19] Ilya Mandel and Richard O'Shaughnessy. Compact Binary Coalescences in the Band of Ground-based Gravitational-Wave Detectors. *Class. Quant. Grav.*, 27:114007, 2010.

[20] B. P. Abbott et al. Astrophysical Implications of the Binary Black-Hole Merger GW150914. *Astrophys. J.*, 818(2):L22, 2016.

[21] Will M. Farr, Simon Stevenson, M. Coleman Miller, Ilya Mandel, Ben Farr, and Alberto Vecchio. Distinguishing Spin-Aligned and Isotropic Black Hole Populations With Gravitational Waves. *Nature*, 548:426, 2017.

[22] M.L. Lidov. The evolution of orbits of artificial satellites of planets under the action of gravitational perturbations of external bodies. *Planetary and Space Science*, 9(10):719 – 759, 1962.

[23] Yoshihide Kozai. Secular perturbations of asteroids with high inclination and eccentricity. *Astron. J.*, 67:591–598, 1962.

[24] V. Tiwari, S. Klimenko, N. Christensen, E. A. Huerta, S. R. P. Mohapatra, A. Gopakumar, M. Haney, P. Ajith, S. T. McWilliams, G. Vedovato, M. Drago, F. Salemi, G. A. Prodi, C. Lazzaro, S. Tiwari, G. Mitselmakher, and F. Da Silva. Proposed search for the detection of gravitational waves from eccentric binary black holes. *Phys. Rev. D*, 93:043007, Feb 2016.

[25] B. P. Abbott and et al. Search for eccentric binary black hole mergers with advanced LIGO and advanced virgo during their first and second observing runs. *The Astrophysical Journal*, 883(2):149, sep 2019.

[26] Alexander H. Nitz, Amber Lenon, and Duncan A. Brown. Search for Eccentric Binary Neutron Star Mergers in the first and second observing runs of Advanced LIGO. *Astrophys. J.*, 890:1, 12 2019.

[27] Bruce Allen, Warren G. Anderson, Patrick R. Brady, Duncan A. Brown, and Jolien D. E. Creighton. Findchirp: An algorithm for detection of gravitational waves from inspiraling compact binaries. *Phys. Rev. D*, 85:122006, Jun 2012.

[28] Samantha A. Usman et al. The PyCBC search for gravitational waves from compact binary coalescence. *Class. Quant. Grav.*, 33(21):215004, 2016.

[29] S. Klimenko, I. Yakushin, A. Mercer, and Guenakh Mitselmakher. Coherent method for detection of gravitational wave bursts. *Class. Quant. Grav.*, 25:114029, 2008.

[30] S. Klimenko, G. Vedovato, M. Drago, F. Salemi, V. Tiwari, G. A. Prodi, C. Lazzaro, K. Ackley, S. Tiwari, C. F. Da Silva, and G. Mitselmakher. Method for detection and reconstruction of gravitational wave transients with networks of advanced detectors. *Phys. Rev. D*, 93:042004, Feb 2016.

[31] B. S. Sathyaprakash and B. F. Schutz. Physics, Astrophysics and Cosmology with Gravitational Waves. *Living Rev. Rel.*, 12:2, 2009.

[32] Lee Samuel Finn and David F. Chernoff. Observing binary inspiral in gravitational radiation: One interferometer. *Phys. Rev. D*, 47:2198–2219, Mar 1993.

[33] Piotr Jaranowski, Andrzej Królak, and Bernard F. Schutz. Data analysis of gravitational-wave signals from spinning neutron stars: The signal and its detection. *Phys. Rev. D*, 58:063001, Aug 1998.

[34] Frank Loffler et al. The Einstein Toolkit: A Community Computational Infrastructure for Relativistic Astrophysics. *Class. Quant. Grav.*, 29:115001, 2012.

[35] Maria Babiuc-Hamilton et al. The Einstein Toolkit, October 2019. To find out more, visit http://einsteintoolkit.org.

[36] SXS collaboration. https://www.black-holes.org/SpEC.html.

[37] Antoni Ramos-Buades, Sascha Husa, Geraint Pratten, Héctor Estellés, Cecilio García-Quirós, Maite Mateu-Lucena, Marta Colleoni, and Rafel Jaume. First survey of spinning eccen-

tric black hole mergers: Numerical relativity simulations, hybrid waveforms, and parameter estimation. *Phys. Rev. D*, 101(8):083015, 2020.

[38] Ian Hinder, Lawrence E. Kidder, and Harald P. Pfeiffer. Eccentric binary black hole inspiral-merger-ringdown gravitational waveform model from numerical relativity and post-newtonian theory. *Phys. Rev. D*, 98:044015, Aug 2018.

[39] V. Tiwari, S. Klimenko, N. Christensen, E. A. Huerta, S. R. P. Mohapatra, A. Gopakumar, M. Haney, P. Ajith, S. T. McWilliams, G. Vedovato, M. Drago, F. Salemi, G. A. Prodi, C. Lazzaro, S. Tiwari, G. Mitselmakher, and F. Da Silva. Proposed search for the detection of gravitational waves from eccentric binary black holes. *Phys. Rev. D*, 93:043007, Feb 2016.

[40] Sascha Husa, Mark Hannam, Jose A. Gonzalez, Ulrich Sperhake, and Bernd Bruegmann. Reducing eccentricity in black-hole binary evolutions with initial parameters from post-Newtonian inspiral. *Phys. Rev.*, D77:044037, 2008.

[41] Harald P. Pfeiffer, Duncan A. Brown, Lawrence E. Kidder, Lee Lindblom, Geoffrey Lovelace, and Mark A. Scheel. Reducing orbital eccentricity in binary black hole simulations. *Class. Quant. Grav.*, 24:S59–S82, 2007.

[42] Wolfgang Tichy and Pedro Marronetti. A Simple method to set up low eccentricity initial data for moving puncture simulations. *Phys. Rev.*, D83:024012, 2011.

[43] Alessandra Buonanno, Lawrence E. Kidder, Abdul H. Mroue, Harald P. Pfeiffer, and Andrea Taracchini. Reducing orbital eccentricity of precessing black-hole binaries. *Phys. Rev.*, D83:104034, 2011.

[44] Abdul H. Mroue, Harald P. Pfeiffer, Lawrence E. Kidder, and Saul A. Teukolsky. Measuring orbital eccentricity and periastron advance in quasi-circular black hole simulations. *Phys. Rev.*, D82:124016, 2010.

[45] Michael Pürrer, Sascha Husa, and Mark Hannam. An efficient iterative method to reduce eccentricity in numerical-relativity simulations of compact binary inspiral. *Phys. Rev. D*, 85(12), Jun 2012.

[46] Antoni Ramos-Buades, Sascha Husa, and Geraint Pratten. Simple procedures to reduce eccentricity of binary black hole simulations. *Phys. Rev. D*, 99:023003, Jan 2019.

[47] Miriam Cabero, Alex B. Nielsen, Andrew P. Lundgren, and Collin D. Capano. Minimum energy and the end of the inspiral in the post-newtonian approximation. *Phys. Rev. D*, 95:064016, Mar 2017.

[48] Héctor Estellés, Antoni Ramos-Buades, Sascha Husa, Cecilio García-Quirós, and Leila Haegel. IMRPhenomTP: A phenomenological time domain model for dominant quadrupole gravitational wave signal of coalescing binary black holes. 2020. in preparation.

[49] K. G. Arun, Luc Blanchet, Bala R. Iyer, and Siddhartha Sinha. Third post-newtonian angular momentum flux and the secular evolution of orbital elements for inspiralling compact binaries in quasi-elliptical orbits. *Phys. Rev. D*, 80:124018, Dec 2009.

[50] T. Damour and N. Deruelle. General relativistic celestial mechanics of binary systems. I. The post-Newtonian motion. *Ann. Inst. Henri Poincaré Phys. Théor., Vol. 43, No. 1, p. 107 - 132*, 1985.

[51] Rich Abbott et al. Open data from the first and second observing runs of Advanced LIGO and Advanced Virgo. 12 2019.

[52] B P Abbott et al. Characterization of transient noise in advanced LIGO relevant to gravitational wave signal GW150914. *Classical and Quantum Gravity*, 33(13):134001, jun 2016.

[53] J. Aasi et al. The characterization of Virgo data and its impact on gravitational-wave searches. *Class. Quant. Grav.*, 29:155002, 2012.

[54] Samantha A. Usman, Alexander H. Nitz, Ian W. Harry, Christopher M. Biwer, Duncan A. Brown, Miriam Cabero, Collin D. Capano, Tito Dal Canton, Thomas Dent, Stephen Fairhurst, Marcel S. Kehl, Drew Keppel, Badri Krishnan, Amber Lenon, Andrew Lundgren, Alex B. Nielsen, Larne P. Pekowsky, Harald P. Pfeiffer, Peter R. Saulson, Matthew West, and Joshua L. Willis. The PyCBC search for gravitational waves from compact binary coalescence. *Classical and Quantum Gravity*, 33(21):215004, November 2016.

[55] Bruce Allen, Warren G. Anderson, Patrick R. Brady, Duncan A. Brown, and Jolien D. E. Creighton. Findchirp: An algorithm for detection of gravitational waves from inspiraling compact binaries. *Phys. Rev. D*, 85:122006, Jun 2012.

[56] Bruce Allen. χ^2 time-frequency discriminator for gravitational wave detection. *Phys. Rev. D*, 71:062001, Mar 2005.

[57] Alexander H. Nitz, Thomas Dent, Tito Dal Canton, Stephen Fairhurst, and Duncan A. Brown. Detecting binary compact-object mergers with gravitational waves: Understanding and improving the sensitivity of the PyCBC search. *The Astrophysical Journal*, 849(2):118, nov 2017.

[58] Tito Dal Canton and Ian W. Harry. Designing a template bank to observe compact binary coalescences in Advanced LIGO's second observing run. *arXiv e-prints*, page arXiv:1705.01845, May 2017.

[59] Duncan A. Brown and Peter J. Zimmerman. Effect of eccentricity on searches for gravitational waves from coalescing compact binaries in ground-based detectors. *Phys. Rev. D*, 81:024007, Jan 2010.

[60] E. A. Huerta, C. J. Moore, Prayush Kumar, Daniel George, Alvin J. K. Chua, Roland Haas, Erik Wessel, Daniel Johnson, Derek Glennon, Adam Rebei, A. Miguel Holgado, Jonathan R. Gair, and Harald P. Pfeiffer. Eccentric, nonspinning, inspiral, gaussian-process merger approximant for the detection and characterization of eccentric binary black hole mergers. *Phys. Rev. D*, 97:024031, Jan 2018.

[61] V. Tiwari, S. Klimenko, V. Necula, and G. Mitselmakher. Reconstruction of chirp mass in searches for gravitational wave transients. *Classical and Quantum Gravity*, 33(1):01LT01, January 2016.

[62] Vaibhav Tiwari. Estimation of the sensitive volume for gravitational-wave source populations using weighted Monte Carlo integration. *Classical and Quantum Gravity*, 35(14):145009, July 2018.

[63] F. Antonini, S. Chatterjee, C. L. Rodriguez, M. Morscher, B. Pattabiraman, V. Kalogera, and F. A. Rasio. Black Hole Mergers and Blue Stragglers from Hierarchical Triples Formed in Globular Clusters. *Astrophys. J.*, 816:65, January 2016.

[64] F. Antonini and F. A. Rasio. Merging Black Hole Binaries in Galactic Nuclei: Implications for Advanced-LIGO Detections. *Astrophys. J.*, 831:187, November 2016.

[65] L. Gondán, B. Kocsis, P. Raffai, and Z. Frei. Eccentric Black Hole Gravitational-wave Capture Sources in Galactic Nuclei: Distribution of Binary Parameters. *Astrophys. J.*, 860:5, June 2018.

[66] J. Samsing. Eccentric black hole mergers forming in globular clusters. *PRD*, 97(10):103014, May 2018.

[67] B. P. Abbott and et al. Binary black hole population properties inferred from the first and second observing runs of advanced LIGO and advanced virgo. *The Astrophysical Journal*, 882(2):L24, sep 2019.

Chapter 8

Conclusions

The advent of the gravitational wave astronomy demands increasingly more accurate waveform models in order to improve the detection and parameter estimation of the upcoming signals. The increase of accuracy of the models does not only mean augmenting the quality of the numerical relativity simulations, to which all current inspiral-merger-ringdown waveform models are calibrated, but also populating the huge parameter space of a binary by including more and more physical effects, like spin-precession or eccentricity. The main work during this thesis has been the production of the numerical relativity simulations for generic binary black-hole mergers and the study of their implications for waveform modelling, detection and parameter estimation.

The content of this thesis is balanced between the first introductory part and the second one devoted to the original scientific work. For the benefit of the author and the reader, pedagogical explanations on basics concepts of gravitational wave astronomy have been provided in the first three chapters of the thesis. Chapter 1 provides the fundamentals of gravitational wave physics focused to the radiation produced by compact binary coalescences. Chapter 2 extends the solutions of the two-body problem in general relativity, with an overview on analytical solutions within the post-Newtonian theory and numerical approximations within numerical relativity. Finally, Chapter 3 focuses on the theoretical framework for detection and estimation of parameters from signals emitted by binary black holes, providing also details on the algorithms and the methods used by different parameter estimation codes and detection pipelines. Overall, these three chapters aim to contextualize the reader in the main topics addressed by the thesis providing notation and basic notions on concepts developed in the second part of the thesis.

The second part of this thesis includes original research results. We have summarized in the following three sections the main results.

Eccentricity in numerical relativity simulations

We present a simple procedure to reduce the eccentricity of numerical relativity simulations of binary black-hole mergers in Chap. 4 . This method allows one to control the amount of initial eccentricity on numerical simulations with a computationally efficient and simple iterative procedure based on post-Newtonian expressions. The validity of this method has been tested with generic black-hole binary NR simulations and it permits the reduction of the residual eccentricity up to values of 10^{-4} in a few iterations [1].

In Chap. 5 we exploit the procedure developed in Chap. 4 to specify initial parameters for highly eccentric NR simulations. We produce a data set of 60 eccentric NR simulations, non-spinning up to mass ratio $q = m_1/m_2 = 4$ and including dimensionless spins aligned with the orbital angular momentum of the system up to $|\chi_i| = 0.75$,

$i = 1, 2$, with the BAM and the EinsteinToolkit codes. This data set together with the 20 non-spinning eccentric SXS simulations of [2] give a total of 80 simulations, which we use to test the quasi-circularity of the final state of the binary extending previous results to the spinning case. Furthermore, we apply a simple procedure to generate PN-NR eccentric hybrid waveforms for the $(2, 2)$ mode [3]. Finally, we use the generated waveforms to show examples of parameter estimation using three different quasi-circular waveform models, IMRPhenomD [4, 5], IMRPhenomHM [6] and IMRPhenomPv2 [7], as approximants and quantifying the bias in the recovered parameters for each model. We find that the IMRPhenomHM model shows less bias in some parameters, like the luminosity distance and mass ratio, with increasing eccentricity than IMRPhenomD and IMRPhenomPv2, while other parameters like the chirp mass or the effective spin parameter show comparable biases with increasing eccentricity for the three approximants.

Validity of modelling approximations for precessing binaries including higher order modes with numerical relativity

In Chapter 6 we turned our attention to spin-precession in quasi-circular BBH mergers with emphasis on the analysis of two main approximations used by phenomenological waveform models of precessing black hole binaries. Our main objective in this work has been testing these approximations and assessing their accuracy for higher order harmonics in the co-precessing and the inertial frames. Due to the lack of precessing PN/EOB-NR hybrid waveforms we have restricted to pure NR waveforms from three different codes BAM, ET and the spectral code SpEc [8].

We quantify differences between waveforms using different quantities like the *mismatch*, noise weighted inner product between two waveforms, or the gravitational wave radiated energy per (l, m)-mode [9]. We find that the discrepancies between precessing and approximate precessing waveforms increase substantially for higher order modes, where for some specific modes, like the $(3, \pm 2)$ and $(4, \pm 3)$, single mode mismatches increase above 3% for more than 70% of our data set, due to the negligence of a proper ringdown mode-mixing treatment of these modes. For the rest of (l, m)-modes studied differences are reduced. We have also studied possible improvements of the analysed approximations by adopting strategies already used by the precessing surrogate models [10, 11], which we show can alleviate such discrepancies.

Sensitivity of two search pipelines to eccentric signals

In Chap. 7 we have analysed the sensitivity of two search pipelines used by the LIGO and Virgo collaborations during the O2 Science Run to the full gravitational wave signal of eccentric binary black holes. In this work we have quantified the impact of eccentricity on two search pipelines: a matched-filter algorithm, PyCBC, based on aligned-spin $(2, 2)$-mode binary black hole waveform templates, and an unmodeled search algorithm, cWB, based on a coherent excess of power in a detector network.

The sensitivity of both pipelines is estimated injecting eccentric signals computed from numerical relativity simulations, including public SXS [2] and non-public ET waveforms presented in [3], the latter including spins aligned with the orbital angular momentum of the system. We find that sensitivity distances decrease significantly more for PyCBC with increasing than for cWB, whose sensitivity is quite insensitive to the increase of eccentricity. As a consequence, we can consider cWB a robust tool to detect GW signals with moderate eccentricities.

Outlook and future research

The work presented in this thesis is just a small step towards modelling generic black hole binaries. Regarding spin precession, the study performed in Chap. 6 can help to compare waveforms in different frames and implement possible improvements in the current phenomenological precessing waveform models, like the modification of the precessing angles used in the waveform models to account for mode asymmetries and accurately describe final spin modifications.

The other main topic has been the development of basic tools required to produce simple inspiral-merger-ringdown eccentric waveform models, like the production of a data set of numerical relativity waveforms and their hybridization with post-Newtonian waveforms for the dominant $(2, 2)$-mode.

The generation of an eccentric IMR waveform model is challenging due to the lack of accurate enough post-Newtonian results for the amplitude and the frequency which allow applying a robust fitting procedure across the parameter space. As a consequence, the generation of the eccentric IMR waveform model is one of the future goals of the thesis applicant, in which it is currently working.

Another project in which the applicant is currently involved is the generation of multi-mode eccentric hybrid waveforms including higher order modes. These waveforms are of potential interest because they allow one to work in the low frequency limit, and extend data analysis studies like the one presented in Chap. 7 to a low mass range. Additionally, those multi-mode eccentric hybrids could also be used to generate a eccentric IMR model including higher order modes.

During the four years of Ph.D. the candidate has been a member of the LSC, which in that time has published 40 scientific articles where the applicant appears as a co-author. I have also participated in the development of the new PhenomX waveform family which has led to several short author papers in which I am a co-author.

- Geraint Pratten, Sascha Husa, Cecilio García-Quirós, Marta Colleoni, Antoni Ramos-Buades, Héctor Estellés, Rafel Jaume. *Setting the cornerstone for the IMRPhenomX family of models for gravitational waves from compact binaries: The dominant harmonic for non-precessing quasi-circular black holes.* arxiv:2001.1142 [gr-qc] (2020). Submitted to Physical Review D.

- Cecilio García-Quirós, Marta Colleoni, Sascha Husa, Héctor Estellés, Geraint Pratten, Antoni Ramos-Buades, Maite Mateu-Lucena, Rafel Jaume. *IMRPhenomXHM: A multi-mode frequency-domain model for the gravitational wave signal from non-precessing black-hole binaries.* arXiv:2001.10914 [gr-qc] (2020). Submitted to Physical Review D.

- Geraint Pratten, Cecilio García-Quirós, Marta Colleoni, Antoni Ramos-Buades, Héctor Estellés, Maite Mateu-Lucena, Rafel Jaume, Maria Haney, David Keitel, Jonathan E. Thompson, Sascha Husa. *Let's twist again: computationally efficient models for the dominant and sub-dominant harmonic modes of precessing binary black holes.* arXiv:2004.06503 [gr-qc] (2020). Submitted to Physical Review D.

These models have undergone a waveform review of the LIGO-Virgo collaboration and are publicly available as part of the `LALsuite` software [12] software. Furthermore,

I have also contributed to the new time domain phenomenological IMRPhenomTP waveform model.

- Héctor Estellés, Antoni Ramos-Buades, Sascha Husa, Cecilio García-Quirós, Marta Colleoni, Leïla Haegel and Rafel Jaume. *IMRPhenomTP: A phenomenological time domain model for dominant quadrupole gravitational wave signal of coalescing binary black holes.* arxiv:2004.08302 [gr-qc] (2020). Submitted to Physical Review D.

These models can be used in the future to reduce the limitations from systematic errors in studies like the ones performed in Chapters 5 and 6, and they are expected to become a standard tool in GW data analysis. One of the big remaining challenges is to extend such models to eccentricity, which is my current focus of research.

References

[1] Antoni Ramos-Buades, Sascha Husa, and Geraint Pratten. Simple procedures to reduce eccentricity of binary black hole simulations. *Phys. Rev. D*, 99(2):023003, 2019. arXiv:1810.00036 [gr-qc].

[2] Ian Hinder, Lawrence E. Kidder, and Harald P. Pfeiffer. Eccentric binary black hole inspiral-merger-ringdown gravitational waveform model from numerical relativity and post-Newtonian theory. *Phys. Rev. D*, 98(4):044015, 2018. arXiv:1709.02007 [gr-qc].

[3] Antoni Ramos-Buades, Sascha Husa, Geraint Pratten, Héctor Estellés, Cecilio García-Quirós, Maite Mateu-Lucena, Marta Colleoni, and Rafel Jaume. First survey of spinning eccentric black hole mergers: Numerical relativity simulations, hybrid waveforms, and parameter estimation. *Phys. Rev. D*, 101(8):083015, 2020. arXiv:1909.11011 [gr-qc].

[4] Sascha Husa, Sebastian Khan, Mark Hannam, Michael Pürrer, Frank Ohme, Xisco Jiménez Forteza, and Alejandro Bohé. Frequency-domain gravitational waves from nonprecessing black-hole binaries. I. New numerical waveforms and anatomy of the signal. *Phys. Rev. D*, 93(4):044006, 2016. arXiv:1508.07250 [gr-qc].

[5] Sebastian Khan, Sascha Husa, Mark Hannam, Frank Ohme, Michael Pürrer, Xisco Jiménez Forteza, and Alejandro Bohé. Frequency-domain gravitational waves from nonprecessing black-hole binaries. II. A phenomenological model for the advanced detector era. *Phys. Rev.*, D93(4):044007, 2016. arXiv:1508.07253 [gr-qc].

[6] Lionel London, Sebastian Khan, Edward Fauchon-Jones, Cecilio García, Mark Hannam, Sascha Husa, Xisco Jiménez-Forteza, Chinmay Kalaghatgi, Frank Ohme, and Francesco Pannarale. First higher-multipole model of gravitational waves from spinning and coalescing black-hole binaries. *Phys. Rev. Lett.*, 120(16):161102, 2018. arXiv:1708.00404 [gr-qc].

[7] Mark Hannam, Patricia Schmidt, Alejandro Bohé, Leïla Haegel, Sascha Husa, Frank Ohme, Geraint Pratten, and Michael Pürrer. Simple Model of Complete Precessing Black-Hole-Binary Gravitational Waveforms. *Phys. Rev. Lett.*, 113(15):151101, 2014. arXiv:1308.3271 [gr-qc].

[8] http://www.black holes.org/waveforms. The SXS binary black hole simulations catalog. 2013.

[9] Antoni Ramos-Buades, Patricia Schmidt, Geraint Pratten, and Sascha Husa. Validity of common modeling approximations for precessing binary black holes with higher-order modes. *Phys. Rev. D*, 101(10):103014, 2020. arXiv:2001.10936 [gr-qc].

[10] Jonathan Blackman, Scott E. Field, Mark A. Scheel, Chad R. Galley, Daniel A. Hemberger, Patricia Schmidt, and Rory Smith. A Surrogate Model of Gravitational Waveforms from Numerical Relativity Simulations of Precessing Binary Black Hole Mergers. *Phys. Rev.*, D95(10):104023, 2017. arXiv:1701.00550 [gr-qc].

[11] Vijay Varma, Scott E. Field, Mark A. Scheel, Jonathan Blackman, Davide Gerosa, Leo C. Stein, Lawrence E. Kidder, and Harald P. Pfeiffer. Surrogate

models for precessing binary black hole simulations with unequal masses. *Phys. Rev. Research.*, 1:033015, 2019. arXiv:1905.09300 [gr-qc].

[12] The LIGO Scientific Collaboration.   LALSuite: LSC Algorithm Library Suite.   https://www.lsc-group.phys.uwm.edu/daswg/projects/lalsuite.html, 2015.

Appendix A

Permissions for Chapter 4

Universitat
de les Illes Balears

Dr Sascha Husa, as co-author of the following article

Title: Simple procedures to reduce eccentricity of binary black hole simulations

Journal ref. : Phys. Rev. D 99, 023003 (2019)

Authors: Antoni Ramos-Buades, Sascha Husa, Geraint Pratten

I DECLARE:

Accepts that Mr Antoni Ramos Buades presents the cited article as the principal author and as a part of his doctoral thesis and that said article cannot, therefore, form part of any doctoral thesis.

And for all intents and purposes, hereby signs this document.

Signature

Palma de Mallorca, 03/05/2020

Universitat
de les Illes Balears

Dr. Geraint Pratten, as co-author of the following article

Title: Simple procedures to reduce eccentricity of binary black hole simulations
Journal ref. : arxiv:18010.00036 [gr-qc]
Phys. Rev. D 99, 023003 (2019)
Authors: Antoni Ramos-Buades, Sascha Husa, Geraint Pratten

I DECLARE:

Accepts that Mr. Antoni Ramos Buades presents the cited articles as the principal author and as a part of his doctoral thesis and that said articles cannot, therefore, form part of any doctoral thesis.

And for all intents and purposes, hereby signs this document.

Signature

G. Pratten

Palma de Mallorca, 29/04/2020

Appendix B

Permissions for Chapter 5

Dr Sascha Husa, as co-author of the following article

 Title: A first survey of spinning eccentric black hole mergers: numerical relativity
simulations, hybrid waveforms, and parameter estimation

*Journal ref. : Phys. Rev. D **101**, 083015 (2020)*

Authors: Antoni-Ramos-Buades, Sascha Husa, Geraint Pratten, Héctor Estellés, Cecilio
García-Quirós, Maite Mateu-Lucena, Marta Colleoni, Rafel Jaume.

I DECLARE:

Accepts that Mr Antoni Ramos Buades presents the cited article as the principal author
and as a part of his doctoral thesis and that said article cannot, therefore, form part of
any doctoral thesis.

And for all intents and purposes, hereby signs this document.

Signature

Palma de Mallorca, 03/05/2020

Dr. Geraint Pratten, as co-author of the following article

Title: First survey of spinning eccentric black hole mergers: Numerical relativity simulations, hybrid waveforms, and parameter estimation

Journal ref. : *Phys. Rev. D **101**, 083015 (2020)*

Authors: Antoni Ramos-Buades, Sascha Husa, Geraint Pratten, Héctor Estellés, Cecilio García-Quirós, Maite Mateu-Lucena, Marta Colleoni, Rafel Jaume.

I DECLARE:

Accepts that Mr. Antoni Ramos Buades presents the cited article as the principal author and as a part of his doctoral thesis and that said article cannot, therefore, form part of any doctoral thesis.

And for all intents and purposes, hereby signs this document.

Signature

G. Pratten

Palma de Mallorca, 29/04/2020

Universitat
de les Illes Balears

Mr. Cecilio García Quirós, as co-author of the following article

1) Title: A first survey of spinning eccentric black hole mergers: numerical relativity simulations, hybrid waveforms, and parameter estimation

*Journal ref. : Phys. Rev. D **101**, 083015 (2020)*

Authors: Antoni Ramos-Buades, Sascha Husa, Geraint Pratten, Héctor Estellés, Cecilio García-Quirós, Maite Mateu-Lucena, Marta Colleoni, Rafel Jaume.

I DECLARE:

Accepts that Mr. Antoni Ramos Buades presents the cited articles as the principal author and as a part of his doctoral thesis and that said articles cannot, therefore, form part of any doctoral thesis.

And for all intents and purposes, hereby signs this document.

Signature

Palma de Mallorca, 20/04/2020

Universitat
de les Illes Balears

Ms. Marta Colleoni, as co-author of the following article

1) Title: A first survey of spinning eccentric black hole mergers: numerical relativity simulations, hybrid waveforms, and parameter estimation

*Journal ref. : Phys. Rev. D **101**, 083015 (2020)*

Authors: Antoni Ramos-Buades , Sascha Husa, Geraint Pratten, Héctor Estellés, Cecilio García-Quirós, Maite Mateu-Lucena, Marta Colleoni, Rafel Jaume.

I DECLARE:

Accepts that Mr. Antoni Ramos Buades presents the cited articles as the principal author and as a part of his doctoral thesis and that said articles cannot, therefore, form part of any doctoral thesis.

And for all intents and purposes, hereby signs this document.

Signature

Palma de Mallorca, 20/04/2020

Universitat
de les Illes Balears

Ms. María Teresa Mateu Lucena, as co-author of the following article

1) Title: A first survey of spinning eccentric black hole mergers: numerical relativity simulations, hybrid waveforms, and parameter estimation

*Journal ref. : Phys. Rev. D **101**, 083015 (2020)*

Authors: Antoni Ramos-Buades, Sascha Husa, Geraint Pratten, Héctor Estellés, Cecilio García-Quirós, Maite Mateu-Lucena, Marta Colleoni, Rafel Jaume.

I DECLARE:

Accepts that Mr. Antoni Ramos Buades presents the cited articles as the principal author and as a part of his doctoral thesis and that said articles cannot, therefore, form part of any doctoral thesis.

And for all intents and purposes, hereby signs this document.

Signature

Palma de Mallorca, 20/04/2020

Mr. Rafel Jaume Amengual, as co-author of the following article

Title: A first survey of spinning eccentric black hole mergers: numerical relativity simulations, hybrid waveforms, and parameter estimation

*Journal ref. : Phys. Rev. D **101**, 083015 (2020)*

Authors: Antoni Ramos-Buades, Sascha Husa, Geraint Pratten, Héctor Estellés, Cecilio García-Quirós, Maite Mateu-Lucena, Marta Colleoni, Rafel Jaume.

I DECLARE:

Accepts that Mr. Antoni Ramos Buades presents the cited article as the principal author and as a part of his doctoral thesis and that said article cannot, therefore, form part of any doctoral thesis.

And for all intents and purposes, hereby signs this document.

Signature

Palma de Mallorca, 29/04/2020

Appendix C

Permissions for Chapter 6

UIB | **Universitat**
de les Illes Balears

Dr. Patricia Schmidt, as co-author of the following article

Title: Validity of common modelling approximations for precessing binary black holes with higher-order modes

*Journal ref. :   Phys. Rev. D **101**, 103014 (2020)*

Authors: Antoni Ramos-Buades, Patricia Schmidt, Geraint Pratten, Sascha Husa.

I DECLARE:

Accepts that Mr. Antoni Ramos Buades presents the cited article as the principal author and as a part of his doctoral thesis and that said articles cannot, therefore, form part of any doctoral thesis.

And for all intents and purposes, hereby signs this document.

Signature

Palma de Mallorca, 11/05/2020

Dr. Geraint Pratten, as co-author of the following article

 Title: Validity of common modelling approximations for precessing binary black holes with higher-order modes

*Journal ref. : Phys. Rev. D **101***, 103014 (2020)*

Authors: Antoni Ramos-Buades, Patricia Schmidt, Geraint Pratten, Sascha Husa.

I DECLARE:

Accepts that Mr. Antoni Ramos Buades presents the cited article as the principal author and as a part of his doctoral thesis and that said article cannot, therefore, form part of any doctoral thesis.

And for all intents and purposes, hereby signs this document.

Signature

G. Pratten

Palma de Mallorca, 11/05/2020

Universitat
de les Illes Balears

Dr Sascha Husa, as co-author of the following article

 Title: Validity of common modelling approximations for precessing binary black holes
with higher-order modes

*Journal ref. :   Phys. Rev. D **101**, 103014 (2020)*

Authors: Antoni-Ramos-Buades, Patricia Schmidt, Geraint Pratten, Sascha Husa.

I DECLARE:

Accepts that Mr Antoni Ramos Buades presents the cited article as the principal author
and as a part of his doctoral thesis and that said article cannot, therefore, form part of
any doctoral thesis.

And for all intents and purposes, hereby signs this document.

Signature

Palma de Mallorca, 11/05/2020

Abbreviations

ADM	**A**rnowitt **D**eser Misner
BAM	Bifunctional**A**daptive**M**esh
BH	**B**lack **H**ole
BBH	**B**inary **B**lack **H**ole
BNS	**B**inary **N**eutron **S**tar
BSSNOK	**B**aumgarte **S**hapiro **S**hibata **N**akamura **O**ohara **K**ojima
CBC	**C**ompact **B**inary **C**oalescence
CPU	**C**entral **P**rocessing **U**nit
cWB	**c**oherent **W**ave **B**urst
eBBH	**e**ccentric **B**inary **B**lack **H**ole
DPF	**D**ominant **P**olarization **F**rame
EM	**E**lectro**M**agnetic
EMRI	**E**xtreme **M**ass **R**atio **I**nspiral
EOB	**E**ffective **O**ne **B**ody
EOS	**E**quation **O**f **S**tate
ET	**E**instein**T**oolkit
FAD	**F**alse **A**larm **D**ismissal
FAP	**F**alse **A**larm **P**robability
FAR	**F**alse **A**larm **R**ate
GR	**G**eneral **R**elativity
GRB	**G**amma **R**ay **B**urst
GW	**G**ravitational **W**aves
IMBH	**I**ntermediate **B**lack **H**ole
IMR	**I**nspiral **M**erger **R**ingdown
ISCO	**I**nner**M**ost **S**table **C**ircular **O**rbit
LIGO	**L**aser **I**nterferometer **G**ravitational **W**ave **O**bservatory
LSC	**L**IGO **S**cientific **C**ollaboration
LISA	**L**aser **I**nterferometer **S**pace **A**ntenna
NSBH	**N**eutron **S**tar **B**lack **H**ole
NR	**N**umerical **R**elativity
MCMC	**M**arkov **C**hain **M**onte**C**arlo
MECO	**M**inimum **E**nergy **C**ircular **O**rbit
O1	First **O**bserving run of the LIGO gravitational wave detectors.
O2	Second **O**bserving run of the LIGO and Virgo gravitational wave detectors
O3	Third **O**bserving run of the LIGO and Virgo gravitational wave detectors
PN	**P**ost **N**ewtonian
PE	**P**arameter **E**stimation
PSD	**P**ower **S**pectral **D**ensity
QC	**Q**uasi **C**ircular
QK	**Q**uasi **K**eplerian
QNM	**Q**uasi**N**ormal **Mode**
SNR	**S**ignal to **N**oise **R**atio

SNIa	**S**uper**N**ovae type Ia
SPA	**S**tationary **P**hase **A**pproximation
TF	**T**ime **F**requency
TT	**T**ransverse **T**raceless
WDM	**W**ilson **D**aubechies **M**eyer